Universität Zürich[UZH]

Physik-Institut

Annual Report
April 2013 - March 2014

Universität Zürich[UZH]

Physik-Institut

Annual Report
April 2013 - March 2014

Winterthurerstrasse 190, CH-8057 Zürich/Schweiz

Front picture: smiling faces in front of the FlashCam camera structure (see Sec.7) built up in the workshop assembly hall. From left to right: Kurt Bösiger, Stefan Steiner, Achim Vollhardt, Arno Gadola and Roman Gredig. The picture on the back cover shows actuators of the Active Mirror Control, meanwhile installed on a prototype telescope in Zeuthen.

Secretariat	044 635 5721	sekretariat@physik.uzh.ch
Prof. L. Baudis	044 635 5777	lbaudis@physik.uzh.ch
Prof. F. Canelli	044 635 5784	canelli@physik.uzh.ch
Prof. V. Chiochia	022 767 6041	vincenzo.chiochia@cern.ch
Prof. H.-W. Fink	044 635 5801	hwfink@physik.uzh.ch
Prof. T. Gehrmann	044 635 5818	thomas.gehrmann@physik.uzh.ch
Prof. H. Keller	044 635 5748	keller@physik.uzh.ch
Prof. B. Kilminster	044 635 5802	bjk@physik.uzh.ch
Prof. J. Osterwalder	044 635 5827	osterwal@physik.uzh.ch
Prof. S. Pozzorini	044 635 6014	pozzorin@physik.uzh.ch
Prof. A. Schilling	044 635 5791	schilling@physik.uzh.ch
Prof. N. Serra	022 767 9942	nicola.serra@cern.ch
Prof. A. Signer	056 310 3661	adrian.signer@psi.ch
Prof. D. Wyler	044 635 5817	wyler@physik.uzh.ch
Prof. U.D. Straumann	044 635 5768	strauman@physik.uzh.ch

The annual reports are available on the internet: http://www.physik.uzh.ch/reports.shtml.

Preface

As of January 1st, 2014, the theoretical and experimental physics institutes of the University of Zurich re-united into a single department. After extensive discussions about how to merge the different cultures and regulations into a successful new organisation. This step will further strengthen the existing cooperations between experimental and theoretical research groups in elementary particle physics. In the context of the merging process a new professor position in theoretical condensed matter physics has been created, both to support the experimental research activities and to re-establish profound teaching of theoretical methods, mainly at the master level.

At the same time parts of the former theory institute founded a new *Institute for Computational Science* concentrating on the development of simulation algorithms applicable in high performance computers with the goal to expand into other disciplines like bio-informatics, neuro-informatics, statistics, applied mathematics, medicine, chemistry and geography.

With great sadness we learned that our colleague Peter Meier, retired professor for theoretical condensed matter physics, died in March 2014 at age 74. Peter was an intriguing physicist, a charming person and a great mentor for his students. We will miss him. The obituary below summarizes his scientific career and his contributions to the institute in particular.

Theoretical physics at the *Physikalisches Institut* of our university started in 1909, when a chair for theoretical physics was created for Albert Einstein, his first professorship at any university. He was followed by other famous physicists, like Peter Debye, Max von Laue, Erwin Schrödinger and Gregor Wentzel. In 1949 Hans H. Staub and Walter Heitler became professors for experimental and theoretical physics, respectively. H.H. Staub concentrated on nuclear physics research and also initiated the method of nuclear magnetic resonance (NMR), which had been invented shortly before by Felix Bloch in Stanford. W. Heitler worked, among other topics, on renormalization problems and quantum effects in electromagnetic radiation and wrote a famous text book: *The Quantum Theory of Radiation*. At this time, Walter Heitler used *Seminar für theoretische Physik* as his address.

In the early 1950's a strong expansion of the number of students at our university started. Until then their number was only about one-tenth of what it is now and most fields were represented by just one Ordinarius. Many new professor positions were created during this period, also in physics, starting in 1950 with H. Wäffler, an experimental physicist, who worked with cosmic rays on the Jungfraujoch.

In 1958 the institute moved from Rämistrasse 69 to Schönberggasse 9, into a new building designed to the visions of Staub. At that occasion the name of our department was changed into *Physik-Institut*. In the same year Armin Thellung became the second professor in theoretical physics, working in the fields of statistical mechanics and condensed matter and shortly after we find the first mentioning of the *Institut für theoretische Physik*. These innovative activities during the 1950's laid the foundation of the fundamental physics research at our university for the following decades.

55 years later the two institutes merged again and presently the *Physik-Institut* comprises eight experimental and three theoretical chairs, three assistant professors supported by the Swiss National Science Foundation and two additional independent research groups. The institute covers a broad spectrum of research in experimental and theoretical physics, including the physics of biological systems, of nanometer structures, of fundamental properties of materials and of high temperature superconductors as well as surface physics and accelerator and non-accelerator based elementary particle and astroparticle physics.

This report summarizes the activities and achievements of our sixteen research groups during the past year. During the reporting period the institute's 155 employees achieved many new results, as documented by no less than 179 presentations at international conferences, 223 original publications and 17 PhD theses.

Besides pushing back the frontiers of knowledge in our different research projects, communicating our achievements to the public remains a major task which goes beyond the obvious responsibility for the physics education of students at our university. Members of the institute gave talks for the general public and carried out courses about new research developments for high school teachers. We guided school children through our labs, and contributed lectures and demonstration experiments to the *Kinderuniversität*. We organized information days for pupils of the *Gymnasium* and regularly participate in the *European Masterclasses for Particle Physics*. There were 27 such outreach events in 2013, corresponding to about 870 working hours in total.

An important part of the success of our research and our international visibility is based on the excellent technical infrastructure (mechanical and electronics workshop, information technology) and on the highly qualified and strongly motivated technical experts. This allows us to construct state-of-the-art laboratory equipment, and to push experimental methods beyond existing technical limits. Our reliable and efficient administrative staff plays a very important role in creating the excellent working climate which is so beneficial for all of us.

Zürich, June 2014

Prof. Dr. Ueli Straumann

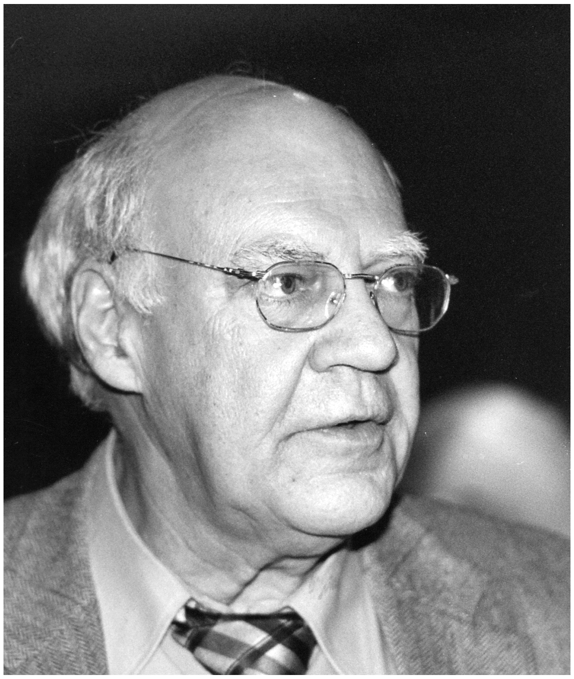

Obituary

Prof. Dr. Peter Fritz Meier

22 April 1940 - 31 March 2014

Peter Meier, longtime staff member of the *Physik-Institut*, died of complications from a difficult surgery on March 31, 2014. He was an *emeritus Titularprofessor* of theoretical condensed matter physics at the University of Zurich.

Peter was born on April 22, 1940 in Aarau (Switzerland). After high school graduation he studied physics at the University of Zurich and received a PhD in theoretical physics in 1968. Peter continued his studies as a postdoc at the University of Nijmegen and at the IBM Research Laboratory in Rüschlikon. Next, he worked for two years as a research associate in the theory group at SIN (Swiss Institute of Nuclear Research) and completed his *Habilitation* at the University of Zurich. In 1977, Peter became a senior research associate (*Oberassistent*) in the group of Prof. Walter Kündig, and in 1981 he was promoted to *Titularprofessor*, conducting his own very active research team since 1992.

Peter's contributions to the field of theoretical condensed matter physics and computational solid state physics have been both manifold and substantial. He was always in close dialog with the experimental physicists in and outside the *Physik-Institut*. Some of his contributions are briefly mentioned here. In his early work he was interested in the interpretation of μSR data of magnetic systems and muonium states semiconductors and isolators with numerical methods. In collaboration with the experimental groups of Prof. Ernst Brun and Prof. Franz Waldner he was also strongly involved in chaos research in nonlinear systems. Soon after the discovery of high-temperature superconductivity in cuprates, Peter started comprehensive investigations of the complex magnetic and electronic properties of cuprate high-temperature superconductors using *ab initio* calculations. In particular, his novel interpretation of NMR and NQR experiments in cuprates was well received. His broad scientific interest is also reflected in an interdisciplinary project with the Medical Faculty of our University dealing with the search for precursors and predictors of epileptic seizures by means of methods devised in nonlinear dynamics.

Peter's lectures in theoretical solid state physics were admired by his students and he was also the founder of the course *Spezielle Informatik für Naturwissenschafter (SPIN)*. He was able to attract many talented students to perform their diploma or PhD work in his group. They characterize him as an honored researcher, teacher, and colleague. Moreover, Peter was an enthusiastic soccer fan, in particular for his home team FC Aarau, and a competent expert on the physics of that game which he even demonstrated on TV on several occasions.

Peter Meier retired end of April, 2005. His friendly and open minded character, his different acts of kindness, his deep insight, and his natural sense of humor made him a respected and trusted person at the *Physik-Institut* and in the physics community world-wide. His legacy is not just in his remarkable contributions to research and teaching, but in the younger generations he inspired. Peter was a great mentor and colleague. We will miss him dearly.

Hugo Keller

Personnel

Scientific personnel

PD Dr. Christof	Aegerter	Sec. 18
Dr. Jonathan	Anderson	Sec. 12
Rubina	Arulanantham	Sec. 16
Daniel	Assmann	Sec. 18
Dr. Martin	Auger	Sec. 4
Peter	Barrow	Sec. 4
Prof. Laura	Baudis	Sec. 3, 4, 5
Dr. Annika	Behrens	Sec. 4, 5
Giovanni	Benato	Sec. 3, 5
Dr. Markus	Bendele	Sec. 14
Carlo	Bernard	Sec. 16
Dr. Roland	Bernet	Sec. 12
Dr. Ruxandra	Bondarescu	Sec. 2
Dr. Saskia	Bosma	Sec. 14
Olaf	Bossen	Sec. 15
Espen	Bowen	Sec. 12
Albert	Bursche	Sec. 12
Lea	Caminada	Sec. 13
Prof. Florencia	Canelli	Sec. 7, 13
Fabio	Cascioli	Sec. 1
Dr. Luca	Castiglioni	Sec. 16
Nicola	Chiapolini	Sec. 12
Prof. Vincenzo	Chiochia	Sec. 13
Marcin	Chrząszcz	Sec. 12
Dr. Huanyao	Cun	Sec. 16
Dr. James	Currie	Sec. 1
Annapaola	de Cosa	Sec. 13
Dr. Michel	de Cian	Sec. 12
Luis Henrique	de Lima	Sec. 16
Lorenzo	de Vittori	Sec. 2
Prof. Jan-Hugo	Dil	Sec. 16
Dominik	Eder	Sec. 18
Christian	Elsasser	Sec. 12
Dr. Andreas	Engel	Sec. 15
Dr. Conrad	Escher	Sec. 17
Carlotta	Favaro	Sec. 13
Prof. Hans-Werner	Fink	Sec. 17
Dr. Arno	Gadola	Sec. 7
Camilla	Galloni	Sec. 13
Prof. Thomas	Gehrmann	Sec. 1
Giulia	Ghielmetti	Sec. 18
Elena	Graverini	Sec. 11, 12
PD Dr. Massimiliano	Grazzini	Sec. 1
Prof. Thomas	Greber	Sec. 16
Roman	Gredig	Sec. 8
Michael	Greif	Sec. 16
Henrik	Grundmann	Sec. 15
Dr. Zurab	Guguchia	Sec. 14
Dr. Kiran K.	Guthikonda	Sec. 3
Patrick	Helfenstein	Sec. 17
Adrian	Hemmi	Sec. 16
Dr. Matthias	Hengsberger	Sec. 16
Andreas	Hinzmann	Sec. 13
Dr. Ludovic	Howald	Sec. 14
Cédric	Huwyler	Sec. 2
Dr. Tomas	Hreus	Sec. 13
Prof. Philippe	Jetzer	Sec. 2
Matthieu	Jaquier	Sec. 1
Dr. Stefan	Kallweit	Sec. 1
Dominik	Kara	Sec. 1
Prof. Hugo	Keller	Sec. 14
Gaudenz	Kessler	Sec. 4
Prof. Benjamin	Kilminster	Sec. 6, 13
Dr. Alexander	Kish	Sec. 4, 5
Rafael	Küng	Sec. 2
Gabriel	Landolt	Sec. 16
Flavio	Lanfranconi	Sec. 18
Clemens	Lange	Sec. 13
Junhui	Liao	Sec. 6
Jonas	Lindert	Sec. 1
Dr. Tatiana	Latychevskaia	Sec. 17
Federica	Lionetto	Sec. 12
Dr. Jean-Nicolas	Longchamp	Sec. 17
Marianna	Lorenzo	Sec. 17
Peter	Lowdon	Sec. 1, 12
Dr. Aaron	Manalaysay	Sec. 3, 7
Gerson	Mette	Sec. 16
Daniel	Mayani Paras	Sec. 4
Irshad	Mohammed	Sec. 2
Niccolo	Moretti	Sec. 1
Dr. Katharina	Müller	Sec. 10, 12
Jan	Niehues	Sec. 1
Ulrike	Nienhaus	Sec. 18
Jennifer	Ngadiuba	Sec. 13
Prof. Jürg	Osterwalder	Sec. 16
Deniz Gizem	Oeztürk	Sec. 1
Payam	Pakarha	Sec. 4
Dr. Andreas	Papaefstathiou	Sec. 1
Gwendolyne	Pascua	Sec. 14
Lionel	Philippoz	Sec. 2
Francesco	Piastra	Sec. 4
Deborah	Pinna	Sec. 13
Prof. Stefano	Pozzorini	Sec. 1
Dirk	Rathlev	Sec. 1

Dr. Peter	Robmann	Sec. 6, 8, 9, 13
Silvan	Roth	Sec. 16
Ronny	Rüttimann	Sec. 16
PD Dr. Prasenjit	Saha	Sec. 2
Daniel	Salerno	Sec. 13
Mirna	Saliba	Sec. 17
Hayk	Sargsyan	Sec. 1
Andreas	Schärer	Sec. 2
Prof. Andreas	Schilling	Sec. 15
Thomas	Schluck	Sec. 18
Adrian	Schuler	Sec. 16
Prof. Nicola	Serra	Sec. 11, 12
Prof. Adrian	Signer	Sec. 1
Roland	Stania	Sec. 16
Dr. Olaf	Steinkamp	Sec. 12
Evelyn	Stilp	Sec. 14
Dr. Barbara	Storaci	Sec. 11, 12
Prof. Ulrich	Straumann	Sec. 7, 8, 10, 12
Lorenzo	Tancredi	Sec. 1
Dr. Silvia	Taroni	Sec. 13
Alessandro	Torre	Sec. 1
Paolo	Torrielli	Sec. 1
Marco	Tresch	Sec. 12
Dr. Andries	van der Schaaf	Sec. 9
Jonas	Verges	Sec. 17
Mauro	Verzetti	Sec. 13
Andreas	Visconti	Sec. 1
Dr. Achim	Vollhardt	Sec. 7, 12, 20
Fabian	von Rohr	Sec. 15
Manuel	Walter	Sec. 3, 5
Dr. Rasmus	Westerström	Sec. 16
Flavio	Wicki	Sec. 17
Dr. Marius	Wiesemann	Sec. 1
Prof. Daniel	Wyler	Sec. 1
Yong	Yang	Sec. 13
Xiaofu	Zhang	Sec. 15

Technical and adminstrative personnel

Kurt	Bösiger	Sec. 19
Tiziano	Crudeli	Technical support
Denis	Dürst	Sec. 19
Daniel	Florin	Sec. 20
Dario	Gabrielli	Sec. 19
Carmelina	Genovese	Secretariat
Ruth	Halter	Secretariat
Alina	Horwege	Sec. 17
Andreas	James	Sec. 3,4
Thomas	Kälin	Sec. 16
Hanspeter	Koch	Lecture demonstrations
Bruno	Lussi	Sec. 19
Reto	Maier	Sec. 19
Brandon	Markwalder	Sec. 19
Esther	Meier	Secretariat
Lucien	Pauli	Lecture demonstrations
Monika	Röllin	Secretariat
Sandra	Saornil Gamarra	Sec. 12
Marcel	Schaffner	Sec. 19
Silvio	Scherr	Sec. 19
Regina	Schmid	Secretariat
Stefan	Siegrist	Sec. 15, 14
Peter	Soland	Sec. 20
Stefan	Steiner	Sec. 7, 12
Pascal	Weyeneth	Sec. 19

Contents

1 Theory of Elementary Particles

F. Cascioli, J. Currie, T. Gehrmann, M. Grazzini, M. Jaquier, S. Kallweit, D. Kara, J. Lindert, P. Lowdon, T. Lübbert, P. Maierhöfer, P.F. Monni, N. Moretti, J. Niehues, G. Oeztürk, A. Papaefstathiou, S. Pozzorini, D. Rathlev, H. Sargsyan, A. Signer, L. Tancredi, A. Torre, P. Torrielli, A. Visconti, G. Watt, E. Weihs, M. Wiesemann, D. Wyler

in collaboration with:
Durham University, INFN Firenze, University of Buenos Aires, Freiburg University, Mainz University, INFN Milano, MPI Munich, INFN Padova, Peking University, Oxford University, INFN Roma, SLAC, ETH Zürich

The particle theory group at the Physik-Institut works on a broad spectrum of research projects dealing with the interpretation of data from high energy particle colliders. Our studies cover precision calculations of benchmark observables, simulation of full collider events, identification of optimal observables for searches and measurements, as well as developments of calculational techniques. We summarize some highlights of last year's research below.

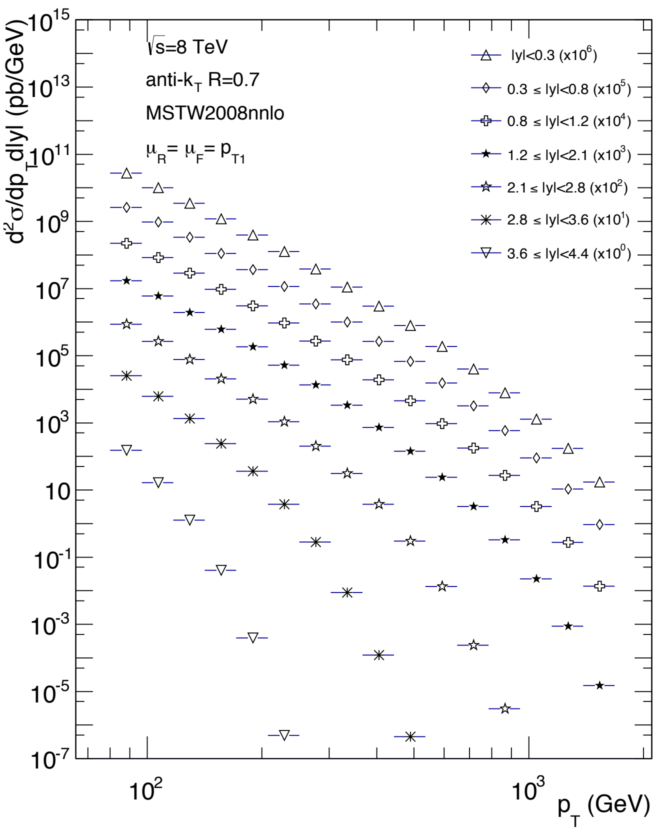

FIG. 1.1 – Doubly differential inclusive jet transverse energy distribution, $d^2\sigma/dp_T d|y|$, at $\sqrt{s} = 8$ TeV for the anti-k_T algorithm with $R = 0.7$ and for $p_T > 80$ GeV and various $|y|$ slices at NNLO.

1.1 NNLO corrections to jet production at hadron colliders

Single jet, inclusive jet and dijet observables are the most fundamental QCD quantities measured at hadron colliders. They describe the basic parton-parton scattering in $2 \to 2$ kinematics, and thus allow for a determination of the parton distribution functions in the proton and for a direct probe of the strong coupling constant α_s up to the highest energy scales that can be attained in collider experiments.

At present, these observables are calculated to next-to-leading order (NLO) precision in QCD, which is insufficient to fully exploit the highly accurate data now available from the LHC experiments. We are currently working towards the computation of the NNLO corrections to jet production at hadron colliders. The major challenge in these calculations is the handling of infrared singular configurations in different subprocesses, which cancel only once they are summed. To implement the different subprocesses in a numerical parton-level event generator program, we have developed the antenna subtraction method, which allows to shift infrared singular contributions between different processes to ensure all cancellations prior to implementation. We have applied this method in the calculation of NNLO corrections to gluon induced jet production [1, 2].

In Fig. 1.1 we present the inclusive jet cross section in double differential form at NNLO as it is measured at the LHC and Tevatron. The inclusive jet cross section is computed in jet p_T and rapidity bins over the range $0.0 - 4.4$ covering central and forward jets. To quantify the impact of the NNLO correction we present the double differential K-factors containing ratios of NNLO, NLO and LO cross sections in Fig. 1.2. We observe that the NNLO correction increases the cross section between 26% at low pT to 14% at high p_T with respect to the NLO calculation. This behaviour is similar for each of the three rapidity slices presented.

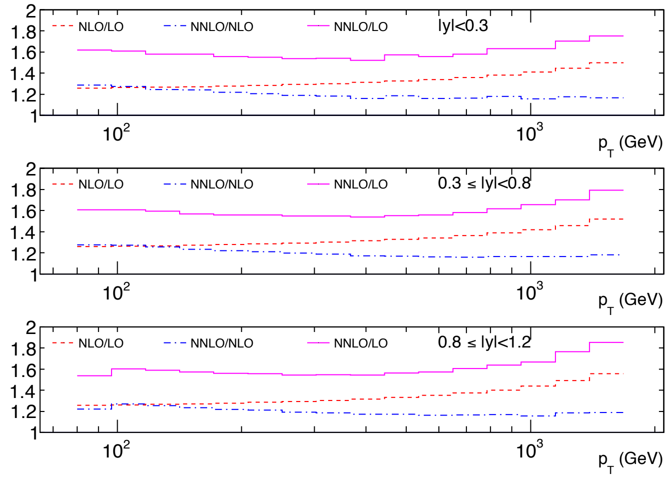

FIG. 1.2 – Ratios of NNLO, NLO and LO cross sections for three rapidity slices: $|y| < 0.3$, $0.3 < |y| < 0.8$ and $0.8 < |y| < 1.2$.

By studying the dependence of the theory prediction on unphysical renormalization and factorization scales, it is possible to estimate the potential magnitude of yet unknown higher order contributions. Going from NLO to NNLO accuracy, we observed a substantial reduction of
2 this scale uncertainty, thus leading to a theoretical precision at the few per cent level. Work on the quark-initiated processes is well underway [3], such that full results on the NNLO corrections at hadron colliders can be expected in due course.

[1] A. Gehrmann-De Ridder, T. Gehrmann, E. W. N. Glover and J. Pires, Phys. Rev. Lett. **110** (2013) 16, 162003.

[2] J. Currie, A. Gehrmann-De Ridder, E. W. N. Glover and J. Pires, JHEP **1401** (2014) 110.

[3] J. Currie, E. W. N. Glover and S. Wells, JHEP **1304** (2013) 066.

1.2 Loop integrals for precision calculations

The calculation of higher order corrections in quantum field theory requires computation of multi-loop Feynman integrals. In particular, NNLO corrections to basic scattering processes require the derivation of two-loop four-point functions for the kinematical situation under consideration. In the framework of dimensional regularization, many powerful techniques have been developed in order to make the computation of two-loop corrections to three- and four-point functions feasible.

Using computer algebra methods, the large number of Feynman integrals appearing in the two-loop four-point function can be reduced to a limited set of so-called master integrals. To compute these master integrals, the differential equation technique has proven to be particularly powerful. Using this technique, we have computed the two-loop master integrals relevant for pair production of massive gauge bosons [1], and for fermionic corrections to top quark pair production [2], thereby enabling the calculation of NNLO corrections to these benchmark processes.

[1] T. Gehrmann, L. Tancredi and E. Weihs, JHEP **1308** (2013) 070.

[2] R. Bonciani, A. Ferroglia, T. Gehrmann, A. von Manteuffel and C. Studerus, JHEP **1312** (2013) 038.

1.3 Heavy quark mass effects in Higgs boson production at the LHC

In July 2012 ATLAS and CMS experiments at the LHC announced the observation of a new scalar resonance of mass $m_H \sim 125$ GeV. To establish to which extent the new resonance is consistent with the long sought Higgs boson predicted by the SM accurate theoretical predictions for the Higgs production cross section and the associated distributions are required. The dominant production channel for the Higgs boson at hadron colliders is gluon fusion, through a heavy-quark loop. For simplicity the calculations are usually performed in the large m_t limit, in which the top loop shrinks to a point. The effects of the finite quark masses are, however, known to significantly affect the shape of the distributions, especially at large transverse momenta of the Higgs boson and or its decay products. In Ref. [1] we have studied the effects of the finite top and bottom masses in the Higgs p_T spectrum.

The implementation of the top-mass dependence does not lead to substantial complications. By contrast, since $m_b \ll m_H$, the inclusion of the exact bottom-mass dependence in the resummed p_T spectrum implies the solution of a non-trivial three-scale problem. We have studied the analytical behaviour of the relevant QCD matrix elements, showing that, when the bottom-quark contribution is considered, naive factorization is valid only in a limited region of the phase space, i.e. when $p_T \lesssim 2m_b$. We have provided a simple solution to this issue by controlling the resummed bottom-quark contribution through an additional resummation scale Q_2, which was chosen of the order of the bottom mass m_b. We have shown that this solution has a clear advantage: it limits the impact of the resummation to the region where it is really needed, i.e. $p_T \lesssim 2m_b$, and our resummed result for the bottom quark contributions smoothly merges with the fixed order NLO result at $p_T \gtrsim 2m_b$, where the resummation is not anymore justified.

We have studied the impact of mass effects on the NLL+NLO calculation, by showing that the effect of heavy-quark masses is significant, although at this order large uncertainties affect the resummed p_T spectrum.

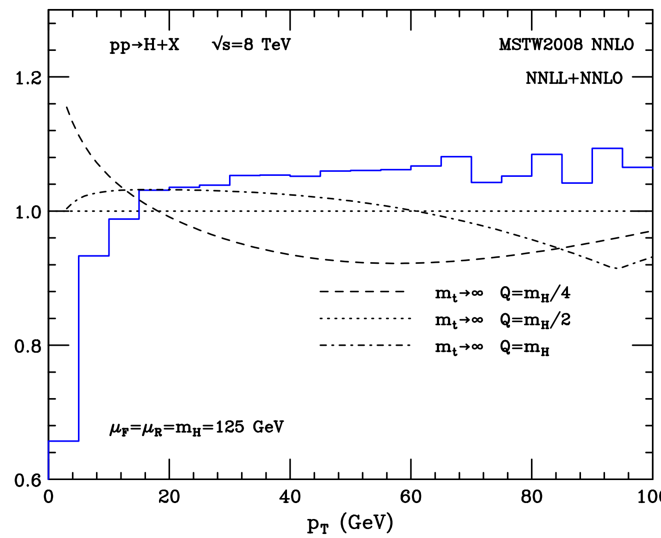

FIG. 1.3 – Transverse momentum spectrum at NNLL+NNLO with full dependence on heavy quark masses ($Q_2 = m_b$) normalized to the result in the large-m_t limit (solid histogram). The result is compared to the NNLL+NNLO results in the large-m_t limit obtained with $Q = m_H, m_H/4$.

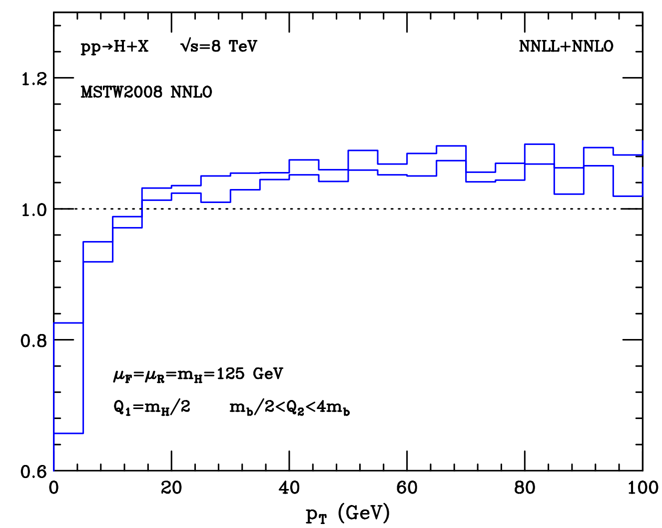

FIG. 1.4 – Transverse momentum spectra at NNLL+NNLO for $m_b/2 < Q_2 < 4m_b$ normalized to the result in the large-m_t limit.

When going to NNLL+NNLO, where the perturbative uncertainties are much smaller, the impact of heavy-quark masses still distorts the spectrum in the low-p_T region (see Figures 1.3 and 1.4). The calculations are implemented in updated versions of the `HNNLO` and `HRes` numerical programs.

[1] M. Grazzini and H. Sargsyan, JHEP **1309** (2013) 129.

1.4 $Z\gamma$ production in NNLO QCD

Vector-boson pair production is crucial in physics studies within and beyond the Standard Model (SM). In particular, the production of neutral vector-boson pairs, like $Z\gamma$, is well suited to search for anomalous couplings.

In Ref. [1] the first complete computation of $pp \to Z\gamma + X$ in NNLO QCD has been reported. We note that the notation "$Z\gamma$" is misleading, as it suggests the production of an on-shell Z boson plus a photon, followed by a factorized decay of the Z boson. Instead, the calculation of Ref. [1] regards the process $pp \to l^+l^-\gamma + X$, where the lepton pair l^+l^- is produced either by a Z boson or a virtual photon, and the contributions in which the final-state photon is radiated from the leptons is consistently included. The NNLO calculation, which relies on the method of Ref. [2] and the results of Ref. [3], is implemented in a numerical program which allows arbitrary cuts on the final state leptons, the photon and the associated jet activity.

The impact of the NNLO corrections strongly depends on the selection cuts. In the ATLAS results the photon is required to have a transverse momentum $p_T^\gamma > 15$ GeV and pseudorapidity $|\eta^\gamma| < 2.37$. The charged leptons are required to have $p_T^l > 25$ GeV and $|\eta^l| < 2.47$, and their invariant mass m_{ll} must fulfil $m_{ll} > 40$ GeV. The separation in rapidity and azimuth ΔR between the leptons and the photon must be $\Delta R(l,\gamma) > 0.7$. Jets are reconstructed with the anti-k_T algorithm with radius parameter $D = 0.4$. A jet must have $E_T^{\text{jet}} > 30$ GeV and $|\eta^{\text{jet}}| < 4.4$. The separation ΔR between the leptons (photon) and the jets must be $\Delta R(l/\gamma, \text{jet}) > 0.3$. With these cuts the NNLO corrections are found to increase the NLO result by 6%. The loop-induced gg contribution amounts to 8% of the $\mathcal{O}(\alpha_S^2)$ correction and thus to less than 1% of σ_{NNLO}.

In Fig. 1.5 a comparison of the NLO and NNLO theoretical predictions with the ATLAS data is presented. We see that the data agree with the NLO and NNLO theoretical predictions within the uncertainties, and that the NNLO corrections slightly improve this agreement.

ATLAS also considers an additional set up with $p_T^\gamma > 40$ GeV. In this case the NNLO corrections are more significant, and increase the NLO result by 15%.

[1] M. Grazzini, S. Kallweit, D. Rathlev and A. Torre, Phys. Lett. B **731** (2014) 204.

[2] S. Catani and M. Grazzini, Phys. Rev. Lett. **98** (2007) 222002.

[3] S. Catani, L. Cieri, D. de Florian, G. Ferrera and M. Grazzini, Nucl. Phys. B **881** (2014) 414.

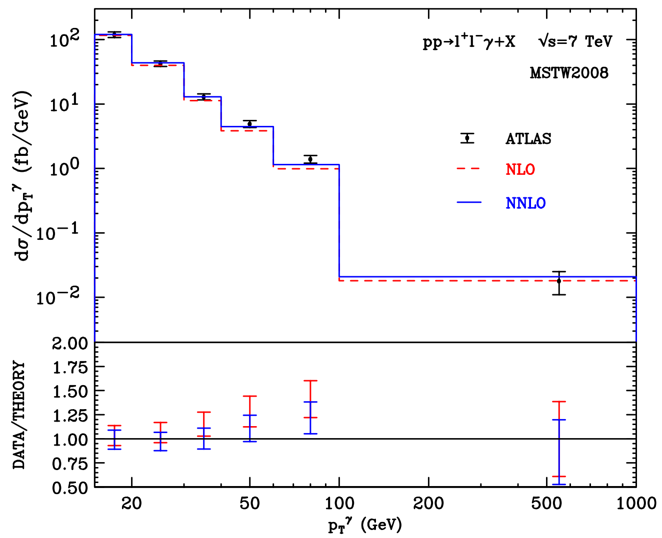

FIG. 1.5 – Transverse momentum spectrum of the photon at NLO and NNLO compared with ATLAS data. The lower panel shows the ratio data/theory.

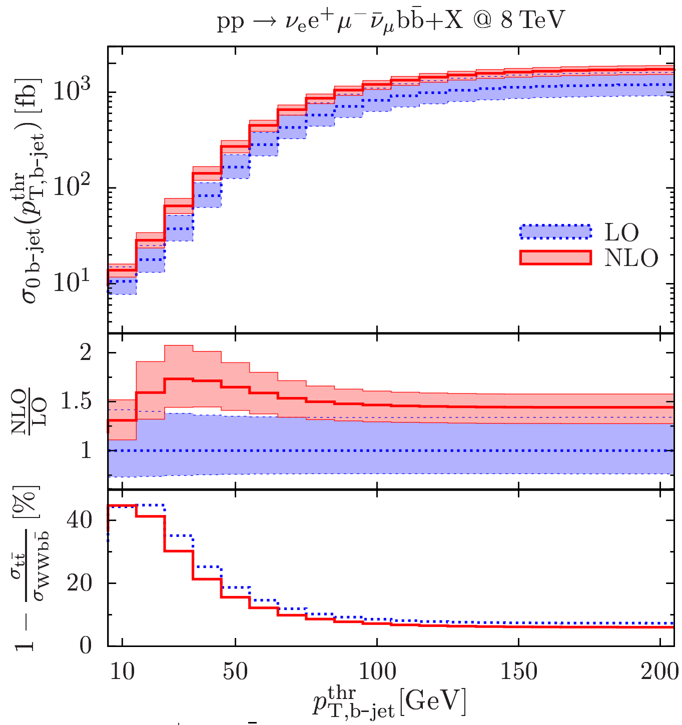

FIG. 1.6 – $W^+W^-b\bar{b}$ cross section as a function of a b-jet veto, $p_{\mathrm{T},b} < p_{\mathrm{T}}^{\mathrm{thr}}$ [2]. The middle and lower frames show the NLO corrections and the corrections with respect to zero-width approximation, respectively.

1.5 A unified description of top-pair and single-top production at the LHC

4

Top quarks are the heaviest fundamental particles known, and the precise theoretical understanding of their production and decay mechanism, within or beyond the Standard Model, has deep implications on many aspects of the LHC physics program.

At the LHC, top quarks can be produced as top-antitop ($t\bar{t}$) pairs or in single-top production modes, where the top quark (or anti-quark) is accompanied either by a light jet or by a W boson. The single-top production modes play an important role as direct probes of top-quark weak interactions and of their flavour structure.

The importance of precise theoretical simulations for the various top-production modes is reflected in a rich and continuously growing literature of higher-order perturbative calculations. In order to keep the complexity of the computations at a manageable level, the production of top pairs, $pp \to t\bar{t}$, and the subsequent top-decays, $t \to W^+b$ and $\bar{t} \to W^-\bar{b}$, are typically handled as separate processes which corresponds to the limit $\Gamma_t \to 0$. An exact treatment requires simulations of the full six-particle processes $pp \to W^+W^-b\bar{b}$, including contributions from off-shell intermediate top quarks pairs as well as intermediate states without or with only one top.

NLO calculations of $pp \to W^+W^-b\bar{b}$ production with finite b-quark masses [2] became possible very recently with the advent of a new generation of NLO algorithms which are based on the OpenLoops method [1], a fast and fully general technique for multi-particle NLO calculations that has been developed by our group. The inclusion of a finite b-quark mass permits, for the first time, to describe regions of the $W^+W^-b\bar{b}$ phase space where one or both b-quarks remain unresolved, and where the massless approximation would give rise to collinear singularities. In particular, the method gives access to final states that are dominated by Wt single-top production. These calculations provide the first unified NLO treatment of top-pair and Wt production, including the quantum interference between these two channels and overcome serious limitations inherent in previous heuristic attempts to treat $t\bar{t}$ and Wt production separately.

Fig. 1.6 shows the $W^+W^-b\bar{b}$ cross section as a function of a b-jet veto, $p_{\mathrm{T},b} < p_{\mathrm{T}}^{\mathrm{thr}}$. The benefit of NLO predictions is evident from the reduced uncertainty band as compared to leading order (LO). In the limit of large jet vetoes, corresponding to the total cross section, deviations from the zero-width approximation are just below 10% (see lower frame). These effects are mainly due to Wt single-top production, and their impact is strongly enhanced by the jet veto, reaching up to 50% of the vetoed cross section. These results demonstrate the relevance of a $W^+W^-b\bar{b}$ calculation for a consistent simulation of top-pair and single-top contributions in presence of jet vetoes or jet bins. This is of great importance for Higgs-boson studies in the $H \to W^+W^-$ decay channel and for any other analysis involving large top backgrounds at the LHC. This calculation is also an ideal theoretical tool for the rich program of top-mass precision measurements at the LHC.

[1] F. Cascioli, P. Maierhöfer and S. Pozzorini, Phys. Rev. Lett. **108** (2012) 111601.

[2] F. Cascioli, S. Kallweit, P. Maierhöfer and S. Pozzorini, Eur. Phys. J. C **74** (2014) 2783.

1.6 Impact of off-shell effects and scheme dependence on the determination of the top quark mass

The top quark mass, m_t, is presently known with an accuracy of $\pm 0.5\%$. To match this precision on the theory side, the process $h_1 h_2 \to t\bar{t} \to W^+ J_b W^- J_{\bar{b}}$, where J_b denotes a b-jet and $h_i \in \{p, \bar{p}\}$, has to be studied very carefully, controlling off-shell effects and sub-leading effects due to interference with so-called background processes.

We have developed an efficient method [1] to take into account these effects near the resonance region. In the single-top case $p\, p \to t\, J \to W^+ J_b\, J$ this method has been compared to a full calculation [2] and excellent agreement has been found in the resonance region.

As an application of this method we have studied [3] the impact of these corrections on observables that are very sensitive to m_t. An example is the transverse mass $M_T(J_b\, W^+)$ of the reconstructed top. At tree level $M_T \leq m_t$ and, therefore, the distribution has a sharp edge, a feature that potentially can be used to measure m_t. As shown in Fig. 1.7, the off-shell and subleading corrections are small except near the edge so these effects need to be taken into account for an accurate determination of m_t.

We have also studied the use of different mass schemes and found scheme ambiguities of the order of 500 MeV for m_t [3]. Usually m_t is identified with the pole mass. However, the pole mass is known to suffer from renormalisation ambiguities. Thus other schemes might be preferable and should be studied carefully.

[1] P. Falgari, F. Giannuzzi, P. Mellor and A. Signer, Phys. Rev. D **83** (2011) 094013.

[2] A. S. Papanastasiou *et al.*, Phys. Lett. B **726** (2013) 223.

[3] P. Falgari, A. S. Papanastasiou and A. Signer, JHEP **1305** (2013) 156.

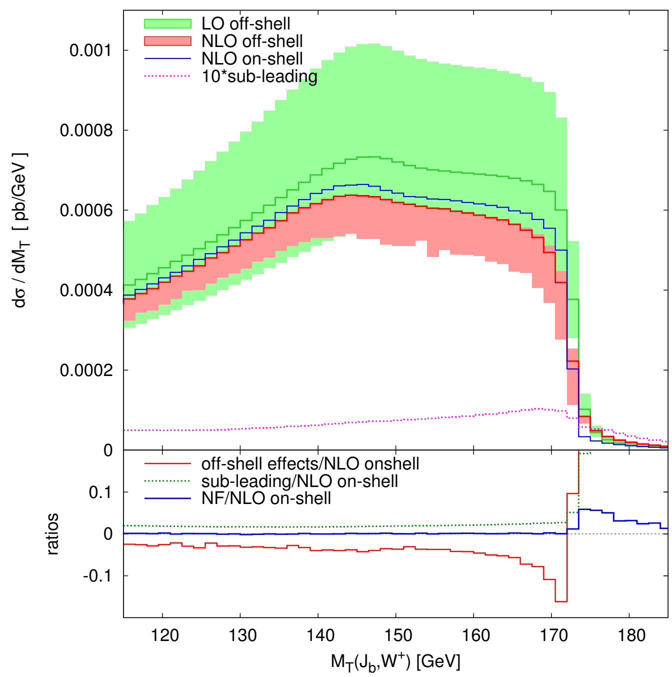

FIG. 1.7 – Transverse mass distribution at the Tevatron for the reconstructed top quark.

2 Astrophysics and General Relativity

R. Angèlil, S. Balmelli, R. Bondarescu, L. De Vittori, C. Huwyler, Ph. Jetzer, R. Küng, I. Mohammed, L. Philippoz, P. Saha and A. Schärer

2.1 Gravitational Lensing

2.1.1 Microlensing

We worked on different aspects of galactic gravitational microlensing. The PLAN (Pixel Lensing ANdromeda) Collaboration, of which we are a member, got observing time both at the 1.5 m Loiano telescope at the Osservatorio Astronomico di Bologna (2006 till 2010) and at the 2 m HCT (Himalayan Chandra Telescope) telescope in India (during 2010). Recently, we published our final results based on a fully automated pipeline for the search and the characterization of microlensing flux variations: altogether we detected 3 microlensing candidates. We evaluated the expected signal with the help of a Monte Carlo simulation of the experiment completed with an analysis of the reconstruction efficiency of our pipeline. We considered both "self lensing"and "MACHO lensing" lens populations, given by M31 stars and dark matter halo MACHOs, in the M31 and the Milky Way, respectively. The small number of events at disposal, did not allow us to put strong constraints on the nature of the events. Rather, the hypothesis, suggested by a previous analysis, on the MACHO nature of OAB-07-N2, one of the microlensing candidates, translated into a sizeable lower limit for the halo mass fraction in form of the would be MACHO population of about 15% for 0.5 $M_{\odot}$ MACHOs.

We completed an analysis of the results of the EROS-2, OGLE-II, and OGLE-III microlensing campaigns towards the Small Magellanic Cloud (SMC). Through a statistical analysis we addressed the issue of the nature of the reported microlensing candidate events, whether to be attributed to lenses belonging to known population (the SMC luminous components or the Milky Way disc, to which we broadly refer to as "self lensing") or to the would be population of dark matter compact halo objects (MACHOs). Our analysis showed that in terms of number of events the expected self lensing signal may indeed explain the observed rate. However, the characteristics of the events, spatial distribution and duration (and for one event, the projected velocity) rather suggested a non-self lensing origin for a few of them [1, 2].

2.1.2 Cluster lensing

We developed a statistical strong lensing approach to probe the cosmological parameters exploiting multiple redshift image systems behind massive galaxy clusters [3]. Our method relies on free-form inversion of galaxy clusters by considering the statistical dispersion of the parameter space describing the mass distribution. This provides information about the assumed cosmological model and thus an estimate of the cosmological parameters, but requires to sample a high-dimensional convex polytope in 100 or more dimensions. Previous sampling strategies used for free-form reconstruction of gravitational lenses were unable to produce unbiased samples.

Another work was a new analysis of a strong-lensing cluster (ACO 3827), showing robust evidence for offsets of a few kiloparsecs between the galaxies and mass peaks [4]. Several possible explanations for this are considered, the most intriguing being interactions between baryons and dark matter.

2.2 Gravitational waves and LISA

Within our group we addressed various topics on gravitational wave physics. We studied gravitational waves emitted by compact binaries on unbound orbits (hyperbolic encounters). Since it is desirable to have ready-to-use search templates, consisting of the two GW polarization states h_+ and $h_\times$, in order to detect waves with the new generation ground-based and the proposed space-borne interferometric detectors, we developed an efficient and accurate prescription to find the explicit waveform radiated during such an encounter. We provided a semi-analytical approach using the traditional post-Newtonian expansion up to 1PN order in the dynamics, including leading order spin-orbit interaction, which has never been done before.

We studied the impact of alternative general relativistic (GR) theories on the parameter estimation for coalescing massive black holes as could be performed by a LISA-type detector, such as eLISA. This has been achieved by introducing correction parameters that account for modified gravity into the second post-Newtonian gravitational wave phase for circular, black hole binaries with precessing spins. In order to find LISA's measurement accuracy for physical parameters of the binaries, we used the Fisher matrix approach and carried out Monte Carlo simulations for several black hole binary mass combinations. Moreover, we made a detailed study on the adopted criteria on the choice of a critical orbit at which the integrations need to be stopped. We found that the corrections can be measured with sufficient accuracy for total binary black hole masses up to a few $10^7\ M_\odot$ at redshift $z = 1$, errors increasing with redshift. The introduction of alternative theory parameters still leads to a reasonable accuracy of the binary parameters such as masses and spins.

Currently we are investigating more realistic scenarios. While in our previous study, theoretical estimates of the expected error distributions of suggested alternative theory parameters could be made, it is still uncertain whether eLISA will be able to actually recover such alternative theory parameters. We are working on a Markov Chain Monte Carlo framework which tests eLISA's ability to recover the alternative theory parameters of a gravitational wave signal injected into the expected noise background. This will allow us to see whether in practice eLISA will be able to distinguish the underlying theory from GR at all or whether some other spacecraft configuration could be more favorable.

Coalescing black hole binaries are expected to be one of the most relevant gravitational wave sources for the currently operating (LIGO, Virgo) and planned (eLISA) detectors. Up to now, the Effective-one-body (EOB) approach is the only (semi-)analytical method which has been able to reproduce the waveform of the full evolution (inspiral, merge and ringdown) of coalescing black holes. Our work has focused on improving the description of spinning black holes within the EOB formalism. The main motivation lies in the fact that black holes are generally expected to have a spin, and that gravitational wave signals from co-rotating black holes are stronger than in the non-spinning case. Moreover, the EOB approach is currently not sufficiently accurate to reproduce reliable waveforms if the black holes are rapidly spinning [5, 6].

2.2.1 LISA Pathfinder

We are member of the LISA and LISA Pathfinder science teams and of its consortium. LISA Pathfinder is a dedicated technology demonstrator for the joint ESA/NASA Laser Interferometer Space Antenna (LISA) mission. The technologies required for LISA are extremely challenging. LISA Pathfinder essentially mimics one arm of the LISA constellation by shrinking the 5 million kilometer arm length down to a few tens of centimeters, giving up the sensitivity to gravitational waves, but keeping the measurement technology: the distance between the two test masses is measured using a laser interferometric technique similar to one aspect of the LISA interferometry system. The scientific objective of the LISA Pathfinder mission consists then of the first in-flight test of low frequency gravitational wave detection metrology [7–9].

2.3 Space clocks and relativity

It is well known that GPS satellites are sensitive to general-relativistic effects (specifically gravitational time dilation). Clock technology has advanced greatly in recent years, and space-based clocks now being planned would be able to measure space curvature and frame dragging to a planet as well [10].

2.4 Further topics

Some further topics were explored, together with Masters students.

2.4.1 Lens Modeling

R. Küng in his MSc project developed a system for volunteers, who are not professionals but do have amateur expertise in the topic, to model gravitational lens candidates. This is part of the *Spacewarps* citizen-science project to discover new gravitational lenses.

2.4.2 Next-Generation Interferometry

T. Wentz in her MSc project studied the possibility of measuring phase in the Hanbury Brown and Twiss effect, following up on work involving our group suggesting three-point HBT interferometry for astronomical sources [11].

[1] PLAN Collaboration, S. Calchi Novati *et al.*, ApJ **783** (2014), 86.

[2] S. Calchi Novati, S. Mirzoyan, P. Jetzer and G. Scarpetta, MNRAS **435** (2013), 1582.

[3] M. Lubini, M. Sereno, J. Coles, P. Jetzer and P. Saha, MNRAS **437** (2014), 2461.

[4] I. Mohammed, J. Liesenborgs, P. Saha and L. L. R. Williams, MNRAS **439** (2014), 2651.

[5] S. Balmelli and P. Jetzer, Phys Rev D **87** (2013), 124036.

[6] L. De Vittori, P. Jetzer and A. Klein, *Power Spectrum of Gravitational Waves from Unbound Compact Binaries*, 9th LISA Symposium, ASPC Series **467** (2013), 331.

[7] P. McNamara *et al.*, *The LISA Pathfinder Mission*, 9th LISA Symposium, ASPC Series **467** (2013), 5.

[8] M. Nofrarias *et al.*, *State Space Modeling and Data Analysis Exercises in LISA Pathfinder*, 9th LISA Symposium, ASPC Series **467** (2013), 161.

[9] P. Amaro-Seoane *et al.*, GW Notes **6** (2013), 4.

[10] R. Angélil, P. Saha, R. Bondarescu, P. Jetzer, A. Schärer and A. Lundgren, Phys Rev D**89** (2014), 064067.

[11] V. Malvimat, O. Wucknitz and P. Saha, MNRAS**437** (2014), 798.

3 GERDA: Neutrinoless Double Beta Decay in Ge

L. Baudis, G. Benato, K. Guthikonda (until September 2013), A. James, M. Walter

in collaboration with: INFN Laboratori Nazionali del Gran Sasso LNGS, Institute of Physics, Jagellonian University Cracow, Institut für Kern- und Teilchenphysik Technische Universität Dresden, Joint Institute for Nuclear Research Dubna, Institute for Reference Materials and Measurements Geel, Max Planck Institut für Kernphysik Heidelberg, Universitá di Milano Bicocca e INFN Milano, Institute for Nuclear Research of the Russian Academy of Sciences, Institute for Theoretical and Experimental Physics Moscow, Russian Research Center Kurchatov Institute, Max-Planck-Institut für Physik München, Dipartimento di Fisica dell Universitá di Padova e INFN, Physikalisches Institut Eberhard Karls Universität Tübingen.

(GERDA Collaboration)

When neutrinos propagate over macroscopic distances they can change their flavor eigenstate (so lepton flavor is not conserved), which means that neutrinos have mass. However, some important neutrino properties still remain unknown, such as the absolute mass scale, the full neutrino mixing matrix (including CP-violating phases) and their nature (Dirac versus Majorana). The Majorana nature of neutrinos can be revealed in experiments searching for neutrinoless double beta decay ($0\nu\beta\beta$), in which an atomic nucleus decays by emitting two electrons sharing the Q-value of the process. If the neutrino is a Majorana particle, this transition is allowed in all isotopes that undergo the allowed standard double beta decay ($2\nu\beta\beta$).

GERDA is an experiment searching for the $0\nu\beta\beta$ decay in ^{76}Ge ($Q = 2039.006 \pm 0.050$ keV). The material is enriched in ^{76}Ge, and provides simultaneously the source and detector with an energy resolution of 0.1-0.2 % FWHM at 2 MeV. A novel shielding concept features bare germanium diodes operated in a 65 m^3 cryostat filled with liquid argon and surrounded by a 3 m thick water Cerenkov shield which moderates and captures external and muon-induced neutrons. The argon is used for cooling the diodes and as a passive shield against the residual environmental background [2].

The experiment proceeds in two phases. Phase I uses eleven HPGe detectors, eight enriched in ^{76}Ge and three detectors made of ^{nat}Ge, with the total masses of 17.7 kg and 7.6 kg, respectively. The goal at this stage is to improve the current sensitivity levels and scrutinize the results of the Heidelberg-Moscow experiment [1]. Data taking took place between November 2011 and June 2013 at a background level of 10^{-2} counts$\cdot$keV$^{-1}\cdot$kg$^{-1}\cdot$yr^{-1} [3]. A total exposure of 21.6 kg$\cdot$yr resulted in an experimental limit on the $0\nu\beta\beta$ half life $T^{0\nu}_{1/2} > 2.1\cdot10^{25}$yr [4].

Phase II will use additional enriched broad-energy germanium (BEGe) detectors with enhanced pulse shape discrimination (PSD) performance and aims at a total exposure of 100 kg$\cdot$yr. The design background is 10^{-3} counts$\cdot$keV$^{-1}\cdot$kg$^{-1}\cdot$yr^{-1} thanks to the instrumentation of the liquid argon with photon detectors allowing to veto background induced by extrinsic radioactive impurities. Data taking will start in summer 2014 and the projected sensitivity after three years of data acquisition is $2\cdot10^{26}$ yr.

[1] H.V. Klapdor-Kleingrothaus *et al.*, Phys. Lett. **B586**, 198 (2004).

[2] M. Agostini *et al.* (GERDA Collaboration), Eur. Phys. J. C73, 2330 (2013).

[3] M. Agostini *et al.* (GERDA Collaboration), Eur. Phys. J. C74, 2764 (2014).

[4] M. Agostini *et al.* (GERDA Collaboration), Phys. Rev. Lett. 111, 122503 (2013).

3.1 Analysis of the Phase I calibration data

Large attention was paid to the energy resolution which directly affects the background level. The calibration of the energy scale and resolution of the individual detectors was performed weekly with the insertion of three ^{228}Th sources in the vicinity of the detectors. The frequent calibration of a dozen detectors requires an automated analysis. After basic quality cuts are applied,

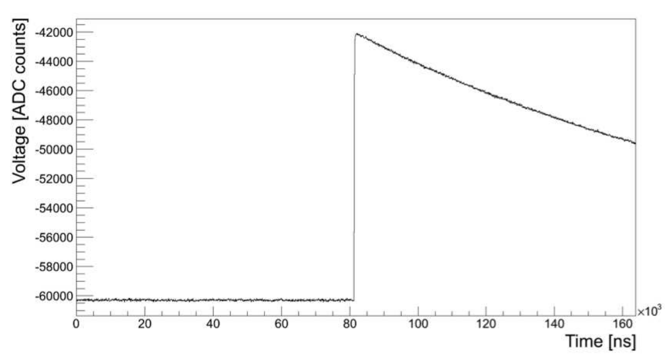

FIG. 3.1 – Original waveform recorded by GERDA.

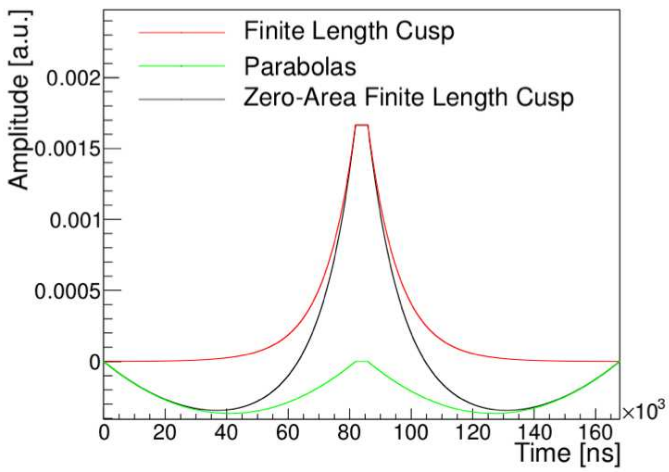

FIG. 3.2 – Finite-length cusp filter matching the 170 μs waveform records. The flat top maximizes the charge integration and the "zero-area" removes low-frequency baseline fluctuations.

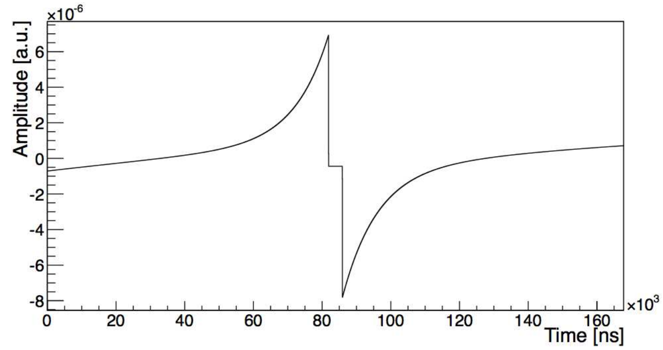

FIG. 3.3 – Filter resulting after convolution with the response function of the charge-integrating pre-amplifier.

and coincidence and pile-up events are rejected, gamma-peaks are identified and fitted. We observed that the energy resolution was deteriorated in the presence of low-frequency fluctuations in the baselines of the recorded pre-amplifier waveforms (see Fig. 3.1). A digital shaping filter with enhanced low-frequency rejection has been developed [1]. Cusp filters are known to maximize the noise whitening [2]. The filter was defined on the full region of the recorded waveform and biased to give zero total area for minimal sensitivity to baseline fluctuations. A flat top garantees optimal charge integration. Fig. 3.2 illustrates the procedure. The signal shaping induced by the preamplifier is taken into account by a convolution with the preamplifier's response function; the result is shown in Fig. 3.3. The filter parameters have been tuned for optimal performance for each detector individually.

All Phase I data were reprocessed with this new filter, leading to an average improvement of 0.3 keV at $Q_{\beta\beta}$ for the calibration data, as shown in Fig. 3.4. The improvement is even better for the background data ($\sim$0.5 keV), due to the strong noise reduction property of the cusp filter, which minimizes the peaks broadening in the data merged from different runs. The resolution improvement in the physics reach of GERDA Phase I results in $\sim$5% improvement of the median sensitivity. Thus, the developed cusp filter will be used as a default shaping filter for the Phase II data analysis.

[1] G. Benato, V. D'Andrea *et al.*, *"Performances of germanium detectors by optimized readout and digital filtering techniques in the framework of the GERDA experiment"*, poster presented at the TAUP conference, Asilomar, California USA (September 2013).

[2] M.O. Deigthon, IEEE Trans. Nucl. Sci. 16, 68-75 (1969).

[3] E. Gatti *et al.*, Nucl. Instr. Meth. A 523, 167Ð185 (2004).

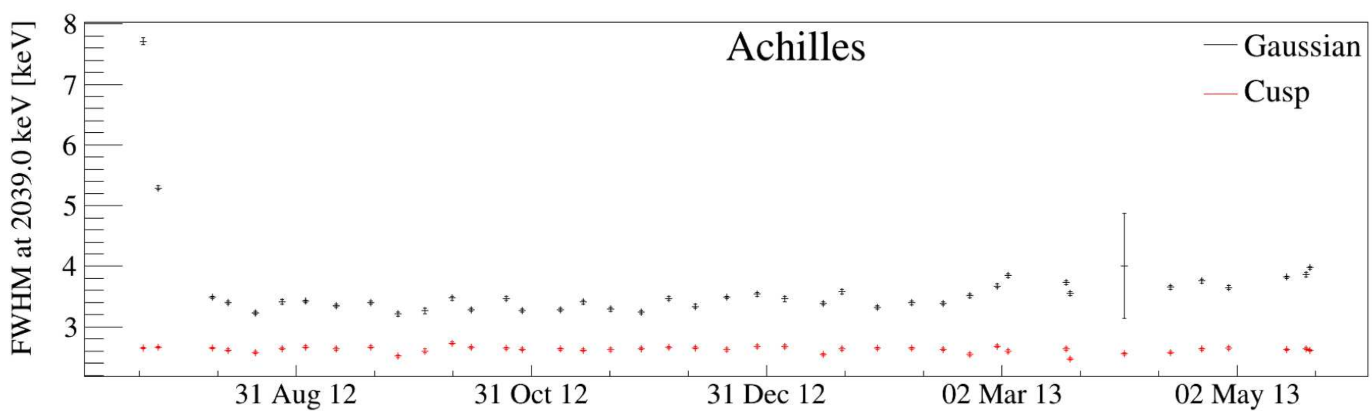

FIG. 3.4 – The energy resolution at $Q_{\beta\beta}$ during the GERDA Phase I data acquisition period for one of the detectors. Note a very significant improvement in resolution (from $\sim$3.5 keV to $\sim$2.8 keV) when moving from Gaussian to cusp filtering.

3.2 Production and characterization of the calibration sources for Phase II

Our group is responsible for the production and characterization of the ^{228}Th calibration sources for the Phase II of the GERDA experiment. The advantages of using ^{228}Th are its relatively long half life (1.9 yr), the presence of a dozen lines in the spectrum and of a double-escape peak at 1592 keV - thus not far from the GERDA region of interest - which is used for tuning the pulse shape discrimination algorithms. The disadvantage is the emission of α-particles by some isotopes of the Th chain, which can induce (α,n) reactions in the materials surrounding the detectors. The produced radiogenic neutrons might then activate the Ge during the calibration measurements.

A reduction of about one order of magnitude in the neutron flux emitted by the sources can be obtained if the ^{228}Th sample is contained in a high-Z material instead of the standard ceramic [1]. Four sources have been produced in December 2013 by depositing $ThCl_4$ solution onto a gold foil, and are now being encapsulated in stainless steel to prevent any loss of radioactive material. The measurement of their activity will be performed in the next months, together with a customized leak test to verify the capsules tightness at cryogenic temperature.

The neutron flux emitted by the sources will be measured with a low-background LiI(Eu) detector operated underground at LNGS (for details see [2]). Calibrations with AmBe neutron source and several measurements with gamma sources were performed in May 2013, which revealed the possible presence of light loss, with a consequent degraded energy resolution. An improvement of the performance was obtained by a more accurate coupling of the LiI(Eu) crystal to the PMT and an additional PTFE sealing (Fig. 3.5), increasing the scintillation light collection efficiency, leading to an improvement of ~30% in the energy resolution of the gamma lines. Since November 2013 the setup is taking background data underground, with an environmental neutron flux of about 0.2 neutrons/day. Results are shown in Fig. 3.6.

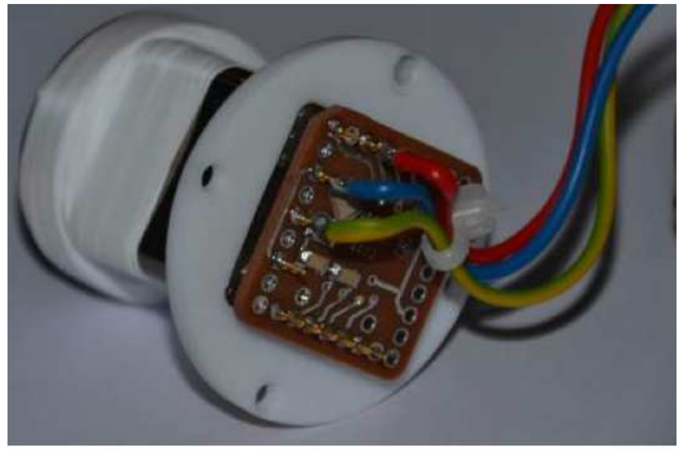

FIG. 3.5 – The LiI(Eu) crystal coupled to a 1-inch Hamamatsu R8520 low-background PMT. The PTFE sealing for light loss reduction is also seen.

[1] W. Maneschg, L. Baudis *et al.*, Nucl. Instrum. Meth. A680, 161-167, (2012).

[2] M. Tarka, *"Studies of the neutron flux suppression from a γ-ray source and the GERDA calibration system"*, PhD Thesis, UZH (2012).

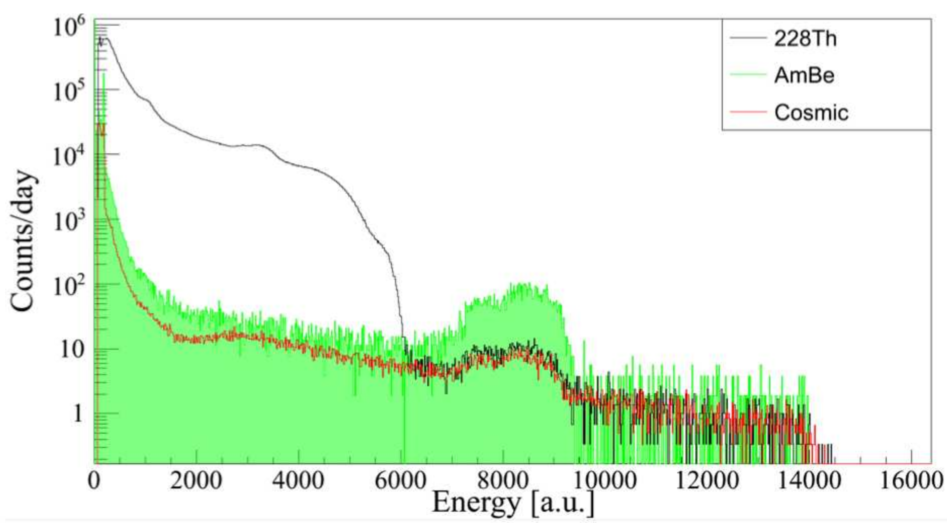

FIG. 3.6 – Spectra acquired with a strong ^{228}Th source, a ^{241}AmBe neutron source, and with cosmic radiation in the external laboratory at LNGS.

4 Cold Dark Matter Search with XENON

M. Auger, P. Barrow, L. Baudis, A. Behrens (until December 2013), A. James, G. Kessler, A. Kish, D. Mayani, F. Piastra

in collaboration with: Columbia University, UCLA, INFN, University of Münster, Coimbra University, Subatech, The Weizmann Institute of Science, University of Mainz, SJTU, MPIK Heidelberg, Rice University, University of Bologna, Nikhef, Purdue University, Albert Einstein Center for Fundamental Physics Bern

(XENON Collaboration)

The XENON project aims at the direct detection of dark matter in the form of Weakly Interacting Massive Particles (WIMPs). Presently, a second generation detector (XENON100 [1]) is in operation at the Laboratory Nazionali del Gran Sasso (LNGS, Italy). A 161 kg double-phase Xe time-projection chamber (TPC) employs two arrays of low-radioactivity, VUV-sensitive photomultipliers (PMTs) to detect the prompt (S1) and proportional (S2) scintillation light signals induced by particles interacting in the active detector region, containing 62 kg of ultra-pure liquid xenon (LXe). The remaining 99 kg of LXe act as an active veto shield against background events.

A data acquisition period with a total lifetime of ~150 days was recently completed, extending the detector operation to the fifth year and increasing the sensitivity of the search for an annual modulation. The analysis of these data is in an advanced stage and unblinding is expected within a couple of months. A study of the XENON100 response to single electrons has been published recently [2], improving our understanding of the double-phase xenon-based TPC, and enabling searches for low energy events (i.e. WIMP-electron interactions for WIMP masses below 1 GeV/c^2) based on S2 signal alone.

The next phase in the XENON dark matter search program, the XENON1T experiment, is housed in Hall B at LNGS. The detector contains 3 t of LXe surrounded by a 9.6 m diameter water Cerenkov shield. The cryostat will be a double-walled super-insulated pressure vessel, made of stainless steel. The inner vessel will house the liquid xenon, the TPC and two arrays of photomultiplier tubes (PMTs). The TPC will be made of interlocking PTFE panels, and the drift field homogeneity will be achieved with equidistant OFHC field shaping rings connected with high-ohmic HV resistors. The photosensors will be arranged in two arrays, containing 127 PMTs above the target in the gas phase, and 121 PMTs at the bottom of the sensitive liquid xenon volume.

Our group is responsible for constructing the TPC field cage, as well as for the PMT arrays assembly (together with MPIK-Heidelberg). The photodetectors for the XENON1T experiment are 3-inch R11410-21 PMTs with an average quantum efficiency (QE) at the xenon scintillation wavelength (178 nm) of 36%, developed and optimized by Hamamatsu Photonics in close collaboration with our research group at UZH. As the results of the extensive testing and measurements, we provided information on their performance in cryogenic xenon environments and on radioactive contamination.

[1] E. Aprile *et al.*, Astropart. Phys. 35, 573-590 (2012).
[2] E. Aprile *et al.* (XENON Collaboration), J. Phys. G: Nucl. Part. Phys. 41, 035201 (2014).

4.1 Radioactive contamination of the photosensors

All XENON1T tubes are screened with high-purity Ge detectors, in particular Gator [1] operated by the UZH group, and with mass-spectrometry before their installation into the detector in order to verify their low radioactivity values. In order to ensure a safe and consistent handling of all PMTs during the screening process, a low-background PTFE holder was fabricated, shown in Fig. 4.1 with 16 photosensors in the screening chamber which is the largest number of tubes that can be measured at once. For most relevant isotopes a sensitivity below 1 mBq/PMT can be reached after about 18 days of measuring time. As an example the spectrum for batch C is shown in Fig. 4.2 along with the background spectrum of the Ge detector itself.

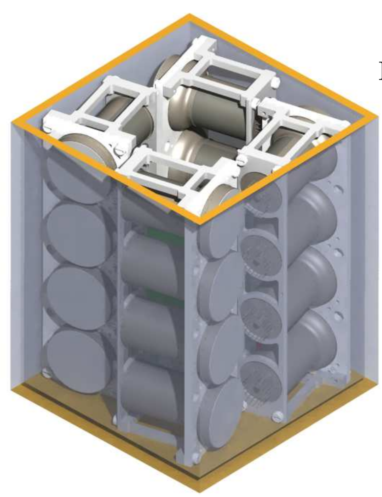

Fig. 4.1 – Sixteen Hamamatsu R11410 PMTs in the Ge detector chamber, fixed by custom-made, low-background PTFE holders.

Tab. 4.1 – Results of the gamma-spectroscopy screening for the various R11410 PMT batches. The number of measured tubes and the measuring time are indicated. Upper limits are given at 90% confidence level, and the quoted errors include statistical and systematic errors. The ^{137}Cs activity is $(0.2 - 0.3)$ mBq/PMT for all batches.

batch	PMTs	days	Activity [mBq/PMT]							
			^{238}U	^{226}Ra	^{235}U	^{232}Th	^{228}Th	^{40}K	^{60}Co	^{110m}Ag
A	10	26	< 18	0.4(1)	0.5(1)	< 1.1	0.4(1)	12(2)	0.7(1)	0.89(1)
B	16	15	< 16	0.5(1)	0.29(9)	< 0.85	< 0.61	13(2)	0.79(8)	1.1(2)
C	15	11	< 20	< 0.82	< 0.52	< 1.1	0.5(2)	13(2)	0.73(9)	0.51(7)
D	15	22	< 13	0.5(1)	0.35(9)	0.4(1)	0.4(1)	12(2)	0.73(9)	0.21(4)
E	15	16	< 17	0.6(1)	< 0.57	< 0.93	< 0.62	14(2)	0.63(7)	0.22(6)
F	11	23	< 15	0.6(1)	< 0.55	< 0.77	0.7(1)	14(2)	0.71(7)	0.23(4)

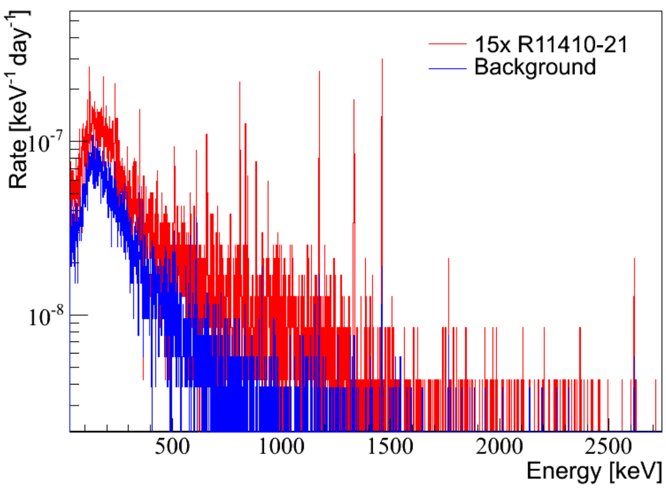

Fig. 4.2 – Energy spectrum of batch C measured in July 2013. The background is obtained by removing the PMTs.

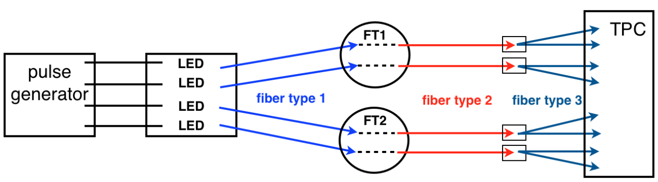

Fig. 4.3 – Schematics of the PMT calibration setup. A 4-channel pulse generator drives four blue LEDs. The LED light is transmitted by standard optical fibers to two dual CF40 optical feedthroughs on the detector flange. From there uncoated 800 μm quartz fibers guide the light into the cryostat. At the TPC end each fiber is split into 2 to 4 branches (180 μm PMMA-PFA fibers).

The screening results for the most relevant radioactive isotopes are shown in Table 4.1. An observed contamination by ^{110m}Ag ($T_{1/2} = 250$ d) was traced back to the silver solder of the ceramic PMT stem.

[1] L. Baudis, A. Ferella *et al.*, JINST 6, P08010 (2011).

4.2 PMT calibration for XENON1T

Long-term operation of the XENON1T detector requires regular calibration of the 248 photosensors. The schematics of our calibration system is shown in Fig. 4.3. Light from external InGaN LEDs ($\lambda = 470$ nm) is uniformly distributed over the sensors through different types of optical fibers. Inside the vacuum quartz fibers with special thermal coating are used, which can be baked up to 200°C. To achieve a uniform illumination of the PMTs, at the TPC end the fibers are split into several branches by means of thin uncoated polymethylmethacrylate (PMMA) fiber bundles with 180 μm core. The system gives a uniform illumination of the PMT arrays and in addition some redundancy in case of failure. PMMA is more flexible than quartz, and hence more suited for the small bending radii inside the cryostat.

The 4-channel pulse generator (BNC-505-4C) is software-controllable via RS-232 interface allowing to remote calibrations. The four LEDs are installed in light-tight enclosures (Fig. 4.4). The initial tests of the calibration system were performed with the UZH test facility for the XENON1T PMTs, the Marmot XL LXe chamber.

Fig. 4.4 – LED modules and matching pulse generator designed by our technician A. James. The picture on the right shows the light-tight enclosure inside an LED module. The light output is provided through an optical SMA connector.

5 DARWIN: dark matter WIMP search in noble liquids

M. Auger, L. Baudis, A. Behrens (until December 2013), G. Benato, A. James, A. Kish, A. Manalaysay (until August 2013), M. Walter

in collaboration with ETHZ, University of Bern, INFN, University of Münster, TU Dresden, Subatech, Weizmann Institute of Science, University of Mainz, MPIK Heidelberg, Rice University, University of Bologna, Nikhef, Karlsruhe University, Columbia University, UCLA, Princeton University, University of Naples, Imperial College London, Arizona State University

DARWIN Consortium

DARk Matter WImp search with Noble Liquids (DARWIN) is an initiative to build the ultimate, multi-ton dark matter detector[1]. The project unites the ample expertise in Europe on liquid noble gas detectors, low-background techniques, cryogenic and underground infrastructures and on the physics issues related to direct dark matter and neutrino detection.

DARWIN's primary goal is to probe the spin-independent WIMP-nucleon scattering cross section for $\sim$50 GeV/c^2 WIMPs down to 10^{-49} cm^2 where irreducible neutrino backgrounds set in. Two other major physics goals are the search for the neutrinoless double beta decay of ^{136}Xe and the first real-time observation of solar pp-neutrinos with high statistics. The pp- and ^{7}Be-neutrinos together account for more than 98% of the total neutrino flux and the real-time measurement of pp-neutrinos would test the main heat production mechanism in the Sun. The flux of ^{7}Be-neutrinos, measured by the Borexino experiment, is $(2.78 \pm 0.13) \times 10^9\,\mathrm{cm}^{-2}\mathrm{s}^{-1}$ [3] assuming pure ν_e neutrinos. However, the most robust predictions of the Standard Solar Model are for the pp-neutrino flux, which is heavily constrained by the solar luminosity and an accurate measurement of the pp-neutrino flux will allow to distinguish between different neutrino oscillation scenarios.

In its baseline scenario, DARWIN would operate a cylindrical $\sim$2.1 m $\times$ 2.1 m liquid xenon time-projection chamber (TPC) in a low-background cryostat, installed in the water shield of the XENON1T and XENONnT at LNGS. Improved external shielding is possible by adding a liquid scintillator veto shield around the cryostat inside the water. To achieve the required drift field (0.5 - 1.0 kV/cm), the cathode on the bottom of the TPC will be biased with voltages around or beyond -100 kV, and the field homogeneity will be optimized by using massive field shaping rings made from oxygen-free high-conductivity (OFHC) copper. The primary scintillation (S1), as well as the proportional scintillation signal from the charge (S2) are detected by two arrays of photosensors installed above and below the liquid xenon target.

Assuming 14 t LXe fiducial mass and an energy window of 2–30 keV, about 5900 pp-neutrinos are expected in DARWIN after 5 years of data collection. The upper energy boundary is motivated by the energy at which the solar neutrino induced electron recoil spectrum and the two-electron spectrum from the $2\nu\beta\beta$-decay of ^{136}Xe intersect.

A detailed study of the DARWIN sensitivity to low-energy solar neutrinos, to coherent neutrino-nucleus scattering and to neutrinoless double beta decay has been performed by our group [2]. The overall background spectrum from the various detector materials including the radioactivity intrinsic to the liquid xenon, such as the $2\nu\beta\beta$-decay of ^{136}Xe with $T_{1/2} = 2.11 \times 10^{21}$ yr [4], is shown in Fig. 5.1. The intrinsic background to xenon as a detection medium poses strong requirements on internal radio-activity levels: a contamination of the liquid xenon with natural krypton of about 0.1 ppt and a radon level in the liquid of about 0.1 μBq/kg are to be ensured. This can be achieved by purifying the noble gas with krypton-distillation columns and with ultra-clean, charcoal-based radon filters, and by the use of materials with low radon

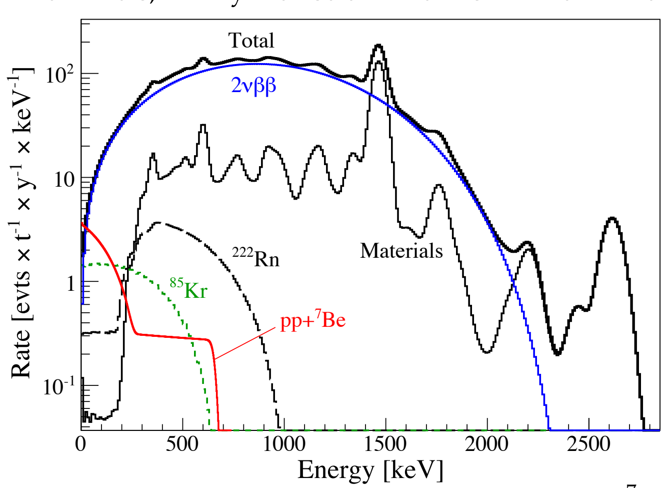

FIG. 5.1 – Total neutrino energy spectrum from pp and ^{7}Be, for a central 14 t region of the detector, compared to the predicted background from detector construction materials and internal contaminations. The background components from 0.1 ppt of natural krypton, 0.1 μBq/kg ^{222}Rn decays and ^{136}Xe $2\nu\beta\beta$-decays are shown separately.

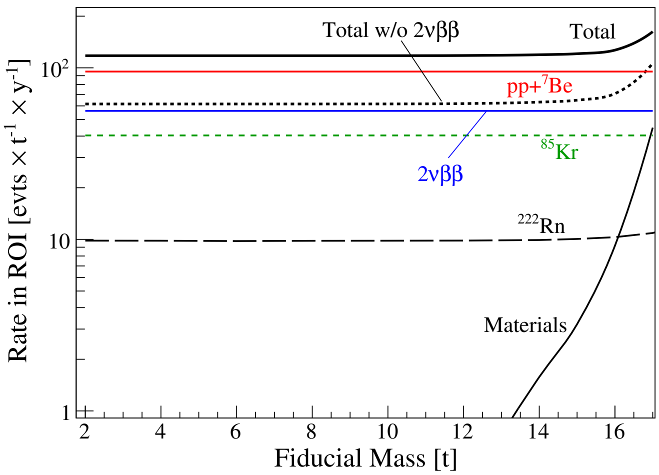

FIG. 5.2 – Predicted signal and background rates in the 2–30 keV energy region versus fiducial liquid xenon mass.

emanation. With 99.8% rejection of ^{214}Bi events using the ^{214}Bi-^{214}Po coincidence [2], the radon-induced background drops about 30% at low energies. The predicted internal background amounts to $\sim$700 events/yr in the region 2–30 keV and, assuming 99.5% rejection of electronic recoils, about 1 event/yr in the region 2–10 keV. This rate is comparable to the ^{136}Xe $2\nu\beta\beta$ background.

External background varies with the fiducial xenon mass (see Fig. 5.2) and we define the central 14 t of LXe as detector region. The external background is dominated by the photosensors, followed by the cryostat, the TPC and the diving bell. In the range 2–30 keV without electronic recoil rejection, DARWIN would observe 19 background events per year. Assuming 99.5% rejection of electronic recoils in the region 2–10 keV, relevant for the dark matter search, this rate drops to 3×10^{-2} events/yr.

The $Q-$value of the double beta decay of ^{136}Xe is (2458.7$\pm$0.6) keV [5]. Employing as energy measure a linear combination of the charge and light signals, which

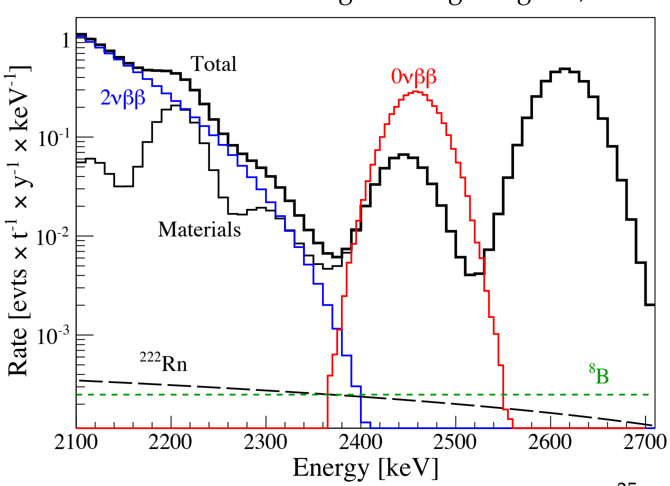

FIG. 5.3 – Hypothetical $0\nu\beta\beta$ signal for $T_{1/2}$=1.6$\times10^{25}$ yr and predicted background for 6 t fiducial mass. The background is completely dominated by detector materials with small contributions from 0.1 μBq/kg of ^{222}Rn in the LXe, ^{8}B neutrino scatters and $2\nu\beta\beta$-decays.

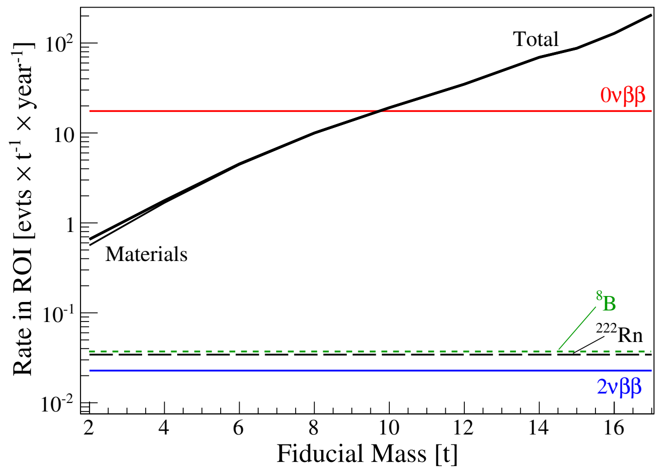

FIG. 5.4 – Integral background rate in $\pm3\sigma$ energy region around the $Q-$value (2385–2533 keV) as a function of fiducial LXe mass.

are anti-correlated in liquid xenon TPCs [6], the energy resolution is $\sigma/E \approx 1\%$. Hypothetical signal and expected background are shown in Fig. 5.3.

As illustrated in Fig. 5.4, at double beta decay energy the fiducial volume cut is less effective in reducing material backgrounds which results from the much longer mean free path of photons in this energy region. Hence, for this search we consider a reduced fiducial LXe mass of 6 t which contains 534 kg of ^{136}Xe for the natural abundance of 8.9%. The materials background is dominated by ^{214}Bi and ^{208}Tl decays in the photosensors and the cryostat which can only be further reduced by selecting materials with lower ^{226}Ra and ^{228}Th concentrations. The background contribution from internal radon can be efficiently rejected by so-called ^{214}Bi-^{214}Po tagging. It exploits the fact that the ^{214}Bi β-decay (Q_β= 3.3 MeV) and the ^{214}Po α-decay (Q_α= 7.8 MeV) occur close in time, given the ^{214}Po lifetime of 237 μs. We assume a tagging efficiency of 99.8%, as achieved in EXO-200 [7] and confirmed by us in a Monte Carlo simulation, assuming that ^{214}Po decays can be detected up to 1 ms after the initial ^{214}Bi decay.

[1] L. Baudis (DARWIN Consortium), J. Phys. Conf. Ser. 375, 012028 (2012).

[2] L. Baudis *et al.*, JCAP 01, 044 (2014).

[3] G. Bellini *et al.* (Borexino Collaboration), Phys. Rev. Lett. 107, 141302 (2011).

[4] N. Ackerman *et al.* (EXO-200 Collaboration), Phys. Rev. Lett. 107, 212501 (2011).

[5] P.M. Cowan and R.C. Barber, Phys. Rev. C 82, 024603 (2010).

[6] A. Manalaysay *et al.*, Rev. Sci. Instrum. 81, 073303 (2010).

[7] J.B. Albert *et al.* (EXO-200 Collaboration), Phys. Rev. C 82, 024603 (2010).

6 DAMIC: search for dark matter using CCD detectors

J. Liao, B. Kilminster, and P. Robmann

in collaboration with: Fermi National Accelerator Laboratory, University of Chicago, University of Michigan, Universidad Nacional Autónoma de México, Universidad Nacional de Asunción de Paraguay

(DAMIC Collaboration)

DAMIC (Dark Matter in CCDs) is an experiment designed to provide the highest sensitivity to dark matter with mass around 5 GeV. The dominant contribution of matter in the universe is dark matter (DM) as has been determined through its gravitational effects and through its influence on the structure of the cosmos being five times more prevalent than expected from the known matter [1–4]. The earth is expected to be traversing a galactic halo of non-relativistic DM particles with a density of 0.3 GeV/cm^3 and a rigorous program to identify possible particle interactions of DM is a major focus of particle physics experiments. If DM particles interact weakly, earth-based experiments should be able to directly detect them through their nuclear recoils with detector material.

Most current and proposed DM direct-detection experiments are optimized for detecting DM particles with masses on the order of 100 GeV, which is the most natural scale for Weakly Interactive Massive Particles (WIMPs) theorized by supersymmetry [5]. This is appealing because the electroweak cross-section for producing 100-GeV to 1-TeV scale particles is such that the correct abundance of DM in the universe would freeze out as the universe cooled after the big bang. While this scenario is still a strong possibility, direct searches for supersymmetry at the LHC are increasingly ruling out the most natural versions of supersymmetry, reducing the parameter space available for a WIMP DM candidate. There is, however, another natural mass scale for DM motivated by another coincidence. The DM and baryon abundances are similar, $\rho_{DM}/\rho_B \sim 5$, which suggests a theoretical correlation between them [6]. This relationship can arise naturally when the DM has an asymmetry in the number density of matter over anti-matter similar to that of baryons:

$$n_\chi - n_{\bar{\chi}} \simeq n_b - n_{\bar{b}},$$

where n_χ and $n_{\bar{\chi}}$ are the DM and anti-DM densities, and n_b and $n_{\bar{b}}$ are the baryon and anti-baryon densities.

Since $\rho_{DM}/\rho_B \sim 5$, this suggests that the mass of the DM particle $m_\chi \sim 5 \times m_p \simeq 5$ GeV. Therefore, the proton mass scale sets the DM mass scale. This possibility has the added benefit that the the difference between the DM mass scale and the baryon mass scale arises from the relationship between the weak scale and the QCD confinement scale. Many new asymmetric DM theories originating from [7] have been hypothesized in the last few years exploring this possibility. In addition to the theoretical interest in low mass DM, there are now four direct DM detection experiments [8–11] with excesses in the 5-10 GeV DM mass region, with DAMA/Libra reporting a significance of more than 8 σ [8].

[1] F. Zwicky, Helvetica Physica Acta 6 (1933) 110.

[2] D. Larson *et al.*, Astrophysical Journal Supplement Series **192** (2011) 16.

[3] W.J. Percival *et al.*, Monthly Notices of the Royal Astronomical Society **401** (2010) 2148.

[4] P.A.R. Ade *et al.* (Planck Collaboration), arXiv:1303.5062 [astro-ph.CO].

[5] B.W. Lee and S. Weinberg, Phys. Rev. Lett. **39** 165 (1977); Murayama, *the Fabric of Spacetime*, Les Houches Summer School, July 31 - August 25, 2006, arXiv:0704.2276v1.

[6] D.B. Kaplan, Phys. Rev. Lett. **68**, 741 (1992).

[7] D.E. Kaplan, M.A. Luty and K.M. Zurek, Phys. Rev. D **79**, 115016 (2009).

[8] R. Bernabei *et al.*, Eur. Phys. J. C **67** (2010) 39; R. Bernabei *et al.*, Nucl. Instr. & Meth. A **592** (2008) 297; R. Bernabei *et al.* Eur. Phys. J. C **56** (2008) 333.

[9] Phys. Rev. Lett., **107**, 141301 (2011); Phys. Rev. Lett., **106**, 131301; Phys. Rev. Lett., **101**, 251301 (2008).

[10] R. Agnese *et al.* (CDMS Collaboration), arXiv:1304.4279 [hep-ex].

[11] G. Angloher *et al.*, Eur. Phys. J. C **72**, 1971 (2012).

6.1 First results

The main challenge in searching for low mass DM is measuring the low energy deposit of the associated nuclear recoils in the detection material. DAMIC uses CCDs with an electronics noise of σ=7.2 eV. This leads to a 5σ=36 eV threshold, which is the lowest of any current DM detector. CCD detectors are silicon pixel detectors that shift charge from the capacitor of one pixel to the next by generating potential wells until reaching a charge amplifier which converts the charge to voltage (see Fig. 6.1). The DAMIC CCD detectors were fabricated by Lawrence Berkeley

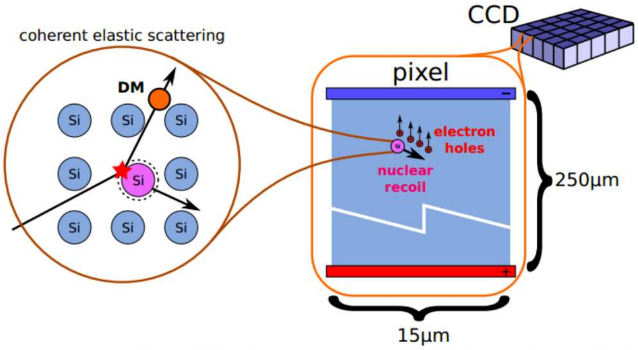

FIG. 6.1 – DAMIC detection principle: hypothetical dark matter particles scatter coherently off silicon nuclei, producing a nuclear recoil that is recorded as charge on pixels in the CCD.

National Laboratory [1] originally for the Dark Energy Camera (DECam) [2, 3]. Each CCD has up to 16 million 15 μm x 15 μm pixels and is read by two amplifiers in parallel. The electronic gain is $\sim$ 2.5 μV/e. The signal is digitized after correlated double sampling (CDS) and the noise performance improves by reducing the readout speed. The lowest noise, $\sigma < 2e^-$ (R.M.S.) per pixel, was achieved with readout times of 50 μs per pixel [5].

The second major feature that makes the DECam CCDs [4] good candidates for a DM search is their relatively large thickness (ten times thicker than usual), which directly affects the detection efficiency.

First results were obtained with a single 0.5 g CCD, installed ≈100 m underground in the NuMI [6] near-detector hall at Fermilab. Data were collected during 11 months in 2011. Standard techniques were used to interpret the results as a cross section limit for spin-independent DM interactions [7], and parameterizations were used allowing the direct comparison with other limits on low mass DM particles. The DAMIC limit constituted the best constraint on DM particles with mass below 4 GeV.

[1] S.E. Holland *et al.*,
IEEE Trans. Electron Dev., **50** 225 (2003).

[2] B. Flaugher, *Ground-based and Airborne Instrumentation for Astronomy*, Ian S. McLean editor; Iye, Masanori, Proceedings of the SPIE, Volume 6269, (2006).

[3] Dark Energy Survey Collaboration, astro-ph/0510346.

[4] J. Estrada and R. Schmidt, *Scientific Detectors for Astronomy 2005*, J.E. Beletic, J.W. Beletic and P. Amico editors, Springer (2006).

[5] Estrada *et al.*, Proceedings of SPIE 2010.

[6] http://www-numi.fnal.gov/PublicInfo/forscientists.html.

[7] J. Barreto *et al.* (DAMIC Collaboration),
Phys. Lett. B **711**, 264 (2012).

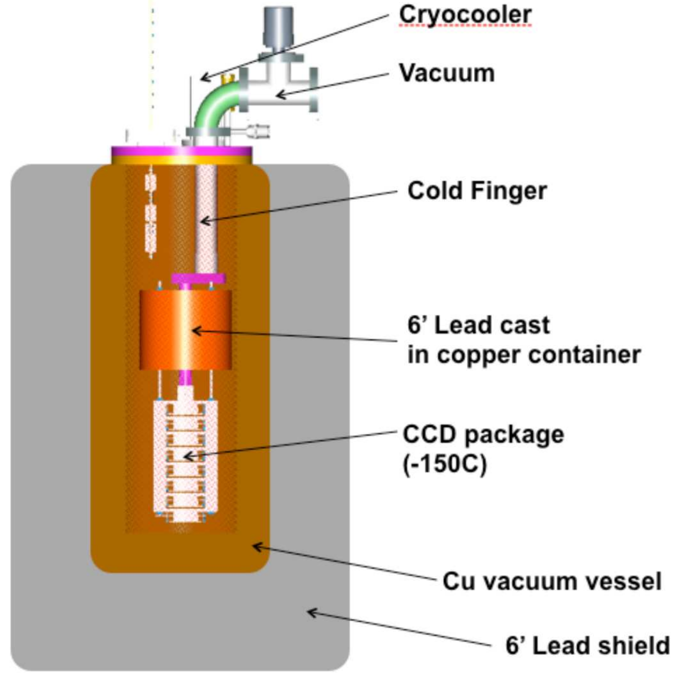

FIG. 6.2 – Schematic of the DAMIC-100 vacuum vessel with copper and lead shielding.

6.2 DAMIC-100

Our next experiment is DAMIC-100, which will begin collecting data in the summer of 2014. The experiment moved deep underground to Snolab, where prototypes of newly designed CCDs for DAMIC-100 have been running since December 2012. A schematic of the new setup is shown in Fig. 6.2. The CCDs, with a total mass of 100 g, are installed inside a copper box cooled to -150°C to reduce dark current. The cold copper also shields the detectors against infrared radiation. A closed cycle helium gas refrigerator is used to maintain the low temperature. The detector is connected through a readout cable to the preamplifiers located outside the lead shield. The detector package is housed in a cylindrical vacuum vessel fabricated with oxygen-free copper, and maintained at 10^{-7} Torr with a turbo molecular pump. Lead and polyethylene shield against γ-rays and neutrons. Fig. 6.3 shows existing parts. The projected DAMIC-100 sensitivity region is shown in Fig. 6.4 together with results from the previous DAMIC search and other experiments.

6.2.1 Calibration and testing

Energy calibration of a DM detector is factorized in (i), the ionisation energy calibration as determined from direct X-rays and carbon and oxygen fluorescent X-rays from a Fe^{55} source and (ii), the signal quenching observed for

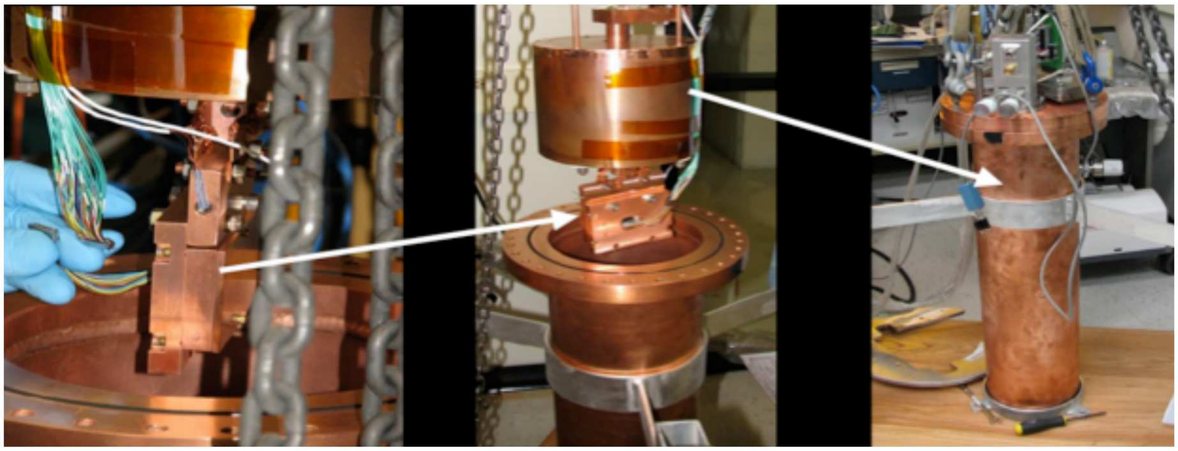

FIG. 6.3 – Vacuum vessel with copper IR shield. Above the IR shield there is a lead shield. Not shown is an outer polyethylene shield.

highly ionizing nuclear recoils. The quenching factor has been measured in Si for recoil energies above 4 keV [1], showing good agreement with the Lindhard model [2, 3].

We have helped design and test an experimental set up at the Tandem Van der Graaf of the University of Notre Dame in which monochromatic neutrons are scattered off a silicon target and the scattering angle and neutron time-of-flight are used to determine the nuclear recoil energy. The scattered neutrons are detected with a set of 20 scintillating bar counters placed at the small angles that correspond to the low recoil energies of interest (down to an unprecedented 1 keV). We are currently studying the signals and achievable timing resolution of the bars and hope to have results in summer 2014.

We are building a copy of the DAMIC detector (see Sec.19) which will be studied with X-rays and neutrons from the 2.5 MeV neutron beam at our institute. We will use the apparatus to measure the noise components of the CCD detectors. Our group has characterized the CCD noise signals and determined the optimal settings minimizing the noise. We will also measure the lateral pixel diffusion of recoil signals resulting in neighboring pixels sharing the recoil energy. The effect can be reduced by increasing the voltage applied to the silicon substrate.

[1] J.D. Lewin and P.F. Smith, Astropart. Phys. 6, 87 (1996).

[2] J. Lindhard, V. Nielsen, M. Scharff, and P.V. Thomsen, Mat. Fys. Medd. Dan. Selsk **33**, 10 (1963).

[3] H. Chagani *et al.*, JINST 3 (2008) P06003.

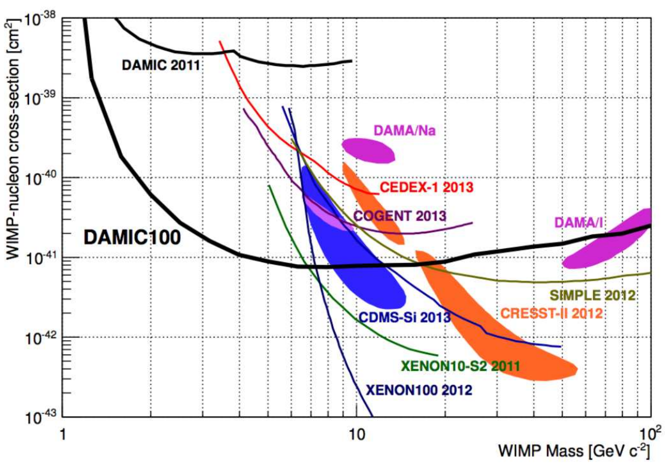

FIG. 6.4 – Signal regions (colored areas) and exclusion boundaries (colored lines) from direct DM searches. Limits from DAMIC 2011 and projected sensitivity for DAMIC-100 are shown as well.

6.2.2 Monitoring and data analysis

To reach the projected sensitivity of DAMIC-100 shown in Fig. 6.4 we will need to understand the noise, dark current, energy response, backgrounds, map of dead and hot pixels for each CCD, and calibrate them with optical light and X-ray sources. Our group has developed a monitoring system which records temperature, voltage, and pressure inside the detector cryostat, and correlates this information with dark current, RMS detector noise, X-ray radio-impurities of each individual CCD. For each of the thousands of exposures expected in one year of data taking, this monitoring software will determine the data quality and usability in the final analysis. There is an web page interface to visualize the information in real time, and store everything for offline usage. We will study the selection criteria optimizing the signal efficiency versus background rejection. First results for DAMIC-100 are expected towards the end of 2014, but of course, more time would be needed to demonstrate an annual modulation of a DM signal resulting from the earth's orbit through the galactic DM halo.

7 Very High Energy Gamma Ray Astronomy with CTA

F. Canelli, D. Florin, A. Gadola, A. Manalaysay (until August 2013), S. Steiner, U. Straumann, A. Vollhardt

in collaboration with: ETH Zürich, Jagiellonian University Cracow, MPI für Kernphysik Heidelberg, Universität Tübingen, Universität Erlangen, Universität Innsbruck and over hundred institutes from 27 countries

(CTA)

The Cherenkov Telescope Array (CTA) is the next generation array of Imaging Atmospheric Cherenkov Telescopes (IACTs), and is the successor to the current generation of IACTs including MAGIC [1], H.E.S.S [2], and VERITAS [3]. These telescopes are used to detect gamma rays in the range of tens of GeV to tens of TeV, emitted from exotic (i.e. non-thermal) astrophysical sources such as quasars, supernovae and their remnants, gamma-ray bursts, and dark matter annihilations. When these gamma rays enter the Earth's upper atmosphere, they create an electromagnetic shower comprising many highly-energetic charged particles. Those particles traveling faster than light in the atmosphere produce Cherenkov photons that travel in a cone to the ground. The IACTs can detect these Cherenkov photons and reconstruct the electromagnetic shower by imaging it with multiple telescopes, taking into account the photon arrival times. The reconstructed shower can then be used to determine the direction and energy of the initial gamma ray.

The goal of CTA is to build improved and larger versions of the current IACTs, based upon the lessons learned and exploiting new technologies. CTA is approaching the final R&D stage and heading towards first telescope prototypes. Efforts at UZH include primarily a mirror alignment system and a first fully digital IACT camera.

[1] J. A. Coarasa *et al.*, (MAGIC Collaboration), J. Phys. Soc. Jap. Suppl. 77B (2008) 49.

[2] B. Opitz *et al.*, (HESS Collaboration), AIP Conf. Proc. 1223 (2010) 140.

[3] D. Hanna *et al.*, (VERITAS Collaboration), J. Phys. Conf. Ser. 203 (2010) 012118.

7.1 Mirror actuators

The mirror actuators are mounted to the primary mirror segments to enable an automatic alignment of each segment. In-house and field tests of the past couple of years have demonstrated that the actuators work reliably, and that all requirements are fulfilled. A first serious test with a large number of actuators was possible after the commissioning of the first mid-size telescope (MST) prototype in Berlin. The experiences gained in Berlin were incorporated in the next generation of actuators of which 450 have been ordered for the first large-size telescope (LST).

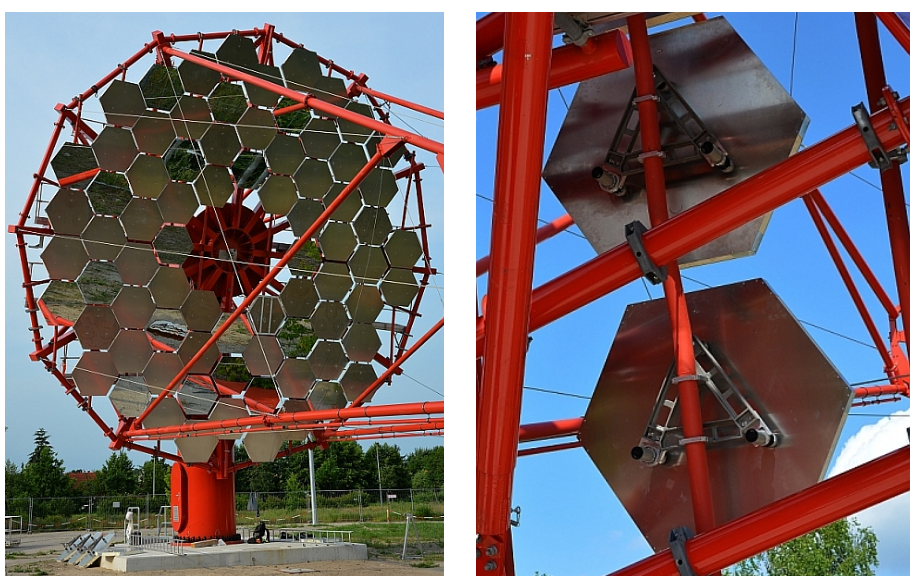

FIG. 7.1 – The MST prototype in Adlershof Berlin with real and dummy mirrors (*left*), and the UZH actuators mounted on the support of the telescope structure seen from the back (*right*).

FIG. 7.2 – Pictures of the camera body. From left to right: front view with half closed lid, rear view with closed doors and rear view with open doors showing the two electronic racks.

7.1.1 Pre-series for MST prototype

After having mounted some actuators on the quarter dish at the DESY Zeuthen Institute, a pre-series has been produced which was installed in May 2013 on the first mid-size telescope prototype in Adlershof, Berlin next to the synchrotron source BESSY II. Figure 7.1 shows the 12 m diameter dish of the MST prototype equipped with real and dummy mirrors. Sixteen mirrors have been equipped with actuators from the University of Tübingen and the remaining sixty with UZH actuators. The mounting was done by us while the cabling and the commissioning were done by colleagues from DESY Zeuthen.

7.1.2 Series production for the first LST prototype

After the production, the installation and the operation of the actuators on the MST prototype, a slightly modified version of the actuator has been designed and ordered in larger numbers (225 sets, each consisting of two actuators and a fix point) in collaboration with the University of Tokyo and the MPI München, both heavily involved in the development and production of the LST. Most parts have been delivered and are ready to be assembled at IWAZ, a home for agility disabled people in Wetzikon.

7.2 The FlashCam camera

FlashCam [1] is a camera design for CTA incorporating a fully digital data and trigger pathway. In the more traditional IACT design the data first enter an analogue trigger pipeline where a decision is made whether or not to digitize the stored analogue data. Such schemes typically feature an effective sampling rate around 2 GS/s. A continuously digitizing 2 GS/s pathway is, however, prohibitive both in terms of cost and power consumption for an array of hundreds of cameras with thousands of channels each. Interestingly, our collaborators at the Max Planck Institute for Nuclear Physics (MPI-K) in Heidelberg have demonstrated with simulations that adequate performance can be achieved with a 250 MS/s sampling rate. The scheme has been studied during the past years and has meanwhile entered the prototyping phase. FlashCam is essentially divided into four main parts: the detector plane with the photo sensors, the readout electronics, the slow control including the cooling, and the camera body. The body and the detector plane are the two main parts developed, built and tested here at UZH.

[1] G. Pühlhofer *et al.*, (FlashCam Collaboration), arXiv 1211.3684 [astro-ph.IM] (2012).

7.2.1 The camera body

The in-house design rigid camera body (see Fig. 7.2) houses the photon-detector plane (Sec. 7.2.2) and the readout electronics as well as the slow control electronics required for the many actuators and sensors. Most components were made in our mechanical workshop but particularly large parts were ordered from appropriately equipped companies. The camera body is built around an inner frame. The sandwich-like front plate has 1764 holes for the photo sensors equipped with light concentrators and detector modules described further below.

The case was produced by Krapf in Amriswil, a company specialized in temperature-insulated van bodies, and indeed shows the typical look of such a van body.

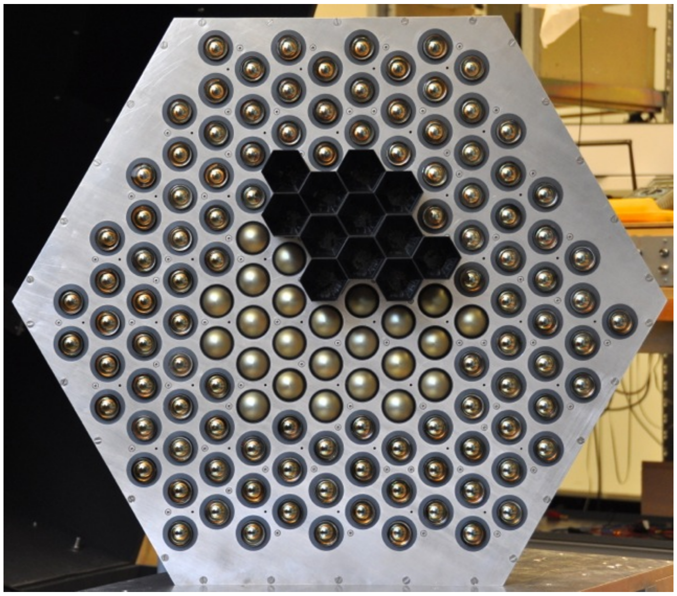

FIG. 7.3 – The 144-pixel prototype photon detector.

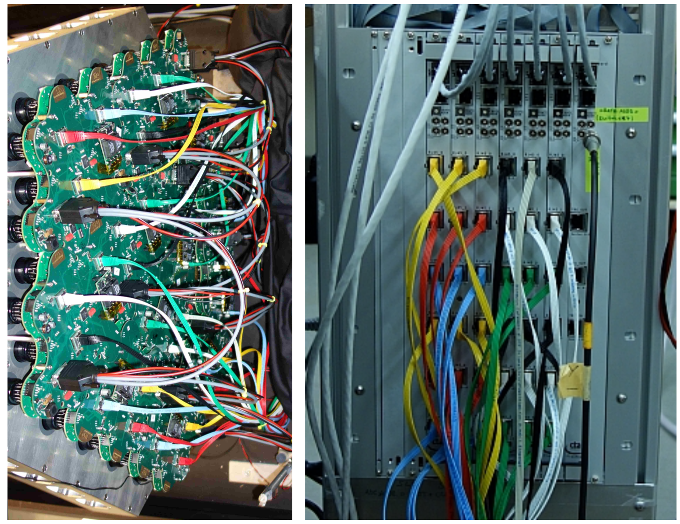

FIG. 7.4 – Left: the photon-detector plane from the back. Right: the readout mini-crate with six FADC boards and one trigger board.

The case insulation helps to better control the temperature inside the camera. The camera weight including cooling and all electronics will be around 1.6 to 1.7 t. The large steel frame needed to hold and rotate the heavy camera body was made by our mechanical workshop. Some mechanical parts like the movable sealing of the lid and various sensors for ambient light, smoke, water, etc. still remain to be installed.

7.2.2 The photon-detector plane

Last year the photon-detector-plane (PDP) electronics of FlashCam has been specified. The PDP is built on individual boards, each containing 12 photo detectors (photomultiplier tubes = PMTs), a high voltage generator, analogue signal amplification and slow control for the board functionalities. Twelve prototype boards were ordered for a 144 pixel mini-camera (Fig. 7.3 and 7.4). Three modules contain Hamamatsu PMTs, the current favorite PMT of CTA, and the remaining nine modules contain spare Photonis PMTs as used in the H.E.S.S. cameras. September last year the first light was seen with all 144 pixels simultaneously. The characterization of the whole setup is now almost completed and the results look very promising. Figure 7.5 shows as an example the dependence of the charge resolution on number of photo-electrons measured with a Hamamatsu and a Photonis PMT. The results not only satisfy the CTA requirements but even the design goals.

After finishing the characterization of the present PDP modules and the associated readout electronics an improved version will be tested before ordering the $\mathcal{O}(70)$ modules needed for a fully equipped camera.

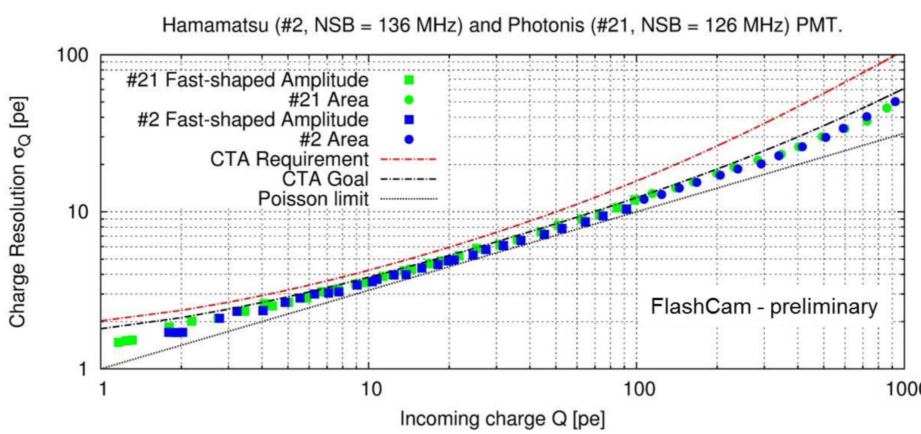

FIG. 7.5 – Dependence of the charge resolution on number of photo-electrons measured with a Hamamatsu and a Photonis PMT.

8 Search for the rare decay $\mu^+ \to e^+e^-e^+$

R. Gredig, P. Robmann, and U. Straumann

in collaboration with University of Geneva, Paul Scherrer Institute, ETH Zürich, University of Heidelberg

(Mu3e Collaboration)

Neutrino oscillations, as observed by experiments such as SuperKamiokande [1], SNO [2], and KamLAND [3] are a direct proof of lepton flavour violation (LFV). Charged LFV (CLFV) would lead to $\mu \to e$ and $\tau \to \mu$ transitions without neutrinos in the final state. In the standard model CLFV can be induced by neutrino mixing but such processes are highly suppressed by the tiny neutrino masses. The observation of CLFV would therefore directly signal physics beyond the standard model. Muon number violation has already been searched in different channels (see Tab. 8.1). When these processes would be observed their relative strengths would guide the attempts to identify the underlying mechanism.

TAB. 8.1 –
Experimental upper limits on the branching ratios B of LFV muon decays

Decay channel	Experiment	B upper limit	Ref.
$\mu \to e\gamma$	MEGA	1.2×10^{-11}	[4]
	MEG	2.4×10^{-12}	[5]
$\mu \to eee$	SINDRUM	1.0×10^{-12}	[6]
$\mu^-\mathrm{Au} \to e^-\mathrm{Au}$	SINDRUM II	7×10^{-13}	[7]

A new $\mu^+ \to e^+e^-e^+$ search at PSI ultimately aims at a sensitivity down to $B < 10^{-16}$ [8], four orders of magnitude beyond the 26 year old SINDRUM result. The setup (see Fig. 8.1) contains cylindrical layers of silicon pixels and scintillating fibres, placed in a solenoidal magnetic field.

In a first phase, ready to take data by 2016, the setup will include the central pixel detectors, the fibre tracker, and one complete set of recurl stations and the beam-intensity will be 10^8 μ^+/s. Assuming the phase I detector works as expected, phase II components should be ready in 2017. There will be two sets of recurl stations and a new muon beam line should give at least one order of magnitude larger stop rate.

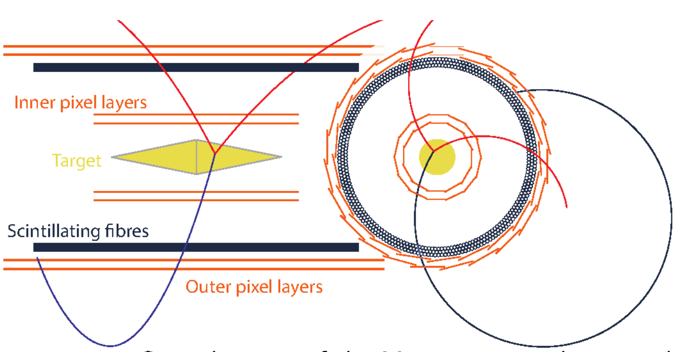

FIG. 8.1 – Central region of the Mu3e setup in the zy and xy projections. The central fibre tracker consists of three layers of 250 μm fibres with a length of 36 cm.

[1] Y. Fukuda *et al.* (Super-Kamiokande Collaboration), Phys. Rev. Lett. 81 (1998) 1562.

[2] Q.R. Ahmad *et al.* (SNO Collaboration), Phys. Rev. Lett. 87 (2001) 071301.

[3] K. Eguchi *et al.* (KamLAND Collaboration), Phys. Rev. Lett. 90 (2003) 021802.

[4] M. L. Brooks *et al.* (MEGA Collaboration), Phys. Rev. Lett. 83 (1999) 1521.

[5] J. Adam *et al.* (MEG Collaboration), Phys. Rev. Lett. 107 (2011) 171801.

[6] U. Bellgardt *et al.* (SINDRUM Collaboration), Nucl. Phys. B299 (1988) 1.

[7] W. Bertl *et al.* (SINDRUM II Collaboration), Eur. Phys. J. C47 (2006) 337.

[8] A. Blondel *et al.* (Mu3e Collabaration), *Research Proposal for an Experiment to Search for the Decay* $\mu \to 3e$, submitted to PSI (2013), ArXiv 1301.6113.

8.1 Scintillating Fibres

The University of Zürich, in close collaboration with the University of Geneva and the ETH Zürich, is strongly involved in the R&D for the scintillating fibre tracker which is part of the proposed detector. The fibres are read out with silicon photomultipliers (SiPM) which allow a suf-

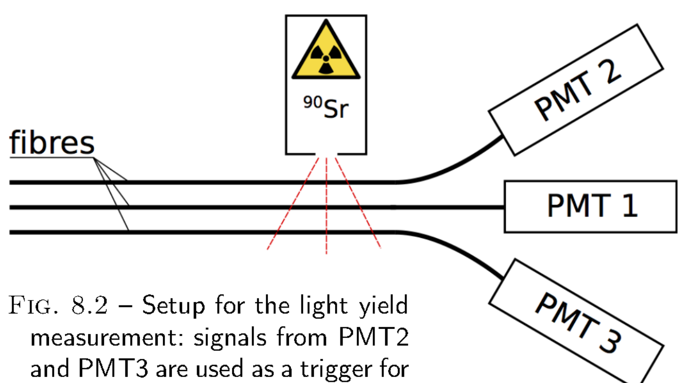

FIG. 8.2 – Setup for the light yield measurement: signals from PMT2 and PMT3 are used as a trigger for the measurement of the number of photo-electrons in PMT1.

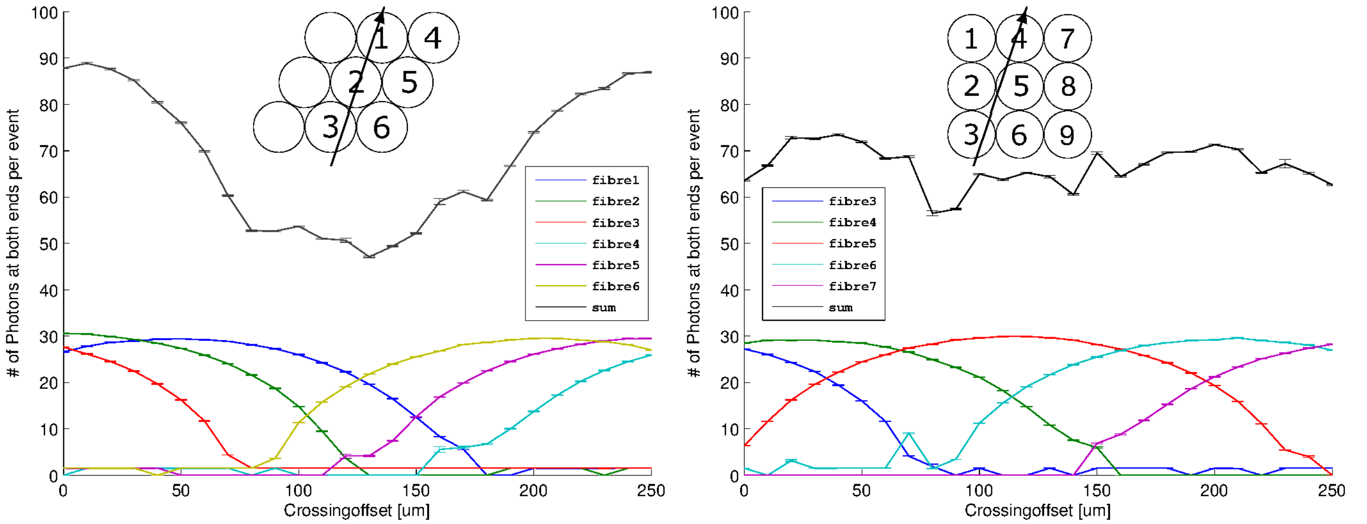

FIG. 8.3 – Predicted number of photons versus positron crossing position at the most likely crossing angle for two alternative staggering geometries as indicated by the insets; the trajectory correponding to zero crossing position is shown too.

ficiently dense staggering and can be operated in high magnetic fields.

Detailed simulation studies of the light propagation within the fibres have been completed resulting in a parametrization of the photon yield and time distribution over the detector surface to be used as input in the full event simulation. The simulation has been verified with a test setup consisting of three 250 μm fibres irradiated with a ^{90}Sr source (see Fig. 8.2). A coincidence between the two outer fibres is used as trigger and the signal of the middle fibre is registered. The simulation includes the passive support material and accounts for the energy spectrum of the source. The observed light yield is ≈20% below the prediction which we consider satisfactory, given the large number of reflections. The predicted time resolution of about 400 ps has been confirmed by a test measurement at the University of Geneva.

Next, a study was made of the fibre configuration since the photon yield depends on the way how the ribbons are staggered (Fig 8.3). The final configuration will be a trade-off between light yield, multiple scattering and mechanical feasibility.

8.2 Readout Electronics

Together with the University of Geneva, multi channel readout electronics has been developed. For maximum flexibility the SiPM sensors have been separated from the amplifier board itself allowing to test different sensors and amplifier boards. Fig 8.4 shows a daughterboard with a 4x4 SiPM sensor-array. This board can be connected to an amplifier array with 16 channels (Fig. 8.5). Two of these sets can be combined to read out 32 fibres from a fibre ribbon. The amplifier electronics is designed in such a way that it can later be integrated in an ASIC design. As the final detector will have thousands of channels, the electronics need to be highly integrated because of spatial limitations.

First experiences at a DESY electron test beam helped to improve the data acquisition software and the readout electronics. From the next beam tests at PSI first results of the fibre ribbon performance in beam are expected.

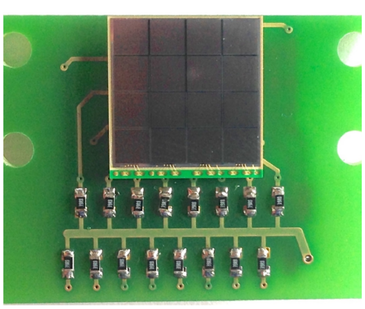

FIG. 8.4 – Daughterboard with a 4x4 Hamamatsu array.

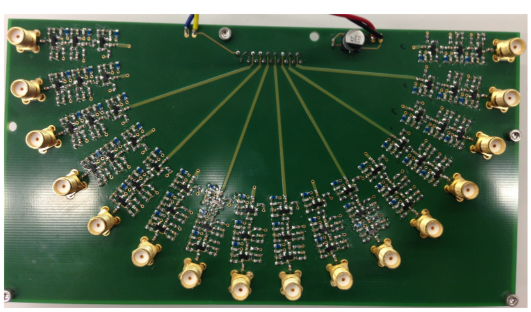

FIG. 8.5 – 16-channel motherboard.

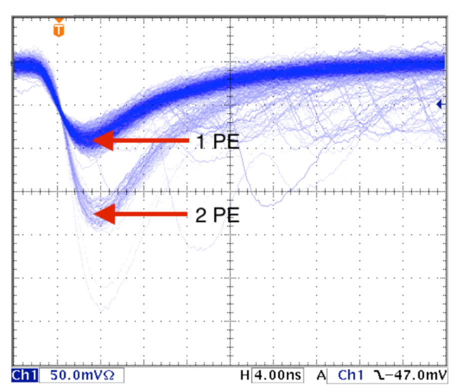

FIG. 8.6 – SiPM signals showing clean one and two photoelectron events.

9 The $\pi^+ \to e^+\nu_e$ / $\pi^+ \to \mu^+\nu_\mu$ branching ratio

P. Robmann, A. van der Schaaf and P. Truöl

in collaboration with University of Virginia, Charlottesville, USA; Institute for Nuclear Studies, Swierk, Poland; JINR, Dubna, Russia; PSI, Villigen, Switzerland and Rudjer Bošković Intitute, Zagreb, Croatia

(PEN Collaboration)

Charged pions decay weakly into lepton pairs, $l_i\nu_i$, of the lower two generations ($i = 1, 2$) through an intermediate W boson. As discussed in some detail in last years' report, the ratio between the partial decay rates for $\pi^+ \to e^+\nu_e$ and $\pi^+ \to \mu^+\nu_\mu$ depends primarily on the masses of the particles involved:

$$R^{\pi}_{e/\mu} \equiv \frac{\Gamma(\pi \to e\nu_e)}{\Gamma(\pi \to \mu\nu_\mu)} \simeq \left(\frac{m_e}{m_\mu} \times \frac{m_\pi - m_\mu}{m_\pi} \times \frac{g_e}{g_\mu}\right)^2,$$

where g_i denotes the coupling strength of the $Wl_i\nu_i$ vertex ($g_e = g_\mu$ in the Standard Model). One readily identifies the factors associated with the helicity suppression, the Q-value, and the universality violation. Table 9.1 compares the theoretical value including all bells and whistles, which is a few percent below the above simple estimate, with the two-decades old experimental one. This comparison still gives the best constraint on a flavour dependent coupling of W bosons to leptons. Two new experiments [3] aiming at improvements in accuracy by almost one order of magnitude finished data taking and are in the process of extracting $R^{\pi}_{e/\mu}$.

For pions at rest the decay $\pi^+ \to e^+\nu$ is characterized by an electron with $E = \frac{1}{2}m_\pi c^2 = 69.8$ MeV emitted with an exponential time distribution with $\tau_{\pi^+} = 26.0$ ns. Since the 4.2 MeV muon from $\pi^+ \to \mu^+\nu$ at rest travels just $\sim$0.1 g/cm^2 and stays in the π^+ stopping target this decay can be observed through the subsequent decay $\mu^+ \to e^+\nu\bar{\nu}$. The decay chain is characterized by an electron with $E < \frac{1}{2}m_\mu c^2 = 52.8$ MeV emitted with a time distribution first rising with τ_{π^+} and then falling with $\tau_\mu = 2.20\ \mu$s. Ideally, the two decay modes can be perfectly distinguished by the positron energy alone but radiative corrections and imperfections in the experimental setup result in a low-energy tail in the $\pi^+ \to e^+(\gamma)\nu$ positron energy distribution leaking into the region populated by $\pi^+ \to \mu^+\nu$. The uncertainty in this tail fraction is in fact the major source of systematic error in determinations of $R^{\pi}_{e/\mu}$.

Tab. 9.1 –
SM predictions and measured values for $R^{\pi}_{e/\mu}$.

	$\Gamma_{\pi^+\to e^+\nu}/\Gamma_{\pi^+\to\mu^+\nu}$	
theory	$1.2353(1) \times 10^{-4}$	[1]
experiment	$1.2312(37) \times 10^{-4}$	[2]

[1] V. Cirigliano and I. Rosell, JHEP **10** (2007) 5.
V. Cirigliano and I. Rosell,
Phys. Rev. Lett. **99** (2007) 231801.

[2] G. Czapek *et al.*, Phys. Rev. Lett. **70** (1993) 17;
D. I. Britton *et al.*, Phys. Rev. Lett. **68** (1992) 3000.

[3] PEN Collaboration, PSI experiment R-05-01 (2005),
D. Počanić and A. van der Schaaf, spokespersons;
PIENU Collaboration, TRIUMF proposal 1072 (2006),
D. Bryman and T. Numao, spokespersons.

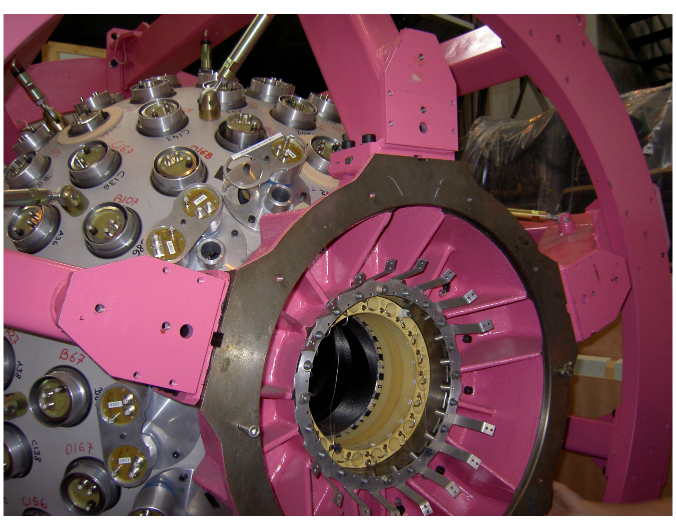

9.1 the PEN experiment

PEN took data at the πE1 beam line at PSI during 2008 – 2010. The most important (and expensive) detector, a 240-element CsI calorimeter shown in Fig. 9.1, was refurbished from the PIBETA experiment [1]. A 75 MeV/c π^+ beam from the πE1 channel was brought to rest in a small plastic scintillator. The beam crossed various scintillators, allowing individual momentum measurements through time-of-flight and dE/dx, and a mini-TPC for tracking.

Fig. 9.1 – The PEN 3π Sr pure-CsI calorimeter before cabling. The carbon-fiber cylinder seen inside the sphere supports the plastic scintillator hodoscope.

These detectors were read both with 2 GS/s waveform digitizers and with 16 μs-range TDC's used to detect preceding beam particles. Secondary particles emitted from the target were tracked in cylindrical MWPC's and crossed a plastic scintillator hodoscope before reaching the calorimeter.

Detector calibrations are done now for all years and reconstruction algorithms have been pushed to perfection. State of the art event simulation all the way down to the data format of the measured events is available but needs some fine-tuning still so detailed studies of the systematic uncertainties haven't started yet.

9.1.1 target waveform analysis

The active target may be called the heart of the detection system since that's where the decays take place and all particles leave their traces. The recorded target waveforms allow a very efficient separation of the two event types of interest in addition to the traditional scheme based on the e^+ energy and the time delay between π^+ stop and e^+ appearance ("decay time"). The procedure is illustrated in Figures 9.2 through 9.4. In a first step the waveform is filtered by folding with a 400-element vector trained to remove all distortions after a few ns (time scale set by the mean scintillator decay time). These distortions are caused by imperfect signal transmission including reflections. In a second step predicted π^+ and e^+ signals are subtracted. These predictions are based on information from almost all detectors but the target itself. The largest uncertainty resides in the prediction of the e^+ signal amplitude which is hampered by Landau fluctuations in the energy loss for given path length (see Fig. 9.3). In a final third step the net waveform is scanned for the appearance of the mono-energetic muon signal by searching for the minimum in the difference in χ^2 for the two hypotheses (see Fig. 9.4). Note that this quantity does not depend on any features of the waveform outside the region of the muon since the difference is zero there.

9.1.2 decay time distributions

The trigger for data readout required a decay positron within a (−30,+220) ns window around the time of an incoming pion. Whereas practically all $\pi \to e\nu$ decays fall within this window, the $\pi \to \mu\nu$, $\mu \to e\nu\bar{\nu}$ decay chain triggers in less than 10% of the cases. Events with positron energies below ~48 MeV were pre-scaled by 1:64 so the total suppression of the dominant $\pi \to \mu \to e$ chain was three orders of magnitude, which still selects significantly

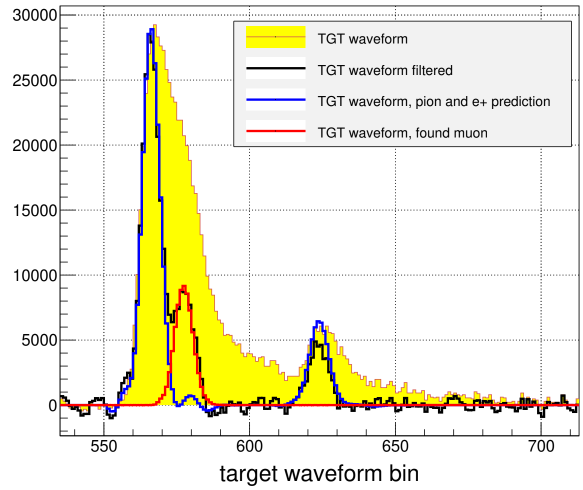

FIG. 9.2 – Target waveform of a $\pi \to \mu \to e$ event before and after waveform filtering. Removal of the predicted pion and positron signals leaves a clean 4 MeV muon signal.

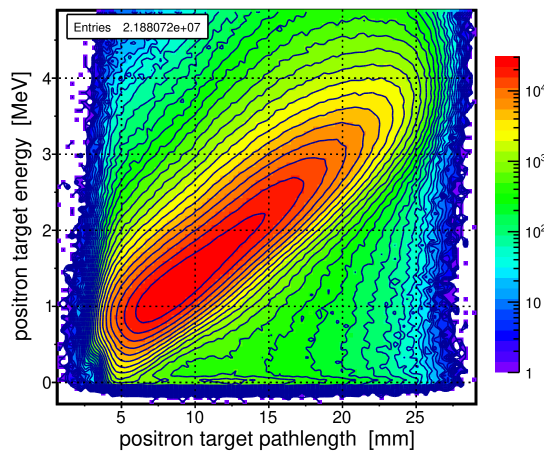

FIG. 9.3 – Observed e^+ target energy vs. reconstructed e^+ path length for events with an isolated e^+ signal. The correlation is exploited in the prediction of e^+ signal in the waveform.

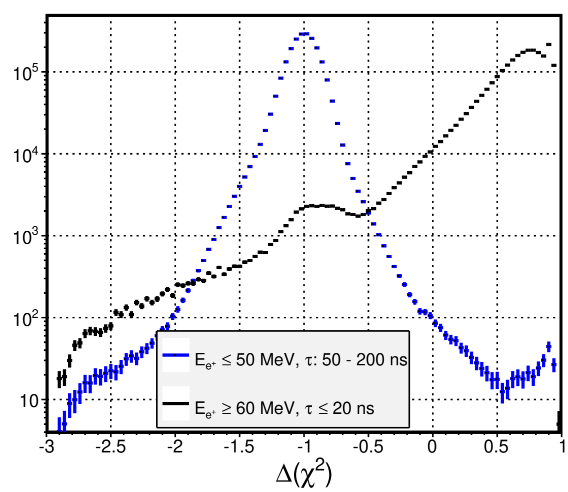

FIG. 9.4 – Distributions of $\Delta(\chi^2)$ (see text) of the target waveform for $\pi \to e$ and for $\pi \to \mu \to e$. The algorithm returns a value within the region shown for any waveform.

more events than in the $\pi \to e$ channel. Fig. 9.5 gives a flavour of the quality of the recorded data. Shown are the decay time distributions of two 2010 event samples enriched in $\pi \to e$ and $\pi \to \mu \to e$, primarily by cuts on e^+ energy and $\Delta(\chi^2)$ of the target waveform. Almost perfect agreement is observed with excursions from expectation below the percent level per 0.5 ns bin.

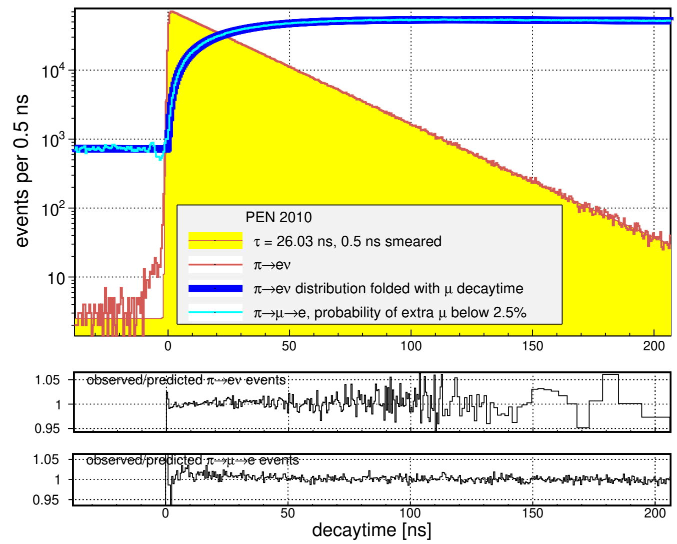

FIG. 9.5 – Histograms of the time delay between incoming π^+ and outgoing e^+. The $\pi \to e\nu$ distribution is perfectly described by the exponential known from literature. The $\pi \to \mu \to e$ distribution is compared with the prediction obtained by folding the observed $\pi \to e\nu$ histogram with the muon decay time distribution. Those who wish to read the branching ratio from this figure should keep in mind that the e^+ energy region below 50 MeV (populated by muon decay) was pre-scaled 1:64 in the readout trigger.

9.1.3 $\pi \to e\nu\gamma$

When experiments enter new territory, either kinematically or in statistical accuracy, there are often rewards outside the main goal. The "bread and butter" may sometimes even look more interesting for parts of the physics community. As it appears, the PEN data allow for the first time the analysis of the $\pi \to e\nu\gamma$ mode in almost the full phase space. More or less by accident the readout trigger (based on the total CsI energy) selected all $\pi \to e\nu\gamma$ events in the geometric acceptance defined by the CsI calorimeter. Equally important, the target waveform analysis removes any traces of $\mu \to e\nu\bar{\nu}\gamma$ background remaining after a cut on the $e\gamma$ invariant mass (total energy plus total momentum equals pion mass). All background that remains are $\pi \to e\nu$ events in which the e^+ shower is split in two (see below).

The decay $\pi \to e\nu\gamma$ is of interest since, contrary to the inner Bremsstrahlung (IB) contribution, the structure-dependent (SD) contributions are not helicity suppressed and can be extracted from their characteristic kinematic distributions. In the limit $m_e/m_\pi \to 0$:

$$IB(x,y) = \frac{(1-y)((1+(1-x)^2)}{x^2(x+y-1)}$$
$$SD^+(x,y) = (1-x)(x+y-1)^2$$
$$SD^-(x,y) = (1-x)(1-y)^2$$

where x and y are the γ and e^+ energies, respectively, normalized to their maximum value $m_\pi c^2/2$.

By far the best $\pi \to e\nu\gamma$ measurement known in literature was performed by parts of the present PEN collaboration [2]. As explained above, the new PEN data, shown in Fig. 9.6, are much cleaner, even when the total number of events is lower by maybe a factor 2. Much more speculative is the question how well a $\pi \to 3e\nu$ signal can be extracted. This process was studied long ago with the SINDRUM I magnetic spectrometer [3]. PEN accumulated less pion stops but this is more than compensated by the larger acceptance of the non-magnetic setup. At present we refrain from more quantitative statements.

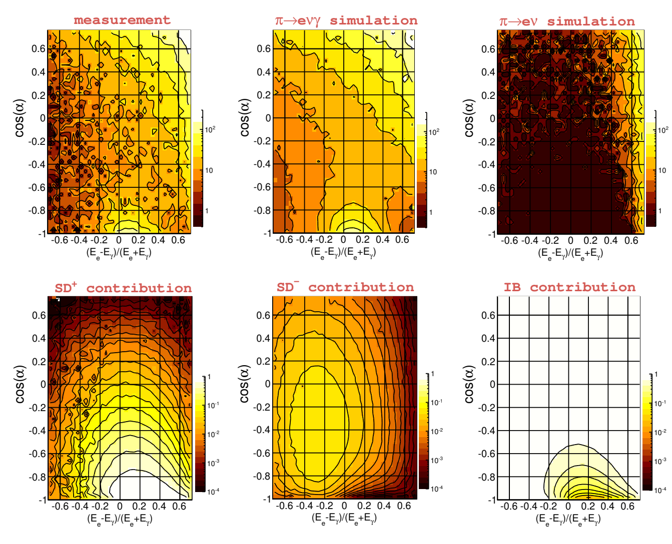

FIG. 9.6 – Kinematic distributions of $\pi \to e\nu\gamma$ (α is the $e^+\gamma$ opening angle). Top row: the distribution from our 2009/10 data (left panel) is compared with the predictions from simulation for signal (middle panel) and $\pi \to e\nu$ background (right panel). 33.140 events are found in the region selected for the figure. Lower row: relative contributions from the two structure-dependent and the inner-Bremsstrahlung contributions in the $\pi \to e\nu\gamma$ simulation. SD$^-$ contributes up to 6%.

[1] D. Počanić *et al.*, Phys. Rev. Lett. **93** (2004) 181803.

[2] M. Bychkov *et al.*, Phys. Rev. Lett. **103** (2009) 051802.

[3] S. Egli *et al.* (SINDRUM Collaboration), Phys. Lett. **222** (1989) 553.

10 Particle Physics at DESY/HERA (H1)

K. Müller, P. Robmann, U. Straumann, and P. Truöl

in collaboration with: C. Grab (Institut für Teilchenphysik der ETH, Zürich), S. Egli, M. Hildebrandt and R. Horisberger (Paul–Scherrer–Institut, Villigen), and 39 institutes outside Switzerland

(H1 - Collaboration)

Working groups with representatives from both the H1- and the ZEUS-collaboration have finished combining the full body of deep-inelastic neutral and charged current scattering data taken at the HERA collider. We recall that HERA was operated in two phases: HERA-I, from 1992 to 2000, and HERA-II, from 2002 to 2007. Whereas the electron or positron beam energy was 27.5 GeV during all these years, the proton energy varied as E_p = 460, 575, 820 and 920 GeV corresponding to maximum centre-of-mass energies $\sqrt{s}$ = 225, 252, 301 and 319 GeV, respectively.

The total luminosity collected by H1 and ZEUS together was ≈500 pb^{-1}, shared about equally between e^+p and e^-p. The results briefly referred to below [1, 2] combine all published H1 and ZEUS measurements [3]. The HERA-II measurements with polarized beams were individually averaged to obtain cross sections for unpolarized beams used as inputs to the combination: 2927 initial data points were combined into 1307 in the final set. Combining data points requires averaging, shifting the points to a common grid in Bjorken-x and momentum transfer Q^2 (see Fig. 10.1) which introduces model dependent corrections at the percent level. Fig. 10.2 illustrates the procedure for a subset of the data.

In the previous annual report we detailed how parton density functions (PDF) are extracted. PDF's evolved to leading order (LO) in α_s are essential for the proper simulation of parton showers (PS) and underlying event properties in LO+PS Monte Carlo (MC) event generators. In the light of the imminent restart of the LHC with increased E_p, new tunes for the underlying events and minimum bias studies are needed for the various MC generators. Higher proton energy corresponds to lower Bjorken-x and the HERA PDF sets with their special emphasis on low-x structure functions are crucial in this program. The new PDF version HERAPDF2.0 (prel.) NNLO [4] based on the procedures mentioned above will eventually replace the HERAPDF1.5 NNLO [5], widely used at present. Typical results of the new fit are shown in Fig. 10.3. Fig. 10.4 directly compares the two PDF sets.

For a few exclusive channels preliminary results were shown at conferences and some final data appeared in print. The D^* production data have been combined from the two HERA experiments [6] (see Fig. 10.5). Diffraction models are tested in the dijet channel [7, 8]

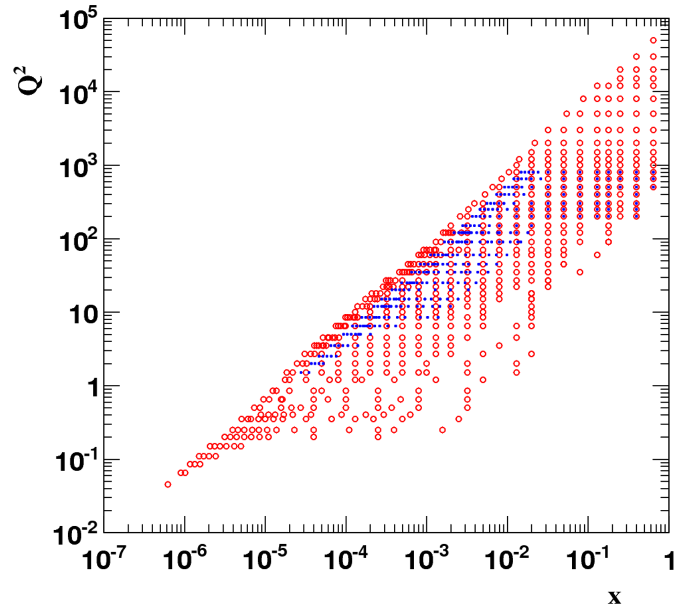

FIG. 10.1 – The grids for E_p = 920 and 820 GeV (red circles) as well as E_p = 575 GeV and 460 GeV (blue squares). The latter grid has a finer x binning.

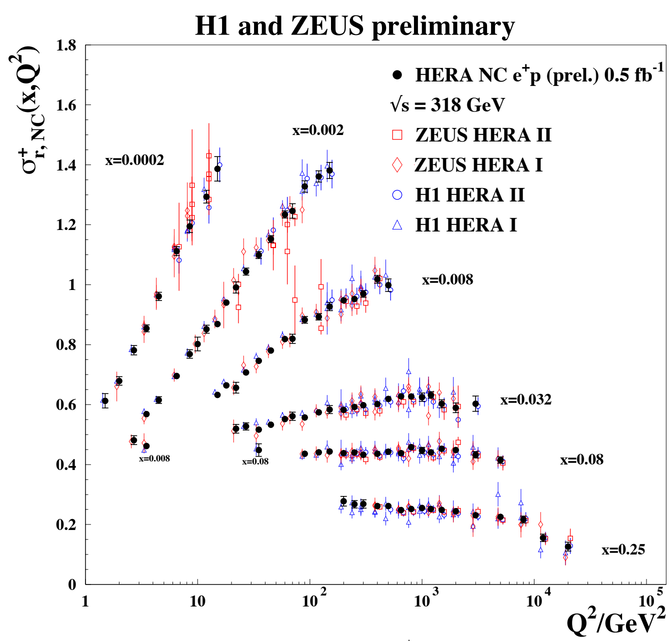

FIG. 10.2 – HERA combined NC e^+p reduced cross section as a function of Q^2 for six selected x-bins compared to the separate H1 and ZEUS results used as input. The individual measurements are displaced horizontally for better visibility. Error bars represent total uncertainties.

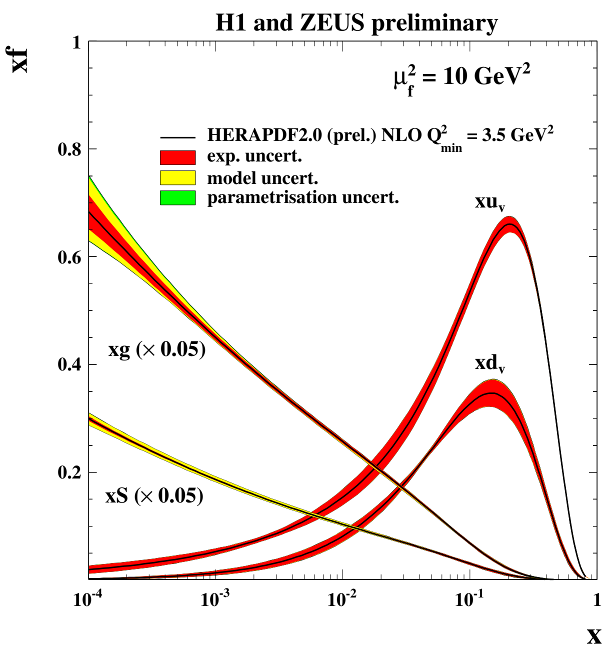

FIG. 10.3 – Valence, sea and gluon x distributions of HERAPDF2.0 (prel.) NNLO with $Q^2_{min} = 3.5$ GeV^2. The different sources of uncertainty are indicated.

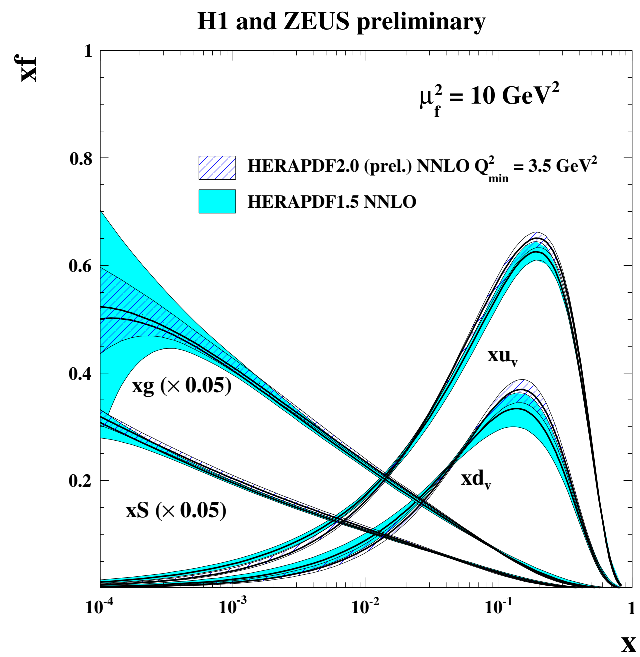

FIG. 10.4 – Comparison between HERAPDF2.0 (prel.) NNLO and HERAPDF1.5 NNLO.

and addressed in single particle production channels where use is being made of the forward proton and neutron counter data [9, 10].

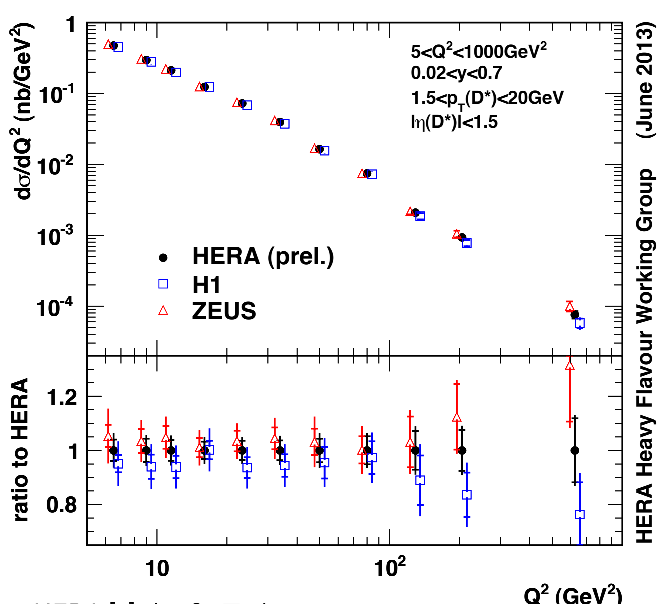

FIG. 10.5 – D^* production cross section vs. Q^2. Shown are results from H1 and ZEUS, and their combination. The inner error bars indicate the statistical uncertainties before combination, and the uncorrelated part of the uncertainties after combination. The outer error bars represent the total uncertainties. The bottom part shows the ratio between these cross sections and the central value of the combined result.

[1] *Combination of inclusive $e^{\pm}p$ cross section measurements at HERA* [2], by O. Turkot.

[2] XXII Int. Workshop on *Deep-Inelastic Scattering and Related Subjects*, DIS2014, April 28 - May 2 2014, Warsaw, Poland.

[3] V. Andreev *et al.* (H1-Collaboration), Eur. Phys. J. C **74** (2014), 2814.

[4] *HERAPDF2.0 fits including all HERAI+II inclusive data sets* [2], by V. Radescu.

[5] *HERAPDF1.5LO PDF set with experimental uncertainties* [2], by M. Cooper-Sarkar.

[6] *Combination of D^* differential cross section measurements in deep-inelastic ep scattering at HERA* [2], by M. Lisovyi.

[7] *Dijet production with large rapidity gap in deep-inelastic scattering at HERA* [2], by B. Pokorny.

[8] *Diffractive dijet production with a leading proton in ep collisions at HERA* [2], by R. Zlebcik.

[9] *Measurement of Feynman-x spectra of photons and neutrons in the very forward direction in deep-inelastic scattering at HERA*, V. Andreev *et al.* (H1-Collaboration), submitted to Eur. Phys. J. C, arXiv:1404.0201 [hep-ex].

[10] *Exclusive photoproduction of ρ^0 with leading neutron at HERA* [2], by S. Levonian.

11 The SHIP Experiment

E. Graverini, N. Serra, and B. Storaci

in collaboration with:
CERN, EPFL Lausanne, INFN Cagliari, Università Federico II and INFN Napoli, Imperial College London

Two of the main reasons not to consider the Standard Model (SM) a complete theory of fundamental interactions are the existence of dark matter and the baryon-antibaryon asymmetry in the universe. However, the only direct evidence of physics beyond the SM is the violation of lepton flavour in the neutrino sector observed in neutrino oscillations [1]. Intriguingly, models with right-handed majorana neutrinos or heavy neutral leptons (HNLs) can give a simultaneous explanation to neutrino masses and mixings, baryon-antibaryon asymmetry and dark matter. The most promising of these models is the ν Minimal Standard Model (νMSM). In this model the lightest of these neutrinos (N_1), has a mass in the keV region and it is sufficiently stable to play the role of dark matter. The other two neutrinos ($N_{2,3}$) are almost degenerate in mass, have a mass in the GeV region and are responsible for neutrino oscillations and baryon-antibaryon asymmetry in the universe.

The search for these particles is experimentally very challenging since they couple very weakly to SM particles and have a long lifetime. Searches for these particles have been performed in the past but present constraints are mostly outside the cosmologically interesting region where baryogenesis, dark matter and neutrino oscillations can be simultaneously explained. Fig. 11.1 shows constraints on the $N_{2,3}$ mass and the mixing of HNLs with the muon neutrinos U^2_μ.

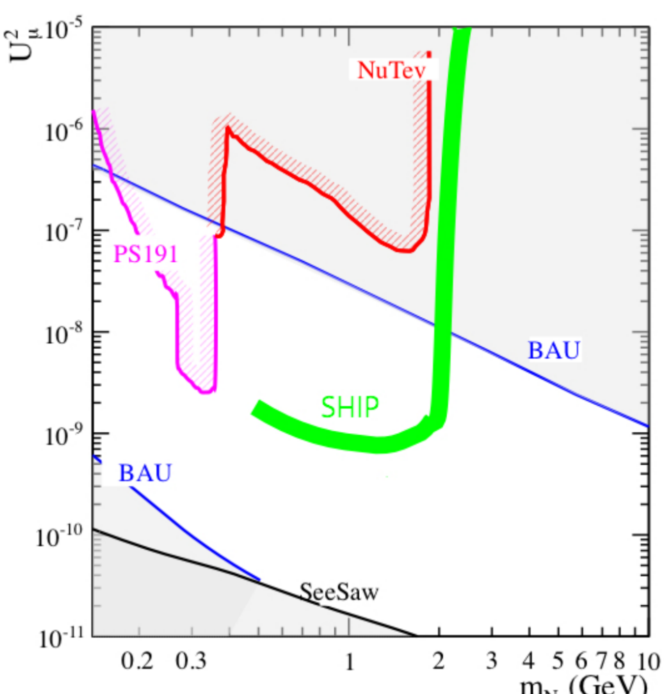

FIG. 11.1 – Experimental and theoretical constraints on the νMSM as a function of the mass of $N_{2,3}$ and their mixing with ν_μ. The SHIP sensitivity is indicated.

HNLs can be produced in (semi)-leptonic decays of mesons, by mixing with active SM neutrinos. Recently, a new fixed target experiment (SHIP) was proposed at SPS of CERN to search for HNLs. The SHIP experiment will probe the high intensity frontier, i.e. extensions of the SM with weakly coupled long lived particles, and is complementary to the high energy frontier explored by large general purpose detectors. The Expression Of Interest of the SHIP experiment [2] was submitted to the SPS committee (SPSC) in October 2013. The SPSC recognized the scientific value of the proposal and encouraged the preparation of a Technical Proposal for the experiment. A preliminary design of the SHIP experiment is shown in Fig. 11.2.

The 400 GeV proton beam of the SPS will be dumped into a heavy target. A hadron absorber will be placed behind the target to stop secondary pions and kaons before they decay (semi)leptonically, so that only muons survive after the absorber. In order to reduce the muon flux to an acceptable level, a 50 m muon shield consisting of heavy material (either Tungsten or Uranium) is proposed. Following the muon shield there is a 2×50 m long, 5 m diameter vacuum tank. This tank is used as a fiducial decay volume, i.e. only decays within this volume will be considered for the analysis. The pressure inside the vacuum tank is about 10^{-2}mbar, which reduces the background due to neutrino interactions with the air in the decay volume to a negligible level. The detector itself consists of two identical elements placed inside the vacuum tank. They are composed of a veto system, four tracking stations, a dipole magnet, a calorimeter and a muon detector (see Fig. 11.2). N. Serra performed the necessary MC studies of the experimental sensitivity and was strongly involved in the optimization of the detector concept. The expected sensitivity to HNLs for muonic decays is shown in Fig. 11.1. The SHIP experiment will offer the possibility to search for HNLs in the cosmologically most interesting region, improving by several orders of magnitude present sensitivities. In addition to models with HNLs,

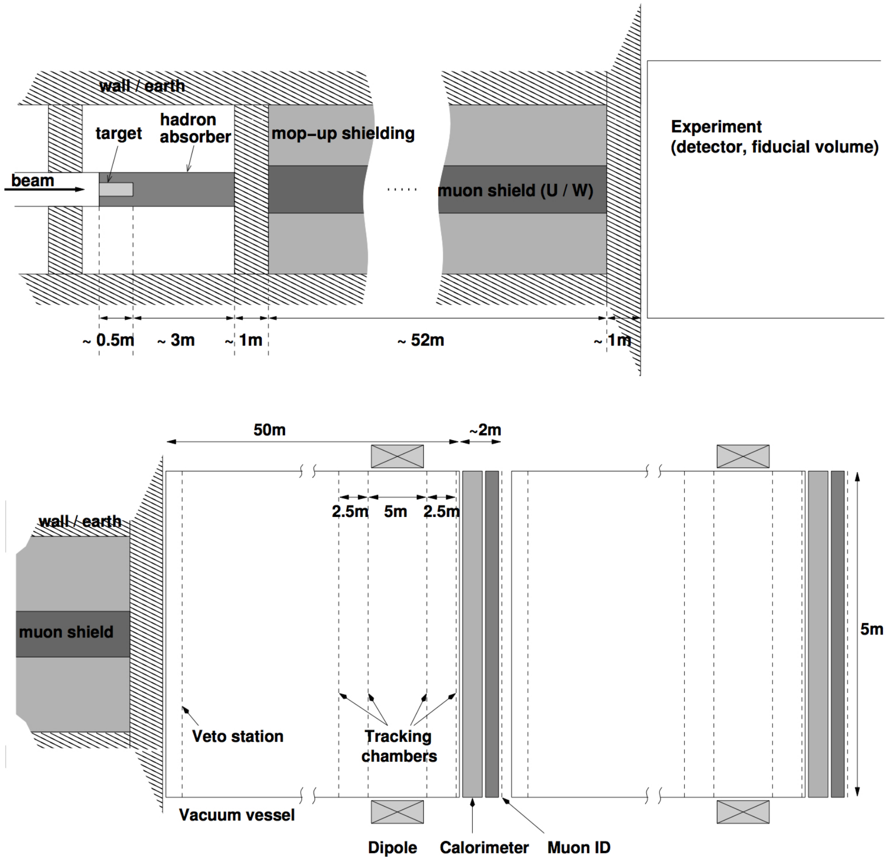

FIG. 11.2 – Schematic view of the target, hadron absorber and muon shield (top). Fiducial decay volume and the SHIP detector (bottom).

there are several other models that predict the existence of long lived hidden particles, the so called secluded sector [3]. The secluded sector interacts with the SM via portals, which are renormalizable interactions between the SM fields and hypothetical SM-singlets. Given the small couplings and the long lifetime of such particles, high statistics and large detectors are needed to discover these particles directly.

An incomplete list of models for which the SHIP experiment can probe a region of the parameter space challenging or not accessible by other experiments follows:

- Light sgoldstinos as SUSY partners of the goldstino, axion- and dilaton-like particles in SUSY extensions of the SM (see for instance [4])

- Light R-parity violating neutralinos in SUSY may be produced in decays such as $D \to \ell\chi$, and then decay into three-body final states, e.g. $\chi \to \ell^+\ell^-$.

- Light (axial) vectors in secluded Dark Matter models, as for instance massive paraphotons from a hidden sector [3]. They may be produced in heavy hadron decays like $\Sigma \to pV$ and decay into pairs of SM particles, e.g. $V \to \ell^+\ell^-$.

[1] Super-Kamiokande Collab., S. Fukuda *et al.*, Phys. Lett. B 539 (2002) 179.

[2] W. Bonivento *et al.*, arXiv:1310.1762, submitted to the SPSC.

[3] M. Pospelov, A. Ritz and M. B. Voloshin, Phys. Lett. B 662 (2008) 53.

[4] D. Gorbunov, Nucl. Phys. B 602 (2001) 213.

12 Particle Physics with LHCb

J. Anderson, R. Bernet, E. Bowen, A. Bursche, N. Chiapolini, M. De Cian (until June 2013), M. Chrząszcz[1] (since July 2013), Ch. Elsasser, E. Graverini (since February 2014), F. Lionetto (since November 2013), P. Lowdon, K. Müller, S. Saornil, N. Serra, St. Steiner, O. Steinkamp, B. Storaci, U. Straumann, M. Tresch, and A. Vollhardt

[1] also at Henryk Niewodniczanski Institute of Nuclear Physics, Polish Academy of Sciences, Kraków, Poland

The full LHCb collaboration consists of 67 institutes from Brazil, China, France, Germany, Ireland, Italy, Poland, Romania, Russia, Spain, Switzerland, the Netherlands, Turkey, Ukraine, the United Kingdom and the United States of America.

(LHCb Collaboration)

The LHCb experiment [1] at CERN's Large Hadron Collider (LHC) was designed to perform precision measurements of *CP* violating observables and to study rare decays of hadrons containing a b or c quark. Its main physics goals are to study the flavour structure in the quark sector and to search for possible New Physics (NP) beyond the Standard Model (SM) of particle physics. Of special interest for NP searches are processes that involve loop diagrams, such as box or penguin diagrams. Heavy new particles, which are predicted by most NP models, can appear virtually in the loops and modify production cross sections and angular distributions of final state particles with respect to SM predictions.

The forward acceptance of the detector and the ability to trigger on particles with relatively low transverse momentum also open up unique opportunities for particle production studies in proton-proton (pp) collisions at the LHC. The scope of such studies was extended to proton-lead collisions during dedicated data taking periods in early 2013.

The present long shutdown (LS1) of the LHC is being used by LHCb to install scintillator counters around the beam line for a better identification of diffractive events and to improve the software trigger for the next data taking period, which is scheduled to begin in spring 2015.

Our group contributed significantly to the construction and operation of the LHCb detector. We make crucial contributions to two key analyses of rare B meson decays. We lead studies of the production of W and Z bosons and low mass Drell-Yan pairs. We lead the development of improved algorithms for the trajectory reconstruction of charged particles in the trigger, both for the LHCb upgrade and for the data taking period starting in 2015. Finally, we have started to contribute to the R&D of the upgraded LHCb detector.

[1] A. A. Alves Jr. *et al.* [LHCb Collab.], JINST 3 S08005 (2008).

12.1 LHCb detector

The LHCb detector [1] is a single-arm forward spectrometer with pseudo-rapidity coverage in the range 2 to 5. The detector has excellent vertex and momentum resolution, needed to distinguish between primary and secondary vertices and to provide high invariant mass resolution. Two Ring Imaging Cherenkov (RICH) detectors allow discrimination between pions and kaons over a wide momentum range. The detector and its performance have been described in previous annual reports [2].

The Zurich group is responsible for the operation and maintenance of the Silicon Tracker (ST) system, in particular for the Tracker Turicensis (TT), a large planar silicon-strip tracking detector located in front of the LHCb dipole magnet that has been designed and constructed in Zurich.

12.1.1 Shutdown activities

S. Saornil

During LS1 the detectors are operated for short tests only or during regular LHCb commissioning weeks.

The control software of the ST has been completely revised to improve the robustness and maintainability of the code and to significantly shorten the time needed for the configuration of the detector for data taking.

12.1.2 Radiation damage studies

Ch. Elsasser, O. Steinkamp

Radiation damage in the TT is monitored by studying the detector leakage currents and by analysing dedicated charge-collection efficiency (CCE) scans, performed several times per year. Those allow to reconstruct the evolution of the full depletion voltage of the sensors. The results from the CCE scans as well as the luminosity dependence of the leakage currents (Fig. 12.1) show good agreement with the predictions which indicates that the TT

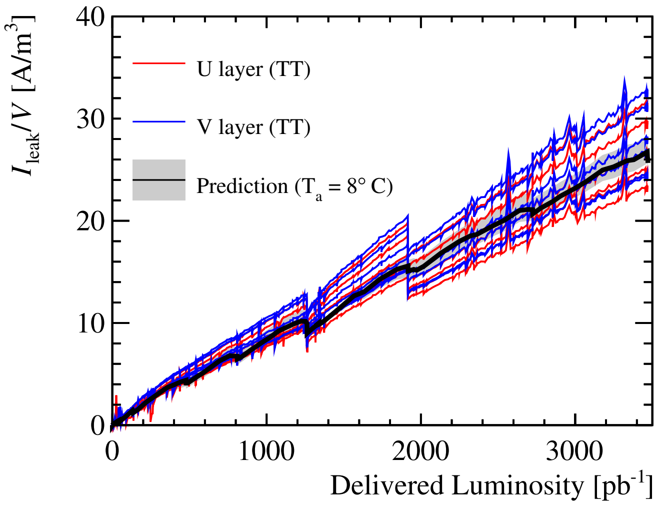

FIG. 12.1 – The measured distributions of volume leakage current versus delivered luminosity show good agreement with the predictions.

will survive well beyond the date of the LHCb upgrade.

[1] A. A. Alves Jr. *et al.* [LHCb Collab.], JINST 3 S08005 (2008).

[2] Physik-Institut, University of Zürich, Annual Reports 1996/7 ff., available at *http://www.physik.uzh.ch/reports.html*.

12.2 LHCb upgrade

The LHCb collaboration plans to perform a comprehensive upgrade of the detector and its readout electronics during the next long shutdown (LS2) resulting in a significant increase in physics reach [1]. The upgrade [2, 3] comprises two main areas: preparing the detector for the larger luminosity of up to 2×10^{33} cm^{-2}s^{-1} and allowing to read out the detector at the higher bunch crossing rate of 40 MHz. It is expected that reconstruction efficiencies for b hadron decays with fully hadronic final states will increase by a factor two.

12.2.1 Development of a new Upstream Tracker

F. Lionetto, S. Saornil, O. Steinkamp

The front-end electronics of the present TT detector is incompatible with the foreseen 40 MHz readout. The main purpose of the new Upstream Tracker (UT) [4], replacing TT, will be to reduce the time required for track reconstruction at trigger level by providing a fast momentum estimate for track candidates. Major improvements over the current TT are:

- less clearance between the beam pipe and the detector to increase the acceptance in the very forward region,
- finer readout granularity along the readout strips for lower strip occupancy and faster and more efficient pattern recognition and
- a finer readout pitch of the silicon sensors closest to the interaction region for higher spatial resolution and lower detector occupancy.

Our group has recently joined the UT detector project, together with Syracuse University and University of Maryland (USA), Universita degli Studi di Milano (Italy) and University of Science and Technology, Krakow (Poland). Building on our experience with TT, we have taken over the responsibility for the detector control system, including the low-voltage and bias-voltage distribution and the monitoring of environmental and operational parameters. In addition, we will participate in silicon sensor prototype studies and quality assurance of detector modules.

12.2.2 Track reconstruction at software trigger level

E. Bowen, E. Graverini, B. Storaci, M. Tresch

The reconstruction of charged tracks at the software trigger level is one of the greatest challenges of the upgrade. We have developed a new pattern recognition algorithm based on UT information which lowers the reconstruction time by a factor 3. The algorithm significantly reduces the fraction of wrongly reconstructed tracks while maintaining high reconstruction efficiency and was adopted as the baseline algorithm for the full software trigger.

We are now adapting this new algorithm to the existing LHCb detector and study if it can be employed already for the upcoming LHC run. Initial studies gave encouraging results.

[1] R. Aaij *et al.* [LHCb Collab.], arXiv:1208.3355 [hep-ex].

[2] R. Aaij *et al.* [LHCb Collab.], *Letter of Intent for the LHCb Upgrade*, CERN-LHCC-2011-001, LHCC-I-018.

[3] I. Bediaga *et al.* [LHCb Collab.], *Framework TDR for the LHCb Upgrade: TDR*, CERN-LHCC-2012-007, LHCb-TDR-012.

[4] A.A. Alves Jr *et al.* [LHCb Collab.], *LHCb Tracker Upgrade TDR*, CERN-LHCC-2014-001, LHCb-TDR-015.

12.3 Physics results

During the past twelve months, LHCb published more than 70 new physics results [1] in a wide range of topics, including measurements of mixing parameters and *CP* violating observables in the beauty and charm meson systems, of branching ratios and angular observables in rare b decays and studies of b hadron and electroweak boson production.

New results of *CP* violating observables included the first observation of *CP* violation in the B_s^0 meson system, using the decay $B_s^0 \to K^-\pi^+$ [2], and a new determination of the CKM angle γ from a combination of $B^\pm \to DK^\pm$ and $B^\pm \to D\pi^\pm$ decays [3]. The γ measurement is competitive and in agreement with earlier measurements from the B factories. LHCb also published the currently most precise measurement of the flavour-specific *CP* violating asymmetry, $a_{\rm sl}^s$, in semileptonic B_s^0 decays [4], in good agreement with the SM prediction of a small asymmetry. The LHCb result does not corroborate the large value found earlier by the D0 collaboration.

LHCb reported the first observation of a non-zero photon polarization in $b \to s\gamma$ transitions, from the analysis of angular distributions in the decay $B^+ \to K^+\pi^+\pi^-$ [5]. In the SM, $b \to s\gamma$ transitions are mediated by the exchange of a virtual W boson and photons are almost 100% (left-handed) polarized. In NP models deviations from full polarization are possible.

Several new measurements of *CP* violating asymmetries in neutral D meson decays were published. Two new measurements were performed of the difference ΔA_{CP} between the decay rates of D^0 and $\overline{D}^0$ mesons into K^+K pairs and into $\pi^+\pi$ pairs. An earlier LHCb measurement of ΔA_{CP}, using a subset of the data collected in 2011, had hinted at an unexpectedly large *CP* asymmetry, triggering intensive theoretical activity. The two new analyses used the full 2011 data set. One analysis [6] used the charge of the pion in $D^{*-} \to \overline{D}^0\pi^-$ decays to distinguish $\overline{D}^0$ and D^0 decays, the other analysis [7] made use of the muon charge in $B^+ \to \overline{D}^0\mu^+\nu_\mu$ decays for this purpose. Both results are in agreement with no direct *CP* asymmetry. Another analysis, looking for possible asymmetries $A_\Gamma(K^+K)$ and $A_\Gamma(\pi^+\pi)$ in the inverse effective lifetimes of D^0 and $\overline{D}^0$ in decays to the K^+K and $\pi^+\pi$ final states, respectively, gave results consistent with no indirect *CP* violation [8]. Finally, measurements of D^0–$\overline{D}^0$ oscillation parameters also result in values consistent with no indirect *CP* violation in mixing [9].

Measurements of b hadron properties included the world's most precise measurement of the B_c^+ lifetime [10] and a new measurement of the Λ_b^0 lifetime relative to the B^0 lifetime [11]. From Heavy Quark Expansion (HQE) theory, the Λ_b^0-to-B^0 lifetime ratio is expected to be close to one. While earlier measurements at LEP had found a ratio around 80%, the LHCb result is good agreement with the predictions.

LHCb also published new measurements of the masses and quantum numbers of the $X(3872)$ and the $Z(4430)^-$, two states that do not seem to fit into the standard spectrum of $q\overline{q}$ states. The $X(3872)$ was discovered ten years ago by the Belle collaboration and has been speculated to be a $D\overline{D}^*$ molecule, a tetraquark state or a charmonium-molecule mixture. The LHCb measurement [12] unambiguously determined the $X(3872)$ quantum numbers to be $J^{PC} = 1^{++}$, compatible with a $D\overline{D}^*$ molecule or a tetraquark state. A classical interpretation of the $X(3872)$ as a pure charmonium state is not excluded by these quantum numbers, but this assignment is made unlikely by the measured mass.

First evidence for the $Z(4430)^-$ was presented by the Belle collaboration in 2008. The recent LHCb measurement [13], using the full combined 2011/2012 dataset, confirms the signal with a significance of 13.9 standard deviations and establishes its resonant nature via a phase-shift analysis. The observed quantum numbers of the state are $J^P = 1^+$. The minimal quark content of this state is $c\overline{c}d\overline{u}$, making this the first unambiguous observation of an exotic particle that cannot be classified within the traditional quark model.

Analyses of the data samples collected in proton-lead ion runs are ongoing, a first published result is the measurement of J/ψ production and cold nuclear matter effects [14].

[1] http://lhcb.web.cern.ch/lhcb/

[2] R. Aaij *et al.* [LHCb], Phys. Rev. Lett. **110** (2013) 22, 221601.

[3] R. Aaij *et al.* [LHCb], Phys. Lett. B **726** (2013) 151.

[4] R. Aaij *et al.* [LHCb], Phys. Lett. B **728** (2014) 607.

[5] R. Aaij *et al.* [LHCb], arXiv:1402.6852 [hep-ex].

[6] LHCb Collab., LHCb-CONF-2013-003.

[7] R. Aaij *et al.* [LHCb], Phys. Lett. B **723** (2013) 33.

[8] R. Aaij *et al.* [LHCb], Phys. Rev. Lett. **112** (2014) 041801.

[9] R. Aaij *et al.* [LHCb], Phys. Rev. Lett. **111** (2013) 251801.

[10] R. Aaij *et al.* [LHCb], arXiv:1401.6932 [hep-ex].

[11] R. Aaij *et al.* [LHCb], Phys. Rev. Lett. **111** (2013) 102003.

[12] R. Aaij *et al.* [LHCb], Phys. Rev. Lett. **110** (2013) 22, 222001.

[13] R. Aaij *et al.* [LHCb], arXiv:1404.1903 [hep-ex].

[14] R. Aaij *et al.* [LHCb], JHEP **1402** (2014) 072.

12.3.1 Search for the lepton flavour violating decay $\tau^- \to \mu^-\mu^+\mu^-$

M. Chrząszcz, N. Serra

The LHCb experiment offers the possibility to search for lepton flavour violating τ decays, such as $\tau^- \to \mu^-\mu^+\mu^-$. The branching ratio of this decay, mediated by neutrino mixing, is negligibly small in the SM but could be strongly enhanced in several extensions of the SM [1], such as Supersymmetry, Extended Extra Dimensions and models with an extended neutrino sector. Limits on the branching ratio of this decay have been set at the B-factories [2] and by LHCb with 1 fb^{-1} [3]. The LHCb limit was the first result for this decay mode at a hadron collider and had a crucial contribution by M. Chrząszcz.

At present, the Zurich group is the driving force for the update of this result with 3 fb^{-1}. The event selection has been optimised taking into account that the τ leptons come from (semi)-leptonic decays of charm and beauty mesons. A multi-variate event selection has been trained to optimise the sensitivity to the admixture of these two sources using a procedure known as "blending". We also contribute to the modelling of the background and the extraction of the branching ratio. The improvements in the event selection result in an upper limit sensitivity of 5.6×10^{-8} at 90% C.L., similar to the limits set by the B-factories in a much cleaner environment.

M. Chrząszcz is a new member of the HFAG collaboration and is contributing to the averaging of τ-lepton properties.

[1] W.J. Marciano, T. Mori and J.M. Roney, Ann. Rev. Nucl. Part. Sci 58 (2008) 315-341.

[2] K. Hayasaka *et al.* [Belle Collab.], Phys. Lett. B 687 (2010) 139 ; J. P. Lees *et al.* [BaBar Collab.], Phys. Rev. D 81 (2010) 111101(R).

[3] R. Aaij *et al.* [LHCb Collaboration], Phys. Lett. B 724 (2013) 36.

12.3.2 $B^0 \to K^*\mu^+\mu^-$

E. Bowen, M. Chrząszcz, N. Serra, B. Storaci and M. Tresch

The rare decay $B^0 \to K^{0*}\mu^+\mu^-$ is a flavour-changing neutral current process that proceeds via box and loop diagrams. This decay has been widely studied in the literature from the theoretical perspective, since its angular distributions and differential branching fraction are sensitive to a large number of NP scenarios (see Ref. [1] and references therein). This decay is kinematically described by three angles and the di-muon invariant mass q^2.

In the year 2012 LHCb determined several angular observables in bins of q^2 and made a first measurement of the zero-crossing point of the forward-backward asymmetry of the di-muon system with a key contribution from our group [2]. The remaining angular observables had never been measured, since they are not accessible via angular projections. We developed a method exploiting the symmetries of the angular distribution. The result, based on 1 fb^{-1}, for the observable P_5' is compared with SM predictions in Fig. 12.2. A 3.7σ discrepancy is observed in the low q^2 region.

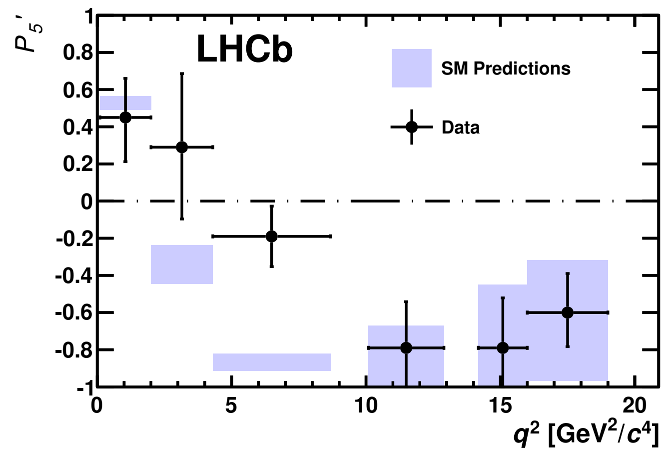

FIG. 12.2 – Observable P_5' as a function of q^2 [4], compared to SM predictions [3].

This result has attracted a considerable interest from the flavour physics community and it is widely discussed in the literature. It has been interpreted as a reduced C_9 Wilson coefficient with respect to the SM prediction [5]. It was also pointed out that it is numerically consistent with the systematically lower branching ratios with respect to predictions, measured at LHCb for several $b \to s\ell^+\ell^-$ transitions. New physics interpretations of a heavy Z' of about 10 TeV have been suggested [6]. It has also been suggested that this discrepancy is explained by an underestimation of the theoretical uncertainty associated with non-factorizable QCD contributions [7]. At the moment we are updating the analysis to include the full 3 fb^{-1} data set. In addition, B. Storaci and N. Serra are trying to extract the theoretical corrections to QCD factorisation directly from data.

[1] J. Matias *et al.*, JHEP 04 (2012) 104.

[2] R. Aaij *et al.* [LHCb Collab.], JHEP 1308 (2013) 131.

[3] S. Descotes-Genon *et al.*, JHEP 1305 (2013) 137.

[4] R. Aaij *et al.* [LHCb Collab.], Phys. Rev. Lett. 111 (2013) 191801.

[5] S. Descotes-Genon, J. Matias and J. Virto, Phys. Rev. D88 (2013) 074002.

[6] R. Gauld, F. Goertz and U. Haisch, JHEP 1401 (2014) 069.

[7] F. Beaujean, C. Bobeth and D. van Dyk, arXiv:1310.2478 [hep-ph].

12.3.3 The decays $B^0_{(s)} \to \mu^+\mu^-$

Ch. Elsasser

The decays $B^0_s \to \mu^+\mu^-$ and $B^0 \to \mu^+\mu^-$ are very rare in the SM, with branching fractions of $(3.23 \pm 0.27) \times 10^{-9}$ and $(1.07 \pm 0.10) \times 10^{-10}$, respectively [1]. NP contributions could be of the same order of magnitude so measurements of these branching fractions, one of the key LHCb measurements, may strongly constrain the allowed parameter space for various NP models.

Our group has made significant contributions to these measurements such as the calibration of the di-muon invariant mass and the multivariate classifier used to distinguish signal and background events. The distributions of both variables were determined from the observed exclusive $B^0_{(s)} \to h^+h^-$ decays, where $h^\pm$ is a kaon or a pion. Information from the RICH detectors is used to separate kaons and pions. The particle identification efficiencies were evaluated using the control channels $B^\pm \to J/\psi(1S)K^\pm$ and $B^0_s \to J/\psi(1S)\phi$. Alternatively, the di-muon invariant mass resolution has been interpolated between values found at the di-muon resonances J/ψ, $\psi(2S)$, $\Upsilon(1S)$, $\Upsilon(2S)$ and $\Upsilon(3S)$. The results of both methods are in perfect agreement.

A combined analysis of 1 fb^{-1} collected in 2011 at a centre-of-mass energy of $\sqrt{s} = 7$ TeV and 2 fb^{-1} collected in 2012 at $\sqrt{s} = 8$ TeV, yielded a 4.0 σ statistical significance for the observation of the decay $B^0_s \to \mu^+\mu^-$. The measured branching fraction

$$\mathcal{B}(B^0_s \to \mu^+\mu^-) = (2.9^{+1.1}_{-1.0}) \times 10^{-9},$$

is in good agreement with the the SM prediction.

The experimental sensitivity for B^0 decays is four times larger than for B^0_s due to the different hadronization fractions. For $B^0 \to \mu^+\mu^-$ the number of candidate events is consistent with the background expectation, yielding an improved limit on the branching fraction [2]:

$$\mathcal{B}(B^0 \to \mu^+\mu^-) < 7.4 \times 10^{-10}, \quad 95\% \text{ C.L.}$$

[1] A. J. Buras *et al.*, Eur. Phys. J. C72 (2012) 2172.

[2] R. Aaij *et al.* [LHCb Collab.], Phys. Rev. Lett. 111 (2013) 101805.

12.3.4 Electroweak boson and low mass Drell-Yan production

J. Anderson, A. Bursche, N. Chiapolini, Ch. Elsasser, P. Lowdon and K. Müller

The inclusive production cross section of the Z boson has been measured by LHCb using final states with pairs of muons [1, 2], electrons [3] or taus [4]. The large statistics available with the 2011 and 2012 data will allow for very precise measurements of differential cross sections as well. The analysis includes a time consuming evaluation of the systematic uncertainties and final results are not yet available.

The large data sets also allow for measurements of Z production with exclusive final states. In the past year, measurements have been published of Z production with jets [5] and Z production in association with a D meson [6], both with a large contribution from our group. A measurement of Z in association with b-quarks will be published soon. All these measurements are sensitive to the substructure of the proton which is described by parton density functions (PDFs). Our group (P. Lowdon) got also involved in the extraction of PDFs from HERA and LHC data sets.

Jet production in association with a Z boson is sensitive to the gluon content of the proton and serves furthermore as a sensitive test of perturbative QCD as higher orders must be included. Results based on an integrated luminosity of 1 fb^{-1} have been published [5] (A. Bursche in close collaboration with the Cambridge group). The dominant uncertainty originates in the jet energy scale. Simulation indicates jet energy resolutions of 10-15% for jets with p_T between 10 and 100 GeV. Studies of events with a Z and a jet back-to-back show agreement between measured and simulated energy scale and resolution. The normalised differential cross section as a function of p_T of the leading jet is shown in Fig. 12.3. Predictions at different order of α_s and with different PDF sets are shown for comparison. As expected, the measurements are best described by the $\mathcal{O}(\alpha_s^2)$ predictions calculated using POWHEG [7] interfaced to PYTHIA [8].

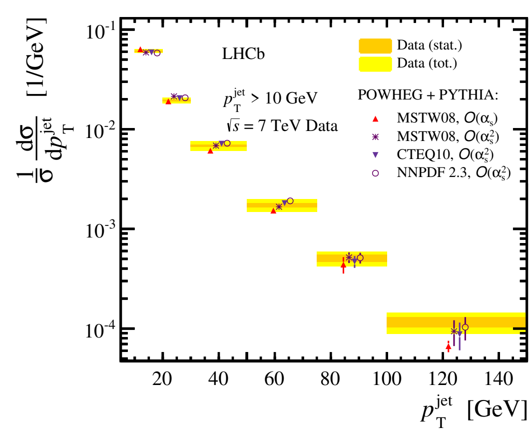

FIG. 12.3 – Normalised experimental cross section of Z production in association with a jet as a function of p_T of the leading jet compared to model predictions at different order of α_s and with different PDF sets.

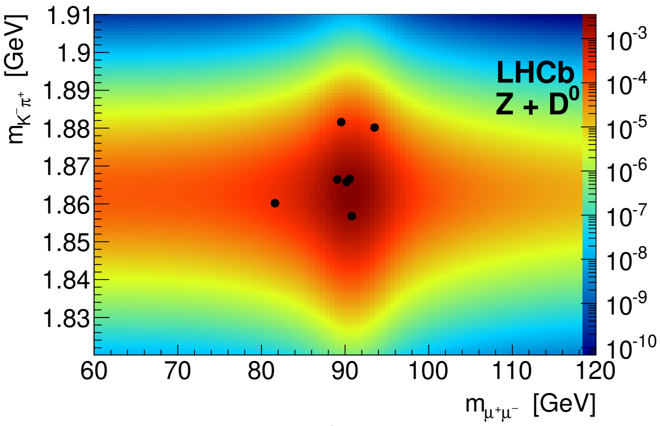

FIG. 12.4 – Distribution of the reconstructed invariant masses of the 7 $Z + D^0$ candidates superimposed on the expected distribution containing both signal and background.

The measurement of Z production with an open charm meson provides information on the charm parton distribution, the charm production mechanism and double parton scattering [9, 10]. For this analysis, the Z boson is reconstructed in the di-muon channel, while charmed mesons are identified in the final states $D^0 \to K^-\pi^+$, $D^+ \to K^-\pi^+\pi^+$. Seven candidates with a D^0 and four with a D^+ are found with a background contamination below 5%. The invariant mass of the Z and D^0 candidates is shown in Fig. 12.4. The full analysis was performed by A. Bursche and published recently [6]. The experience on charmed meson reconstruction gained in this analysis is now applied in a measurement of the double-charm production cross section at a centre of mass energy of 2.76 TeV (master thesis E. Crivelli).

The study of proton-nucleus collisions is a crucial component of the physics program with nuclear beams performed at hadron colliders. Measurements in proton-nucleus collisions can serve as reference for nucleus-nucleus collisions and may be used as an input to nuclear parton distribution function (nPDF) fits. nPDFs are poorly constrained by experimental data, especially in the kinematic region accessible by LHCb. A measurement of the Z production cross section in proton-lead (with the proton beam pointing into the LHCb forward direction) and lead-proton (proton beam pointing backwards) data was performed by Ch. Elsasser. Unfortunately, the available statistics is very low with an integrated luminosity of 1.1 and 0.5 nb^{-1}, respectively. The analysis closely follows Ref. [2] but accounts for the different track multiplicities in proton-proton and proton-lead collisions. The background for both beam configurations is below 0.5%. The results are:

$$\sigma_{Z\to\mu^+\mu^-} = 13.5^{+5.4}_{-4.0}(stat.) \pm 1.2(syst.) \text{ nb, for } p\text{-Pb}$$
$$\sigma_{Z\to\mu^+\mu^-} = 10.7^{+8.4}_{-5.1}(stat.) \pm 1.0(syst.) \text{ nb, for Pb-}p$$

These cross-sections are limited to the fiducial region of 60 - 120 GeV for the di-muon mass, p_T of the muons larger than 20 GeV and pseudo-rapidity in the range range 2.0 - 4.5 and are in agreement with next-to-next-to leading order calculations. The present large uncertainties prevent any conclusion on the presence of nuclear effects but show the great potential of the study of electroweak boson production in proton-lead collisions at LHCb. The result has been submitted for publication [11].

Further ongoing studies in our group are:

- precise measurement of the differential $Z \to \mu^+\mu^-$ production cross section at 7 TeV (J. Anderson),
- low mass Drell-Yan production in the di-muon channel at 7 TeV (J. Anderson, N. Chiapolini, K. Müller) [12],
- a measurement of the low energy $Z \to \mu^+\mu^-$ production cross section at 2.76 TeV (A. Bursche),
- the determination of the di-boson ($Z + \gamma$) production cross section at 8 TeV (master thesis M. Küng),
- studies of W production in proton-lead data (bachelor thesis Ch. Marentini).

[1] R. Aaij *et al.* [LHCb Collab.], JHEP **1206** (2012) 058.
[2] LHCb Collab., LHCb-CONF-2013-005.
[3] R. Aaij *et al.* [LHCb Collab.], JHEP **1302** (2013) 106.
[4] R. Aaij *et al.* [LHCb Collab.], JHEP **1301** (2013) 111.
[5] R. Aaij *et al.* [LHCb Collab.], JHEP **1401** (2014) 033.
[6] R. Aaij *et al.* [LHCb Collab.], arXiv:1401.3245 [hep-ex].
[7] P. Nason, JHEP **0411** (2004) 040.
[8] T. Sjostrand, S. Mrenna and P. Z. Skands, JHEP **0605** (2006) 026.
[9] J. M. Campbell *et al.*, Phys. Rev. D **69** (2004) 074021.
[10] J. M. Campbell, arXiv:0808.3517 [hep-ph].
[11] arXiv:1406.2885 [hep-ph].
[12] LHCb Collab., LHCb-CONF-2012-013.

12.4 Summary and Outlook

The LHCb experiment has collected a large data set at different energies during the data taking period 2010-2013. The results obtained so far have allowed to take a leading role in the field of b and c-physics; to considerably reduce the parameter space for many models beyond the SM and to show world best and world first measurements of B-hadron branching ratios. The physics program of LHCb was significantly extended with measurements with electroweak bosons as well as diffractive physics.

13 Particle physics with the CMS experiment at CERN

L. Caminada, F. Canelli, V. Chiochia, A. de Cosa, C. Favaro, C. Galloni, A. Hinzmann, T. Hreus, B. Kilminster, C. Lange, J. Ngadiuba, D. Pinna, P. Robmann, D. Salerno, S. Taroni, M. Verzetti, and Y. Yang

in collaboration with the:

CMS - Collaboration

Particle physics experiences a very exciting era. On July 4, 2012 the CMS and ATLAS experiments at the CERN LHC announced the discovery of a Higgs-like particle. After 48 years of desperate searches, the last missing ingredient of the Standard Model (SM) of particle physics may well have been found [1, 2].

Whether this indeed is the SM Higgs boson, or possibly one of several Higgs bosons predicted in some theories that go beyond the SM, remains to be seen. The LHC now enters a phase of studying the Higgs boson, measure its properties, including decay modes and additional interactions relating to a new physics scale. These tasks are among the primary goals and challenges of the next LHC run.

The Higgs boson provides a mechanism for mass generation of fundamental particles and electroweak symmetry breaking. Nevertheless, with the existence of a 126 GeV Higgs boson, the question of the stability of its mass has now become urgent. Unless there is an incredible and delicate fine-tuning of the SM, there must be new particles with masses around a TeV that produce loop corrections with the necessary cancellations to stabilize the Higgs boson mass. Theoretical models such as supersymmetry (SUSY) and warped extra dimensions address these and other issues. If these TeV-mass particles exist, the new energy regime of the LHC will allow us to directly produce them and observe their interactions and properties.

Even though the SM describes our universe at the shortest distance scale, it fails extraordinarily at the largest distance scale. Cosmological and astronomical observations have revolutionized our view of the universe by uncovering the existence of dark matter, the vanishingly small relative strength of gravity, the accelerating expansion of the universe, and the matter-antimatter asymmetry. The SM is unable to accommodate any of these observations.

If dark matter is indeed a stable neutral weakly interacting particle with mass less than around a TeV as expected, we must produce it at the LHC. If the relative strength of gravity can be explained, for instance by a universe comprised of both TeV-scale and gravity-scale branes, then new particles will be produced at the LHC. Therefore, the LHC may well bridge the gap between the shortest and the largest distance scales.

[1] CMS collaboration, Phys. Lett. B **716** (2012) 30.

[2] ATLAS collaboration, Phys. Lett. B **716** (2012) 29.

13.1 CMS

CMS [1, 2] is a multipurpose detector designed for a variety of particle physics studies at the LHC. The LHC delivered proton collisions until February 2013 concluding the first three-year running period and entering a two-year shutdown period (Long Shutdown 1, LS1). During this first period CMS collected an integrated luminosity of 23.3 (6.1) fb^{-1} at the center-of-mass energy $\sqrt{s} = 8$ (7) TeV. The large datasets are currently being analyzed. In parallel, LS1 activities are planned until end 2014. LHC is expected to restart operations in early 2015 with proton beams colliding at the center-of-mass energy of 13 TeV.

CMS consists of different detector layers (see Fig. 13.1). An all-silicon tracker, an electromagnetic calorimeter, and a hadronic sampling calorimeter are all contained within a large-bore 3.8 T superconducting solenoid. Beyond the solenoid are four layers of muon detectors. The CMS tracker is composed of the inner pixel detector and the outer silicon strip detector. The pixel detector consists of three barrel layers (BPIX) at 4.4, 7.3, and 10.2 cm, and two forward/backward disks (FPIX) at longitudinal positions of ±34.5 cm and ±46.5 cm and extending in radius from about 6 to 15 cm.

The high segmentation of the pixel detector permits the building of seed clusters for the tracking algorithm reconstruction and also for the fast online track reconstruction in the high level trigger (HLT). The pixel detector is used for electron/photon identification and muon reconstruction, but its precision resolution is crucial for primary vertex and pile-up vertex reconstruction, and identification of long-lived τ-leptons and B-hadrons traveling a few millimeters before decaying. The performance of the current pixel detector during data taking has been excellent. It is noteworthy that the BPIX was built by the CMS Swiss Consortium: PSI, ETH and the University of Zürich.

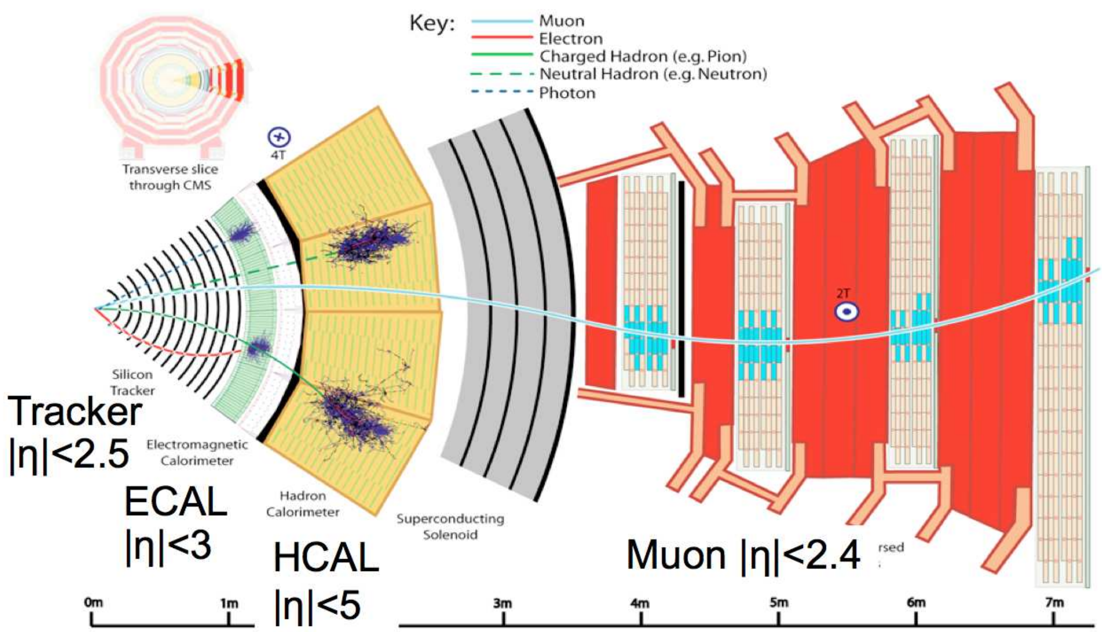

FIG. 13.1 – Schematic view of a sector of the CMS detector, illustrating how muons, electrons, charged hadrons, neutral hadrons and photons are reconstructed.

Members of our group cover important coordination roles within the CMS collaboration. A. de Cosa is the level3 online pixel coordinator, A. Hinzmann is co-convener of the Exotica in jet final states physics group, B. Kilminster is co-convener of the phase 2 upgrade future Higgs physics group, T. Hreus coordinates the Tracker Detector Performance Group, in charge of the tracker offline software and operations, M. Verzetti was editor of the analysis note detailing the searches for associated W/Z bosons and Higgs production in τ decays, while V. Chiochia is a member of the CMS conference committee and B-physics steering group. Most of our group have served as referees of several recent publications. Currently F. Canelli holds the position of group leader.

More than hundred publications were released by the CMS collaboration in the period covered by this report. In what follows, we describe the contributions of our group, which were focused in three main areas of research: physics measurements and searches, analysis techniques that benefit these physics analyses, and the operation and upgrade of one of the detectors vital to these measurements.

[1] *CMS technical design report*, CMS collaboration, CERN-LHCC 2006-001.

[2] S. Chatrchyan *et al.* [CMS Collaboration], JINST **3**, S08004 (2008).

13.2 Measurements and searches

In this subsection, we highlight physics analyses and other contributions we have been engaged in. A primary physics focus was on the better understanding of the Higgs sector. We also searched for new particles motivated by dark matter, the MSSM, and extra dimensions, which could be in reach of LHC energies and luminosities.

13.2.1 Evidence of Higgs boson decaying to τ leptons

It is essential to determine the properties of the discovered particle with some accuracy to establish if it corresponds to the Higgs boson of the SM or of an extended model. The first evidence for the Higgs boson was reported in decays to boson pairs, such as W^+W^-, ZZ and $\gamma\gamma$. At the Tevatron, evidence was found for the Higgs decay to fermions in $H \to b\bar{b}$ [1]. Until recently, no such evidence was reported at the LHC. Decays to τ pairs are a promising channel because of the large event rate expected in the SM compared to the other leptonic decay modes and the smaller background with respect to $b\bar{b}$.

Our group has searched for the SM Higgs boson in the process $pp \to WH \to \ell\nu\tau_\ell\tau_{\rm had}$, where τ_ℓ and $\tau_{\rm had}$ indicate leptonic and hadronic τ decays, respectively. While this production mode has a lower cross section than the direct production channels, such as gluon-gluon fusion, it has a smaller background and may allow a more accurate measurement of the coupling constant.

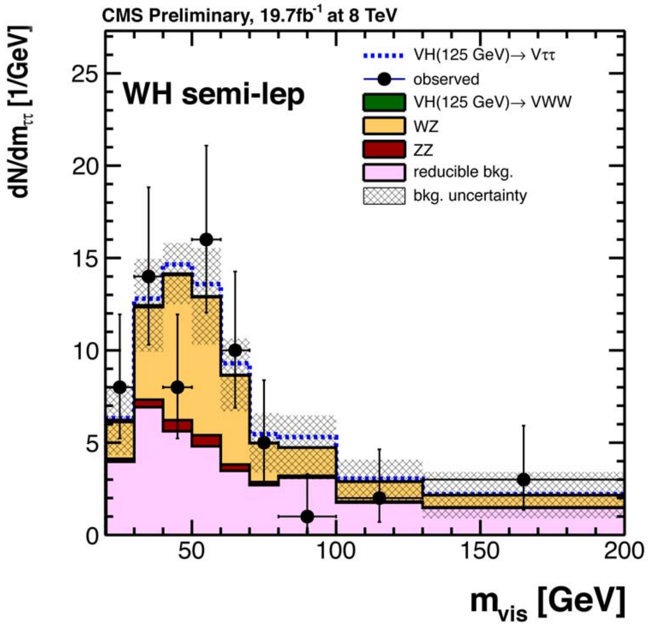

FIG. 13.2 –
The expected and measured $e\mu\tau_{\text{had}}$ and $\mu\mu\tau_{\text{had}}$ visible invariant mass for the 8 TeV data. The dashed line represents the expected contribution from $pp \to WH$ production.

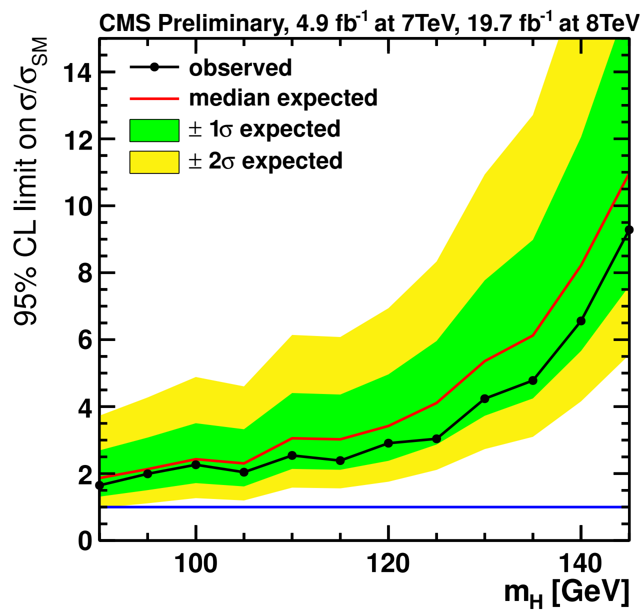

FIG. 13.3 –
Expected and observed 95% C.L. upper limits on SM Higgs boson production for the WH process.

The data analysis was based on 5 (19.7) fb^{-1} collected at 7 (8) TeV. Three final states were considered, where the undetected neutrino from the W decay was contributed to the missing transverse energy in the event: $\mu\mu\tau_{\text{had}}$, $e\mu\tau_{\text{had}}$, and $ee\tau_{\text{had}}$. Results from the first two channels were fully scrutinized and included in the CMS journal article [2]. The $\ell\tau_\ell\tau_{\text{had}}$ backgrounds were into two categories: irreducible WZ and ZZ diboson backgrounds with at least three genuine isolated leptons in the final state, and reducible "misidentified" backgrounds where at least one lepton candidate is a quark or gluon jet misidentified as a τ. The irreducible diboson backgrounds were estimated using Monte Carlo (MC) simulation while the misidentified backgrounds were estimated from data using a k-Nearest Neighbor classifier.

Events were selected with leading (sub-leading) leptons with $p_T > 20$ (10) GeV/c and τ_{had} candidates with $p_T > 20$ GeV/c. The leptons were required to have the same charge to reduce the Drell-Yan and $t\bar{t}$ backgrounds. Given the high correlation of misidentification probability and lepton transverse momenta, events passing the selection were further divided into two categories according to the scalar sum of the p_T of the three final state objects. The visible invariant mass of the final state is shown in Fig. 13.2. The measured distribution is consistent with the sum of all backgrounds and no significant excess is observed. Expected and observed exclusion limits were calculated in the CL$_s$ approach as a function of the Higgs candidate mass and found to be consistent, as shown in Fig. 13.3.

The channels analyzed by our group were found to be the most sensitive at low mass among the final states in which a Higgs boson is produced in association with a W or Z and help improving the overall sensitivity of the CMS searches in τ decays when combined to other channels. Results obtained in the WH and ZH channels were combined with the inclusive $H \to \tau\tau$ searches, including six more decay channels [2]. The combination resulted in a broad excess of events above the background expectation with a local significance above three standard deviations in the mass range between 115 and 130 GeV/c^2, as shown in Fig. 13.4. Assuming the excess to be due to $H \to \tau\tau$ signal leads to a measured mass of $m_H = 122 \pm 7$ GeV, which is consistent with previous measurements. The best fit of the observed $H \to \tau\tau$ signal cross section for $m_H = 125$ GeV/c^2 is 0.78 ± 0.27 times the SM expectation. These observations constitute the first direct evidence for the 125 GeV/c^2 Higgs boson decaying to a pair of τ leptons.

13.2.2 Higgs boson couplings to top quark pairs

Higgs decays involving top quarks will bring invaluable information since the very large top mass results leads to the full strength of the Higgs boson coupling. The magnitude of this coupling can be directly measured through the cross section of Higgs boson production in association with a top pair. We are leading a search for $t\bar{t}H$, where at

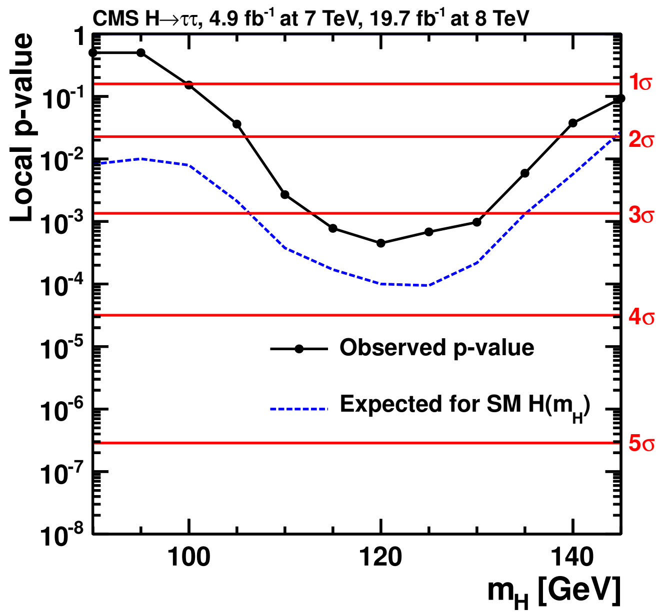

FIG. 13.4 – Local p-value and significance in number of standard deviations as a function of the SM Higgs boson mass hypothesis for the combination of all decay channels.

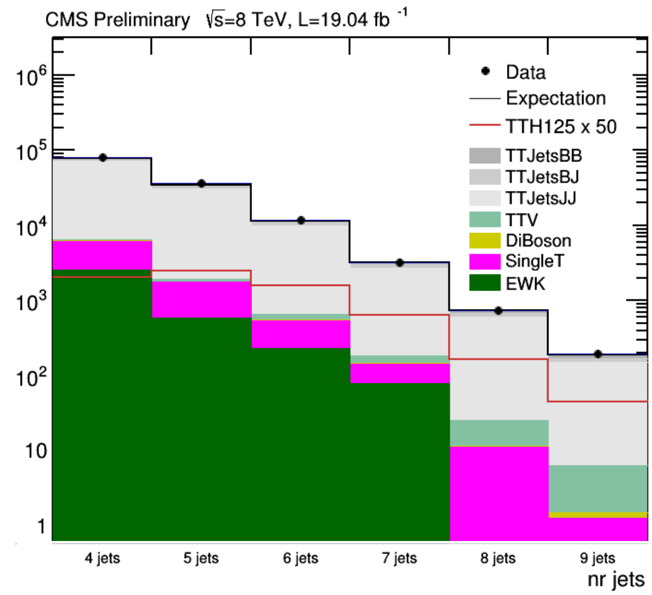

FIG. 13.5 – Multiplicity of jets in SL events with $N_j \geq 4$ and at least two jets passing a medium CSV (b-tagger) cut.

least one of the top-quarks decays leptonically through $t \to bW$, with $W \to \ell\nu_\ell$, $\ell = e, \mu$, whereas one W decay may proceed hadronically, with $W \to q\bar{q}$. The $t\bar{t}H$ production channel comes with experimental challenges due to its small cross section and high QCD background rates. The $H \to b\bar{b}$ decay channel is the most promising thanks to its large branching ratio and to the high efficiency of tagging jets from b-quark hadronization. Nevertheless, the QCD background $pp \to t\bar{t} + b\bar{b}$ remains irreducible with respect to b-tagging, and it has a much larger cross section than the signal [3].

The Matrix Element Method (MEM) [4] provides an optimal separation of signal and background by exploiting both the experimental information and the theoretical model in assigning weights under competing hypotheses. The method also reduces combinatorial self-background arising from matching reconstructed jets to the four b-quarks from the Higgs and top-quark decays. The method calculates the probability $w_i(\mathbf{y}|\lambda)$ of measuring a set of observables $\mathbf{y}$ under a hypothesis i, given model parameters λ. The ratio $w_0(\mathbf{y}|\lambda)/w_1(\mathbf{y}|\lambda)$ provides a good separation between signal and background (i=0,1). The probably density is given by

$$w_i(\mathbf{y}|\lambda) = \frac{1}{\sigma_i(\lambda)} \int_\Omega d\mathbf{x} \int dx_a dx_b \Phi(x_a, x_b) \times$$
$$\delta^4((x_a P_a + x_b P_b) - \sum \mathbf{p}(\mathbf{x})) |\mathcal{M}_i(\mathbf{x}|\lambda)|^2 W(\mathbf{y}|\mathbf{x}, \lambda)$$

The integration is performed over the phase-space of the final state particles $\mathbf{x}$ and over the momentum fractions $x_{a,b}$ of the initiating partons in the infinite momentum frame of the colliding protons which have 4-momenta $P_{a,b} = (\sqrt{s}/2, 0, 0, \pm\sqrt{s}/2)$. The integrand includes the parton flux factor Φ, the scattering amplitude of process i squared $|\mathcal{M}_i|^2$ and the transfer function W, which gives the probability density of measuring a set of observables $\mathbf{y}$ given a phase space point $\mathbf{x}$.

In our analysis, the integral is computed numerically using the `VEGAS` [5] algorithm for each possible quark-to-jet association (permutation) and then summed to give the final probability. The scattering amplitude is evaluated numerically at LO accuracy by the program `OpenLoops` [6] and the narrow width approximation is used to calculate the intermediate particle propagators. The transfer function is determined by the detector characteristics and performance.

Our analysis uses the 8 TeV data from 2012 corresponding to 19.04 fb^{-1}. Events are separated depending on the lepton and jet multiplicities to take advantage of the different signal to background ratio. Single-lepton (SL) and double-lepton (DL) events contain exactly one lepton or an opposite-sign lepton pair, respectively. Figure 13.5 shows the jet multiplicity in the SL channel.

A further selection is applied based on the b-tagger discriminator ξ of jets. For each event, the jet collection is sorted based on ξ and a b-tag likelihood ratio b_{LR} is calculated, which optimally separates the hypotheses that exactly four or two jets originate from b-quarks. Signal events as well as those from the irreducible $t\bar{t} + b\bar{b}$ background contain four b-quarks and thus have a value of

b_{LR} close to 1.0, while those backgrounds containing light quarks have a value closer to zero. A cut is made on b_{LR} depending on the channel and the number of jets. The low purity region is dominated by $t\bar{t} + jj$ and deficient in the signal, and thus provides a good control region. Events passing the b_{LR} selection are further classified into categories to take advantage of the differences between signal and background.

A number of tests to verify the algorithm have been performed. In all cases the MC is found to reproduce the data to within acceptable limits. We are currently in the final stages of completing the 8 TeV analysis and have yet to un-blind the data in the signal region.

The expected 95% CL upper limit on the signal strength modifier $\mu = \sigma_{\mathrm{SM}}/\sigma$ with its $\pm 1\sigma$ and $\pm 2\sigma$ uncertainties have been determined for each category. The combined result is $\mu < 2.9$.

We have found an encouraging improvement of 20% with respect to the analysis done previously by CMS. More improvements have been included to this analysis. The analysis is still under approval by the CMS collaboration and the final version is expected to be released during 2014.

13.2.3 MSSM Higgs boson search

The light SM Higgs boson mass demands a mechanism for its stabilization, since naively radiative corrections should make it many orders of magnitude larger. One such mechanism, SuperSymmetry (SUSY), provides loop corrections to the Higgs boson mass that cancel the loops from known SM particles. Within the MSSM (Minimal Supersymmetric Model), there are four additional heavier Higgs bosons (two oppositely-charged scalars, one neutral scalar, and a neutral pseudoscalar) which should be detectable at the LHC since the favored masses are just above current limits. Our group is searching for neutral Higgs bosons decaying to $b\bar{b}$ produced via the MSSM in association with a b-jet. This is a process whose cross section is enhanced compared to SM $H \to b\bar{b}$ production by a factor of $\tan^2(\beta)$, which could be as large as a 1000.

For $\tan^2(\beta) \geq 3$ the decay to $b\bar{b}$ is the dominant Higgs decay channel with a branching ratio of about 90%. A previous search was done with 7 TeV, setting limits on the MSSM Higgs mass up to 350 GeV [7], which set the most stringent bounds on MSSM Higgs-production in this final state. Since higher MSSM Higgs boson masses are now accessible with 8 TeV, $H \to b\bar{b}$ becomes more boosted, and the fraction of events for which two B-hadrons are merged into a single jet is significant. Our group has found that sensitivity is improved by evaluating these events separately. We have investigated sensitive variables (secondary vertex variables, such as vertex mass) to discriminate single-b from two-b jets and introduced a new discriminant for increasing the sensitivity of the analysis significantly. Dedicated triggers, which perform online b-tagging based on impact-parameter significance are employed to cope with the large hadronic interaction rate at the LHC. Based on these, different mass ranges have been defined for the new data, for which we have optimised the event selection. Furthermore, we have evaluated the non-QCD-multijet background events, and estimated the systematic uncertainties for the analysis.

The new discriminant that we have developed, called event b-tag, is essential to get a handle on the background composition. Since the background consists largely of QCD multi-jet events, the background model is taken from data, where the different flavour fractions are determined from double-b-tag events. A full 2D maximum likelihood fit to the invariant mass of the leading two b-jets and the event b-tag is used to determine the event yields. A potential signal would show up as a bump in the invariant mass spectrum and be a clear sign of physics beyond the Standard Model. The result analyzing the full 2012 dataset with 8 TeV is entering CMS review shortly and will soon be published. We will continue to update this search with the 13 TeV run, which will access a new MSSM Higgs boson mass range.

13.2.4 Study of $pp \to Zb\bar{b}$ production

The production of b-quark pairs in association with Z bosons in the process $pp \to Zb\bar{b}$ is the main SM background to Higgs boson searches in b-quark decays and other searches for new physics. SM predictions at next-to-leading order accuracy have been performed assuming massive or massless b quarks, usually referred as four- and five-flavour calculation schemes, respectively. The validation of the different calculation techniques is of great importance for the correct background estimates in future searches.

Our group performed the first measurement of the total cross section and angular correlations of B hadrons produced in this process, using a data sample corresponding to an integrated luminosity of 5 fb^{-1} at $\sqrt{s} =$ 7 TeV [8]. B hadrons were identified through the displaced vertices from their decays, using the inclusive vertex finder (IVF). The IVF technique [9] is independent from jet reconstruction and allows the full angular range to be probed, including configurations with collinear B hadrons. Figure 13.6 shows distributions of the kinematic variable ΔR_{BB} defined as:

$$\Delta R_{BB} \equiv \sqrt{(\Delta\eta_{BB})^2 + (\Delta\phi_{BB})^2}\ ,$$

with η the pseudorapidity and ϕ the angle in the transverse plane. The cross sections were evaluated in several regions of the Z boson transverse momentum.

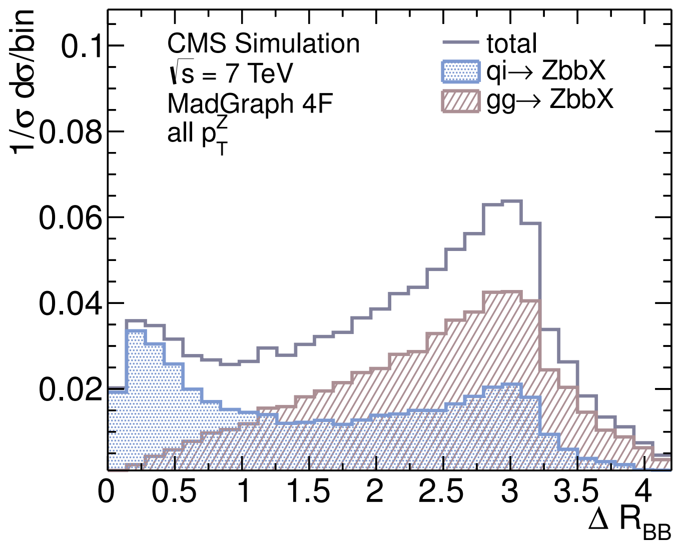

FIG. 13.6 – Distributions of ΔR_{BB} as predicted by MADGRAPH MC. The separate components from $gg \to Zb\bar{b}$ and $qq, qg \to Zb\bar{b}$ are indicated.

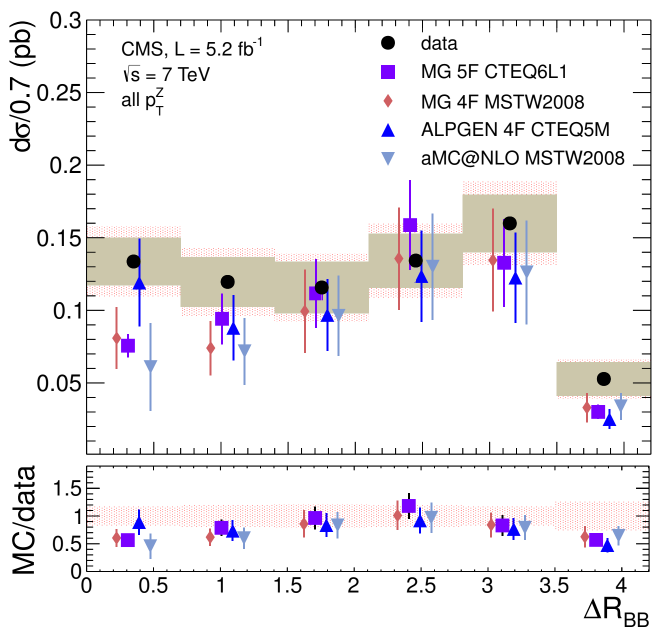

FIG. 13.7 – Differential cross section as a function of ΔR_{BB}. CMS data are compared with hadron-level predictions in the four- and five-flavor schemes, and for NLO QCD.

The measurements were compared with MC simulations implementing different flavour number schemes, as shown in Fig. 13.7. The ΔR_{BB} distribution indicates that the four-flavor prediction implemented in ALPGEN provides the best description of CMS data with five-flavour and NLO predictions below the data for low angular separations. Furthermore the total hadron-level cross section is systematically larger than MC predictions, partly because of the excess in the collinear ΔR_{BB} region.

13.2.5 Search for dark matter particles with top quarks

A popular candidate for dark matter is the weakly interacting massive particle (WIMP), which arises naturally in several models beyond the SM, like supersymmetry. So far, however, there is no established knowledge about its nature and properties, including its mass and interactions with ordinary matter [10, 11].

With minimal assumptions, the interaction Lagrangian between dark matter particles and quarks can be described by an effective field theory (EFT),

$$L_{\mathrm{int}} = C\,(\bar{q}\Gamma^q q)(\bar{\chi}\Gamma^\chi \chi)\;\;,$$

where C represents the coupling constant, which usually depends on the mass of the dark matter particle M_χ and the scale of the interaction M_*, and the operator Γ describes the type of the interaction, including scalar ($\Gamma = 1$), pseudoscalar ($\Gamma = \gamma^5$), vector ($\Gamma = \gamma^\mu$), axial vector ($\Gamma = \gamma^\mu\gamma^5$) and tensor interactions.

The exact form of the constant C depends on the particular type of the interaction considered. In the case of a scalar interaction, the coupling strength is proportional to the mass of the quark,

$$L_{\mathrm{int}} = \frac{m_q}{M_*^3}\bar{q}q\bar{\chi}\chi$$

which means couplings to light quarks are suppressed and traditional inclusive mono-jet searches are not very sensitive [12–15].

We performed a search in the di-lepton channel [16], selecting events with large transverse missing energy ($\not{E}_T$) and at least two jets. No excess was found above SM expectations and we set the first cross section limits on this process. Cross sections higher than 0.09 to 0.31 pb are excluded at the 95% Confidence Level (CL) for M_χ ranging from 1 GeV to 1 TeV. These results translate into new lower limits on M_*, as shown in Fig. 13.8.

Moreover, in the last part of the year we have developed this analysis in the single-lepton and fully hadronic channels. Both channels are expected to improve about 30% of the search sensitivity on the interaction scale.

In addition to top quarks, dark matter can also be produced in association with bottom quark pairs, providing a striking search signature. Dark matter signals are manifested in events with large $\not{E}_T$, one or two b-tagged jets and with no other significant activities recorded in the detector. No results are available yet but the channel has a sensitivity similar to the previous one.

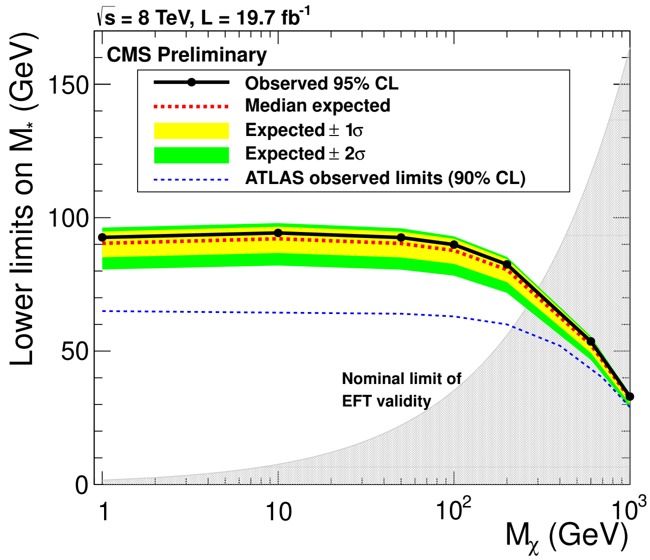

FIG. 13.8 – Observed exclusion limits in the plane of dark matter mass M_χ and interaction scale M_*. The region below the solid curve is excluded at 95% CL. The previous most stringent 90% CL limits (from ATLAS) are also shown. The results expected for 1σ and 2σ fluctuations of the background are indicated. Under typical assumptions, the EFT considered in this analysis is expected not to be valid in the shaded area where $M_\chi^2 > 4\pi^2 M_*^3/m_t$.

[1] T. Aaltonen *et al.* [CDF and D0 Collaborations], Phys. Rev. Lett. **109**, 071804 (2012)

[2] S. Chatrchyan *et al.* [CMS Collaboration], *Evidence for the 125 GeV Higgs boson decaying to a pair of τ leptons*, arXiv:1401.5041 [hep-ex].

[3] A. Bredstein, Phys. Rev. Lett. **103**, (2009) 012002.

[4] DØ collaboration, Nature 429, 638-642 (2004);
DØ collaboration, Phys. Lett. B **617** (2005) 23;
Helicity of the W boson in single-lepton $t\bar{t}$ events, M.F. Canelli; FERMILAB-THESIS-2003-22. DØ collaboration, Phys. Lett. B **617** (2005) 23;
CDF collaboration, Phys. Rev. Lett. **101** 252001 (2008);
CDF collaboration, Phys. Rev. Lett. **103** 092002 (2009);
CDF collaboration, Phys. Rev. Lett. **105** 042002 (2010);
CDF collaboration, Phys. Rev. Lett. **99** 182002 (2007);
CDF collaboration, Phys. Rev. D **84** 071105(R) (2011);
CDF collaboration, Phys. Rev. Lett. **103** 101802 (2009);
CDF collaboration, Phys. Rev. D **85** 072001 (2012).

[5] G.P. Lepage, Journal of Computational Physics **27** (1978) 192-203.

[6] F. Cascioli, Phys. Rev. Lett. **108**, (2009) 111601.

[7] S. Chatrchyan *et al.* [CMS Collaboration], Phys. Lett. B **722**, 207 (2013).

[8] S. Chatrchyan *et al.* [CMS Collaboration], JHEP **1312** (2013) 039.

[9] V. Khachatryan *et al.* [CMS Collaboration], JHEP **1103** (2011) 136.

[10] *Planck 2013 results. XVI. Cosmological parameters*, Planck Collaboration, arXiv:astro-ph/1303.5076.

[11] V. Trimble, Ann. Rev. Astron. Astrophys., **25** (1987) 425; E. Komatsu *et al.*, Astrophys. J. Suppl., **192** (2011) 18; J. L. Feng, Ann. Rev. Astron. Astrophys., **48** (2010) 495.

[12] J.M. Beltran *et al.*, JHEP **17** (2010) 1.

[13] J. Goodman *et al.*, Phys. Lett. B **695** (2011) 185;
J. Goodman *et al.*, Phys. Rev. D, **82** (2010) 116010;
P. J. Fox *et al.*, Phys. Rev. D **85** (2012) 056011;
P. J. Fox *et al.*, Phys. Rev. D **86** (2102) 015010;
Rajaraman *et al.*, Phys. Rev. D **84** (2011) 095013;
T. Lin, E.W. Kolb, and L.-T. Wang, Phys. Rev. D **88** (2013) 063510.

[14] *Search for new physics in monojet events in pp collisions at $\sqrt{s}$= 8 TeV*, CMS collaboration, Tech. Rep. CMS-PAS-EXO-12-048, 2012.

[15] ATLAS collaboration, JHEP, **1304**, 2013; *Search for new phenomena in monojet plus missing transverse momentum final states using 10fb^{-1} of pp collisions at $\sqrt{s}$=8 TeV with the ATLAS detector at the LHC*, ATLAS collaboration, Tech. Rep. ATLAS-CONF-2012-147, CERN, Nov 2012.

[16] S. Chatrchyan *et al.* [CMS Collaboration], CMS-PAS-B2G-13-004.

13.3 New heavy particle searches in CMS

13.3.1 Search for heavy resonances in the W/Z-tagged dijet mass spectrum

One of the unsolved mysteries of the standard model of particle physics is why the strength of the electroweak force and gravity differ by 36 orders of magnitude. The model of large extra dimensions [1], where the gravitational force is allowed to propagate in extra spatial dimensions otherwise invisible to us, can explain this difference. At the same time, this model predicts the production of heavy graviton resonances decaying to pairs of particles in the visible dimensions, accessible with the highest energies of the LHC.

We search the data collected by the CMS detector in 2012 for new heavy particles decaying to pairs of W or Z bosons [2] as predicted by the large extra dimensions model. This final state is favored by extensions of the model in which the decay to lepton and photon pairs is suppressed[3]. The decay modes are also interesting since they are accessible only through novel jet substructure techniques which require a deep understanding of the jet substructure.

W and Z bosons decay predominantly into quarks which transform into jets. For the heavy resonances reachable at the LHC, the bosons have such large mo-

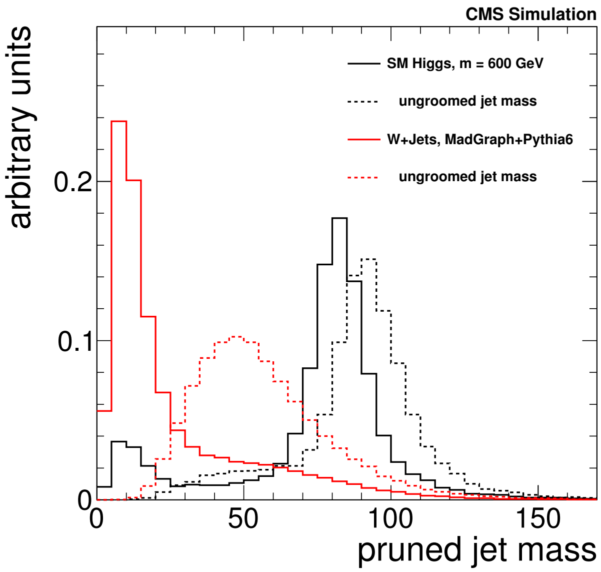

FIG. 13.9 – Simulation of the single-jet mass distribution for a heavy resonant signal and for the background, before and after pruning (see text).

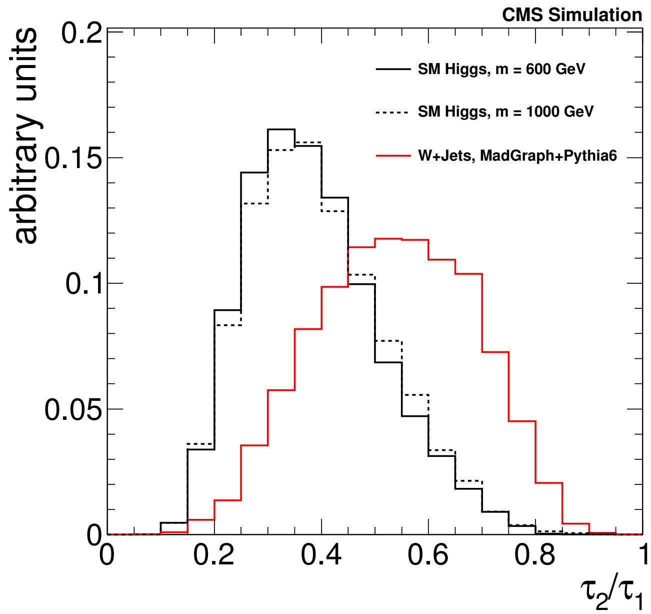

FIG. 13.10 – Distributions of the ratio τ_2/τ_1 for Higgs signal and background after requiring a pruned mass between 60 and 120 GeV. τ_2/τ_1 is a measure of the probability for two sub-jets rather than one.

menta that their decay products merge into a single jet. It is still possible to identify the W and Z bosons by studying the substructure of these merged jets. In recent years these W/Z-tagging algorithms have undergone a fast development. We have studied a variety of new algorithms identified the best one, the so-called pruning algorithm[4], which is based on the Lorentz invariant jet mass. The algorithm removes particles with background-like QCD radiation shown in Fig. 13.9, while keeping the particles from the quarks originating in W/Z decay. Additional selectivity is achieved by considering the N-subjettiness[5], which is a measure of the number of hard quarks in the jet (see Fig. 13.10).

Our ultimate W/Z-tagging algorithm [6] was calibrated with events of top pair production, which contain jets from W bosons with high momentum, and applied in the most recent CMS searches. Once W/Z bosons were identified, we searched for resonances on top of a smoothly falling background (Fig. 13.11). No signal was observed and the exclusion limits [2] are the most stringent to date for particles decaying to WW and reach up to 1.2 - 3.2 TeV depending on the model.

Presently, we focus on improving the reconstruction of jet substructure. By optimizing the calorimeter cluster algorithm, we managed to push the breakdown of reconstruction performance of boosted boson tagging due to detector resolution from p_T = 1 TeV to p_T = 1.5 TeV. By improving the use of the granularity of the electromagnetic calorimeter in the particle flow algorithm we were able to maintain the reconstruction performance up to p_T = 3.5 TeV, as needed for LHC Run II.

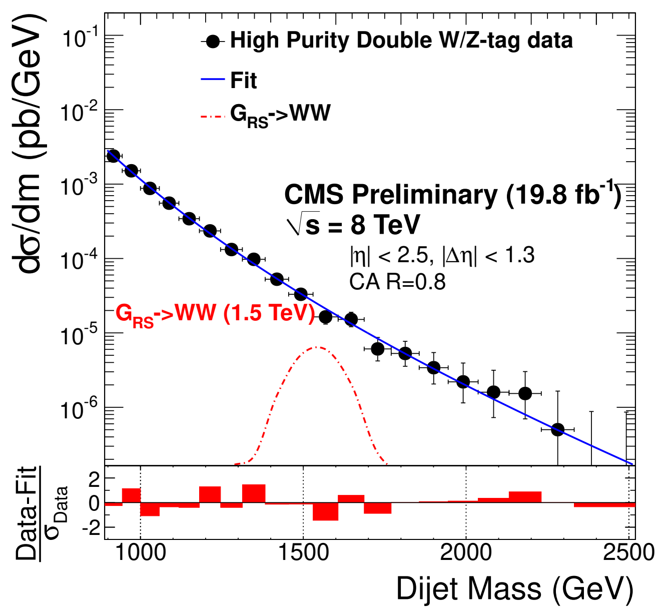

FIG. 13.11 – The final jet mass distribution fit for a signal-like resonance. No signal is observed, and upper limits on the cross-section are set.

13.3.2 Search for new heavy bosons with b-tagged jets and tau leptons in the boosted regime

In many extensions of the SM the spontaneous breaking of the electroweak symmetry is associated with new dynamics at the TeV scale, the origin of which may be new interactions [7] or compositeness [8]. Both concepts predict new resonances that mainly couple to pairs of massive bosons. Composite Higgs Models [9] provide a plausible solution to the hierarchy problem and consider the Higgs boson as a pseudo Nambu-Goldstone boson that couples to the SM particles and to new heavier gauge boson (Z' and W'). The existence of W' or Z' was postulated already in Grand Unification Theories but without predictions for their mass. A mass in the TeV region, accessible at the LHC, would solve the hierarchy problem. W' and Z' decay in these scenarios primarily to heavy particles, such as W , Z and Higgs bosons.

The first channel we are investigating $W' \rightarrow WH$, where the final state signature is given by a leptonic decay of the W and the hadronic decay of the Higgs into two b-quarks. For a W' mass between 1 and 3 TeV, the decay products are highly energetic ("boosted"), such that the final decay products can be difficult to separate. Hence the signature is characterized by a high p_T isolated lepton, large missing transverse energy and two high p_T jets from the b-quarks hadronization. In particular, the two b-jets from the Higgs are expected to merge into a single jet. The jet pruning and n-subjettiness algorithms mentioned previously may discriminate signal and background. Furthermore, the presence of b-quarks in the final state can be exploited to further suppress the background associated with light quark jets.

Our analysis is one of the first attempts to look for exotic final states with a Higgs boson, and indicates that astrongly coupled vector resonance with mass up to 1.5-2 TeV woulkd be detectable. The procedures are presently being developped with the 8 TeV data, with the aim of gaining enough experience to repeat the study with the 14 TeV data expected in 2015 when techniques for resolving boosted $H \rightarrow b\bar{b}$ become even more important and when higher luminosities and beam energies will extend the mass reach.

For boosted $H \rightarrow b\bar{b}$, b tagging, based on precise vertex reconstruction from the pixel detector to identify long-lived b quark decay, is reconsidered. We have produced a study [10] on the performance of CMS b-tagging algorithms in identifying jets containing two b quarks. We have investigated five different b-tagging algorithms, and considered multiple jet cone sizes, and jet-track association cone sizes. Our study showed the most commonly used multivariate algorithm, the Combined Secondary Vertex algorithm [11], was strongly outperformed by a more primitive algorithm, the Jet b Probability Algorithm [12], currently not used by CMS. This showed a need to make b-tagging in CMS to more sensitive to jets containing multiple b quarks.

Our group is also searching for heavy resonances, denoted as X, in the decays $X \rightarrow ZH$ and $X \rightarrow HH \rightarrow b\bar{b}\tau\tau$. The Higgs boson couples to fermions proportionally to their mass and therefore decays primarily to b quarks and secondarily to τ leptons. Since the decay to b quarks is obscured by a large QCD multi-jet background, having one Higgs boson decay to τ leptons is more promising since its backgrounds are mainly from W and Z decays.

The hadronic τ identification is performed by algorithms based on jet reconstruction with particle-flow techniques [13]. In the case of boosted taus decaying into three charged hadrons the tracks tend to overlap. For these cases we have studied discriminators based on the number of tracks and the energy deposits in the hadronic and electromagnetic calorimeter. The algorithm may, however, fail for overlapping energy deposits. To solve this problem, we are itteratively removing from further consideration the energy deposits associated with an identified tau, and recalculate the isolation. This new definition of the isolation improves the reconstruction of the signal event with boosted topology and has a good discrimination power against QCD multi-jet events.

[1] L. Randall and R. Sundrum, Phys. Rev. Lett. **83** (1999) 3370.

[2] V. Khachatryan *et al.* [CMS Collaboration], *Search for massive resonances in dijet systems containing jets tagged as W or Z boson decays in pp collisions at sqrt(s)= 8 TeV*, arXiv:1405.1994 [hep-ex].

[3] K. Agashe, H. Davoudiasl, G. Perez *et al.*, Phys. Rev. D **76** (2007) 036006.

[4] S. D. Ellis, C. K. Vermilion, and J. R. Walsh, Phys.Rev. D81 (2010) 094023.

[5] J. Thaler and K. Van Tilburg, JHEP 1103 (2011) 015.

[6] CMS Collaboration [CMS Collaboration], *Identifying Hadronically Decaying Vector Bosons Merged into a Single Jet*, CMS-PAS-JME-13-006.

[7] L. Susskind, Phys. Lett. D **20** (1979) 2619.

[8] R. Contino,T. Kramer, M. Son and R. Sundrum, JHEP **1208** (2012) 013.

[9] D. Marzocca,M. Serone and J. Shu, JHEP **05** (2007) 074.

[10] T. Arrestad, *Comparison of b-tagging algorithms in CMS for jets with high transverse momenta containing multiple b quarks*, CMS AN-2014/076 (2014).

[11] C. Weiser, *A combined secondary vertex based B-tagging algorithm in CMS*, CERN-CMS-NOTE-2006-014.

[12] A. Rizzi, F. Palla and G. Segneri, *Track impact parameter based b-tagging with CMS*, CERN-CMS-NOTE-2006-019.

[13] the CMS Collaboration, *Particle flow Event reconstruction in CMS and Performance for Jets, Taus and Missing E_T*, CMS PAS PFT-09-001 (2009).

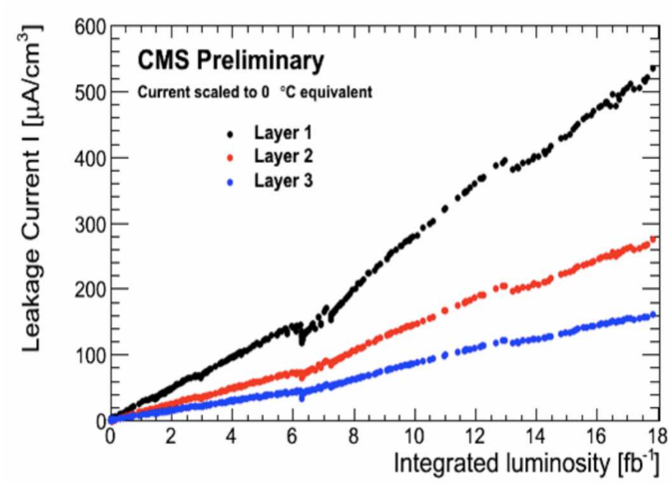

FIG. 13.12 – Leakage currents with integrated luminosity.

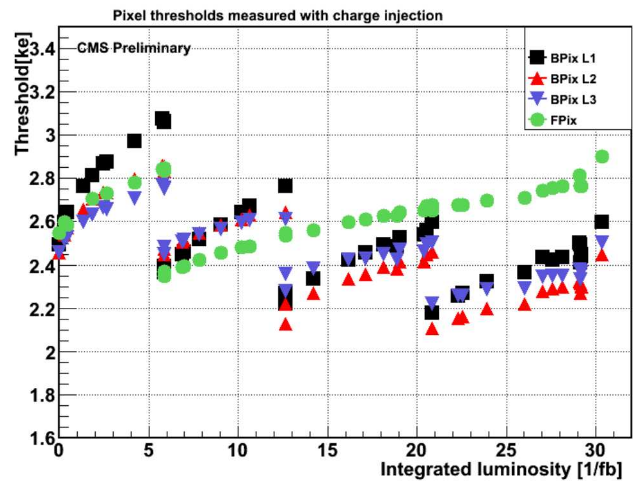

FIG. 13.13 – Pixel thresholds with integrated luminosity.

13.4 Detector maintenance, operations, and upgrades

The extremely high particle fluxes at small distances from the interaction point require the innermost tracking layers to be composed of pixel devices delivering spatial information with high resolution. Over the full acceptance of the CMS detector, the silicon pixel system provides two or more hits per track, which allow secondary vertices to be reconstructed for tagging long-lived objects, like b or c quarks and τ-leptons, and to distinguish them from a large background of light quark and gluon jets [1]. It is also an important detector for identifying the primary vertex, and separating it from dozens of additional pile-up vertices.

Our CMS group is dedicated to operating, maintaining, and upgrading the barrel pixel detector (BPIX), which the University of Zürich helped build. This detector plays a special role in our physics measurements since it is used in identifying b-quark jets which are in the final state of most of the physics analyses in our research portfolio. Our responsibilities are threefold:

- We maintain and operate the current BPIX which will be taking the first data at 13 TeV starting in the middle of 2015.
- We are helping to build the phase I upgraded BPIX detector for installation at the end of 2016.
- We have also started to work on the design and simulations for the phase II upgrade of the pixel detector which is envisioned to take data starting 2023.

13.4.1 Barrel pixel detector maintenance and operations

The Pixel Detector was installed in 2008 and showed excellent performance during the first LHC run. Nevertheless, it has been a subject to severe radiation damage, what resulted in such effects as increase of the leakage current (Fig. 13.12) and of the bias voltage, charge trapping and signal degradation, or changes in the pixel thresholds (Fig. 13.13). Hence, several corrections are needed in order to guarantee correct operation. Our group is responsible for calibrations aimed at finding the optimal settings for the irradiated detector (see Fig. 13.14), which is temporarily installed in the clean room of LHC-P5 (Cessy, France).

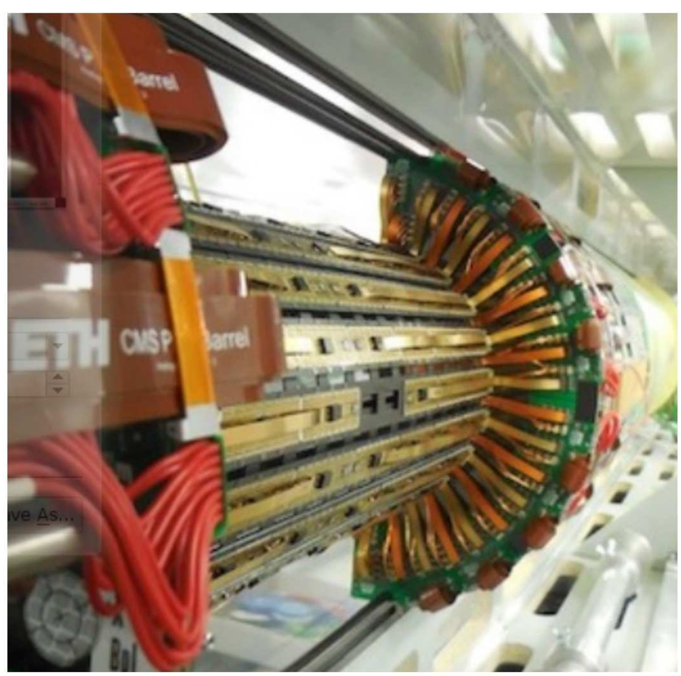

FIG. 13.14 –
Barrel pixel detector temporarily installed in P5.

The barrel pixel detector will record the first LHC collisions after the long shutdown in the middle of 2015 at higher instantaneous luminosities and at a center of mass energy of 13-14 TeV. BPIX and FPIX detectors were extracted in the middle of 2013 to allow access to the beam pipe and for the duration of the current long shutdown. The pixel detector was placed in a refrigerated, climate-controlled room environment located at the CMS experimental site, Point 5. BPIX is currently maintained in two cold boxes in a lab with repair workbenches, and all the electronics and computers necessary to control and readout the detector for tests. In coordination with PSI, who is leading the work on BPIX, our group has installed the DAQ system, and performed the necessary testing, and calibration of the BPIX modules. Our work included setting up the computers that are connected to the VME, as well as the software infrastructure needed to make such tests and calibrations.

The pixel detector has been operated with a coolant temperature of 7.4°C in 2008 - 2011 and 0°C in 2012, which for the pixel sensors translates to values $\sim$ 10°C higher. In order to limit the impact of radiation damage and minimize the leakage current, during the second LHC run the detector must be operated at much lower temperature, down to -20°C. Since the working points and settings are strongly temperature dependent, during this year we performed calibrations down to -15°C, attempting to reach even lower values.

During the previous run 22 out of a total of 768 BPIX modules had problems. For FPIX the problematic fraction was even 7.7%. We have now helped replace and calibrate most of these modules and this job will be completed before the end of this summer. Moreover, two malfunctioning analog optical hybrids, needed to convert the electric analog signal from the readout chips to an optical analog signal for transmission through optical fibers to the readout electronics placed outside the detector. Both have been now replaced and tested.

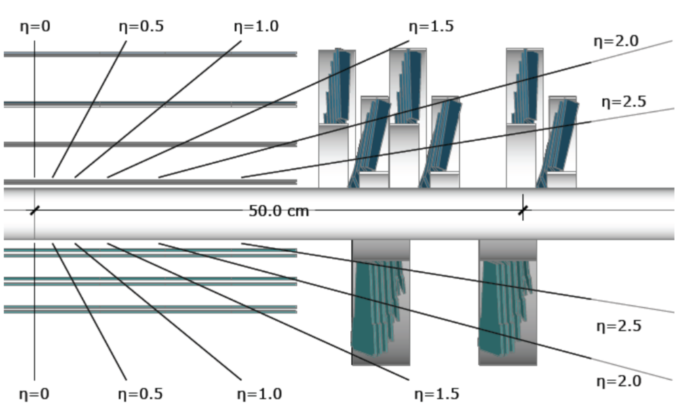

FIG. 13.15 – Schematic of barrel pixel upgrade. Bottom half represents current 3-layer BPIX system, top half shows upgraded 4-layer system in which the innermost detector plane is located within 3 cm of the beam axis.

During the shutdown, several updates to the computers and software have been implemented. Our group updated all the pixel detector online DAQ software packages from 32- to 64-bit and to the latest Scientific Linux version and its compiler. We updated the software version control system to allow for parallel development of several packages by different persons and cleaned up and removed outdated packages. We are developing a new graphical user interface for the control room DAQ system and calibration software, which will allow additional information to be displayed and further automatize the calibration software to enable remote access and control so that remote users will be able to do some levels of shift work.

13.4.2 Barrel pixel detector phase I upgrade

The current pixel detector is not designed for the expected LHC run 2 conditions of 2×10^{34} cm^{-2}s^{-1} at 50 ns. The phase 1 pixel upgrade [2] combines a new pixel readout chip with several other design improvements to keep up performance. The current 3-layer central pixel barrel, 2-disk forward pixel detectors are to be replaced with 4-layer central pixel barrel, 3-disk forward pixel detectors (Fig. 13.15).

The current BPIX detector consists of three 57 cm long layers of silicon pixel modules serviced by 2.2 m of supply tubes which transport cooling tubes, electrical power, and optical signals. The University of Zurich designed and constructed the mechanical support structure, and designed, built, and tested the supply tubes, including the mechanical structure, cooling and service lines, and boards to transfer optical signals (see Fig. 13.16). We are in charge of the phase I upgrade for these components. The additional inner pixel layer requires a complete redesign. To reduce the amount of dead material which has a negative impact on the detector performance a new, light-weight cooling system will be installed. We have now

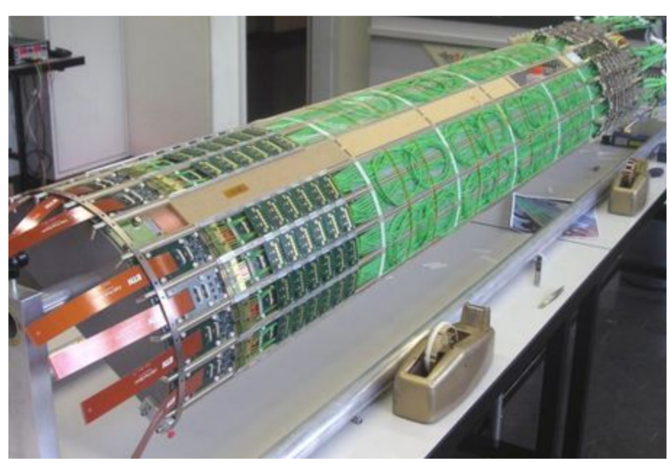

FIG. 13.16 – Current supply tube quarter, outfitted with electronics and cabling, produced at UZH.

constructed two prototype half-barrels of the four necessary for the phase I upgraded cooling structure; one can be seen in Sec. 19. These systems differ from the current system in that the tubes are much narrower, operate at 60 times higher pressure, are constructed in a complicated looping structure in order to cool more components including the newly added DC-DC converters, and use two-phase liquid-gas CO_2 cooling instead of single-phase C_6F_{14} liquid coolant. We have performed leak and deformation tests at 170 atmospheres, twice the operating pressure. The two prototypes are now at CERN for testing.

13.4.3 Beam tests of pixel detectors

We participated in tests of the prototype pixel sensors and frontend chips performed in October 2013 and March 2014 at the Fermi National Accelerator Laboratory. The "MT3 High Rate" tracking area provided 120 GeV protons or 66 GeV pions at intensities up to 4×10^8 /s. The setup consisted of two telescopes, each containing eight identical pixel sensors bump-bonded on readout chips (ROC). Seven planes were used for tracking and one plane as a detector under test (DUT). The first telescope had sensors perpendicular to the beam to test the saturation of time stamp buffer (single-pixel hits mostly), whereas in the second telescope sensors were inclined by 20° to simulate the deflection in the CMS magnetic field. In the latter situation the ionization charge is collected by more than one pixel resulting in a better position resolution.

Several issues were identified during these tests, such as the freezing of the double-column readout and other readout or out-of-sync errors. The former problem was understood as a too slow (above 25 ns) release of the signal used by pixels to notify the chip periphery of a valid hit resulting in spurious timestamps. The problem was resolved in the new ROC version (digV2.1) tested in March.

The hit residuals for the tilted DUT have a Gaussian width (σ) of 24 μm and 15 μm along the two coordinates, and preliminary efficiency measurements are above 98%. The data analysis is currently ongoing and a full understanding of the chip prototype is a prerequisite for the final mass production.

13.4.4 CMS Phase 1 System Test

The barrel pixel supply tube supports ten types of electronics boards which communicate with the pixel modules to handle control signals, power conversion (DC-DC converters) and distribution, data readout, electrical to optical signal conversions, communication with the DAQ, as well as the cooling loop structure. Our group is responsible for building the mechanical support structure, the cooling loop system, some of the electronics components, and the overall installation, integration and testing of the complete system, to be delivered to CERN for installation in 2016. For that purpose we are installing a full CMS-pixel DAQ system at the University of Zürich, commission it and write the necessary software. The system makes use of power supplies, control modules, a DCS system, readout electronics (FEDs), and two readout systems (VME until 2016, μTCA 2017 and after) as well as additional equipment to handle the complex fiber arrangements and to check the fiber connections.

The design of the new components of the control and data acquisition system is ongoing and first prototypes are being produced. We are currently setting up a slice of the full readout chain in order to gain experience in the operation of the new system and validate the individual components in view of the final production. The system will consist of a group of pixel detector modules connected through optical links to the front-end boards for readout and control and powered using a set of DC-DC converters. We have developed some tests of components of the power and control chain, but considerable work is still needed over the coming years to integrate all detector parts to a complete system and in the development of sophisticated software algorithms for testing, calibration and monitoring of all detector components.

13.4.5 Detector studies and hit reconstruction

Irradiation produces defects in silicon devices which cause trapping of charge carriers and modify the electric field profile across the sensor bulk. We studied charge collection in the CMS pixel sensors along their lifetime and as a function of the depth at which charge carriers are produced [4]. The study was based on CMS data collected in 2011 and 2012. During normal LHC operations the pixel sensors were biased at 150 V, however, small datasets were collected also with bias voltages between 70 and 300 V resulting in different Lorentz deflections.

Charge collection as a function of the sensor depth was studied using the grazing angle technique [5] which uses tracks crossing the sensors at shallow angles and releasing ionization charge over a long sequence of pixels, as shown in Fig. 13.17. The measured charge pro-

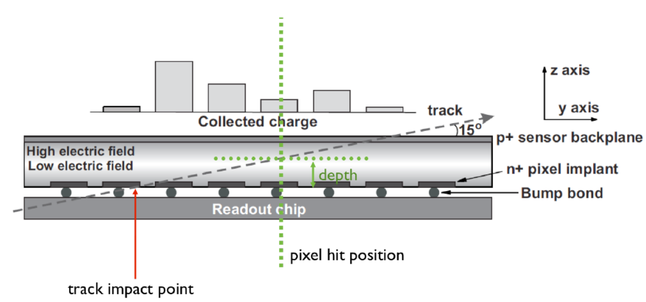

FIG. 13.17 – Sketch of the grazing angle technique

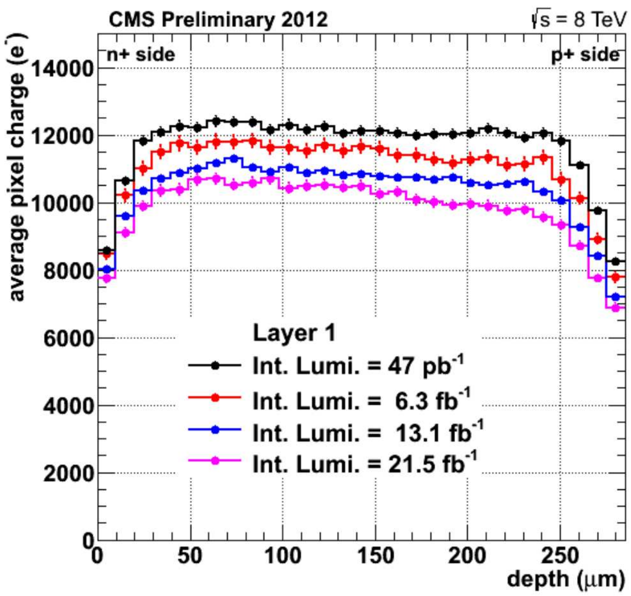

FIG. 13.18 – Average charge profiles as a function of the sensor depth for different integrated luminosities.

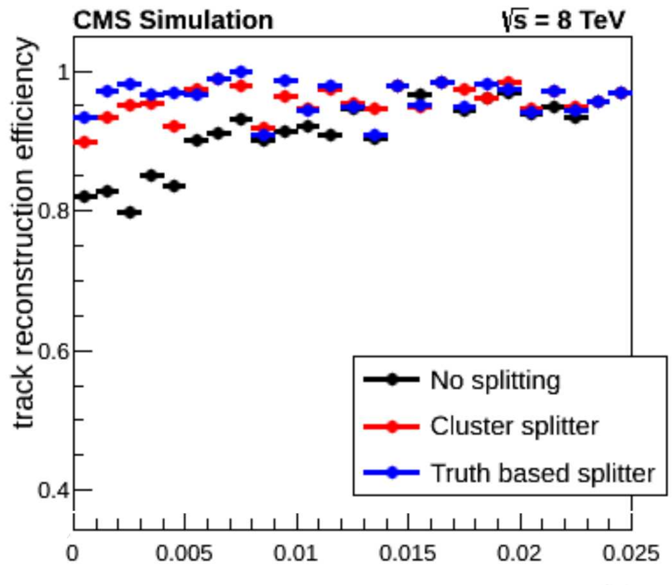

FIG. 13.19 – Track reconstruction efficiency versus angular separation, with and without pixel hit splitting.

files clearly demonstrateate a decrease of collected charge with increasing irradiation (Fig. 13.18). Moreover, charge losses are more pronounced at large depths, due to the long drift distance of charge carriers.

The charge profiles at different bias voltages and irradiations were compared with a detailed sensor simulation, PIXELAV [6–8], and are currently used to optimize our modeling of radiation damage. The PIXELAV simulation computes average cluster shapes, also called *templates*, used during pixel hit reconstruction.

We also worked on improving the reconstruction of pixel hits in narrow particle jets. When two charged particles traverse the sensors in close proximity, the pixel hits may merge into one larger cluster. In the innermost layer of the pixel detector hit overlap occurs if the opening angle between the two particle trajectories is below 5 mrad. For a typical three-prong τ decay this corresponds to a transverse momentum around 150 GeV/c.

Our group, in collaboration with Johns Hopkins University, has developed a technique for splitting merged clusters, which can be identified by the larger dE/dx and resolved by an algorithm that compares the observed cluster charge distribution with the expected template.

We have tested the algorithm in the new CMS tracking setup, imitating the harsh conditions of the 2015 LHC run. A simulated sample of $Z' \to 2\tau$ decays at $m_{Z'} = 1.5$ TeV was used. A significant increase in tracking efficiency is observed in Fig. 13.19 for tracks with angular separation dR< 0.01. For three-prong τ decays at $p_T > 300$ GeV/c the reconstruction efficiency increases by typically 30%.

The algorithm is now integrated in the official CMS software framework and the necessary templates will soon be available from a central database. This way the evolving running conditions will be taken into account automatically and hit splitting will be performed in the distributed data processing.

[1] W. Erdmann (Paul Scherrer Institut), *The CMS pixel detector*, World Scientic Review (2009).

[2] *CMS technical design report for the pixel detector upgrade*, CMS collaboration, CERN-LHCC-2012-016.

[3] V. Khachatryan *et al.* [CMS Collaboration], CERN-LHCC-2012-016. CMS-TDR-11 (2012).

[4] S. Taroni [for the CMS collaboration], Proceedings of the 2013 IEEE-NSS symposium. CMS CR-2013/096.

[5] Y. Allkofer *et al.*, Nucl. Instrum. Meth. A **584** (2008) 25.

[6] M. Swartz, Nucl. Instrum. Meth. A **511** (2003) 88-91.

[7] V. Chiochia *et al.*, IEEE Trans. Nucl. Sci. **52** (2005) 1067-1075.

[8] M. Swartz *et al.*, Nucl. Instrum. Meth. A **565** (2006) 212-220.

14 Superconductivity and Magnetism

M. Bendele (since January 2014), S. Bosma (until December 2013), Z. Guguchia, L. Howald, H. Keller, G. Pascua, E. Stilp

Visiting scientists: B.I. Kochelaev, R. Puzniak, A. Shengelaya

Emeritus members: K. A. Müller (Honorarprofessor), T. Schneider (Titularprofessor), M. Mali, J. Roos

in collaboration with: Brookhaven National Laboratory (I. Božović, A. Gozar), CEA Grenoble (G. Lapertot, P. Dalmas de Réotier, A. Yaouanc), EPFL Lausanne (D. Pavuna), ETH Zürich (M. Döbeli), Friedrich-Schiller-Universität Jena (F. Schmidl), Kazan State University (B. I. Kochelaev), IFW Dresden (R. Hühne, B. Holzapfel), MPI Stuttgart (J. Köhler, A. Bussmann-Holder, R. Kremer, G. Logvenov), TU Darmstadt (B. Albert, L. Alff), TU Dresden (H.-H. Klauss), Paul Scherrer Institute (K. Conder, R. Khasanov, E. Pomjakushina, A. Suter, H. Luetkens, E. Morenzoni), Polish Academy of Sciences (R. Puzniak, Z. Bukowski), Tbilisi State University (A. Shengelaya), University of Rome La Sapienza (A. Bianconi, N.L. Saini), University of British Columbia, Canada (R.F. Kiefl, W. Hardy)

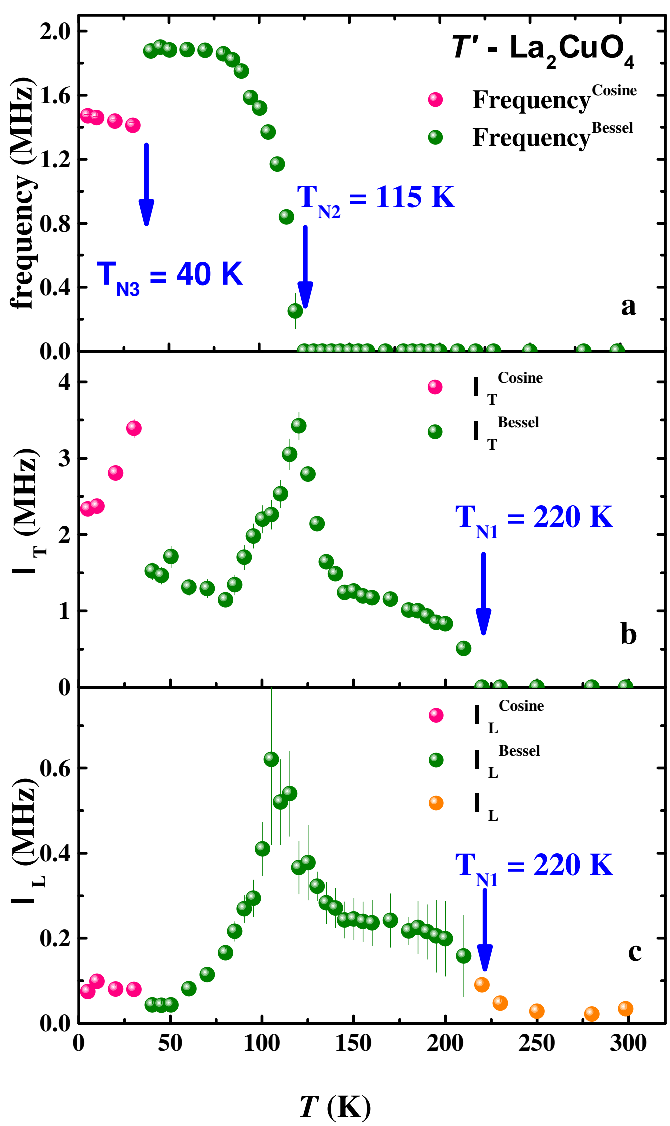

FIG. 14.1 – ZF-μSR parameters for T'-La_2CuO_4: frequency (a), transverse relaxation rate (b), and longitudinal relaxation rate (c) as a function of temperature.

We report on research projects in the field of high-temperature superconductors (HTS's) and materials with novel electronic properties. Our studies involve various complementary techniques, such as muon-spin rotation (μSR), X-ray absorption spectroscopy XAS, and various standard magnetometry techniques. Here we present some results from our recent investigations on cuprate and iron-based HTS's.

14.1 Magnetic Properties of T'-La_2CuO_4

Recently, for the first time bulk undoped La_2CuO_4 was stabilized in the metastable T'-structure by a low-temperature synthesis method [1, 2]. T'-La_2CuO_4, having no apical oxygen above or below the copper ions of the CuO_2-plane, is the true parent compound of the electron-doped cuprates. In contrast, the hole-doped compounds derived from undoped La_2CuO_4 crystallizes in the T-structure.

The magnetic properties of T'-La_2CuO_4 were investigated by means of muon-spin rotation and relaxation (μSR) measurements as shown in Fig. 14.1. μSR results reveal three characteristic temperature regimes that encompass a quasi-static order with slow magnetic fluctuations between 220 K and 115 K and a true static regime with a broad asymmetric field distribution at the muon site between 115 K and 40 K. At 40 K, an abrupt change to a narrow and symmetric field distribution is observed. These magnetic transitions are marked by arrows in Fig. 14.1.

The investigations on the novel and metastable T'-La_2CuO_4 are of striking significance mainly because our findings in this system had surprisingly revealed series of magnetic transitions even with the nonmagnetic ion La^{3+} [3]. This undoubtedly challenged the common belief that the magnetic interaction between the Cu and the RE system is responsible for, e.g., the spin reorientations observed in T'-Nd_2CuO_4 and thus, also questioned if the observed complex magnetic behavior is generic to all body-centered tetragonal (BCT) cuprates independent of the magnetic state of the RE ion, and if the magnetic transitions might have been overlooked in some compounds, e.g., due to the limitations of simple neutron diffraction experiments. Moreover, T'-La_2CuO_4 revealed a strongly reduced Néel temperature compared to the orthorhombic T-La_2CuO_4 and to other T'-RE_2CuO_4 cuprates such as T'-Nd_2CuO_4 and T'-Pr_2CuO_4. This reduction can be traced back to a ten times decrease in the interlayer coupling possibly due to the missing polarizable lanthanide ion in T'-La_2CuO_4. This low interlayer coupling makes our newly synthesized compound the best realization of a cuprate quasi 2D magnet [3].

[1] R. Hord *et al.*, Phys. Rev. B **82**, 180508 (2010).
[2] R. Hord *et al.*, Z. Anorg. Allg. Chem. **637**, 1114 (2011).
[3] G. Pascua, PhD thesis, Universität Zürich, 2014.

14.2 Magnetic penetration depth and spin order in strained LSCO thin films

Strained thin films of the optimally doped cuprate superconductor $La_{1-x}Sr_xCuO_4$ (LSCO) with a doping of $x = 0.16$ were studied by the low energy muon spin rotation technique (LE-μSR). Several films were grown on different substrates in order to modify the superconducting properties without changing the doping. The LSCO films grown on $SrLaAlO_4$ (LSAO) substrate are under compressive strain (a and b axes of LSAO are $\simeq$ 3% smaller than in LSCO). The 30 and 40 nm thick films have similar superconducting transition temperatures of $T_c \simeq 33$ K. In contrary, $T_c \simeq 14$ K in the 40 nm thin film grown on $SrTiO_3$ (STO) is relaxed with lattice constant as in bulk samples.

Surprisingly, the relaxed film grown on STO shows indications for magnetic order in zero field measurements below $T = 10$ K. Depth dependent measurements revealed that the magnetic fraction of the films is located in the region 4-13 nm below the surface. For the films grown on LSAO substrates a significantly smaller magnetic response was observed below 5 K.

The superconducting properties were studied by field dependent measurements in the vortex state at low temperatures. The muon relaxation rate σ measures the field inhomogeneities in the sample arising from the formation of the vortex lattice. Theoretically, it has its maximum where the distance between the vortices is of the order of the effective magnetic penetration depth [1]. The variation in the position of the maximum between films of equal thickness grown on different substrates seen in Fig. 14.2 corresponds to the expectation for samples with different T_c [2]. In contrary, the variation with film thickness exceeds from far the expectation associated with the variation of effective magnetic penetration depth. The increase of σ observed at high fields consistently for all the samples investigated is ascribed to a field induced ordering of magnetic moments in at least some fraction of the LSCO films. Since a magnetic layer was found close to the surface interface of one film and since some magnetic fraction can be generally induced under magnetic field, we might speculate the existence of different domains, with superconductivity never occurring close to the surface interface and leading to a smaller effective film thickness for superconductivity. A non-superconducting layer of constant thickness with (zero) field induced moments ordering would explain all the curves of Fig. 14.2.

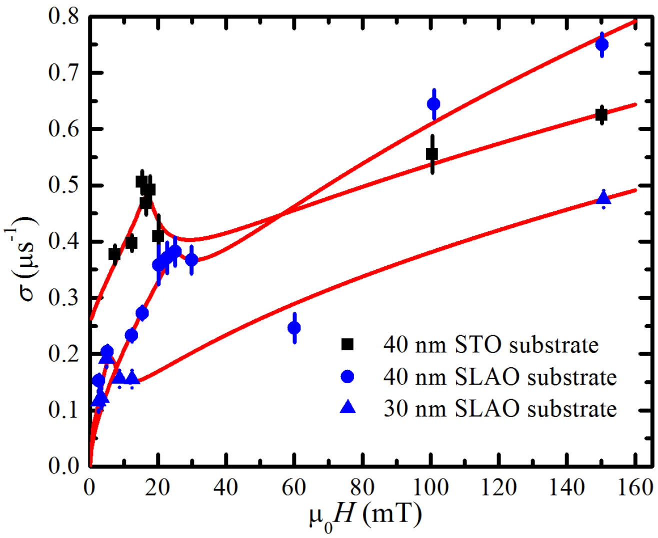

FIG. 14.2 – Magnetic field dependence of the muon relaxation rate σ in LSCO thin films grown on different substrates. The full lines are guides to the eyes.

[1] E. Brandt *et al.*, Phys. Rev. B **71**, 014521 (2005).
[2] Y. J. Uemura *et al.*, Phys. Rev. Lett. **62**, 2317 (1989).

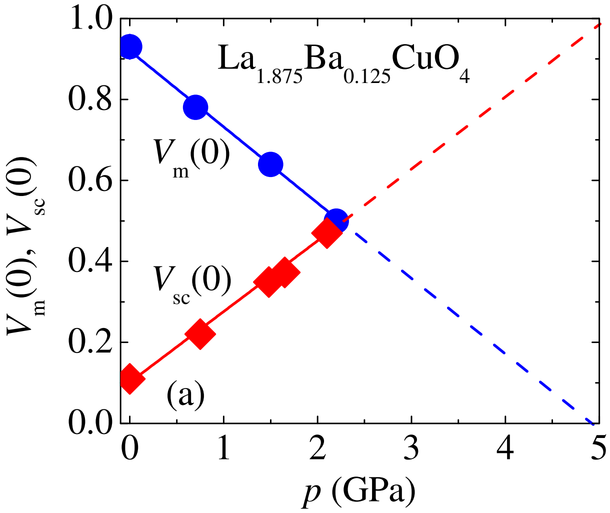

FIG. 14.3 – The pressure dependence of the zero-temperature limit of the magnetic and the SC volume fractions, $V_m(0)$ and $V_{sc}(0)$, respectively, of LBCO-1/8. Solid lines are linear fits to the data [5].

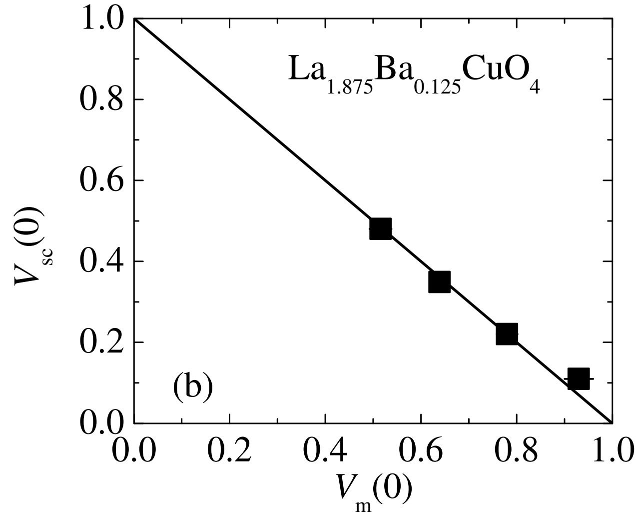

FIG. 14.4 – $V_{sc}(0)$ vs. $V_m(0)$. The straight line is drawn between a hypothetical situation of a fully magnetic ($V_m(0)$ = 1) and a fully SC state ($V_{sc}(0)$ = 1) [5].

14.3 Tuning the static spin-stripe phase and superconductivity in $La_{2-x}Ba_xCuO_4$ ($x = 1/8$) by hydrostatic pressure

$La_{2-x}Ba_xCuO_4$ (LBCO) was the first cuprate system where high-T_c superconductivity was discovered [1]. In LBCO the superconducting (SC) transition temperature T_c has a deep minimum at $x = 1/8$ [2], which is known as the 1/8 anomaly. Here a structural transition from a low-temperature orthorhombic (LTO) to a low-temperature tetragonal (LTT) phase was observed [3]. Neutron diffraction experiments revealed two-dimensional charge and spin order in $La_{1.48}Nd_{0.4}Sr_{0.12}CuO_4$ [4]. It was proposed [4] that the density of the dopant induced charge carriers modulates spatially in a periodic fashion forming a self-organized alternating array of charge and spin stripes and that the carriers are pinned by the lattice modulation in the LTT phase, and T_c is suppressed. Experimental results and theoretical considerations show that in the stripe phase charge and spin order appear to be a generic feature of the cuprates. However, the role of stripes for superconductivity in cuprates is still unclear at present.

Our recent studies of magnetism and superconductivity in LBCO-1/8 as a function of pressure revealed an unusual interplay between spin order and bulk superconductivity [5]. With increasing pressure the spin order temperature and the size of the ordered moment are not changing significantly. However, application of hydrostatic pressure leads to a remarkable decrease of the magnetic volume fraction $V_m(0)$ (see Fig. 14.3). Simultaneously, an increase of the SC volume fraction $V_{sc}(0)$ occurs. Furthermore, it was found that $V_m(0)$ and $V_{sc}(0)$ at all p are linearly correlated: $V_m(0) + V_{sc}(0) \simeq 1$ (Fig. 14.4). This is an important new result, indicating that the magnetic fraction in the sample is directly converted to the SC fraction with increasing pressure. The present results provide evidence for a competition between bulk superconductivity and static magnetic order in the stripe phase of LBCO-1/8, and that static stripe order and bulk superconductivity occur in mutually exclusive spatial regions.

[1] J.G. Bednorz *et al.*, Z. Phys. B **64**, 189 (1986).
[2] A.R. Moodenbaugh *et al.*, Phys. Rev. B **38**, 4596 (1988).
[3] J.D. Axe *et al.*, Phys. Rev. Lett. **62**, 2751 (1989).
[4] J.M. Tranquada *et al.*, Nature **375**, 561 (1995).
[5] Z. Guguchia *et al.*, New Journal of Physics **15**, 093005 (2013).

14.4 Gold nanoparticles on $YBa_2Cu_3O_{7-\delta}$ thin films

Disorder within cuprate high temperature superconductors can strongly affect its superconducting properties. In $YBa_2Cu_3O_{7-\delta}$, for instance, the substitution of Cu atoms by metal ions decreases the superconducting transition temperature T_c [1]. Surprisingly, doping with gold showed the opposite effect: if 10 % of Cu from the Cu-O chains is replaced by Au in single-crystal $YBa_2Cu_3O_{7-\delta}$, T_c is increased by 1.5 K [2].

Recently, Au nanoparticles have been incorporated in $YBa_2Cu_3O_{7-\delta}$ thin films to improve the pinning properties. Beside the expected increase in the critical current density j_c (from $4 \cdot 10^7$ A/cm^2 to $6 \cdot 10^7$ A/cm^2 at 10 K) a higher T_c was observed as well [3]. We utilized low-energy muons to investigate the microscopic changes on

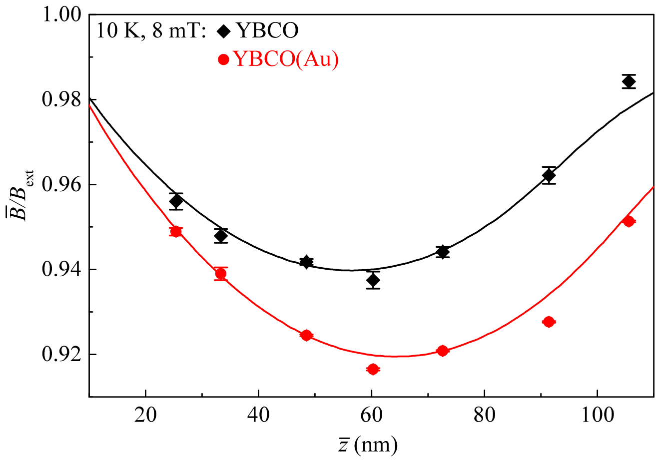

FIG. 14.5 – The average local magnetic field normalized to the applied field $\bar{B}/B_{\text{ext}}$ versus the mean muon implantation depth $\bar{z}$ measured perpendicular to the film surface for thin-film YBCO and YBCO(Au) by low-energy muon spin rotation [4]. The solid lines represent the results of the global fits taking 7 μSR spectra at different $\bar{z}$ into account. The data points are determined from single spectra fits.

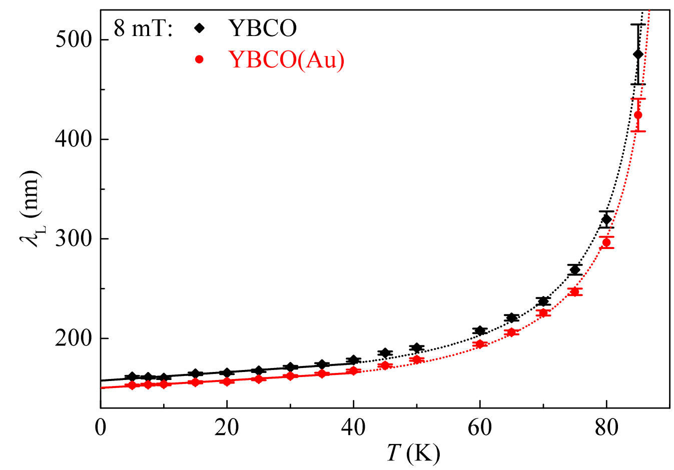

FIG. 14.6 – The London penetration depth λ_{L} versus temperature T for thin-film YBCO and YBCO(Au) determined by low-energy muon spin rotation [4]. The corresponding solid lines are linear fits to the data in the range $5-35$ K. The dotted lines are fits to a power law.

the superconducting properties due to the Au nanoparticles [4]. Therefore, slowed down muons have been implanted in different depths into the sample to investigate the magnetic screening profile $B(z)$ in the Meissner state. By determining the London penetration depth λ_{L} direct conclusion on the superfluid density n_{s} could be drawn, since they are related via the effective mass m^*.

We investigated two sets of thin-film samples, one with [YBCO(Au)] and one without (YBCO) Au nanoparticles. We observed a shift of $\Delta T_{\text{c}} = 0.6(3)$ K between YBCO(Au) and YBCO, determined by resistivity measurements [4]. The magnetic penetration profile $\bar{B}(\bar{z})$, depicted in Fig. 14.5, has the expected shape of a cosh (exponential decay from both interfaces), according to the London equation. The YBCO(Au) samples screen the magnetic field stronger and therefore exhibit a lower London penetration depth. This reduction of λ_{L} may be due a lowered defect density, originating from a condensation of defects at the Au nanoparticles. Diffusion of Au into the $YBa_2Cu_3O_{7-\delta}$ structure may also influence λ_{L} as well as T_{c}.

The temperature dependence of λ_{L} in YBCO(Au) is similar to pristine YBCO in terms of shape and slope, but the absolute scale is shifted (see Fig. 14.6). The penetration depth increases linearly with temperature up to 35 K, which is characteristic for d-wave pairing. At higher temperatures $\lambda_{\text{L}}(T)$ is described by a power law yielding a higher T_{c} for YBCO(Au), in agreement with the resistivity measurements. This implies that incorporated Au nanoparticles do not affect the fundamental properties, like the pairing behavior and the size of the superconducting gap, but the quality of thin-film $YBa_2Cu_3O_{7-\delta}$ is improved remarkably due to the reduced disorder.

[1] L. Shlyk *et al.*, Physica C **377**, 437 (2002)

[2] M. Z. Cieplak *et al.*, Appl. Phys. Lett. **57**, 934 (1990).

[3] C. Katzer *et al.*, Supercond. Sci. Technol. **26**, 125008 (2013).

[4] E. Stilp *et al.*, Phys. Rev. B **89**, 020510(R) (2014).

14.5 Pressure effects in iron-chalcogenides

Among the iron-based superconductors the iron chalcogenide system exhibits the highest superconducting transition temperatures T_{c} [1]. Due to their simple structure they may act as a model system to gain insight into the mechanism of high temperature superconductivity in the iron-based materials. Whereas several authors propose a purely electronic model for the appearance of superconductivity (see, e.g., Refs. [2]), experimental isotope exchange studies demonstrate the significant influence of the lattice in the Cooper pairing [3].

Despite being the simplest among the Fe-based superconductors, the iron chalcogenides are among the most fascinating compounds: intercalation or application of pressure leads to a large increase of T_{c} and highly unexpected and unique effects in the superconducting and magnetic properties. The antiferromagnetic FeTe was predicted to become superconducting under hydrostatic pressure. However, a ferromagnetic ground state requiring similar electronic properties close to the Fermi level as the superconducting ground state is realized. Application of chemical pressure by partial substitution of Se

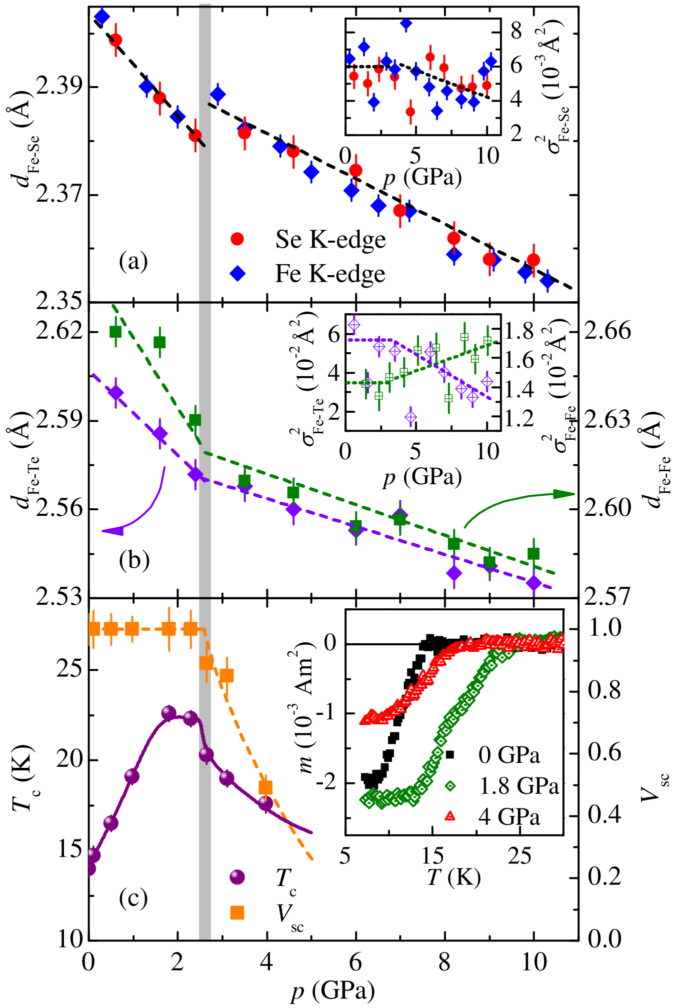

FIG. 14.7 –
(a) Pressure dependence of the Fe-Se bond length $d_{\mathrm{Fe-Se}}$ of $FeSe_{0.5}Te_{0.5}$ at room temperature obtained from Se K-edge and Fe K-edge measurements.
(b) The left and right axes show the pressure evolution of the Fe-Te and Fe-Fe distances.
The insets in (a) and (b) show the corresponding Debye-Waller factors σ^2 representing the disorder of the bonds.
(c) Pressure dependence of the superconducting transition temperature T_c (left axis) and the superconducting volume fraction (right axis). The inset shows magnetization measurements for selected pressures.
The gray bar at $p \simeq 3$ GPa indicates the structural phase transition. The dashed lines are a guide to the eyes.

by Te first leads to an increase of $T_c \simeq 14$ K before the material develops an antiferromagnetic ground state after crossing a coexistence region, in which both electronic ground states coexist.

Considering the above mentioned pressure effects in the iron chalcogenides, it is rather surprising that we find in $FeSe_{0.5}Te_{0.5}$ under pressure a moderate increase of T_c from $\simeq$ 14 to $\simeq$ 23 K until $p \simeq 2.2$ GPa followed by a smooth decrease. The X-ray absorption spectroscopy (XAS) measurements presented in Fig. 14.7 (a) and (b) at the Fe and Se K-edges reveal that compression affects the local structure significantly and in a discontinuous manner across the known tetragonal to monoclinic structural phase transition at $p_S \simeq 3$ GPa [4], whereas it does not have an analogous important effect on the electronic structure. Interestingly, both the superconducting volume fraction and T_c are decreasing as soon as the crystallographic structure changes, i.e. above p_S, underlining the importance of the lattice for the superconducting and magnetic properties (see Fig. 14.7 (c)). However, since the electronic structure shows no significant changes across the structural transition, the modifications in the superconducting properties in this system arise by structural effects.

[1] S. He, *et al.*, Nature Mater. **12**, 605 (2013).

[2] P. J. Hirschfeld, *et al.*, Rev. Prog. Phys. **74**, 124508 (2011); R. M. Fernandes, *et al.*, Nature Physics **10**, 97 (2014).

[3] R. H. Liu, *et al.*, Nature **459**, 64 (2009); R. Khasanov, *et al.*, Phys. Rev. B **82**, 212505 (2010); R. Khasanov, *et al.*, New J. Phys. **12**, 073024 (2010);

[4] N. C. Gresty, *et al.*, J. Am. Chem. Soc. **131**, 16944 (2009).

15 Phase transitions and superconducting photon detectors

X. Zhang, F. von Rohr, H. Grundmann, O. Bossen, S. Siegrist, A. Engel and A. Schilling

in collaboration with: University of Bern (K. Krämer), Karlsruhe Institut für Technologie (K. Il'in), Deutsches Zentrum für Luft- und Raumfahrt (H.-W. Hübers, A. Semenov), FIRST Lab ETH Zürich, PSI Villigen (M. Medarde, K. Conder), McMaster University (H. Dabkowska), IFW Dredsen (V. Kataev, A. Alfonsov), University of S ao Paulo (A. Paduan-Filho), Institute of Nuclear Physics, Tashkent (A. Rakhimov), ETH Zürich (R. Nesper & J. Novotny), Princeton University (R. J. Cava)

(PTMA)

15.1 Superconducting nanowire single-photon detectors for optical and X-ray photons

In recent years there has been growing evidence that magnetic vortices are important for a proper understanding of the working principle of superconducting nanowire single-photon detectors (SNSPD) (see, for example, last year's annual report, in which we reported the first systematic measurements of the magnetic-field dependence of dark counts of SNSPD [1]). Our measurements strongly supported the idea that vortices entering and crossing the superconducting strip are the main contribution to dark counts in SNSPD [2]. A later study [3] showed that there is a magnetic-field dependence on the photon counts as well, which, however, is not described by the currently accepted model. Since there is no comprehensive description of the detection mechanism in SNSPD, we developed a simple, numerical model [5] that is detailed enough to capture the physics in SNSPD and to describe experimental results [4]. Two coupled differential equations describing the generation and the diffusion of quasi-particles after the absorption of a photon are solved numerically. The resulting quasi-particle distributions (shown in Fig. 15.1(a)) are used to compute the current distribution as a function of time, shown in Fig. 15.1(b) for t=2.6 ps. These results can be compared with the outcome of two alternative, analytic detection models ("hard-core model" [6] and "quasi-particle model" [7]). They strongly support a detection mechanism by photon-assisted vortex-crossings which requires lower photon energies than the other detection models for a given experimental situation. In the case of sufficiently high photon energies, such vortex crossings always trigger the formation of the initial normal-conducting cross-section, well before the competing mechanisms would lead to a photon detection event. Furthermore, only the results of the

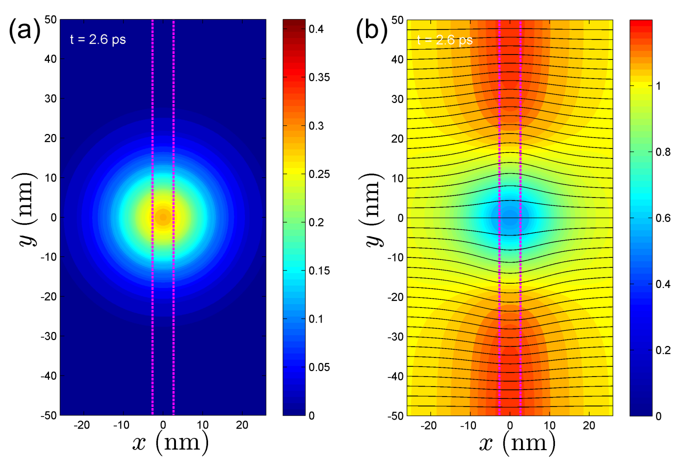

FIG. 15.1 – Results from our calculations for the spatial distributions of the quasi-particles (a) and the current density (b), 2.6 ps after the absorption of a photon with wavelength $\lambda = 1\ \mu$m in a superconducting strip. The process results in an increase of the current density near the edges of the superconducting strip. The dashed vertical lines outline a ξ-slab, the minimum volume that must become normal-conducting in order to trigger a detection event.

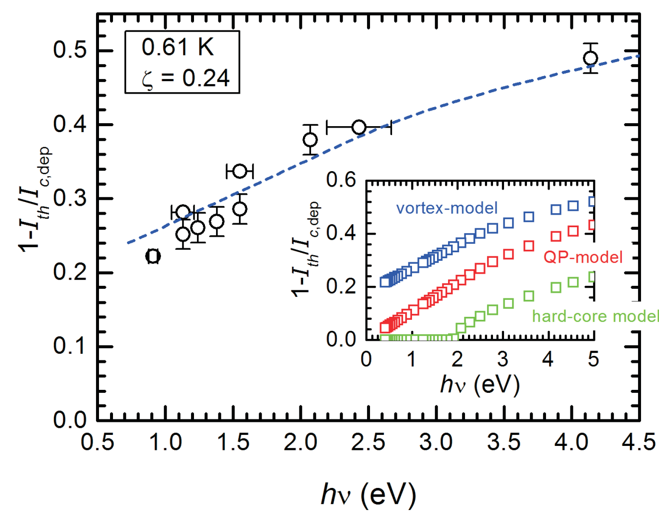

FIG. 15.2 – $1 - I_{th}/I_{c,dep}$ vs. photon energy, where I_{th} is the minimum or threshold bias current and $I_{c,dep}$ the critical depairing-current. Measured values are compared with our simulation results (dashed blue). The quasi-particle multiplication efficiency ζ was the only free parameter in the fit. The inset compares our model with two other models.

vortex-crossing model are consistent with our experimentally determined detector characteristics, *i.e.*, the dependence of the minimum bias current on photon energy (see Fig. 15.2). A very recent detailed study of this kind of detection criterion [8] has confirmed the observed agreement with experiments over a very large range of photon energies.

[1] A. Engel, A. Schilling, K. Il'in, and M. Siegel, Phys. Rev. B, **86**, (2012) 140506(R).

[2] L.N. Bulaevskii *et al.*, Phys. Rev. B, **83**, (2011) 144526.

[3] R. Lusche *et al.*, Phys. Rev. B, **89**, (2014) 104513.

[4] L.N. Bulaevskii, M.J. Graf, and V.G. Kogan, Phys. Rev. B, **85**, (2012) 014505.

[5] A. Engel and A. Schilling, J. Appl. Phys., **114**, (2013) 214501.

[6] G.N. Gol'tsman *et al.*, Appl. Phys. Lett., **79**, (2001) 705.

[7] A. Semenov, A. Engel, H.W. Hübers, K. Il'in, and M. Siegel, Eur. Phys. J. B, **47**, (2005) 495.

[8] J.J. Renema *et al.*, Phys. Rev. Lett., **112**, (2014) 117604.

15.2 Ac-magnetic susceptibility in the peak-effect region of Nb_3Sn

We performed a systematic study of the ac-magnetic susceptibility on an Nb_3Sn single crystal, which displays a strong peak effect near the upper critical field H_{c2} (in collaboration with N. Toyota, Tohoku University, Japan). In external magnetic fields above $\mu_0 H \approx 3$ T, the peak effect manifests itself in a single, distinct peak in the real part $\chi'(T)$ of the ac susceptibility as a function of temperature T, the size of which continuously increases with increasing magnetic field H. In the imaginary part $\chi''(T)$ of the ac susceptibility, on the other hand, a single peak initially grows with increasing H up to a well-defined value, and then splits into two sharp peaks which separate when H is further increased (see Fig. 15.3).

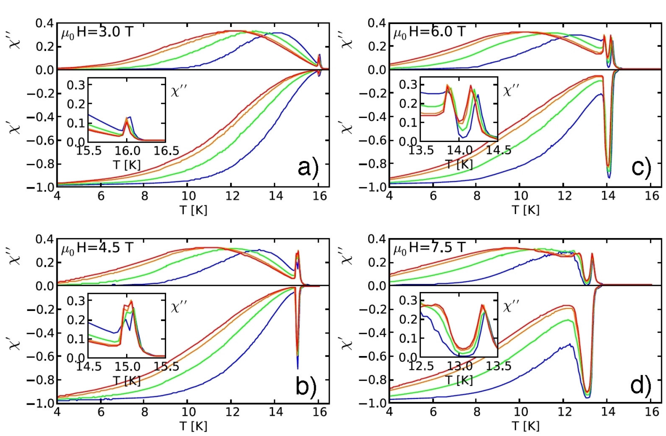

FIG. 15.3 – ac-Magnetic susceptibility data of an Nb_3Sn single crystal. The magnetic field $\mu_0 H \approx 3$ T (panel (a)) corresponds to case b) in Fig. 15.4, and the data taken at larger fields (panels (b) to (d)) to case c).

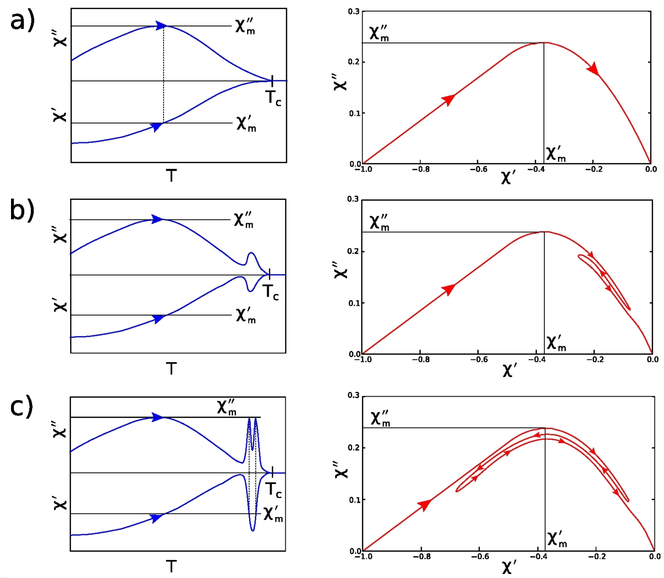

FIG. 15.4 – Left panels: Real and imaginary parts of the ac-magnetic susceptibility for a superconductor displaying a peak effect. Right panels: corresponding χ'' *vs.* χ' representations. Arrows indicate an experiment with increasing temperature.
a): a type II superconductor without peak effect;
b): a type II superconductor with a weak peak effect, producing single peaks in both real and imaginary parts of the ac susceptibility;
c): a type II superconductor showing a strong peak effect, leading to a single peak in the real part but a double-peak structure in the imaginary part.

We could explain this surprising behavior by a flux-creep model and taking into account the enhancement of the critical-current density in the peak-effect region near T_c in which Bean's critical-state model seems to apply [1].

To illustrate the occurrence of single- and double peak structures in $\chi''(T)$ we are plotting a $\chi''(\chi')$ relationship in the right panels of Fig. 15.4, as it is typically assumed in superconductors near T_c. In most known cases, $\chi''(\chi')$ is a single-valued function with a maximum χ''_m for a certain value of χ'_m. Without any peak effect, the critical-current density $j_c(T)$ decreases monotonically with increasing temperature T (direction indicated in Fig. 15.4) and vanishes at $T \sim T_c$. As a result, the real part χ' of the magnetic susceptibility also monotonically increases with T before reaching zero at T_c (see Fig. 15.4a, left panel). If the sample displays a peak effect near T_c, however, the critical-current density increases sharply before dropping to zero at the transition to the normal state [2–4]. This causes a sudden decrease in $\chi'(T)$ near T_c, *i.e.*, a peak in $|\chi'(T)|$ (Figs. 15.4b and c, left panels). Depending on the magnitude of this peak which is determined by the pinning strength in the peak-effect region, the sample geometry and the probing ac magnetic field, this will either lead to a single peak in the imaginary part $\chi''(T)$ of the susceptibility if $|\chi'| \leq |\chi'_m|$ (Fig. 15.4b), or to a double-peak structure as soon as $|\chi'| > |\chi'_m|$ in the peak effect region (Fig. 15.4c).

A refined analysis of our data also revealed that the crystal is in the so-called "flux-creep regime" below the peak-effect region (*i.e.*, in a region in which a non-equilibrium magnetic-flux distribution relaxes to equilibrium on testable laboratory time scales), while in the peak-effect region, the "Bean critical state" is realized, *i.e.*, a state in which a non-equilibrium magnetic-flux distribution can be quasi-stationary [1].

[1] O. Bossen, A. Schilling and N. Toyota, Physica C, **492** (2013) 133.

[2] T.G. Berlincourt, R.R. Hake and D.H. Leslie, Phys. Rev. Lett., **6**, (1961) 671.

[3] M.A.R. LeBlanc and W.A. Little in *Proceedings of the 7th International Conference on Low Temperature Physics*, p. 364, University of Toronto Press, (1961).

[4] A. B. Pippard, Philos. Mag., **19** (1969) 217.

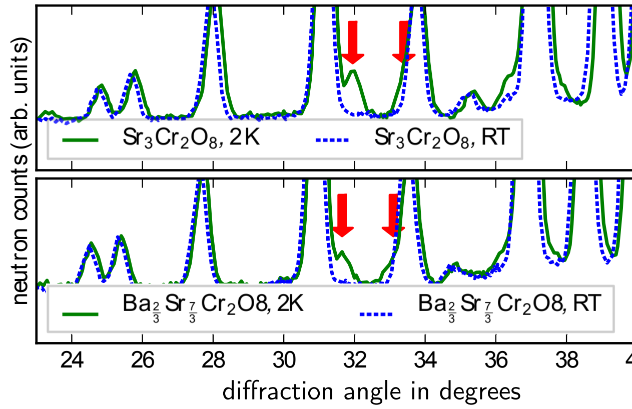

FIG. 15.5 – Additional peaks appearing in the low temperature neutron diffractograms for $Sr_3Cr_2O_8$ and $Ba_{\frac{2}{3}}Sr_{\frac{7}{3}}Cr_2O_8$, indicating the structural phase transition.

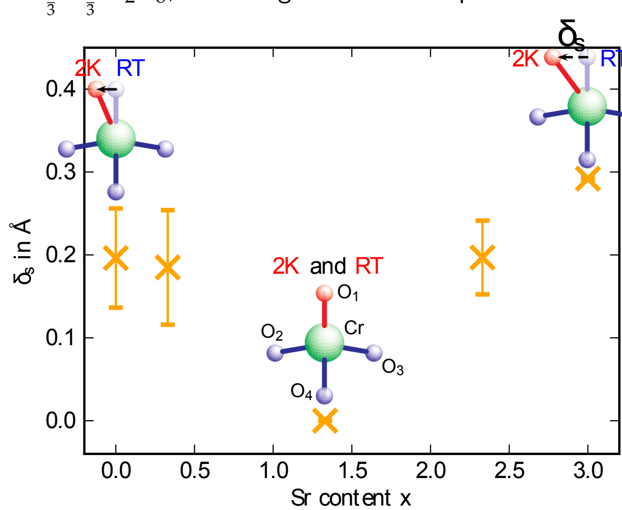

FIG. 15.6 – Distance δ_s of the apical oxygen atom from the dimer axis as a function of the Sr content x. The distance in the corresponding sketch is exaggerated for visual clarity.

15.3 Influence of disorder on the structural phase transition and magnetic interactions in $Ba_{3-x}Sr_xCr_2O_8$

in collaboration with: Paul Scherrer-Institut Villigen (PSI): Marisa Medarde-Barragan, Denis Sheptyakov

In the previous annual report, we reported on the peculiar change of the magnetic interactions in the spin dimer system $Ba_{3-x}Sr_xCr_2O_8$ as a function of the Sr content x. An analysis of the temperature dependence of the magnetization $M(T)$ suggested that the intra-dimer interaction constant J_0 changes in a non-linear way with x[1].

To probe possible structural explanations for the reported change of J_0, we have performed neutron powder diffraction experiments at room temperature and at $T = 2$ K for various values of x at the *High-Resolution Powder Diffractometer for Thermal Neutrons*, HRPT (PSI, Villigen). For $x \in \left\{0, \frac{1}{3}, \frac{7}{3}, 3\right\}$, our analysis suggests a breaking of the threefold rotational symmetry around the dimer axis with decreasing temperature. The corresponding change of the space group from R$\bar{3}$m at room temperature to $C_{2/c}$ at $T = 2$ K is indicated by the appearance of additional diffraction peaks (see Fig. 15.5). This symmetry breaking, which lifts the orbital degeneracy of the Cr^{5+}-ion that is surrounded by an oxygen tetrahedron, has previously been reported for the mother compounds $Ba_3Cr_2O_8$[2] and $Sr_3Cr_2O_8$[3]. It is essentially based on a Jahn-Teller like shift of the apical atom of this tetrahedron away from the symmetry axis (see Fig. 15.6). We found that the value δ_s of this shift depends on the Sr content x and vanishes for $x = \frac{4}{3}$.

The strength of J_0 is mainly given by the exchange energy between the Cr^{5+}-ions. A shift of the oxygen position changes this energy and should therefore strongly influence J_0. Based on the obtained detailed information on the crystallographic structure, we have therefore performed extended Hückel tight binding (ETHB) calculations in order to examine the theoretical value for J_0 at room temperature and $T = 2$ K. As shown in Fig. 15.7, the experimental values for J_0 can be well reproduced by our calculations based on the low temperature structure for all values of x, as reported for pure $Sr_3Cr_2O_8$ [3]. In contrast to that, the room temperature calculations differ substantially from the experimental values for

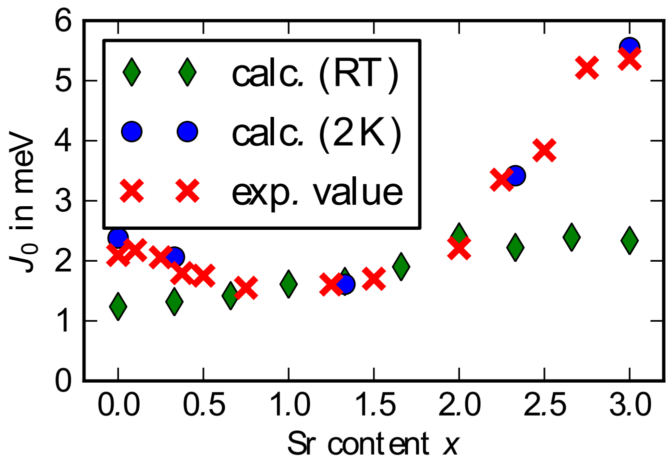

FIG. 15.7 – Intra-dimer interaction constant J_0 for $Ba_{3-x}Sr_xCr_2O_8$ as a function of the Sr content x. The data are obtained from SQUID-measurements (exp.) and estimated based on EHTB-calculations for the crystal structure at room temperature and $T = 2$ K (calc.).

those values of x for which a symmetry breaking could be observed. Hence, we conclude that a gradual disappearance of the Jahn-Teller induced symmetry breaking is responsible for the peculiar minimum of J_0 for intermediate values of x.

Our analysis of the crystal structure shows that all crystallographic parameters vary smoothly and in a strictly monotonous way as functions of x, providing no direct reason for a suppressed Jahn-Teller distortion for intermediate values of x. However, due to the gradual substitution of Ba by Sr, chemical disorder is introduced into the system. The Ba- and Sr-atoms are randomly distributed over the possible atomic positions, changing the local stoichiometry between different unit cells. This random distribution leaves the symmetry group intact *on global average*, but breaks it locally. This local symmetry breaking gradually lifts the orbital degeneracy of the Cr^{5+}-ions so that the possible energy gain through a breaking of the symmetry is reduced, thereby suppressing the Jahn-Teller transition. See [4] for further details.

[1] H. Grundmann *et al.*, Mat. Res. Bul., **48** (2013) 3108.

[2] M. Kofu *et al.*, Phys. Rev. Lett., **102** (2009) 037206.

[3] L. C. Chapon *et al.*, arXiv:0807.0877v2.

[4] H. Grundmann, M. Medarde, D. Sheptyakov and A. Schilling, submitted to Phys. Rev. B.

15.4 Superconductivity and charge-density-wave ordering in $BaTi_2Sb_2O$

Recent studies have shown that $BaTi_2Sb_2O$ exhibits a transition to a density wave ordered state at $T_{DW} \approx 55$ K, and a transition to a bulk superconducting state at $T_c \approx 1$ K [1, 2]. $BaTi_2Sb_2O$ belongs to a large family of stacked, layered titanium oxide pnictide compounds. In these compounds the nominal valence of titanium is Ti^{3+} with its 3d orbitals singly occupied. In this $3d^1$ configuration, Ti is surrounded octahedrally by O and Sb, forming a Ti_2O square sub-lattice. From a structural and chemical perspective, these Ti_2O layers can be interpreted as the $3d^1$-anti-configuration of the $3d^9$ CuO_2 planes in the cuprates.

For the systematic investigation of the physical properties of this material, we have successfully prepared $BaTi_2Sb_2O$ and $Ba_{1-x}A_xTi_2Sb_2O$ (A = Na, Rb) solid solutions by high-temperature solid-state reactions up to 1000 °C. [3, 4] We have used the substitution of Ba by an alkaline earth metal as a strategy to hole-dope and therefore manipulate the Fermi-level of these compounds. In Fig. 15.8 we show the x-ray diffraction pattern at ambient temperature for the sample of nominal composition $Ba_{0.7}Rb_{0.3}Ti_2Sb_2O$ ($x = 0.3$), together with the crystal structure of the compound in the inset. All compounds of the $Ba_{1-x}A_xTi_2Sb_2O$ solid solutions were found to belong to the same crystal

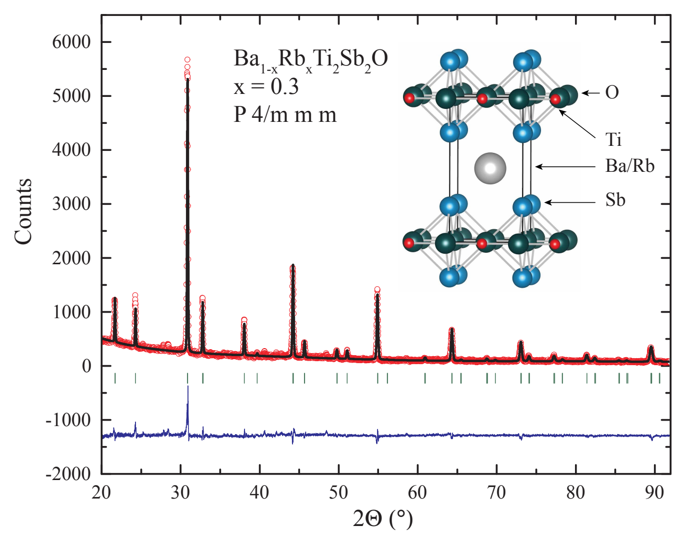

FIG. 15.8 – The powder x-ray diffraction pattern at ambient temperature for the sample of nominal composition $Ba_{0.7}Rb_{0.3}Ti_2Sb_2O$ ($x = 0.3$). The crystal structure ($CeCr_2Si_2C$-type) of the compound is shown in the inset. The vertical dark green lines show the theoretical Bragg peak positions for this phase. The blue pattern on the bottom is the difference plot between the theoretical pattern and the observed intensities.

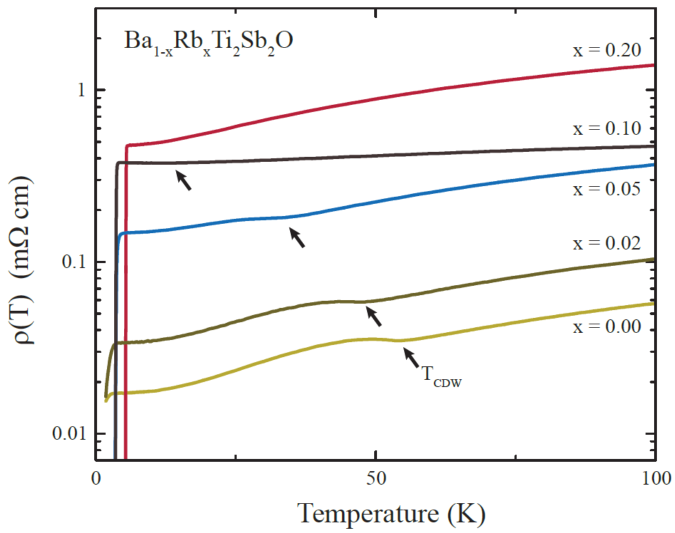

FIG. 15.9 – Resistivities of $Ba_{1-x}Rb_xTi_2Sb_2O$ for $x = 0$, 0.02, 0.05, 0.1, and 0.2 in a temperature range between 1.8 K and 100 K. The CDW transition manifests itself in a sudden increase of the resistivity for the samples $x = 0$, 0.02, 0.05 and 0.1 (marked with a black arrow). This anomaly is absent for the sample with $x = 0.2$. For increasing rubidium contents x (up to $x = 0.2$), the normal state resistivities increase, the CDW ordering transition temperatures T_{CDW} decrease, while the critical temperatures T_c increase.

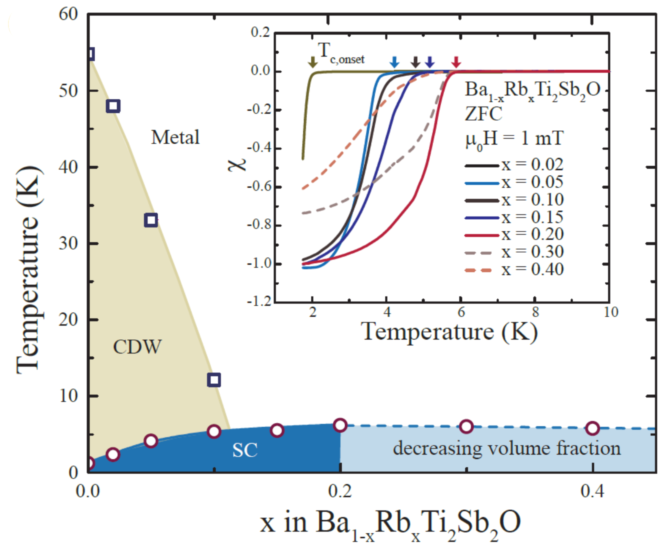

FIG. 15.10 – Phase diagram of the electronic properties of $Ba_{1-x}Rb_xTi_2Sb_2O$ derived from resistivity and magnetization measurements.

structure, which is isopointal to the $CeCr_2Si_2C$-type structure ($P4/mmm$). Within the $Ba_{1-x}Rb_xTi_2Sb_2O$ solid solution $0 \leq x \leq 0.4$ the cell parameter vary only slightly, but continuously with increasing rubidium content.

The resistivities $\rho(T)$ of $Ba_{1-x}Rb_xTi_2Sb_2O$ with $x = 0$, 0.05, 0.1, and 0.2 in a temperature range of $T = 1.8$ K to 100 K are shown in Fig. 15.9. The parent compound ($x = 0$), shows a distinct kink in the resistivity at T_{CDW} = 55 K, which is a characteristic feature of a DW transition. This phase transition temperature T_{DW} is strongly reduced and eventually suppressed with increasing rubidium content. For a relatively small doping of $x = 0.05$ the DW transition is already lowered to 34 K, whereas the critical temperature is increased by more than 2 K to T_c = 3.7 K. Taking the absolute value of the resistivity as a measure for the metallicity of a sample, we can state that the increase of the superconducting transition T_c and the decrease and subsequent suppression of the CDW ordering temperature T_{CDW} go along with a decrease in metallicity.

In Fig. 15.10 we summarize the electronic phase diagram of the $Ba_{1-x}Rb_xTi_2Sb_2O$ solid solution. The critical temperatures T_c used for the phase diagram are the intersections of the slopes of the phase transitions and the normal state magnetizations.

In a series of μSR experiments we have probed the density wave transition and superconducting properties of $BaTi_2Sb_2O$ and the $Ba_{1-x}Na_xTi_2Sb_2O$ (with $x = 0.05$, 0.1, 0.15, 0.2, 0.25, 0.3) solid solution [4]. The zero-filed (ZF) and transverse-field (TF) muon time signals for the parent compound $BaTi_2Sb_2O$ were measured well above $T_{DW} \approx$ 50 K at $T = 100$ K and below at $T = 1.5$ K. The zero field μSR spectra above and below T_{DW} do not exhibit any noticeable change in the relaxation rate, indicating the absence of a spontaneous internal field at the muon stopping site. This is further supported by the weak TF measurements, where no reduction of the asymmetry is observed, as it would be expected in case of magnetic ordering. Therefore, we can exclude that the observed transition at T_{DW} is caused by spin density wave (SDW) ordering in the parent compound $BaTi_2Sb_2O$ as speculated earlier [1, 5]. The observed transition is therefore most likely caused by CDW ordering.

For the optimally doped sample $Ba_{0.8}Na_{0.2}Ti_2Sb_2O$ with a $T_c \approx 5.1$ K, we have performed ZF and TF μSR experiments at $T = 1.5$ K and above T_c at 6 K. The observed strong additional relaxation in the TF measurements below T_c is caused by the formation of the flux-line lattice (FLL) in the Shubnikov phase, as depicted in Fig. 15.11. In Fig. 15.12 we show the temperature dependence of $\lambda^{-2}(T)$ as reconstructed from the Gaussian relaxation rate $\sigma_{sc}(T)$. These measurements suggest that λ^{-2} is virtually temperature independent below $T \simeq 1$ K for the optimally doped sample. The obtained experimental temperature dependence of $\lambda^{-2}(T)$ agrees well with the clean limit approach for a London superconductor with an s-wave gap.

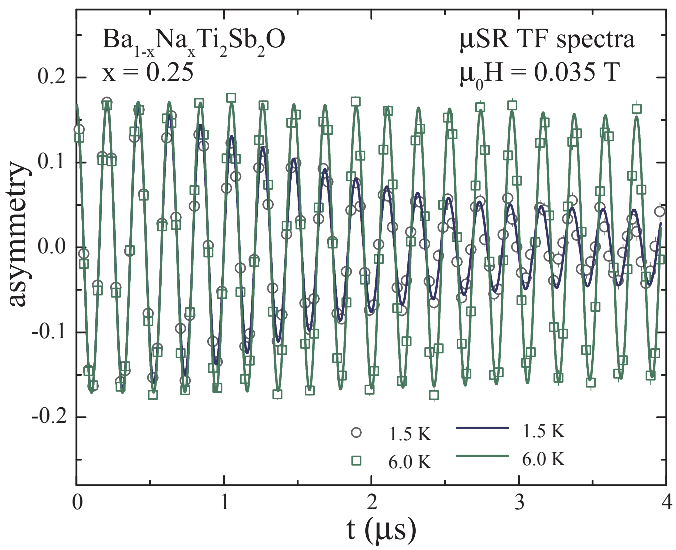

FIG. 15.11 – The TF μSR spectra for $x = 0.25$ above (6 K) and below (1.5 K) T_c. The strong relaxation of the signal at 1.5 K can be ascribed to the presence of the flux-line lattice.

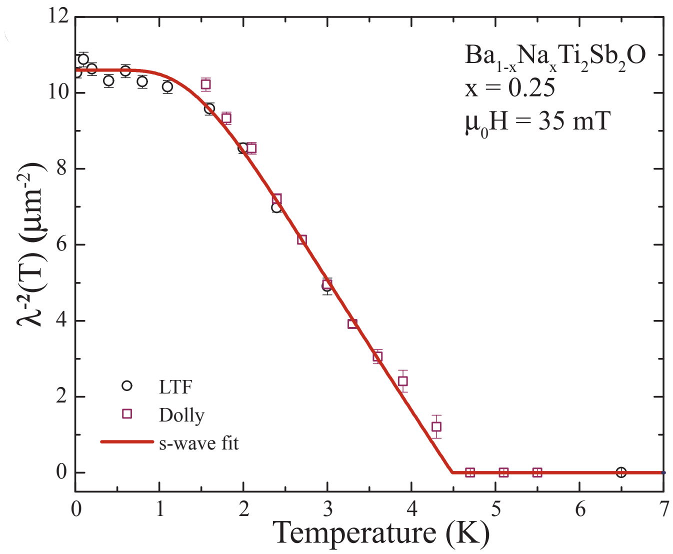

FIG. 15.12 – The temperature dependence of λ^{-2} for $x = 0.2$ as reconstructed from $\sigma_{sc}(T)$, measured in $\mu_0 H = 35$ mT. The solid line corresponds to an conventional London superconductor with an s-wave gap with $2\Delta/(k_B T_c) = 2.9$. Squares: Dolly instrument, circles: LTF instrument.

In our studies we have shown how superconductivity and DW ordering evolve in $Ba_{1-x}Rb_xTi_2Sb_2O$ as a function of the substitution of barium by rubidium. We have evidenced that the density wave ordering transition T_{DW} is continuously lowered and eventually suppressed with increasing rubidium content, while the transition temperature to superconductivity, T_c, is increased, reaching a maximum $T_{c,max}$ = 5.4 K. Our results support the scenario that hole doping by the incorporation of Na^+, K^+, and also Rb^+ is of great importance for the suppression of CDW ordering and the occurrence of superconductivity in these materials. [5, 6] From our μSR studies we are able to conclude that the phase transition observed in the normal state of these compounds is of CDW character, and from our low temperature μSR data we have found evidence for ruling out some scenarios about the microscopic origin of superconductivity in these compounds. The obtained experimental temperature dependence of $\lambda^{-2}(T)$ can be reasonably well explained within the clean limit approach for a conventional London superconductor. We find $BaTi_2Sb_2O$ to be a versatile model-system for the investigation of the competition and coexistence of conventional superconductivity and CDW ordering.

[1] T. Yajima *et al.*, JPSJ, **82** (2013) 103706.

[2] M. Gooch *et al.*, Phys. Rev. B, **88** (2013) 064510.

[3] F. von Rohr, R. Nesper and A. Schilling, Phys. Rev. B, **89** (2014) 094505.

[4] F. von Rohr *et al.*, Phys. Rev. B, **88** (2013) 140501(R).

[5] P. Doan *et al.*, JACS, **134** (2012) 16520.

[6] U. Pachmayr and D. Johrendt, Solid State Sciences, **28** (2014) 31.

16 Surface Physics

T. Greber, M. Hengsberger, J. H. Dil (until July 2013), R. Westerström,
L. Castiglioni, H. Cun, G. Mette, S. Roth, A. Hemmi, G. Landolt, M. Greif, R. Stania,
C. Bernard, L.H. de Lima, A. Schuler, R. Arulanantham, R. Rüttimann, M. Graf,
T. Kälin, J. Osterwalder

After Hugo Dil, one of our former group members, took up an SNF professorship at EPF Lausanne the group made various adjustments to its research program. Hugo will continue the research on spin-orbit effects at surfaces, including those of topological insulators, performed primarily at the end station *COPHEE* for spin- and angle-resolved photoemission spectroscopy at the Swiss Light Source. This instrument had been built and operated highly successfully by our group over the last decade and a half. Discontinuing this research activity allows the group to strengthen its efforts in the remaining projects and to embark on a new activity on surface-supported catalyst molecules in the context of the University Research Priority Program (URPP) *Light to Chemical Energy Conversion (LightChEC)*. Our continuous efforts for the upscaling of the production of boron nitride and graphene made us a consortium member within the Graphene Flagship of the European Union.

For the investigation of surface and interface phenomena at the atomic level, our laboratory is well equipped for the preparation and characterization of clean single-crystalline surfaces, metal and molecular monolayer films, as well as sp^2-bonded single layers on surfaces, using a wide variety of experimental techniques. In addition, we take an active role in the commissioning and operation of the new SLS beamline *PEARL (PhotoEmission and Atomic Resolution Laboratory)*. Within the NCCR *Molecular Ultrafast Science and Technology (MUST)*, our group has built and commissioned a compact and mobile angle-resolved photoemission (ARPES) instrument, which is currently taking data at the attosecond laser facility in the laboratory of U. Keller at ETHZ (see Sec. 16.3).

The research carried out during the report period can be grouped into three topics:

- Monolayer films of hexagonal boron nitride (h-BN) and graphene on metal surfaces
  Over the past several years the group has gathered considerable expertise in the growth and characterization of sp^2-bonded monolayers on transition metal surfaces. The strongly corrugated h-BN layer on Rh(111) - termed boron nitride nanomesh - has been further studied with regards to its modification by low-energy ion implantation. Ar^+ ions with energies of about 100 eV are implanted between the h-BN and the Rh surface layer and immobilized at specific sites of the nanomesh unit cell, forming so-called *nanotents* [1]. The thermal stability of these intercalated species was further characterized [2]. Annealing of these samples leads to the formation of surprisingly regular voids in the film, exposing 2 nm wide patches of metal surface. Implantation of Rb^+ alkali ions was also demonstrated [3].

  A second line of research is directed towards the synthesis of epitaxial layers of graphene and *h*-BN with a view on future electronic devices based on graphene. Due to its insulating properties and similar crystal structure and lattice constant, *h*-BN appears to be the ideal 'gate oxide'. We have succeeded in growing heterostacks of single-layer graphene on top of single-layer *h*-BN on Cu(111) and Rh(111) substrates [5, 6]. While the hetero-films are far from defect-free, they allow to study the structural and electronic characteristics of these stacked two-dimensional (2D) materials. Our recent successes in the up-scaling of the growth processes of h-BN monolayers to the wafer scale are described in Sec. 16.1. A considerable effort is currently going on for the development of methods for transferring these layers onto arbitrary substrates.

- Molecular adsorbates and molecular monolayers
  One focus here is on single-molecule magnets based on endofullerenes. Recent results on dysprosium-scandium based endofullerenes, measured in the form of thin films far above monolayer thickness, are presented in Sec. 16.2. Experiments with endofullerene monolayers, involving also the interaction of the magnetic moments with the substrate, are currently being prepared at the PEARL beamline.

  Within the LightChEC URPP our role is to develop and study model catalyst surfaces that are relevant for solar water splitting. From the group of Roger Alberto from the UZH Chemistry Department we have received a first batch of water reduction catalyst molecules that have shown favourable efficiency and stability in a homogeneous water splitting reactor. A first study of the adsorption behavior of these molecules on Au(111) is ongoing.

- Ultrafast processes at surfaces

  After roughly a year of data taking with the MUST photoemission spectrometer attached to the *attoline* at ETHZ [6], a complete set of RABBITT (Reconstruction of Attosecond Beating By Interference of Two-photon Transitions) traces could be fully analyzed and a first paper has been submitted for publication [7] (see also Sec. 16.3). With this method, absolute delays of the photoemission from the valence d bands from Ag(111) and Au(111) could be measured. They are on the 100 as scale and vary strongly with energy. These experiments are the first of their kind and give us an unprecedented view on the electron dynamics in solids; they are currently extended to other materials and surfaces.

[1] H. Y. Cun *et al.*, Nano Letters 13, 2098 (2013).

[2] H. Y. Cun *et al.*, ACS Nano 8, 1014 (2014).

[3] L. H. de Lima *et al.*, Rev. Sci. Instrum. 84, 126104 (2013).

[4] S. Roth *et al.*, Nano Letters 13, 2668 (2013).

[5] S. Roth, PhD Thesis, Physik-Institut, Universität Zürich, 2013.

[6] R. Locher *et al.*, Rev. Sci. Instrum. 85, 013113 (2014).

[7] R. Locher, L. Castiglioni *et al.*, arXiv: 1403.5449 [cond-mat].

In the following, three highlights of last year's research are presented in more detail.

16.1 Boron nitride nanomesh at the $4''$ wafer scale

in collaboration with Michael Weinl, Stefan Gsell and Matthias Schreck, Physics Department, University of Augsburg; and the EU FET Flagship Graphene.

A strategic goal of our group has been the production of 2D materials such as hexagonal boron nitride at large scales. These efforts were well received by the European Flagship Graphene, where our group is part of the ramp-up phase since fall 2013.

We grow single layers of hexagonal boron nitride in a chemical vapor deposition (CVD) process on transition metal surfaces. In the case of a rhodium substrate the so called "nanomesh" structure [1] forms. It was shown that it can not only be produced on expensive single crystals, but also on single-crystalline Rh thin films grown on Si(111) [2, 3]. In 2010 we started with the set-up of a laboratory for the production of single layer materials on the four-inch wafer scale. A new ultra high vacuum (UHV) system is placed in a dedicated clean room environment (ISO class 7). An overview of the laboratory infrastructure is displayed in Figure 16.1. It allows four-inch wafer handling, wafer cleaning, CVD growth of 2D materials and their initial characterization in UHV and in a laminar flow box. Using the single- crystalline metal thin films from the University of Augsburg, this infrastructure is currently used for the growth of boron nitride monolayers [4], but allows more broadly the large-scale fabrication of atomically ordered structures and 2D materials on surfaces.

The need for better control of the growth parameters for the 2D layers led to the development of new in-situ characterization techniques. We succeeded in the construction of an inexpensive growth monitoring system with sub-monolayer sensitivity. It is based on photoemission yield changes that can be measured with an accuracy of 0.4% with a sampling time of one second. The origin of these yield changes are mainly work function changes during growth or modification of an adlayer on the surface [5]. A pulsed ultra-violet light source (Xe flash lamp) induces the photocurrent. Figure 16.2 shows an example

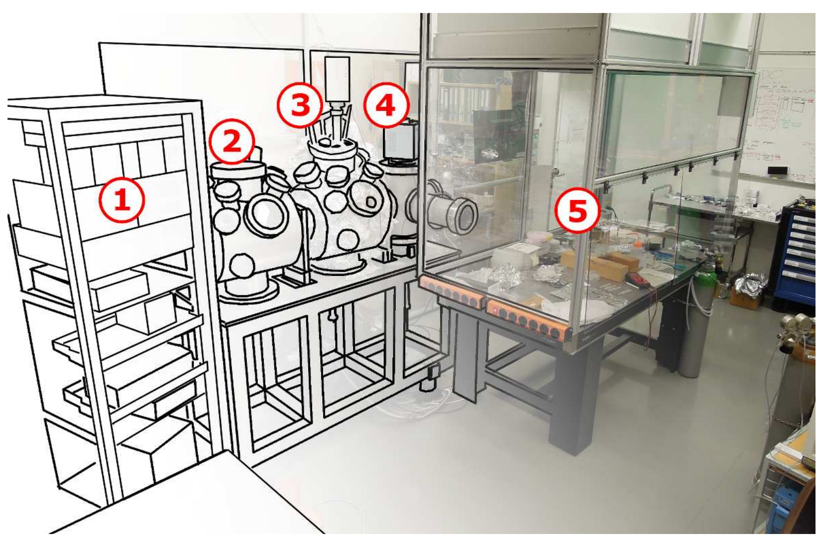

FIG. 16.1 – Schematic view of the laboratory equipment. (1) Electronics rack; (2) analysis chamber; (3) preparation chamber with mass spectrometer; (4) fast entry lock with O_2 plasma cleaner and newly developed four-inch Ar^+ ion sputtering capability; (5) laminar flow box with access to entry lock and optical table with in air experimental set-up. The complete apparatus is located in a clean room which complies with ISO 7 clean room class requirements.

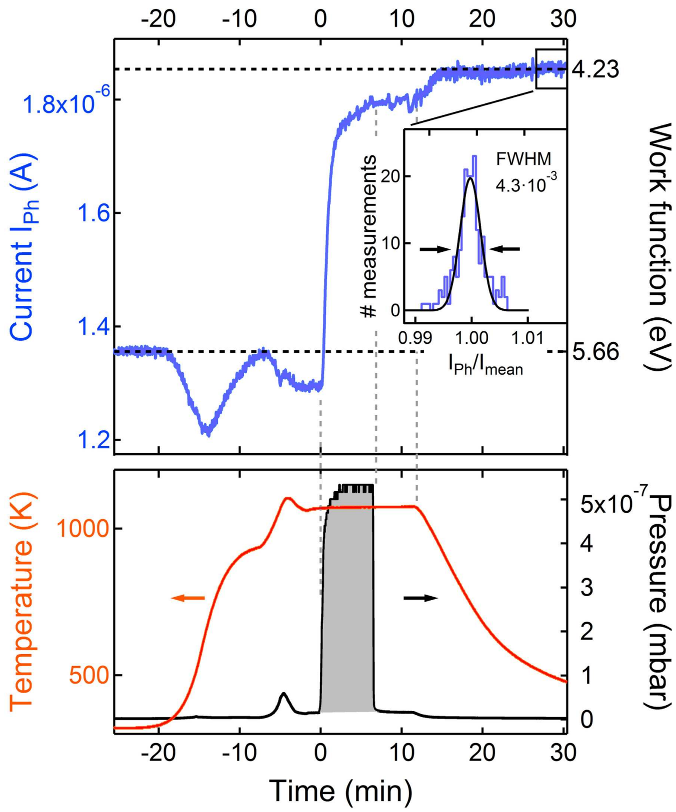

FIG. 16.2 –
The time-evolution of chemical vapor deposition of a hexagonal boron nitride monolayer on a Rh(111) film.
Upper part: photocurrent (I_{Ph}) as recorded by a collector electrode (solid blue) and the work functions (dashed black) as determined by normal emission UPS measurements before and after this preparation. The inset demonstrates the stability of the current in the indicated box.
Lower part: temperature and pressure observed during the process; the shaded area under the pressure curve corresponds to the dosing of the reaction precursor molecule borazine.

of its capability to observe the growth of a single hexagonal boron nitride layer. The method may be used in pressures up to 1 mbar and is thus perfectly suited for the monitoring of heterostructure growth where significantly higher precursor pressures are required [6].

[1] M. Corso, *et al.*, Science 303, 217 (2004).
[2] S. Berner, *et al.*, Angew. Chem. Int. Ed. 46, 5115 (2007).
[3] S. Gsell, *et al.*, J. Cryst. Growth 311, 3731 (2009).
[4] A. Hemmi, *et al.*, Rev. Sci. Instrum. 85, 035101 (2014).
[5] A. Hemmi *et al.*,
J. Vac. Sci. Technol. A 32, 23202 (2014).
[6] S. Roth *et al.*, Nano Letters 13, 2668 (2013).

16.2 Endofullerene nanomagnets

in collaboration with: Alexey Popov, IFW Dresden; Cinthia Piamonteze, Jan Dreiser, and Matthias Muntwiler, Paul Scherrer Institut, Villigen.

The hollow interior of the fullerene carbon cage can be used to encapsulate magnetic clusters that are not found as free species in nature. A fascinating example is the dysprosium-scandium based endofullerenes $Dy_nSc_{3-n}N@C_{80}$ ($n = 1,2,3$), where the endohedral unit combines diamagnetic Sc^{3+} and/or paramagnetic Dy^{3+} species at the corners of a triangle with a central N^{3-} ion (Fig. 16.3). Electrostatic interactions with the surrounding ligands, in particular with the central N^{3-} ion, splits the $2J+1$ degenerate ground state into states separated by an energy barrier that prevents a spontaneous reversal of the magnetization. Moreover, the interactions result in a strong axial anisotropy which restricts the individual magnetic moments to orient themselves parallel, or antiparallel, to their magnetic easy axis which is directed along the Dy_n-N bond [1].

At low temperatures, these endofullerenes exhibit a slow relaxation of the magnetization and belong to a class of compounds called single-molecule magnets (SMMs) [2]. They can exhibit magnetic hysteresis similar to traditional macroscopic magnets as well as quantum properties characteristic of a nanoscale entity. Depending on the number of encapsulated Dy ions (n), the endofullerenes exhibit distinct ground state properties like quantum tunneling of magnetization ($n = 1$), remanence ($n = 2$), or frustration ($n = 3$) [1]. The decisive influence of the number of magnetic moments and their interactions is observed in the three significantly different hysteresis curves (Fig. 16.4).

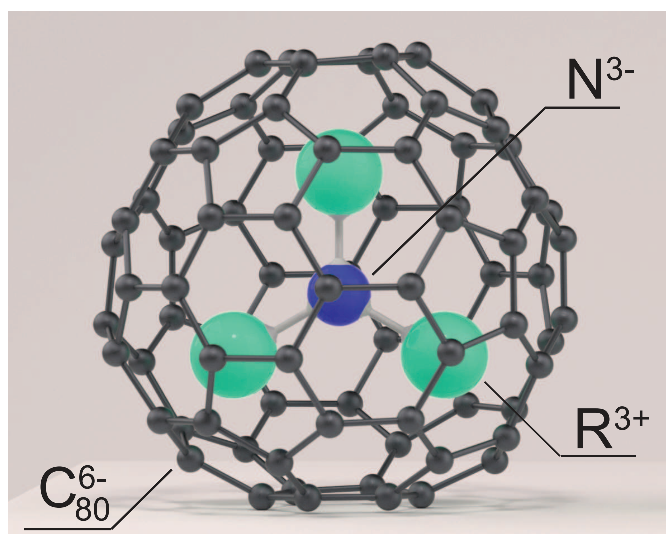

FIG. 16.3 – Model of the nitride cluster fullerene $R_3N@C_{80}$; R = rare earth (here Dy^{3+} or Sc^{3+}).

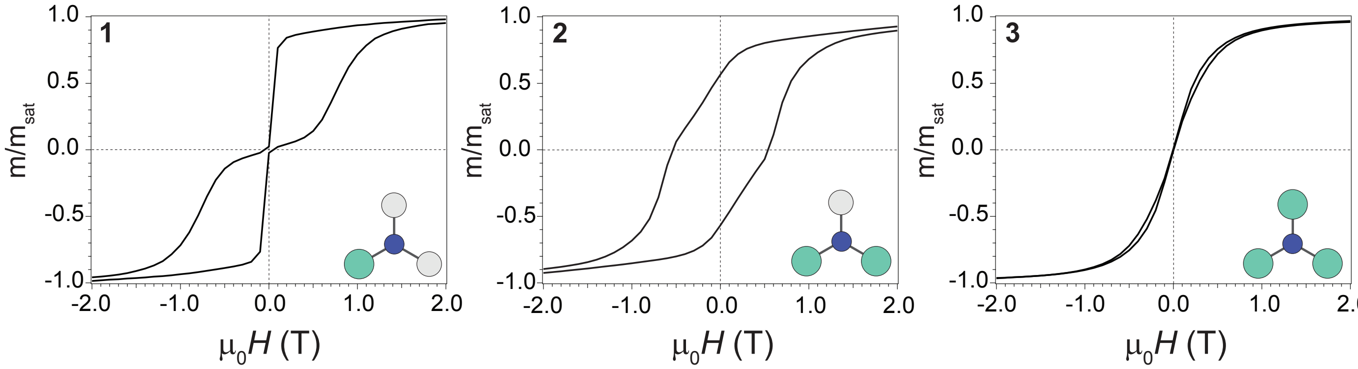

FIG. 16.4 –
Magnetic hysteresis curves recorded from bulk samples of $Dy_nSc_{3-n}N@C_{80}$ ($n = 1, 2, 3$) using a SQUID magnetometer at 2 K. The cluster compositions are shown as insets with Dy = cyan, N = blue, and Sc = grey. From Ref. [1]

The single-ion dysprosium compound ($n = 1$) was the first endofullerene to exhibit magnetic bi-stability [3]. At low temperatures a butterfly-shaped hysteresis curve is observed with an abrupt drop of the magnetization close to zero-field (Fig. 16.4, left panel). This rapid decay is a consequence of quantum tunneling of the magnetization (QTM) where the magnetic moments are short-cutting the energy barrier separating states of opposite magnetization. When adding a second magnetic moment to the cluster ($n = 2$), the intra-molecular interactions lead to an exchange and dipole barrier which suppresses QTM. This results in a significant remnant magnetization (Fig. 16.4, center panel) with a relaxation time of about 1 h at 2 K. Adding a third magnetic moment to the C_{80} cage produces a ferromagnetically coupled frustrated system, which makes the tri-dysprosium compound ($n = 3$) the softest magnet in the series (Fig. 16.4, right panel).

[1] R. Westerström *et al.*, Phys. Rev. B 89, 060406(R) (2014).

[2] D. Gatteschi, R. Sessoli, *Molecular Nanomagnets*,Oxford University Press, New York, 2006.

[3] R. Westerström *et al.*, J. Am. Chem. Soc. 134, 9840 (2012).

16.3 Photoemission delays from attosecond interferometry

in collaboration with: Matteo Lucchini, Reto Locher, Lukas Gallmann and Ursula Keller (attoline project), Physics Department, ETH Zurich; NCCR MUST.

Whereas the energetics of the photoelectric effect are well understood and have been studied in great detail, much less is known about its temporal characteristics. Such electronic processes occur on an attosecond (1 as $= 10^{-18}$ s) timescale due to the characteristic electron velocities and length scales. Recent progress in ultrafast spectroscopy [1] enabled us to study the dynamics of electrons directly in the time domain. Pioneering experiments in gas phase [2, 3] and condensed matter [4] revealed small relative delays between electrons emitted from different initial states.

Reconstruction of attosecond beating by interference of two-photon transitions (RABBITT) [5] was used in gas phase experiments to determine atomic photoemission delays [3]. The extension of RABBITT to noble metal surfaces allowed us to extract energy-dependent photoemission delays from interferometric pump-probe experiments using a short attosecond pulse train in the XUV as pump pulse and a few cycle IR probe pulse [6]. In RABBITT, the absorption of an XUV photon with a specific energy is followed by either absorption or stimulated emission of an IR photon. As shown in Fig. 16.5 this two-photon process gives rise to the appearance of sidebands in the temporal overlap of the XUV and IR pulse. Quantum path interference leads to a beating pattern that entails the spectral photoemission phase.

Our specific experimental setup allows for simultaneous recording of RABBITT traces in a gas and a solid target [7]. The use of photoemission of argon as a temporal reference allowed us to extract absolute photoemission delays from the investigated noble metal surfaces Ag(111) and Au(111) that are depicted in Fig. 16.6 together with the results of our simulations.

The strong variation of the observed delays with energy and in particular the negative delays cannot be reproduced by our simulations that take dipole-transition phase shifts and electron transport to the surface into account. Resonant bulk transitions and many-body effects like screening are likely to contribute significantly to the observed delay times but the theoretical understanding and computation of these effects on attosecond timescales is still in its infancy [8].

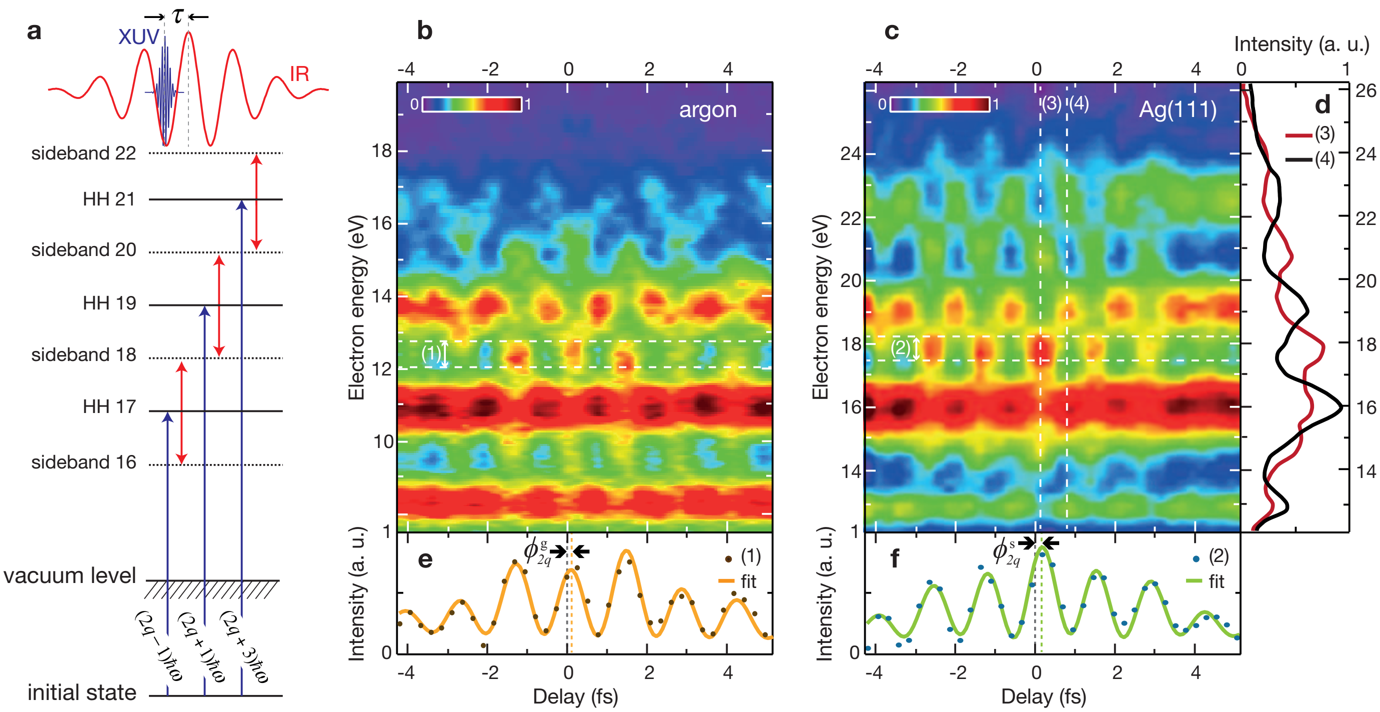

Fig. 16.5 – Experimental RABBITT traces in an Ar gas target and on Ag(111).
(a) Energy level scheme of the RABBITT process. Interfering two-colour two-photon transitions give rise to sidebands between adjacent odd high harmonics (HH).

(b, c) RABBITT traces from Ar and Ag(111) with electrons originating from Ar $3p$ and Ag $4d$ levels, respectively.
(d) Photoelectron spectra from (c) at two different time delays.
(e, f) Integration over the energy range of sideband 18 revealing the oscillation with 2ω. Experimental curves were fitted with $A(t)\cos(2\omega t - \phi_{2q})$ where ϕ_{2q} is the spectral phase and A(t) is the pulse envelope function.

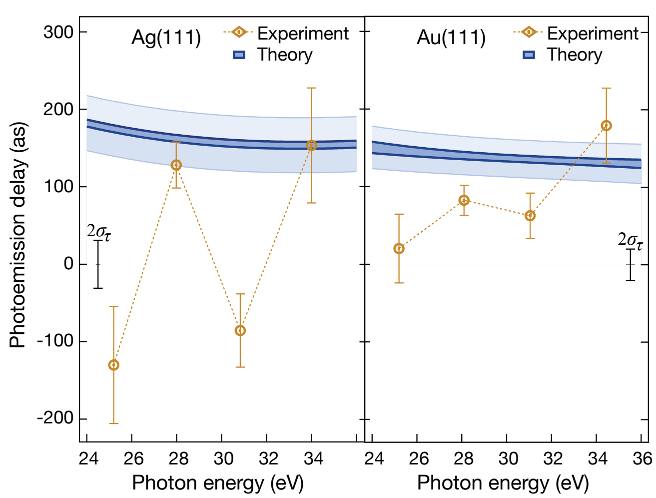

Fig. 16.6 – Photoemission delays for emission from the Ag(111) $4d$-band and Au(111) $5d$-band. The measured data are compared with results of our simulations.
The $(2\sigma_\tau)$ error bars shown at 0 as indicate the experimental resolution of the propagation delay, τ_{prop}, that results in an uncertainty in the absolute delay scale.
The boundaries of the dark blue band indicate the cases with and without screening (upper and lower black lines, respectively). The light-blue shaded band includes σ_τ.

In summary, we built up a new experiment in collaboration with the attoline project at ETHZ, which allows to study light-matter interaction at the fastest possible timescale and sheds new light on the mechanism of the photoelectric effect. Further measurements varying the experimental geometry and electron momenta, as well as investigating more complex samples, are in progress.

[1] M. Hentschel *et al.*, Nature 414, 509 (2001).
[2] M. Schultze *et al.*, Science 328, 1658 (2010).
[3] K. Klünder *et al.*, Phys. Rev. Lett. 106, 143002 (2011).
[4] A. Cavalieri *et al.*, Nature 449, 1029 (2001).
[5] P. M. Paul *et al.*, Science 292, 1689 (2001).
[6] R. Locher, L. Castiglioni *et al.*, submitted for publication (2014); arXiv: 1403.5449 [cond-mat].
[7] R. Locher *et al.*, Rev. Sci. Instr. 85, 013113 (2014).
[8] R. D. Muino *et al.*, Proceedings of the National Academy of Sciences 108, 971 (2011).

17 Physics of Biological Systems

Conrad Escher, Hans-Werner Fink, Tatiana Latychevskaia, Jean-Nicolas Longchamp, Marianna Lorenzo, Mirna Saliba (until November 2013), Jonas Verges, Flavio Wicki

in collaboration with: Eugen Ermantraut, Clondiag Chip Technologies GmbH (Germany); Prof. Jannik C. Meyer, University of Vienna (Austria); Prof. Ute Kaiser, University of Ulm (Germany); Prof. Klaus Kern, Max Planck Institut, Stuttgart (Germany); Dr. Ilona Müllerová and Dr. Luděk Frank, Institute of Scientific Instruments, Brno (Czech Republic); Dr. Fabio Lamattina, EMPA Dübendorf (Switzerland)

The structural investigation of individual biological objects by employing coherent low-energy electrons is the primary goal of our research. It involves inline holography with low-energy electrons as well as coherent diffraction imaging and is assisted by micro-structuring techniques using a focused gallium ion beam device as well as a focused helium ion beam available to us at the at the Swiss Federal Laboratories for materials science and technology (EMPA) in Dübendorf. Our current activities are divided in the following interconnected individual projects listed below.

- Electron Holography and Coherent Diffraction
  Major experimental challenges are to improve the interference resolution, establish methods for creating free-standing thin films of graphene transparent for low-energy electrons as well as appropriate techniques to present a single protein to the coherent electron wave. Next to these experimental issues, a second, equally important aspect for achieving high-resolution structural information is the reconstruction of the electron holograms respectively iterative phase retrieval in coherent diffraction. This is achieved by employing newly developed numerical algorithms to solve the integrals governing these coherent optics problems.

- Coherent Diffraction Imaging of Graphene-Supported Single Biomolecules at Atomic Resolution (Ambizione project of Jean-Nicolas Longchamp)
  Methods to deposit biomolecules onto freestanding graphene, in particular in-situ electrospray deposition are to be explored. The successful deposition and imaging of test biomolecules shall be cross-validated by TEM investigations carried out at the microscopy centre of the University of Zurich. Moreover, the possibility to use other two-dimensional materials, as for instance boron nitride, as substrate for low-energy electron microscopy shall also be investigated. Additionally, with the availability of ultra-clean graphene, low-energy electron holographic imaging of the electron transport in freestanding graphene and in particular scattering processes of conduction electrons at grain boundaries or atomic defect shall be explored.

- Electron and Ion Point Sources
  Field Ion Microscopy and related techniques are employed for fabricating and applying bright electron and ion point sources.

- DNA and Proteins in the Liquid Phase
  The aim of this project is to directly observe the dynamics of single DNA molecules in liquids by video fluorescent microscopy. In combination with molecular anchoring techniques, adopted from Clondiag Chip Technologies in Jena, we also address the energetics of a single DNA molecule. Appropriate DNA modifications for attaching fluorescent proteins are also designed by and shall serve us in our efforts to obtain structural information about proteins by electron holography and coherent diffraction. Thermal desorption spectroscopy of water from fluorescent proteins shall help us to judge under what thermal conditions proteins are still in their native state despite the vacuum environment.

Selected recent achievements referring to the past year shall be discussed in some more detail below.

17.1 Overall Motivation and Research Goals

Most of the protein structural information available today has been obtained from crystallography experiments by means of averaging over many molecules assembled into a crystal. Since biological molecules exhibit different conformations, averaging smears out structural details. That is why a strong desire to gain structural data from just a single molecule is emerging. We are working towards the objective of deriving atomic structure information from experiments carried out on just one individual molecule subject to the interaction with a coherent low-energy electron wave. Meanwhile, it has been thoroughly established that electrons with kinetic energies below 200 eV are the only radiation known today where elastic scattering dominates. Radiation damage-free imaging of a single biological molecule is thus possible by recording holograms and coherent low-energy electron diffraction patterns [1, 2]. So far, we were able to achieve a resolution of 2 Angstroms in imaging a free-standing graphene which appears sufficient to eventually obtain detailed structural information about a single protein.

17.2 Resolution enhancement in digital holography by extrapolation of holograms

It is generally believed that the resolution in digital holography is limited by the size of the captured holographic record. We have developed a method to circumvent this limit by extrapolating experimental holograms beyond the area that is actually captured. This is done by first padding the surroundings of the hologram and then conducting an iterative reconstruction procedure. The wave front beyond the experimentally detected area is thus retrieved and the hologram reconstruction shows enhanced resolution. To demonstrate the power of this concept, we apply it to simulated as well as experimental holograms.

Intrinsic to the principle of holography is that even a fraction of a hologram permits the reconstruction of the entire object [3]. However, in digital holography the overall achievable resolution in the reconstruction is believed to be limited by the size of the captured digital record [4, 5]:

$$R = \frac{\lambda z}{N \Delta_S} \qquad (17.1)$$

where λ is the wavelength, z is the distance between object and screen, N is the number of pixels, and Δ_S is the pixel size of the detector. $N\Delta_S \times N\Delta_S$ is thus the size of the hologram and hence the limiting aperture of the optical system. Therefore, in the case of digitally recorded holograms, the detector size appears to limit the achievable resolution. We make use of the basic notion that the interference distribution recorded in a hologram is created by waves that are continuous and must persist beyond the experimentally recorded area. Consequently, it must be possible to extrapolate a truncated hologram beyond the intensity distribution actually recorded in an experiment. Extrapolation of holograms can be achieved by applying an iterative routine using a constraint based on the physical notion that the amplitude of the elastic scattered object wave must not be larger than the amplitude of the incoming wave [6]. After several iterations, the outer part of the hologram, which was initially not available from the experimental record, is retrieved. The availability of these emerging higher-order fringes in such extrapolated holograms leads to an improved resolution in the object reconstruction.

17.2.1 Simulated example

To demonstrate our method we first use the simulated hologram of two point scatterers, as illustrated in Fig. 17.1. The object area is $2{\times}2$ mm^2, sampled with $2000{\times}2000$ pixels, and the scatterers are separated by six pixels. The hologram is simulated for 500 nm laser light in the inline holographic setup [6, 7], where the distance between the point source and the sample amounts to 4 mm and the distance between the point source and the hologram is 1 m; a screen size of $0.5{\times}0.5$ m^2 is used in the simulation. The resultant simulated hologram is shown in Fig. 17.1(b). According to Eq. 17.1, the resolution intrinsic to this simulated hologram amounts to 1 μm

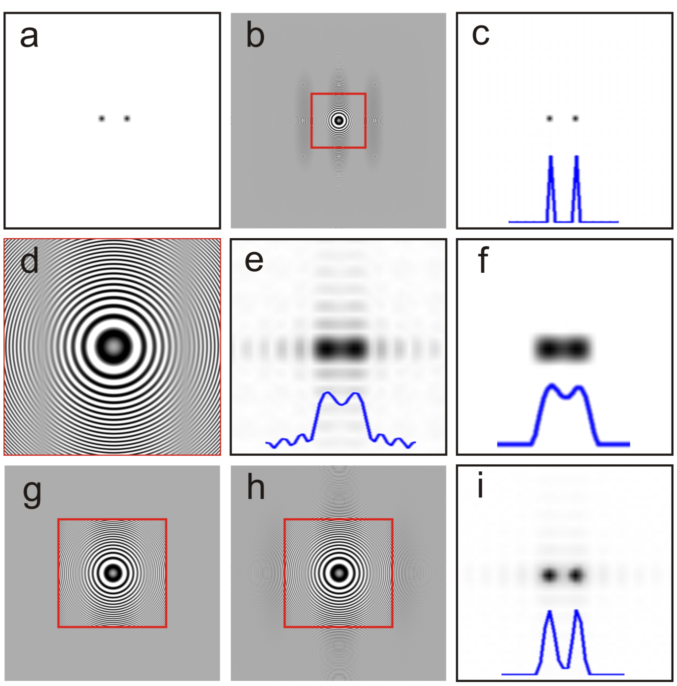

Fig. 17.1 – Simulated example.
(a) Synthetic object, consisting of two point scatterers, separated by six pixels; the central $50{\times}50$ pixels region is shown.
(b) Simulated hologram, $2000{\times}2000$ pixels in size.
(c) Hologram reconstruction, showing the central $50{\times}50$ pixels region.
(d) Selected $500{\times}500$ pixels central region of the original hologram, as marked in (b) by a red square.
(e) Reconstruction of (d). (f) Result of iterative reconstruction of (d) after 300 iterations.
(g) The selected $500{\times}500$ pixels region is padded to $1000{\times}1000$ pixels with a constant background.
(h) Extrapolated hologram after 300 iterations.
(i) Reconstruction of the extrapolated hologram; the central $50{\times}50$ pixels region is shown.
The blue curves in (c), (e), (f), and (i) show the intensity profiles of the reconstructions.

and leads to a perfectly resolved reconstruction of the two points separated by 6 μm, as shown in Fig. 17.1(c). To mimic a hologram limited by detector size, the central 500×500 pixels region of the simulated hologram is cut out as displayed in Fig. 17.1(d). The resolution intrinsic to this truncated hologram amounts to 4 μm, as derived from Eq. 17.1. Accordingly, the reconstruction of this truncated hologram results in two smeared-out regions rather than separated points that are barely resolved, as evident from Fig. 17.1(e). Next, the truncated hologram is iteratively reconstructed [6–8] in the following manner. First, the surroundings of the hologram are filled with a constant background, leading to a padded record of 1000×1000 pixels, as shown in Fig. 17.1(g). For the first iteration, the phase distribution in the hologram plane is given by the phase distribution of the reference wave. During the iterative reconstruction the following constraints are applied. First, in the hologram plane, the amplitude of the central 500×500 pixels region is replaced by the already known data and the values of the outer pixels are updated after each iteration. Second, in the object plane, the object is confined within a limited region by applying an oval mask; the signal outside the mask is set to zero and then a positive absorption filter is applied [6]. After 300 iterations, not only does the holographic image extrapolate itself beyond the 500×500 region, as evident from Fig. 17.1(h), but also the reconstruction of such a extrapolated hologram reveals that the two points are now clearly resolved, as can be seen in Fig. 17.1(i). A theoretical resolution of 2 μm estimated by Eq. 17.1 is observed in the reconstruction. To verify that the effect of the resolution enhancement is not due to the iterative retrieval itself, we also applied the same iterative reconstruction to the non-padded 500×500 pixels truncated hologram. Its reconstruction after 300 iterations, shown in Fig. 17.1(f), does not differ much from the reconstruction shown in Fig. 17.1(e). While the twin image is suppressed, the two points remain barely resolved. The reason is that when there is a larger area available in the hologram plane, the series of wavelets constituting the wavefront in the hologram plane can be fitted better. This hypothesis is confirmed by a closer look at the intensity distributions in the hologram plane. During the iterative procedure the intensity distribution in the hologram is replaced by an "experimental" distribution after each iteration and thus iteratively approaches the "experimental" distribution. The mismatch between the "experimental" amplitude distribution and the amplitude distribution updated after each iteration is quantitatively described by the error function. Fig. 17.2 shows the intensity profiles in the hologram plane: even after 300 iterations the 500×500 pixels truncated hologram does not match the intensity distribution of the original hologram. But the intensity profile of the extrapolated 1000×1000 pixels hologram obtained after

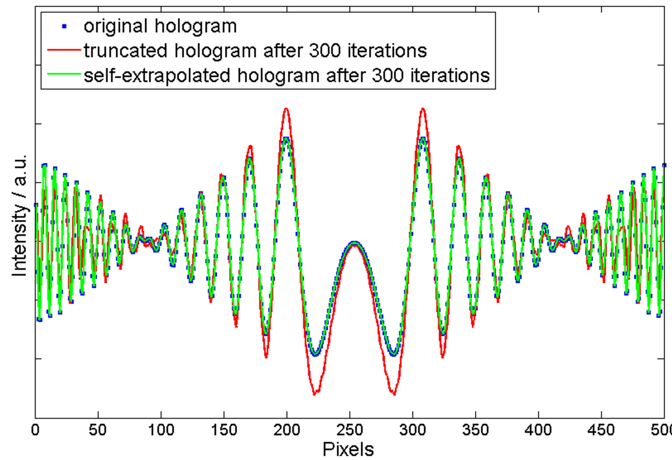

FIG. 17.2 – Profiles of the intensity in the central region of the holograms: original hologram (blue dots), 500×500 pixels truncated hologram after 300 iterations (red line), and 1000×1000 extrapolated hologram after 300 iterations.

300 iterations matches the original distribution perfectly. Thus, when a larger area in the hologram plane where the intensities can be varied is available, a better agreement between the "experimental" and the fitted hologram can be achieved. Although the numerical experiments clearly show that the resolution can be enhanced by extrapolation of the hologram, the enhancement cannot be extended to infinity. We also tried padding from 500×500 pixels to the original value of 2000×2000 pixels, but this only marginally improves the resolution when compared to the resolution obtained by padding only up to 1000×1000 pixels.

17.2.2 Experimental example

We also performed experimental tests of our method using an optical hologram recorded in an inline scheme shown in Fig. 17.3. The optical hologram was recorded using 523 nm laser light; the sample was placed 0.25 mm in front of the divergent source, the distance between source and screen was 75 mm, the size of the hologram was 35×35 mm^2, and it was sampled with 1000×1000 pixels. The sample consisting of four circles with diame-

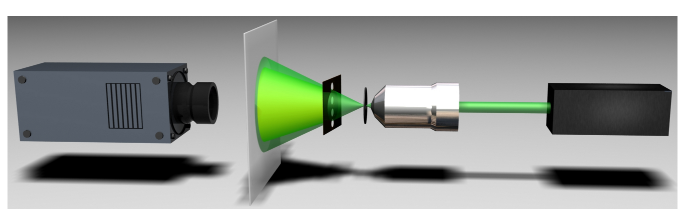

FIG. 17.3 –
Experimental scheme for recording optical inline holograms

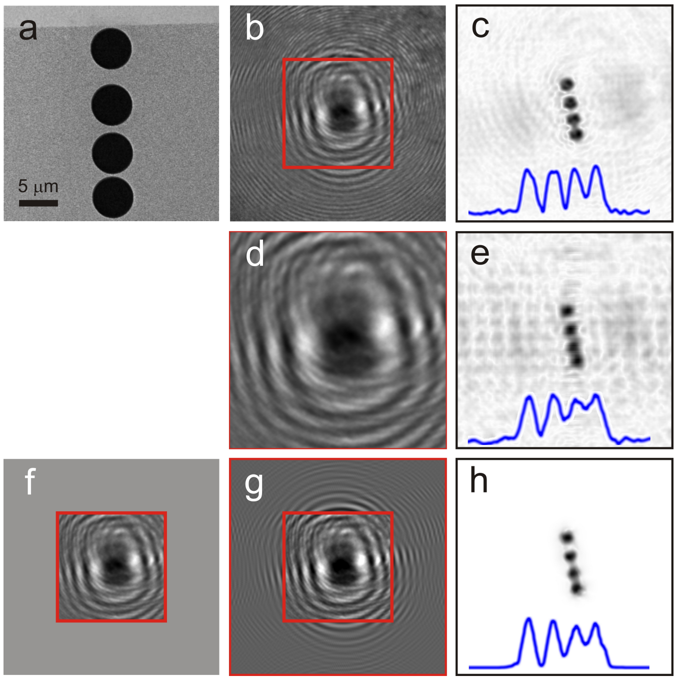

FIG. 17.4 – Experimental verification of the method.
(a) Scanning electron microscope image of the sample.
(b) 1000×1000 pixels experimental optical hologram of the sample and
(c) its reconstruction; the 500×500 pixels central part is shown.
(d) Selected 500×500 pixels central region of the experimental hologram, and
(e) its reconstruction.
(f) The 500×500 pixels hologram padded to 1000×1000 pixels.
(g) The 1000×1000 pixels extrapolated hologram after 100 iterations.
(h) Reconstruction of the extrapolated hologram.
The 500×500 pixels central part is shown. The blue curves in (c), (e) and (h) show the intensity profiles of the reconstructions.

ters of 5 μm each was created by focused ion beam milling in a silicon nitride membrane covered with a 200 nm platinum layer and is shown in Fig. 17.4(a). The experimental hologram is shown in Fig. 17.4(b) and its reconstruction is displayed in Fig. 17.4(c).

When the central region of the hologram corresponding to 500×500 pixels is cut out (Fig. 17.4(d)), the reconstruction of this truncated hologram results in a blurred image of the four circles, shown Fig. 17.4(e). Next, the truncated hologram is padded up to 1000×1000 pixels, as shown in Fig. 17.2(f), and iteratively reconstructed as described above. After every five iterations the reconstructed amplitude was convolved with a 3×3 pixels kernel in the form of a Gaussian distribution to smooth and suppress the accumulation of noisy peaks. After 100 iterations, higher order fringes emerge (see Fig. 17.4(g)), and the reconstruction of the extrapolated hologram exhibits better resolved circles, shown in Fig. 17.4(h).

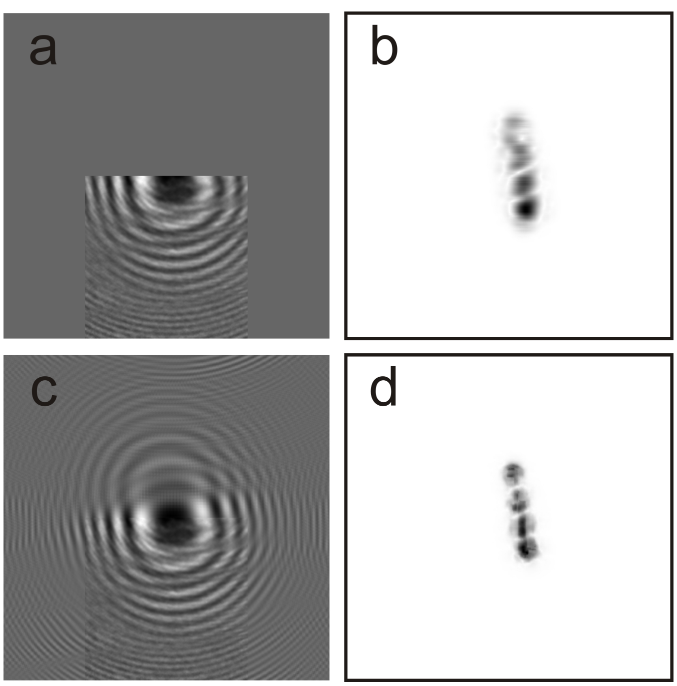

FIG. 17.5 – Extrapolation of a piece of the hologram.
(a) The selected 500×500 pixels part of the hologram is padded up to 1000×1000 pixels; and
(b) its reconstruction; the 500×500 pixels central part is shown.
(c) 1000×1000 pixels extrapolated hologram after 300 iterations and
(d) its reconstruction; the 500×500 pixels central part is shown.

It is also possible to extrapolate a hologram when a significant low-resolution part is missing. To demonstrate it, we cropped the 500×500 pixels lower part of the experimental hologram and padded it up to 1000×1000 pixels (see Fig. 17.5(a)). The corresponding reconstruction presented in Fig. 17.5(b) does not show all four circles. Next, we applied the iterative extrapolation routine; after 300 iterations the hologram had extrapolated itself (see Fig. 17.5(c)), and the reconstruction clearly shows four circles (see Fig. 17.5(d)). Aside from the intensity variations within the reconstructed circles the agreement with the original object is good. The variations in artifact intensity indicate the limits of the method; thus it is better to use the experimentally recorded holographic information when available.

In conclusion, the method presented above improves the resolution of holographic reconstructions by extrapolation of the digital hologram beyond the actual detector size. The method can be applied provided the following conditions are fulfilled:

- The interference pattern is only limited by the size of the detector; in other words, there is an interference pattern at the edges of the hologram.
- The object under study occupies a limited area and thus can be masked in the iterative reconstruction.
- The object has a finite thickness in the z-dimension, which allows an iterative retrieval by field propagation between two planes: the hologram and object planes.
- The available part of the hologram exhibits high dynamics in the intensity distribution. The latter requirement can be explained in terms of the resolution provided by the smallest scatterers whose scattered wave signal is present over the entire hologram area and needs to be detected in the available piece of the hologram. This high-resolution information eventually allows hologram extrapolation and retrieval of the entire object at enhanced resolution.

17.3 Low-energy electron holographic imaging of gold nanorods supported by ultraclean graphene

An ideal support for electron microscopy shall be as thin as possible and interact as little as possible with the primary electrons. Since graphene is atomically thin and made up of carbon atoms arranged in a honeycomb lattice, the potential to use graphene as substrate in electron microscopy is enormous. Until now graphene has hardly ever been used for this purpose because the cleanliness of freestanding graphene before or after deposition of the objects of interest was insufficient. We demonstrate here by means of low-energy electron holographic imaging that freestanding graphene prepared with the platinum-metal catalysis method remains ultraclean even after re-exposure to ambient conditions and deposition of gold nanorods from the liquid phase. In the holographic reconstruction of the gold particles the organic shell surrounding the objects is apparent while it is not detectable in SEM images of the very same sample, demonstrating the tremendous potential of low-energy electron holography for the imaging of graphene-supported single biomolecules.

To be imaged by means of electron microscopy, an object is normally placed onto a substrate. The signal from the object support, arising from the scattering of the impinging primary electrons in transmission electron microscopy, or from the creation of secondary electrons in a scanning electron microscope, is spurious and efforts to reduce these signals have been accomplished since the development and implementation of the first electron microscopes. Ideally, for maximal contrast and resolution, one would like to have the thinnest substrate possible, made up of a low-atomic-number material, in order to reduce the interaction volume and the scattering cross-section of the incoming electrons [9, 10]. The idea of using freestanding single-layer graphene as such ultimate microscopic sample carrier in electron microscopy [11–17] has been around since the isolation of single-layer graphene was achieved in 2004 by Geim and Novoselov [18, 19]. Significant efforts have been undertaken in the past few years to develop techniques for preparing either exfoliated or CVD grown graphene in a freestanding form [17, 20–23]. Unfortunately, the cleanliness of the prepared graphene sheets has never been satisfactory with regards to their use as sample carrier [17, 22, 24, 25]. Only recently, it has become possible to prepare ultraclean freestanding graphene by platinum-metal catalysis [26]. Compared to previous methods, the one applied here leads to large regions, extending up to several square microns of atomically clean freestanding graphene suitable for use in electron microscopy [2, 26, 27]. We were able to show that freestanding graphene prepared by the platinum-metal catalysis method remains clean, even after re-exposure to ambient pressure and subsequent wet deposition of nanometre-sized gold rods. We present low-energy electron holograms of gold nanorods on graphene and cross-validate the presence of the nanorods by scanning electron imaging of the very same sample. Moreover, we compare the appearance of the rods when either imaged with low-energy electron holography or by means of a scanning electron microscope (SEM).

Fig. 17.6 –
(a) The setup for low-energy electron holography. The source-sample distance is 100 – 1000 nm which leads to electron energies of 50 – 250 eV. The distance between sample and detector is 68 mm. The detector diameter is 75 mm, which represents an acceptance angle of 29°.
(b) SEM image of an electrochemically etched W(111) tip acting as field-emitter of a divergent coherent low-energy electron beam.
(c) A gold nanorod lying on ultraclean freestanding graphene suspended over a round hole.

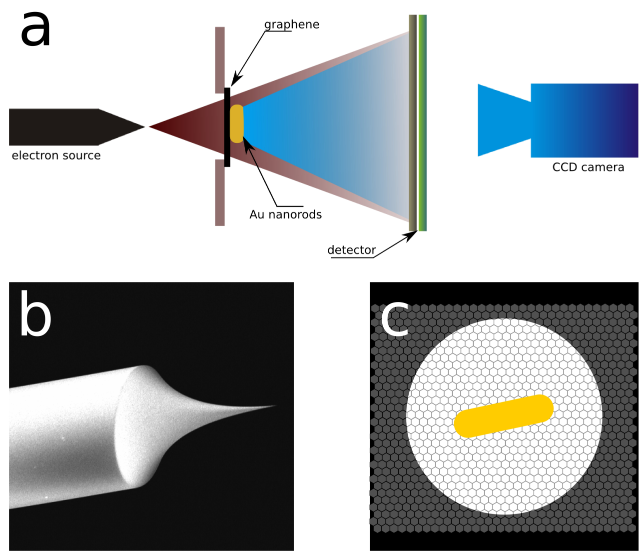

17.3.1 Materials and Methods

Ultraclean freestanding graphene, covering holes of 500 nm in diameter milled in a silicon nitride membrane, is prepared by the platinum-metal catalysis method [26]. The cleanliness of the as-prepared graphene is then inspected in a low-energy electron point source microscope operated under UHV conditions (Fig. 17.6). In this holographic setup, inspired by Gabor's original idea of inline holography [3, 8, 28], a sharp (111)-oriented tungsten tip acts as source of a divergent beam of highly coherent electrons [29–32]. The electron emitter can be brought as close as 200 nm to the sample with the help of a 3-axis nanopositioner. Part of the electron wave impinging onto the sample is elastically scattered and represents the object wave, while the un-scattered part of the wave represents the reference wave [33]. At a distant detector, the interference pattern of the two waves – the hologram – is recorded. The magnification in the image is given by the ratio of detector-tip-distance to sample-tip-distance and is of the order of 10^6.

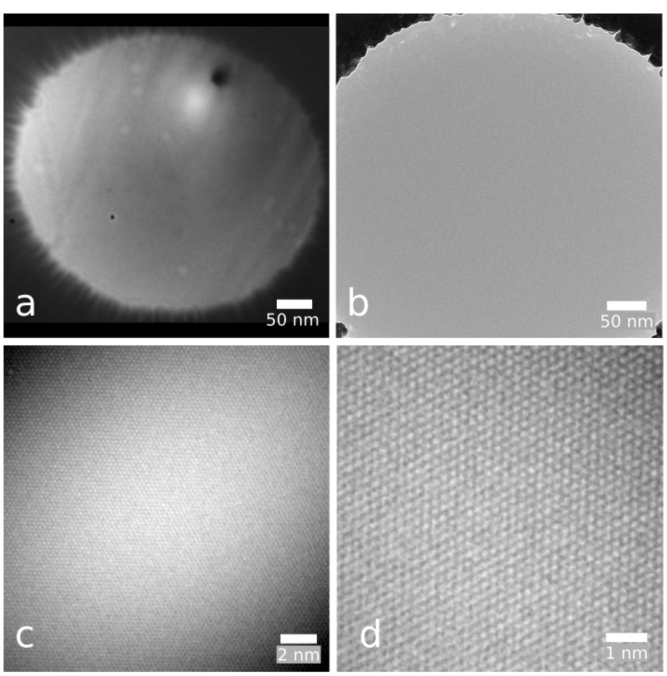

17.3.2 Results and Discussion

Fig. 17.7(a) shows an example of a hole of 500 nm in diameter covered by a single layer of ultraclean graphene, imaged by low-energy electrons. Only the observation of interference fringes, arising due to the presence of a few hydrocarbons less than 1 nm in size, reveals the existence of graphene covering the hole [26]. The cleanliness of the as-prepared graphene has also been investigated by means of high-resolution transmission electron microscopy (TEM) at 80 kV in order to give the reader the possibility to compare the quality of the cleanliness with former TEM results. Fig. 17.7(b) shows a TEM image of graphene, uniformly covering the entire freestanding region, and it is only by imaging the hexagonal atomic arrangement (Fig. 17.7(c)) that the presence of graphene can reliably be confirmed.

Fig. 17.7 –
(a) Low-energy (62 eV) electron transmission image of ultraclean freestanding graphene covering a hole of 500 nm in diameter milled in a silicon nitride membrane.
(b) 80 kV TEM imaging of ultraclean graphene covering a hole of 500 nm in diameter milled in a silicon nitride membrane.
(c) High-resolution TEM imaging of a 19x19 nm^2 region of ultraclean freestanding graphene, the unit cell arrangement is visible and the atomic cleanliness of the graphene is conserved over the whole freestanding area.
(d) High-resolution TEM imaging of a 8x8 nm^2 region of ultraclean freestanding graphene.
TEM data by courtesy of Gerardo Algara-Siller from the University of Ulm.

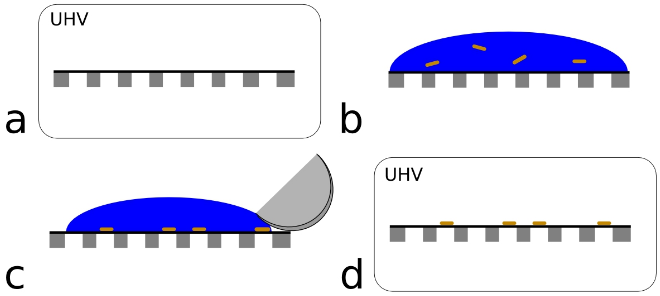

Fig. 17.8 –
(a) The cleanliness of the graphene sample carrier is first inspected by means of low-energy electron holography under UHV conditions.
(b) A drop of the solution containing gold nanorods is applied onto the substrate.
(c) After waiting a few seconds for the sedimentation of the gold nanorods onto the graphene, the excess water is removed with a filter paper.
(d) Before the re-insertion in the UHV low-energy electron microscope, the sample is re-heated to 200^{o}C for 30 min. The nanorods are now ready to be imaged by means of low-energy electron holography.

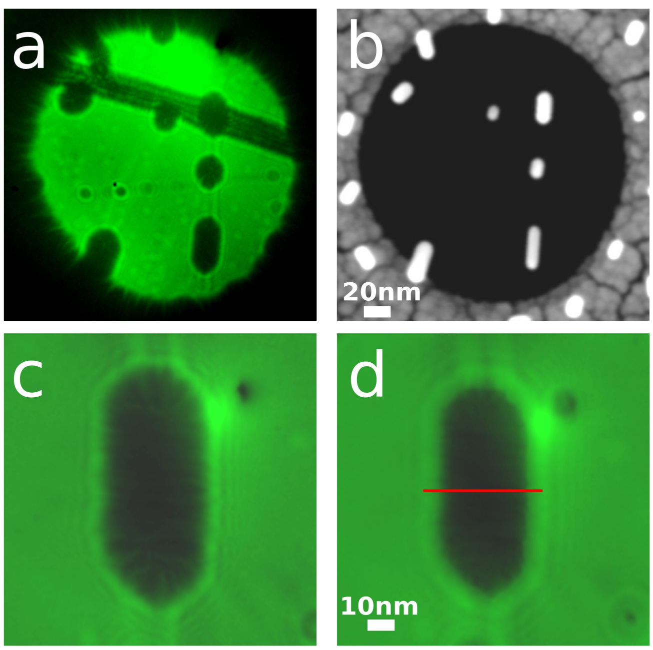

Fig. 17.9 –
(a) Low-energy electron hologram (93 eV) of gold nanorods lying on freestanding graphene. The graphene remained clean even after the deposition of the nanorods.
(b) SEM image (7 kV) of the very same sample presented in (a).
(c) High-magnification low-energy electron hologram (58 eV) of the nanorod on the lower right side presented in (a) and (b).
(d) The shape of the gold nanorod is reconstructed from the hologram in (c) at a source-sample distance of 182 nm. An intensity profile along the red line is displayed in Fig. 17.10.

For the deposition of gold nanorods, a graphene sample prepared as described above is taken out of the low-energy electron microscope. Under ambient conditions, a drop of a 0.5 nm gold nanorod aqueous solution [34] is subsequently applied onto the graphene (Fig. 17.8(b)). A few seconds were given for the rods to sediment before the excess water was removed with filter paper (Fig. 17.8(c)). Prior to the re-introduction of the sample into the electron microscope, the sample is kept at 200^{o}C for 30min.

Fig. 17.9(a) shows an electron hologram of gold nanorods on freestanding graphene recorded with 93 eV kinetic energy electrons. The graphene surrounding the rods remained clean even after the re-exposition to ambient pressure and the deposition of the gold particles from the liquid phase. In Fig. 17.9(b) a SEM image (7 kV) of the very same sample is presented. The nanorods can be associated one-to-one with the objects observed in the holographic image presented in Fig. 17.9(a). The yield of secondary electrons produced by the graphene substrate is so low that the rods, shown in Fig. 17.9(b), seem to levitate, demonstrating the utility of graphene as a substrate for scanning electron microscopy. A high-magnification hologram (58 eV) of a gold nanorod is presented in Fig. 17.9(c) along with its reconstruction, see Fig. 17.9(d), obtained as described in [5, 7]. The object presented in these two images is the very same gold nanorod observed in Fig. 17.9(a) in the low right corner. The remaining interference fringes that can be observed around the object in the reconstruction (Fig. 17.9(d)) are due to the presence of the out-of-focus twin image [6]. The size of the rod in Fig. 17.9(d) accounts for a width of 30 nm and a length of 72 nm. While the length in the holographic reconstruction image matches perfectly the length that can be measured in the SEM image, a discrepancy opens up when one compares the width measured in the two images (30 nm in the holographic reconstruction and 21 nm in the SEM image). We associate this discrepancy with the fact that the gold rods feature an organic coat in order to be soluble in aqueous solution [34]. This organic layer, however, is only present along the rods but not at the face sides. The several-nanometre thick methyl-shell cannot be imaged in an SEM because of the low contrast that it produces and because of the radiation damage provoked by the high-energy electrons. In low-energy electron holography the electron scattering cross-section depends only very weakly on the atomic number, therefore, the organic shell yields a substantial signal. Similarly, in Fig. 17.9(a) a graphene nanoribbon, most likely produced during the CVD growth process, can be detected by low-energy electron holography while it cannot be seen in the SEM image. In Fig. 17.9(d), a plateau at the upper part of the rod and a tip-like shape at the lower part are visible. These observations are in accordance with TEM observations on similar gold nanorods [35]. The terminations of the rods can adopt different configurations in order to reduce the surface free energy. The plateau shape corresponds to a termination with a 001 facet. The tip shape termination is probably due to a very small 001 terrace surrounded by extended 111 facets forming the conical shape of this termination [35, 36]. The geometrical details of the termination of the gold nanorods are accessible in low-energy electron holography imaging; the resolution of an SEM is insufficient to reveal them.

In Fig. 17.10, an intensity profile along the red line in Fig. 17.9(d) is displayed. The intensity oscillations that can be observed around the region corresponding to the nanorod are due to presence of the out-of focus twin image. In order to assign an upper limit for the resolution obtained in the reconstruction of the gold nanorod (Fig. 17.9(d), one may assume a sharp edge between the nanorod and the substrate. An estimate for the resolution is then given by the distance between 10 and 90% of the maximum intensity [37] measured at the edge and amounts to 1.8 nm. This estimation is rather conservative because of the presence of the organic shell around the gold nanorod. Certainly, this shell does not represent an ideal sharp edge but the slight transmission through the organic shell tends to underestimate the resolution power. A resolution of $1 - 1.5$ nanometres is probably a more realistic estimation for the resolution that can be obtained in our low-energy electron holography set-up.

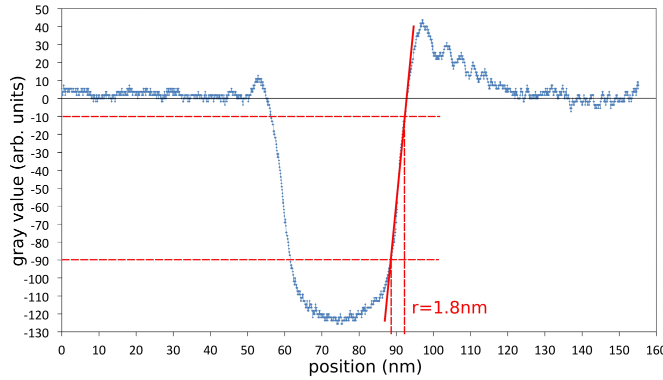

FIG. 17.10 – Intensity profile across the whole reconstructed area of a gold nanorod lying on graphene (Fig. 17.9(d), red line). The resolution in the image is estimated by applying a linear fit to the edge response and amounts to 1.8 nm.

[1] M. Germann *et al.*, Phys. Rev. Lett., (2010) 104(9) 095501.

[2] J.-N. Longchamp *et al.*, Phys. Rev. Lett., (2013) 110(25) 255501.

[3] D. Gabor, Nature, (1948) 161(4098) 777.

[4] U. Schnars and W. Jueptner, *Digital holography*, (2005) Springer.

[5] T. Latychevskaia, J.-N. Longchamp, and H.-W. Fink, Opt. Express, (2012) 20(27) 28871.

[6] T. Latychevskaia and H.-W. Fink, Phys. Rev. Lett., (2007) 98(23) 233901.

[7] T. Latychevskaia and H.-W. Fink, Opt. Express, (2009) 17(13) 10697.

[8] T. Latychevskaia *et al.*, Ultramicroscopy, (2010) 110(5) 472.

[9] L. Reimer, *Transmission electron microscopy*, (1989).

[10] W.H. Dobelle and M. Beer, J. Cell Biol., (1968) 39(3) 733.

[11] R.R. Nair *et al.*, Appl. Phys. Lett., (2010) 97(15) 153102.

[12] K.W. Urban, Nature Mater., (2011) 10(3) 165.

[13] J.Y. Mutus *et al.*, New J. Phys., (2011) 13 063011.

[14] J.C. Meyer *et al.*, Nature, (2007) 446(7131) 60.

[15] N.R. Wilson *et al.*, ACS Nano, (2009) 3(9) 2547.

[16] J.H. Warner *et al.*, ACS Nano, (2010) 4(1) 470.

[17] J.C. Meyer *et al.*, Nature, (2008) 454(7202) 319.

[18] K.S. Novoselov *et al.*, Science, (2004) 306(5696) 666.

[19] K.S. Novoselov *et al.*, Proc. Natl. Acad. Sci. USA, (2005) 102(30) 10451.

[20] Y. Lee *et al.*, Nano Lett., (2010) 10(2) 490.

[21] J.C. Meyer, J.C., *et al.*, Solid State Commun., (2007) 143(1-2) 101.

[22] Z.H. Ni *et al.*, J. Raman Spectrosc., (2010) 41(5) 479.

[23] R.S. Pantelic *et al.*, J. Struct. Biol., (2010) 170(1) 152.

[24] R.S. Pantelic *et al.*, Solid State Commun., (2012) 152(15) 1375.

[25] Y.C. Lin *et al.*, ACS Nano, (2011) 5(3) 2362.

[26] J.-N. Longchamp, C. Escher, and H.-W. Fink, J. Vac. Sci. Technol. B, (2013) 31 020605.

[27] J.-N. Longchamp *et al.*, Appl. Phys. Lett., (2012) 101(11) 113117.

[28] D. Gabor, Holography. Nobel Lecture, (1971).

[29] H.-W. Fink, W. Stocker, and H. Schmid, Phys. Rev. Lett., (1990) 65(10) 1204.

[30] H.-W. Fink, Ultramicroscopy, (1993) 50(1) 101.

[31] H.-W. Fink, IBM Journal of Research and Development, (1986) 30(5) 460.

[32] H.-W. Fink, W. Stocker, and H. Schmid, J. Vac. Sci. Technol., (1990) 8(6) 1323.

[33] H.J. Kreuzer *et al.*, (1992) 45(3-4) 381.

[34] J. Perez-Juste *et al.*, Coord. Chem. Rev., (2005) 249(17-18) 1870.

[35] Z.L. Wang *et al.*, Surf. Sci., (1999) 440(1-2) L809.

[36] H. Katz-Boon *et al.*, Ultramicroscopy, (2013) 124 61.

[37] S.W. Smith, The Scientist & Engineer's Guide to Digital Signal Processing, (1997) San Diego California, California Techical Pub.

18 Disordered and Biological Soft Matter

M. Ackermann (since August 2013), C.M. Aegerter, D. Assmann, D. Eder,
G. Ghielmetti, F. Lanfranconi, U. Nienhaus (till November 2013),
S. Puri (Master student) and T. Schluck (till December 2013)

in collaboration with: Institute of Molecular Life Sciences (K. Basler, T. Aegerter-Wilmsen, S. Luschnig, L. Pelkmans, D. Brunner), ETH Zürich (P. Koumoutsakos), MPI für Planzenforschung Köln (R.S. Smith), University of Fribourg (A. Jazwinska), University of Bern (C. Kulemeier, S. Robinson, P. Barbier de Reuille), Biozentrum Basel (M. Affolter), University of Strasbourg (N. Rivier), University of Konstanz (G. Maret, T. Sperling), New York University (C.C. Maass), Deutsches Luft- und Raumfahrtzentrum (M. Sperl), University of Twente (A. Mosk), Université Joseph Fourier Grenoble (S. Skipetrov, F. Graner), Technion Haifa (E. Akkermans).

In the group of disordered and biological soft-matter, we work on problems where disorder or non-equilibrium are important factors of the systems' physical properties. One aspect of this is biological matter, which is inherently out-of-equilibrium and typically has dynamic and soft elastic properties. In this context we study in particular the influence of mechanical forces on developmental biology, showing that environmental factors can lead to plasticity in development and thus have to be taken into account in the developmental control of an organism. In disordered media, we are investigating the effects of the wave nature of light on its transport in multiple scattering media, ranging from fundamental questions, such as the transition to Anderson localization in three dimensions, to the application in imaging techniques useful to study developmental processes in turbid tissues. Finally in non-equilibrium systems, we are studying the dynamics of granular gases and foams, in particular in the presence of levitation, such that effects due to gravity can be eliminated and the generic process can be studied. In the last year, we have made considerable progress in several of these areas, which are discussed in detail below. These subjects concern microscopy in turbid media, growth control via mechanical feedback, Anderson localization and the coarsening dynamics of levitated foams.

18.1 Microscopy in turbid media

Many biological tissues are turbid and thus not suitable for imaging techniques. While confocal imaging has lead to some improvements, several aspects of biological processes are not amenable to investigation via live imaging. We are in the process of developing a method based on the exploitation of multiple scattering for imaging

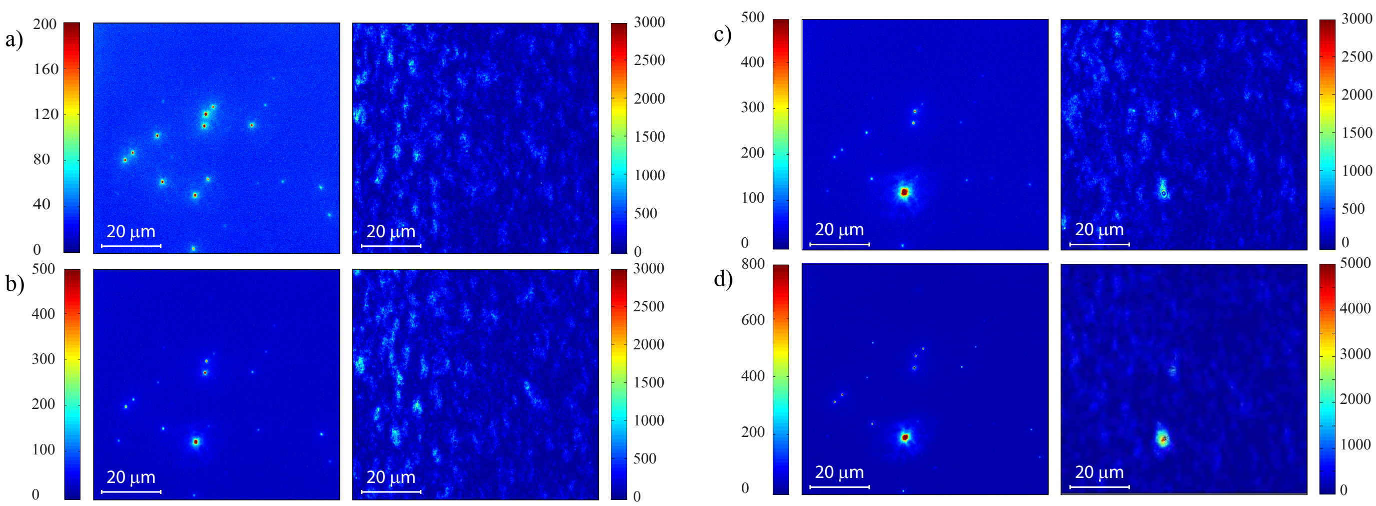

FIG. 18.1 – Illustration of the iterative scheme for finding a focus without optical access in the presence of several sources. The panels on the left show a direct view of the fluorescent sources (without turbid layer), whereas the panels on the right show the transmitted speckle pattern. Here a) is the situation before optimization and b) through d) after iterations with 7x7 (b), 14x14 (c) and 28x28 (d) segments, respectively. As can be seen, there is only a focus on a single fluorescent particle at the end, which can subsequently be scanned using the optical memory effect.

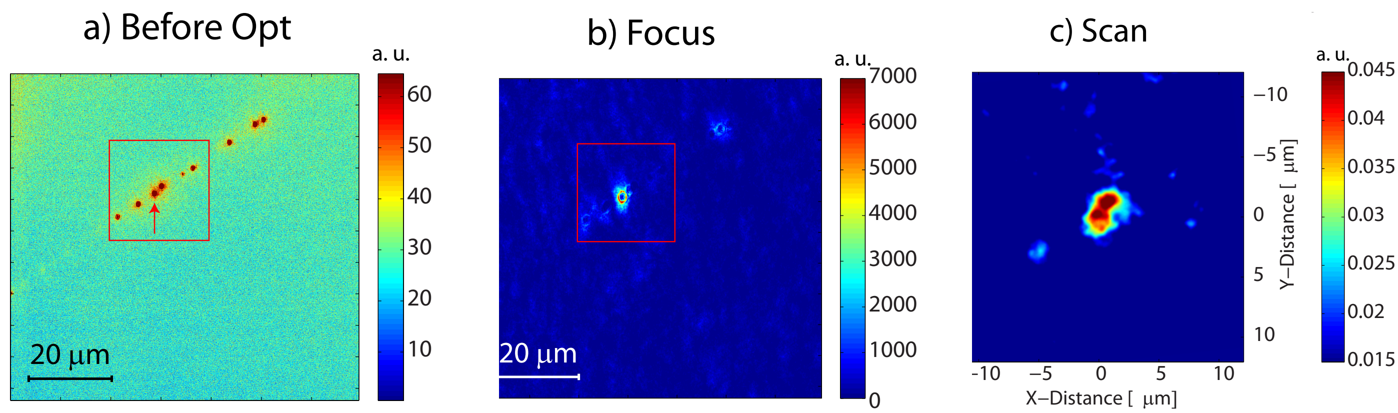

FIG. 18.2 – Scanning microscope images of a collection of fluorescent beads hidden behind a turbid layer:
a) direct view of the fluorescent particles in the absence of a turbid layer,
b) image created after iteratively adjusting the wave-front to the fluorescent signal and
c) the reconstructed image corresponding to the field of view of a) after scanning b) using the optical memory effect.
This result shows that it is possible to obtain diffraction limited resolution behind turbid layers of several mean free paths.

using the technique of wave-front shaping to create a focus behind [1] or inside [2] turbid media. We have previously been able to show that such a focus can be scanned for imaging purposes due to the optical memory effect [3], in both two [4] and three [5] dimensions. Because the focus is created by interference of multiple scattering paths in the turbid medium and the engineered phase shifts between these paths by a spatial light modulator, the resolution of the technique is not limited by the turbidity, but only by the wave-length of light used. Hence diffraction limited imaging is possible behind turbid layers many mean free paths thick.

Now we have been able to create the initial focus without optical access using the integrated fluorescence signal as a feedback for the optimization of the spatial light modulator phase field [6]. Moreover, this has shown that an iterative use of this optimization leads to a specific focusing on a single fluorescent structure (see Fig. 18.1). Thus even in the presence of several sources, iterative wave-front shaping leads to a single scannable focus that can subsequently be used to image the surroundings of the initial focus. This is shown in Fig. 18.2, where the direct fluorescence image of a set of particles is compared with a scattered light fluorescent image obtained with direct focusing on one bead. As an extension of the technique, the field of view for such images can be enlarged by successively bleaching the initially chosen beads and thus scanning several areas in sequence.

[1] I.M. Vellekoop and A.P. Mosk, Opt. Lett. **32**, 2309 (2007).

[2] I.M. Vellekoop, E.G. van Putten, A. Lagendijk, and A.P. Mosk, Opt. Express **16**, 67-80 (2008).

[3] D.L. Fried, J. Opt. Soc. Am. 72, 52 (1982); S. Feng, C. Kane, P.A. Lee, and A.D. Stone, Phys. Rev. Lett. **61**, 834 (1988); I. Freund, M. Rosenbluh, and S. Feng, *ibid*, 2328 (1988).

[4] I.M. Vellekoop and C.M. Aegerter, Opt. Lett. **35**, 1245 (2010).

[5] G. Ghielmetti and C.M. Aegerter, Opt. Express **20**, 3744 (2012).

[6] G. Ghielmetti and C.M. Aegerter, Opt. Express **22**, 1981 (2014).

18.2 Mechanical regulation of growth in the Drosophila wing disc

How an organ regulates its final size remains a big unsolved question in developmental biology. In recent years, the hypothesis that mechanical forces play a key role in this regulation has gained much attention [1, 2], since several conundrums in growth regulation have a natural explanation in this framework. The main object of study for this problem is the wing imaginal disc in Drosophila, which is a precursor organ that will form the final wing during metamorphosis. This is because of the relative simplicity of the tissue, being a single layer quasi-two dimensional sheet of cells and the powerful genetic tools available for studying pathways. While indirect evidence for such a regulation has been accumulating, from the fact that mechanical stresses are present in the wing disc [3–5] to the distribution of packing of the cells reproduced only in models including mechanical feedback [6, 7], there is still no direct evidence for such a regulation.

We have now tackled this problem experimentally and mechanically stressed live wing discs, while determining their proliferation rate. For this purpose, we use a stretch-

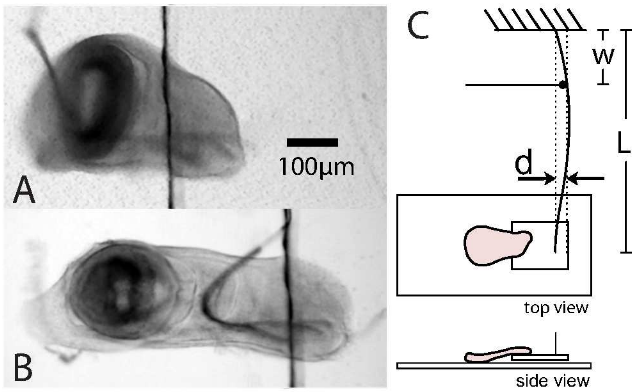

FIG. 18.3 – Illustration of the setup used to mechanically stimulate the wing imaginal disc. A wing disc is attached to two glass coverslips separately, one of which is movable using a spring sheet in order to apply a calibrated force. Panel A shows a wing disc before stretching, and B the same disc after application of 350 μN. The schematic of the setup is shown in C, where the spring sheet of length L is pushed a distance d at position w giving rise to a force on the wing disc of $F = \frac{6EI}{w^2(L-w)}d$. Here, I is the area moment of inertia of the spring sheet and E its elastic modulus.

ing apparatus described in Fig. 18.3 [8], which is capable of applying calibrated forces of the order of 20 to 500 μN to the tissue. With this, strains between a few percent to unity are possible. Mechanically stretching the tissue at different forces allows us to determine the systematics of the growth response in the tissue, which is shown in Fig. 18.4 [9]. As can be seen, after an hour of stretching, the proliferation rate has increased by a factor two. In fact, when applying a compressive force, the tissue is stretched as well due to the appearance of a buckling instability. This can be used to test whether stress or strain is more likely to be the controlling factor. As can be seen in Fig. 18.4B, in case of buckling, where the stresses are highly different to the case of uniaxial tension, the change in growth rates are the same within errors, as is the total strain. This points to the fact that the total strain is the controlling factor, as is also the case in a theoretical model [10]. This model also predicts a molecular mechanism for the regulation of growth, for which there is evidence from other tissues [11].

[1] B.I. Shraiman,
Proc Nat. Acad. Sci. USA **102**, 3318 (2005).

[2] T. Aegerter-Wilmsen, C.M. Aegerter, E. Hafen, and K. Basler, Mechanisms of Development **124**, 318 (2007).

[3] U. Nienhaus, T. Aegerter-Wilmsen, and C.M. Aegerter, Mechanisms of Development **126**, 942 (2009).

[4] S. Ishihara and K. Sugimura,
J. Theor. Biol. **313**, 201 (2012).

[5] U. Nienhaus, T. Aegerter-Wilmsen, and C.M. Aegerter, PLoS One **7**, e47594 (2012).

[6] T. Aegerter-Wilmsen *et al.*,
Development **137**, 499 (2010).

[7] R. Farhadifar, J.C. Röper, C. Aigouy, S. Eaton, and F. Jülicher, Curr Biol. **17**, 2095 (2007).

[8] T. Schluck and C.M. Aegerter,
Eur. Phys. J. E **33**, 111 (2010).

[9] T. Schluck, U. Nienhaus, T. Aegerter-Wilmsen, and C.M. Aegerter, PLoS One **8**, e76171 (2013).

[10] T. Aegerter-Wilmsen *et al.*,
Development **139** 3221 (2012).

[11] S. Dupont, *et al.* Nature **474**, 179 (2011).

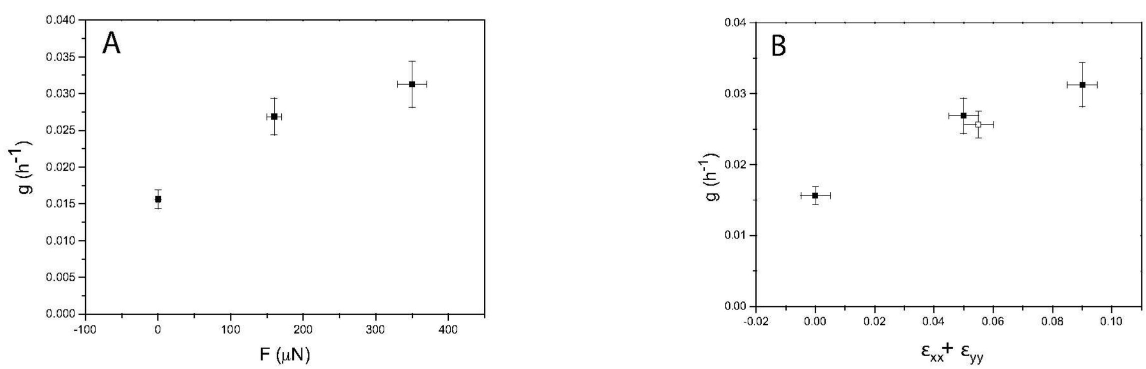

FIG. 18.4 – The proliferation rate of the wing disc tissue has been determined after one hour of stretching for different applied forces. The results are shown here as a function of the applied force (A) as well as of the ensuing total strain in the tissue (B). As can be seen, the proliferation rate strongly increases on the application of mechanical tension. On compressing the tissue, it buckles, leading to a positive strain comparable to a stretching experiment, shown by the open symbol in (B). This implies that the strain rather than the stress of the tissue leads to the increase in growth rate.

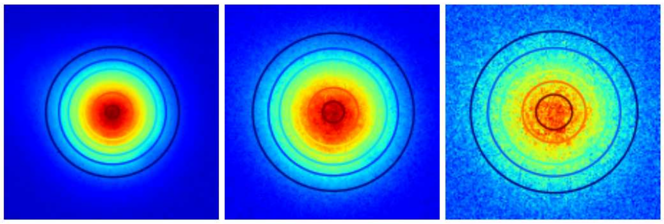

FIG. 18.5 – Spatially resolved intensity distributions behind a sample showing Anderson localization as a function of time after 2 ns, 4 ns, and 6 ns. The diffusive spread of the photons corresponding to the width can be seen to slow down, associated with a transition to localization.

18.3 Localization of light

The fact that multiply scattered waves can show a breakdown of diffusion is known as Anderson localization and has been theoretically predicted a long time ago [1]. Due to the fractal dimension of Brownian motion being two, this localization always appears in low dimensional systems. However in three dimensions, there is a transition to localization only with increasing disorder, when the mean free paths becomes comparable to the wavelength [2]. Due to the extreme nature of the necessary disorder, this transition has been very difficult to observe and many claims have been shown to be due to other effects, such as absorption [3, 4].

Using time resolved transmission experiments, we have been able to clarify the effects of absorption and find evidence for Anderson localization in three dimensional samples [5, 6]. However, the most direct determination of localization, which is completely independent of absorption is in the determination of transmission with both temporal and spatial resolution, such that the spread of the diffusive photon cloud and the stop of this spread can be observed directly, which has been predicted theoretically [7]. We have carried out such experiments (see Fig. 18.5 [8]) in sample previously found to show long time tails in time of flight measurements [5], where we have found an unambiguous saturation of the width, see Fig. 18.6. In order to quantify the properties of the localized modes more accurately, the intensity distribution of these modes needs to be determined, which is predicted to be highly skewed [9]. To do this, we use the non-linear optical properties of TiO_2 [10] to obtain a readout for the intensity distribution inside the sample. Thus we measure the amount of frequency shift in the transmitted light using band pass filters behind the sample, centered at different wave-lengths [11]. This is shown in Fig. 18.6 for a localizing sample. As can be seen, there are non-linear effects, which are important at long times, where there are localized modes, however the non-linearities are sufficiently weak to be treated perturbatively. This also means that these investigations open up a way to experimentally study the interplay between non-linear effects and Anderson localization, which has so far been possible only in theoretical investigations [12].

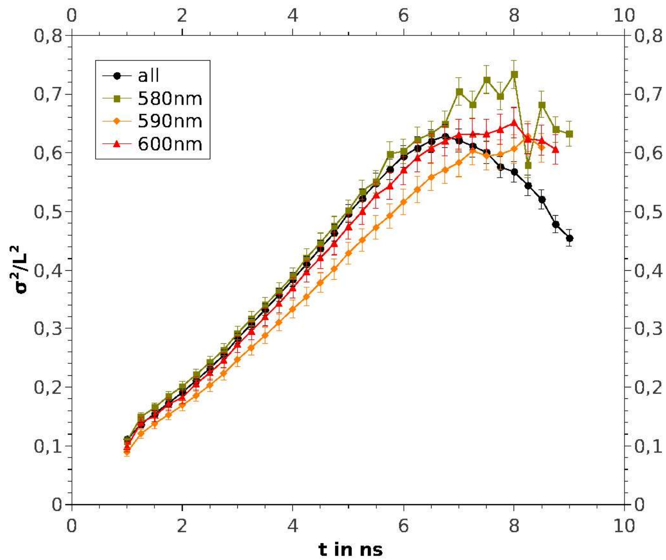

FIG. 18.6 – Time dependence of the width of the photon distribution spectrally resolved for the same sample. Due to the non-linear optical properties of TiO_2, part of the transmitted light exhibits shifts in frequency. This light can be used to study the interplay of non-linear effects with Anderson localization. The fact that both the frequency shifted light as well as the elastically scattered part show a saturation of the profile width demonstrated that the non-linear effects are sufficiently weak to be treated perturbatively.

[1] P.W. Anderson, Phys. Rev. **109**, 5 (1958).

[2] E. Abrahams *et al.*, Phys. Rev. Lett. **42**, 673 (1979).

[3] D.S. Wiersma, P. Bartolini, A. Lagendijk, *et al.*, Nature **390**, 671 (1997).

[4] F. Scheffold, R. Lenke, R. Tweer, *et al.*, Nature **398**, 206 (1999).

[5] M. Störzer, P. Gross, C.M. Aegerter and G. Maret, Phys. Rev. Lett. **96**, 063904 (2006).

[6] C.M. Aegerter M. Störzer, and G. Maret, Europhys. Lett. **75**, 562 (2006).

[7] N. Cherroret, S.E. Skipetrov and B.A. van Tiggelen, Phys. Rev. E **82**, 056603 (2010).

[8] T. Sperling, W. Bührer, C.M. Aegerter, and G. Maret, Nature Photonics **7**, 48 (2013).

[9] T.M. Nieuwenhuizen and M.C. van Rossum, Phys.Rev.Lett. **74**, 2674 (1995).

[10] R. Adair, L.L. Chase and S.A. Payne, Phys.Rev.B, **39**, 3337 (1989).

[11] G. Maret, T. Sperling, W. Bührer, A. Lubatsch, R. Frank, and C.M. Aegerter, Nature Photonics **7**, 934 (2013).

[12] C.Conti, Chin.Phys.Lett. **31** 030501 (2014).

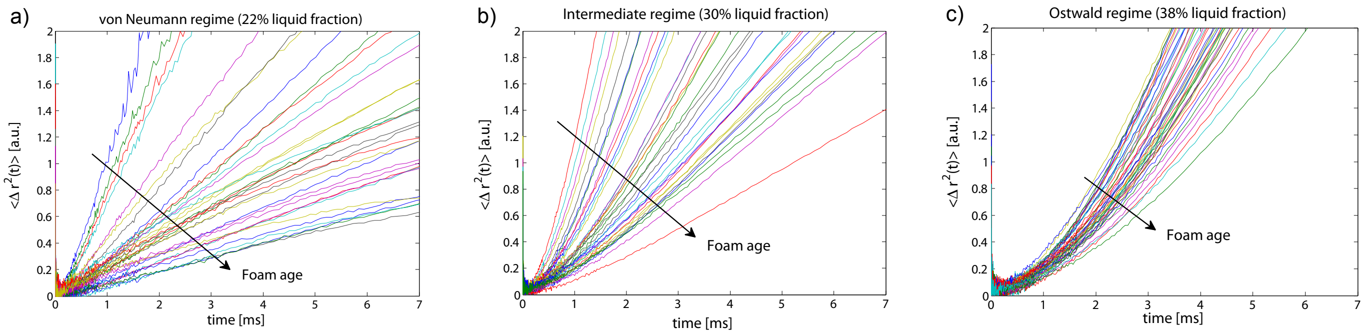

FIG. 18.7 – The mean square displacement of scatterers in the foam is shown as a function of correlation time for three different liquid fractions (a: 22 %, b: 30 % and c: 38%). This shows the local dynamics of bubbles, which can be seen to be diffusive ($\langle \Delta r^2 \rangle \propto t$) in the von Neumann regime and ballistic ($\langle \Delta r^2 \rangle \propto t^2$) in the Ostwald regime.

18.4 Dynamics of levitated foams

Using diamagnetic levitation [1–3], we have studied the coarsening behavior of foams of different liquid fractions [4]. While this has been studied theoretically for a long time yielding different predictions for dry foams by von Neumann [5] and wet foams by Ostwald [6], an experimental investigation has proven difficult due to the drainage of liquid due to gravity. Finding different coarsening dynamics at different liquid fractions according to the predictions [4], we have now studied the microscopic dynamics in the different regimes. Using diffusing wave spectroscopy [7, 8], i.e. the correlation of speckles in multiply scattered light transmitted through the foam, we determine the mean square fluctuations of the foam bubbles for varying liquid fraction. As can be seen in Fig. 18.7 [4], at low liquid fraction, where the bubbles overlap strongly and are deformed, the dynamics is diffusive and the corresponding size increases with foam age, as is expected from the coarsening of the foam. At high liquid fractions, where bubbles are separated and spherical, the dynamics is ballistic and influenced by residual flows in the liquid of the foam. This dynamics also does not change with the age of the foam and thus is not influenced by the coarsening process. At intermediate liquid fractions, the dynamics is more complicated and shows a crossover between diffusive and ballistic dynamics. Similarly, the coarsening process is not homogeneous in time, but is described by van Neumanns law at long times, when the larger bubbles start to overlap and by Ostwald ripening at short times.

[1] W. Braunbeck, Z. Phys. **112**, 764 (1939).

[2] M.V. Berry and A.K. Geim, Europ. J. Phys. **18**, 307 (1997).

[3] C.C. Maass, N. Isert. G. Maret and C.M. Aegerter, Phys. Rev. Lett. **100**, 248001 (2008).

[4] N. Isert, G. Maret, C.M. Aegerter, Europ. Phys. J. E **36**, 116 (2013).

[5] J. von Neumann, in *Metal Interfaces* (C. Herring ed.), 108 (1952).

[6] W. Ostwald, Z. Phys. Chem. **37**, 385 (1901).

[7] G. Maret and P.E. Wolf, Z. Phys. B **65**, 409 (1987).

[8] D.J. Pine, D.A. Weitz, J.X. Zhu and E. Herbolzheimer, J. Phys. **51**, 2101 (1990).

19 Mechanical Workshop

K. Bösiger, B. Lussi, R. Maier, M. Schaffner, S. Scherr, D. Dürst (until July 2013), D. Gabrielli (apprentice), B. Markwalder (apprentice since August 2013) and P. Weyeneth (apprentice since August 2013)

Last year the Cherenkov Telescope Array (CTA) and the CMS barrel pixel upgrade projects were in the main focus of the mechanical workshop. Apart from the usual repairs and maintenance work we produced parts for other departments of the university, the ETH and contractors. Over 30 institutes and local high schools were supplied with materials and technical support by the central metal and technical material store maintained by our staff. [1]

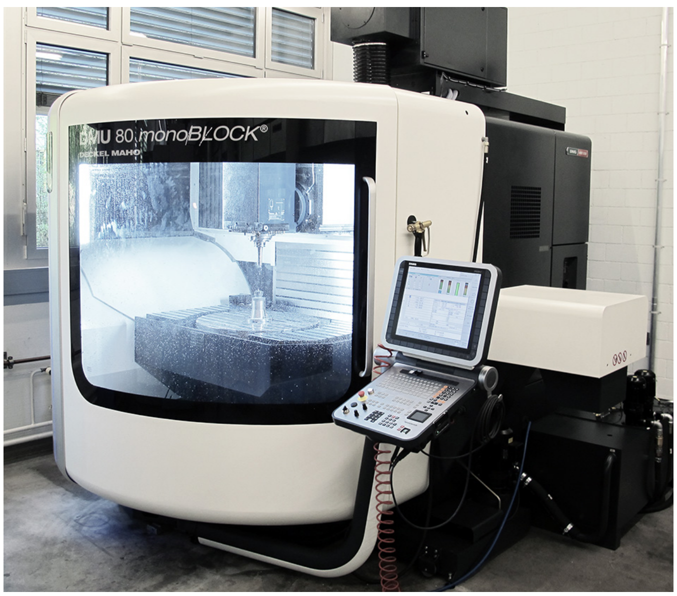

- The new milling machine

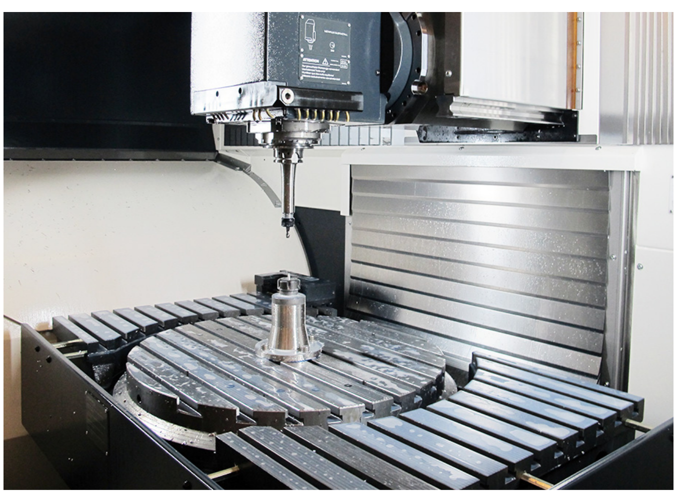

- The 1250 mm x 700 mm work area with 70 cm rotary table

The workshop staff conducted the basic mechanical workshop courses for the bachelor students in physics during 8 weeks. During this time, 11 courses were carried out at 35 hours each. In October 2013 we organized again the welding courses for the physics laboratory assistant apprentices from the ETH. For people interested in a grade as a poly-technician we provided two one-week trial apprenticeships.

There is an increasing demand for optimized and more precise production of complicated parts, both for single work pieces and small series, so we replaced a 23-year old milling machine by a state-of-the-art device. The modular design ensures the necessary sturdiness and provides optimal ergonomics and easy handling through a door that gives wide access to the large work area. The table moves vertically with speeds of up to 1 m/s and can rotate with up to 1 revolution per second around the rotary axes. Work pieces up to 850 mm x 600 mm x 600 mm can be processed with spindle speeds up to 300 revolutions per second. This is actually the largest milling machine available at the University. Extensive standard equipment, a large range of expansion options, advanced CNC controls and numerous software features make the machine perfectly equipped for complete 5-axes simultaneous machining.

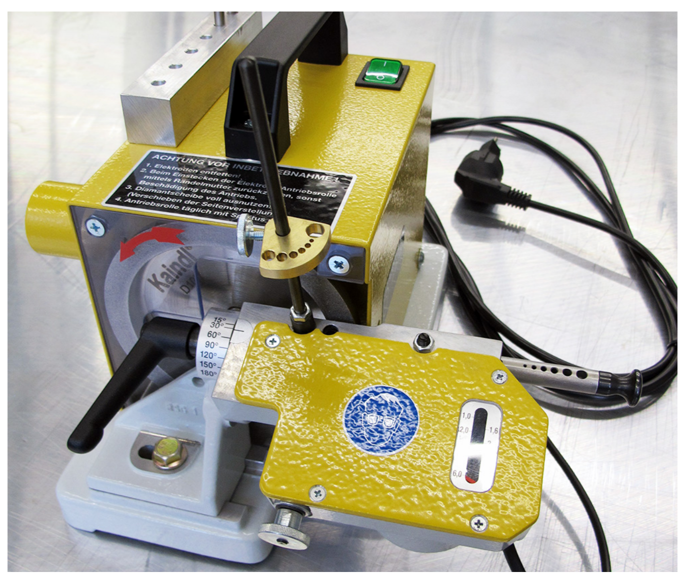

- The new electrode grinding machine

[1]For a catalogue see http://www.physik.uzh.ch/groups/werkstatt/

A new electrode grinding machine now helps to improve the welding quality. The diamond grinding wheel is ideal for grinding of Tungsten carbide welding electrodes with diameter 1.0 - 4.0 mm with a top angle from 15 - 180 deg. Accurate centering in longitudinal direction grants a stable arc and a longer lifetime of the electrodes.

To make the welding process more efficient we purchased a universal beveling machine used for processing of bevels and radii on plates, containers, inner and outer edges, contour profiles, drilling and pipe ends. The device combines a patented system for fast exchange of the milling head with a patented spring technology for vibration-free operation resulting in longer tool life. In addition to milling heads for 0-80 deg bevels and 2-4 mm radii there exist diamond crowns and abrasive belt heads for efficient edge processing.

Below we mention a selection of our activities:

- Demonstration and laboratory experiments and Science Lab of the University
  We repaired and improved different experiments used for the demonstrations in the basic physics lectures and in the laboratory courses. The Science Lab of the University is a research and learning laboratory for students, pupils and teachers. The program will encompass the subjects of physics, mathematics, chemistry and geography as well as interdisciplinary topics. We produced a set of parts for experiments in connection with magnetism.

- CTA Cherenkov Telescope Array (Sec. 7)
  Test setups for the FlashCam camera, mounting tools for the camera housing assembly and a support frame were produced. In the welding shop a special large size welding table was installed necessary to complete the parts. Distribution boxes, rails and detectors mounts were manufactured. We supported the research group also in the assembly of the individual components.

- The FlashCam camera support frame

- The new beveling machine

- Parts for a Science Lab experiment.

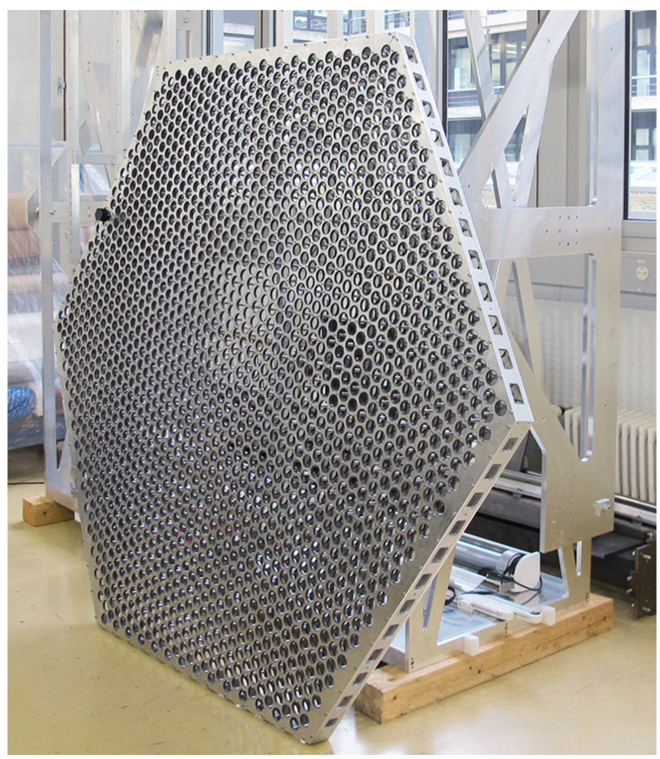

- The FlashCam camera structure built up in the workshop assembly hall

- Surface Physics (Sec. 16)
  For the extensions of the Sinergia apparatus we manufactured different parts. The flange shown in the figure on the right is used to support an additional electron source. We made parts for bachelor thesis projects carried out in the surface physics group and did maintenance and repair work. Again a small series of dedicated molybdenum sample holders was fabricated.

- Stainless steel flange for the Sinergia apparatus

- Astroparticle Physics (Sec. 3, 4)
  New steel bands for the calibration system of the GERDA experiment, test setups and different Teflon reflectors were fabricated. For a new larger time projection chamber (TPC) of the XENON experiment we made first prototypes of ring electrodes used in the electric field forming structure. The ring electrode consists of oxygen-free copper and has a diameter of 985 mm and a cross-section of 5 mm x 10 mm.

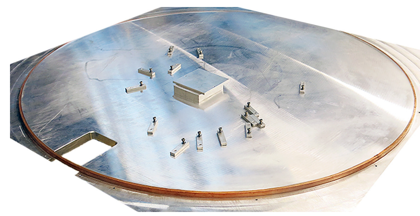

- Voltage divider ring after the welding process

- Physics on the nanometer scale (Sec. 17)
  The vapor deposition device with six coating stations was modified and maintained. We produced new evaporation masks and a door with hinge-joints for a homemade load-lock chamber for fast insertion of samples in an ultra high vacuum (UHV) coherent low-energy electron microscope. The aperture in the middle of the door permits the mounting of a wobble stick for samples manipulation. We built support structures for electrical contacts used to heat samples in a UHV chamber.

- Door installed on the load-lock chamber with the wobble stick for the sample manipulation

- CMS Barrel Pixel detector upgrade (Sec. 13)
  A new pixel detector has been designed for the CMS experiment at CERN (Phase I Pixel Upgrade), in order to preserve the high tracking quality at luminosity and pile-up beyond the original specifications. It features four layers in the barrel, one more than the present detector. The new CO_2 cooling system combined with a modified cabling scheme and new lightweight mechanics will contribute greatly to the material budget reduction in the tracking acceptance. The demanded performances aim for 15 kW of cooling power at -20 C evaporation temperature. The system has a so far unmatched size for an evaporative CO_2 cooling system used in a high energy physics detector. For the necessary functional tests of the complete cooling system we manufactured two full-size cooling test-system prototypes. The cooling structures are made out of stainless steel tubes with over 500 solder joints and is pressure tested at 160 bar.

- Cooling test system for the CMS Barrel Pixel upgrade; in the foreground the part which cools the four detector layers.

- DAMIC Dark Matter in CCDs (Sec. 6)
  Thanks to the low electronic noise DAMIC reaches a detection threshold below 0.5 keV nuclear recoil energy, making the search for dark matter particles with masses below 10 GeV possible. We manufactured the parts for a test setup (the AlpineCube) for studies of different CCD types.

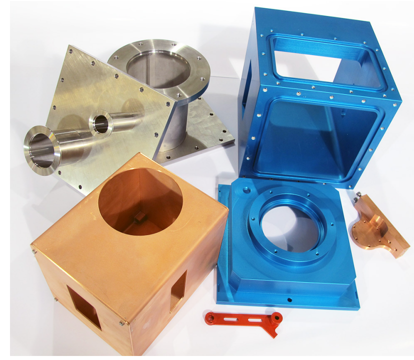

- Parts for the AlpineCube test setup

- Education of the workshop staff and apprentices
  Courses in computer aided design (CAD) and manufacturing (CAM) were attended. We attended welding training courses and went to the regular meetings devoted to the education of the apprentices. We visited machinery and tool manufacturers, and exhibitions. In May and June the apprentices passed their examinations with great success. In the final work the candidate made a special gimbal suspension for a photo camera. The device is used at the Remote Sensing Laboratories RSL at the department of geography. In August two apprentices started their education at the workshop. In addition to the compulsory Swissmechanic courses our apprentices attended advanced training courses in turning and milling, CNC programming, pneumatics and electronics.

- The gimbal camera suspension

- Activities for other departments and outside companies
  For several institutes and departments of the University work was performed.
  We designed, manufactured and assembled new portable specimen holder containers for the department of pathology. The computer controlled movable cross table allows an automatic deposition of the various samples in the specimen holder.
  For the Zoological Museum we made picture frames and small test-series of adjustable LED lamps used for a special exhibition.
  New transfer cars for 240 liter nitrogen tanks were designed and fabricated. The built-in lifting mechanism allows a comfortable and safe transportation of the 300 kg vessels at the department of virology.

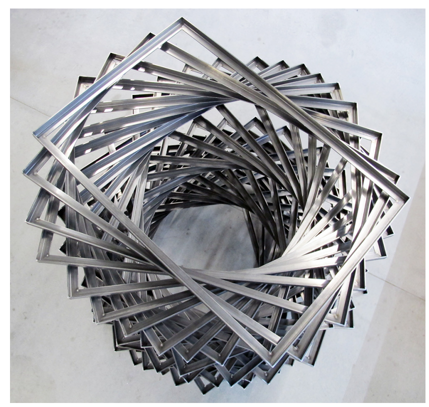

- Metal picture frames for a special exhibition at the Zoological Museum

- Portable computer controlled cross table with specimen holder

- Liquid nitrogen vessel transfer car

In collaboration with researchers of the Centre Suisse d'Electronique et de Microtechnique (CSEM) we manufactured an electro-mechanical frame made out of Invar used for X-ray grating-based phase contrast imaging for bio-medical applications. The light weight design ensures mechanical and thermal stability of the grating interferometer during operation on a rotating gantry. The project is a collaboration between CSEM and PSI and is supported by the CCMX Analytical Platform.
New LED lamps with a power of 60 W and a more efficient heat sink design for the outdoor and indoor use were produced for a lighting company.

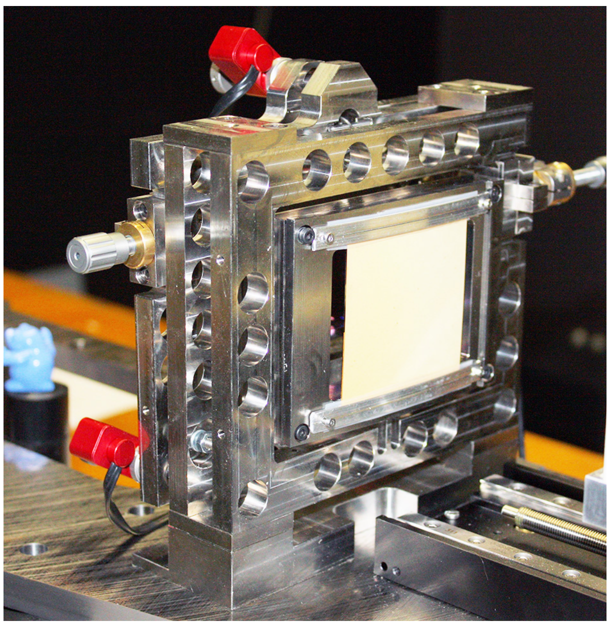

- Electro-mechanical frame made out of Invar

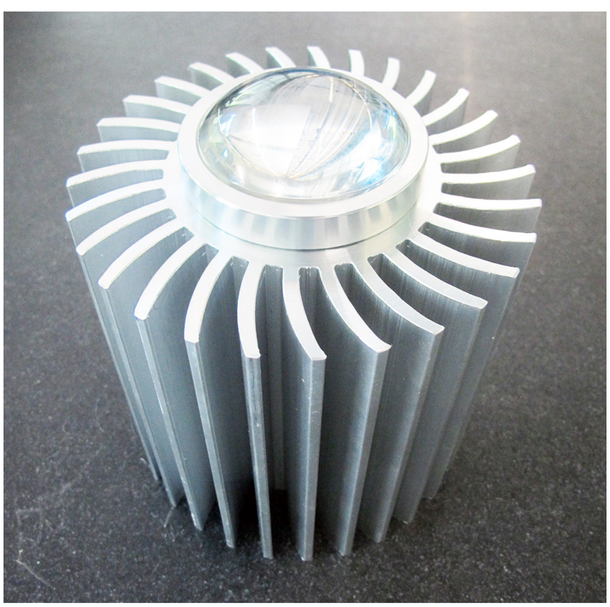

- Led lamp

20 Electronics Workshop

D. Florin, P. Soland, and A. Vollhardt

Besides the usual repair work we built test setups for ongoing projects, purchased components for the various research groups and did maintenance work for the LHCb experiment at CERN.

A thermoelectric generator was developed for the phase transitions, materials and application research group (Sec. 15). It contains several Peltier elements and super-capacitors for energy storage. Setups were assembled, which allow to test the device.

A compact RIO module with White Rabbit functionality was designed for the use in a new laboratory experiment (Sec. 7). White Rabbit is a project developed at CERN and GSI, aiming at real-time synchronization and Ethernet functionality through a standard glass fiber connection. Our contributions include the design of a printed circuit board fullfilling the compact RIO module specifications by National Instruments and the necessary adjustments to the FPGA firmware. The module will be installed in a commercial system.

For the Cherenkov Telescope Array (CTA) experiment (Sec. 7) 200 servo motors, needed for mirror positioning, were mounted on the Medium-Size Telescope (MST) prototype in Zeuthen. For tests on the Large Size Telescope (LST) prototype another batch of 440 units was produced in collaboration with our mechanical workshop and the University of Tokyo. In parallel, the development of the pre-amplifier electronics for the focal plane instrumentation of the FlashCam project continues. For mechanical and thermal tests of the prototype FlashCam camera body built in our mechanical workshop, we installed sensors and the associated readout and control electronics.

Various projects were carried out for the group of Laura Baudis:

- We designed and manufactured adapters and printed circuit boards for Xurich II.
- We made studies and prepared the series production of the photomultiplier base boards for GERDA.
- For XENON1T we developed a 2-channel low noise PMT amplifier. The amphenol type plug directly connects to the Xurich test detector. Input and output impedance are 50 ohms and the unconditionally stable gain can be switched by a factor 10.
- For the same project we produced a prototype 4-channel amplifier with fixed gain and two output signals.

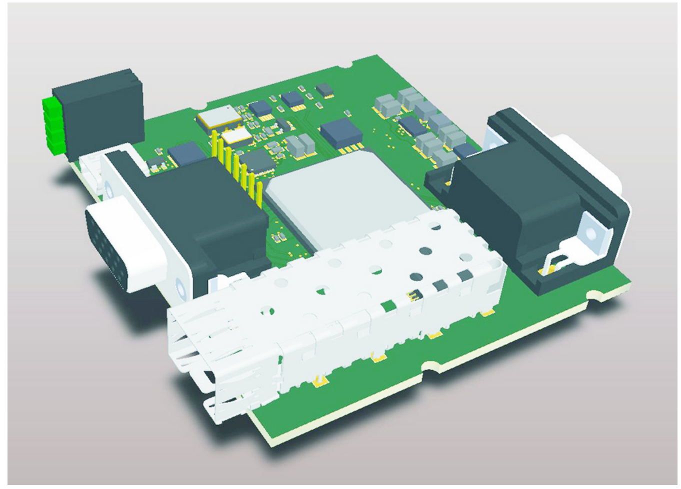

- CAD model of the compact RIO module

- Two-channel PMT amplifier

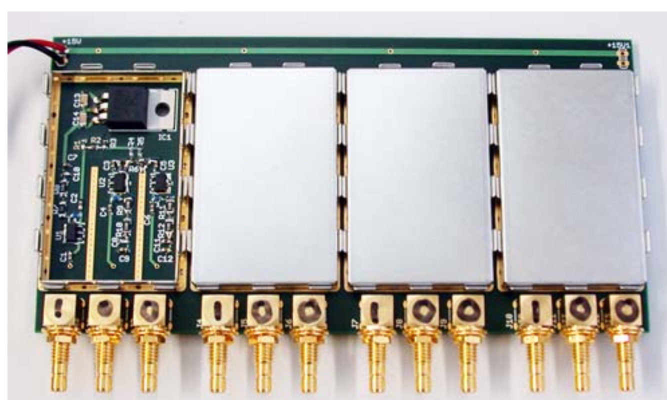

- Four-channel prototype amplifier for XENON1T

21 Publications

21.1 Theoretical physics

21.1.1 Elementary particles

Articles

- A framework for Higgs characterisation
  P. Artoisenet, P. Aquino, F. Demartin, R. Frederix, S. Frixione, F. Maltoni, M.K. Mandal, P. Mathews, K. Mawatari, V. Ravindran, S. Seth, P. Torrielli, and M. Zaro, JHEP 1311 (2013) 043.

- Light-quark two-loop corrections to heavy-quark pair production in the gluon fusion channel
  R. Bonciani, A. Ferroglia, T. Gehrmann, A. Manteuffel, and C. Studerus, JHEP 1312 (2013) 38.

- Soft-gluon resummation for single particle inclusive hadroproduction at high transverse momentum
  S. Catani, M. Grazzini, and A. Torre, Nucl. Phys. **B**874 (2013) 720.

- Dimensional reduction without continuous extra dimensions
  A.H. Chamseddine, J. Fröhlich, B. Schubnel, and D. Wyler, J. of Math. Phys. 54 (2013) 012302.

- Infrared structure at NNLO using antenna subtraction
  J. Currie, E.W.N. Glover, and S. Wells, JHEP 1304 (2013), 066.

- The two-loop soft current in dimensional regularization
  C. Duhr and T. Gehrmann, Phys. Lett. **B** 727 (2013) 452.

- Probing top quark electromagnetic dipole moments in single-top-plus-photon production
  M. Fael and T. Gehrmann, Phys. Rev. **D** 88 (2013) 033003.

- Higgs production through vector-boson fusion at the NLO matched with parton showers
  S. Frixione, P. Torrielli, and M. Zaro, Phys. Lett. **B** 726 273.

- Photon isolation effects at NLO in gamma+gamma+jet final states in hadronic collisions
  T. Gehrmann, N. Greiner, and G. Heinrich, JHEP 1306 (2013) 058.

- Precise QCD predictions for the production of a photon pair in association with two jets
  T. Gehrmann, N. Greiner, and G. Heinrich, Phys. Rev. Lett. 111 (2013) 222002.

- NLO QCD matrix elements + parton showers in e+e- to hadrons
  T. Gehrmann, S. Höche, F. Krauss, M. Schönherr, and F. Siegert, JHEP 1301 (2013) 144.

- Power corrections in the dispersive model for a determination of the strong coupling constant from the thrust distribution
  T. Gehrmann, G. Luisoni, and P.F. Monni, Eur. Phys. J. C 73 (2013) 2265.

- Two-loop master integrals for $q\bar{q} \to VV$: the planar topologies
  T. Gehrmann, L. Tancredi, and E. Weihs, JHEP 1308 (2013) 070.

- Two-loop QCD helicity amplitudes for gg to Z g and gg to Zgamma
  T. Gehrmann, L. Tancredi, and E. Weihs, JHEP 1304 (2013) 101.

- Second-order QCD corrections to jet production at hadron colliders: the all-gluon contribution
  A. Gehrmann-De Ridder, T. Gehrmann, E.W.N. Glover, and J. Pires, Phys. Rev. Lett. 110 (2013) 162003.

- Higgs boson self-coupling measurements using ratios of cross sections
  F. Goertz, A. Papaefstathiou, L.J. Yang, and J. Zurita, JHEP 1306 (2013) 016.

- Heavy-quark mass effects in Higgs boson production at the LHC
  M. Grazzini and H. Sargsyan, JHEP (2013) 129.

- Probing the colour structure of the top quark forward-backward asymmetry
  B. Gripaios, A. Papaefstathiou, and B. Webber, JHEP 13011 (2013) 105.

- Complete three-loop QCD corrections to the decay Higgs to gamma gamma
  P. Maierhöfer and P. Marquard, Phys. Lett. **B** 721 (2013) 131.

- Higgs boson pair production at the LHC in the $bb \to W^+W^-$ channel
  A. Papaefstathiou, L. Yang, and J. Zurita, Phys. Rev. **D** 87 (2013) 011301(R).

Theses

- Resummation of Jet Observables
  Pier Francesco Monni, PhD thesis, 26.4.2013

- Dark Higgs Studies and Diboson Production at the Large Hadron Collider
  Erich Weihs, PhD thesis, 15.8.2013

- Transverse Parton Distribution Functions at Next-to-next-to-leading Order
  Thomas Lübbert, PhD thesis, 27.10.2013

- Electromagnetic dipole moments of fermions
  Matteo Fael, PhD thesis 17.3.2014

Oral Presentations

- Philipp Maierhöfer: Automatic one-loop calculations with OpenLoops
  ACAT 2013 Conference, Beijing, 18.05.2013

- Philipp Maierhöfer: Status of OpenLoops and simulation of $H \to WW$ backgrounds
  RADCOR 2013 Conference, Durham, 24.09.2013

- Philipp Maierhöfer: NLO automation with OpenLoops and applications to $H \to WW$ and ttH backgrounds
  Seminar, Karlsruhe, 15.11.2013

- Philipp Maierhöfer: Predictions for $H \to WW$ background in exclusive jet bins with Sherpa+OpenLoops
  Helmholtz Alliance Workshop *Physics at the Terascale*, Karlsruhe, 02.12.2013

- Philipp Maierhöfer: Predictions for $H \to WW$ background in exclusive jet bins with Sherpa+OpenLoops
  LHCPhenoNet Meeting, CERN, 03.12.2013

- Thomas Gehrmann: Precision physics with jet observables
  Kolloquium Freiburg, 18.06.2013

- Thomas Gehrmann: Jet physics at NNLO
  KITP LHC Workshop, Santa Barbara, 11.07.2013

- Thomas Gehrmann: Hard QCD
  QCD@LHC, DESY Hamburg, 02.09.2013

- Thomas Gehrmann: Precision physics with jet observables
  Kolloquium Nikhef Amsterdam, 17.10.2013

- Thomas Gehrmann: Status of QCD
  Annual Theory Meeting, IPPP Durham, 16.12.2013

- Thomas Gehrmann: Precision Physics with Jet Observables
  Colloquium, Univ. Roma *La Sapienza*, 27.1.2014

- Thomas Gehrmann: Theory Summary
  49th Rencontres de Moriond: *QCD and High Energy Interactions*, La Thuile, 29.3.2014

- Massimiliano Grazzini: QCD and Higgs physics: theoretical issues
  Rencontres de Physique de la Vallee d'Aoste, La Thuile, Italy

- Massimiliano Grazzini: Uncertainties in Higgs boson production
  LHC Workshop, Genova, Italy, May 8 2013.
- Massimiliano Grazzini: Mass effects in the Higgs pt spectrum
  ATLAS Higgs meeting, CERN, June 2013.
- Massimiliano Grazzini: The Higgs boson one year later
  Seminar Lyon, October 29, 2013.
- Massimiliano Grazzini: The Higgs boson one year later
  Seminar Munich, October 24, 2013.
- Massimiliano Grazzini: Higgs pt with Hres
  ATLAS workshop, CERN, December 16, 2013.
- Paolo Torrielli: Issues with the PYTHIA8 shower, status, and EW MC counterterms
  ERC miniworkshop, CERN, 05-06/08/2013.
- Paolo Torrielli: Status of parton showers at NLO
  ERC miniworkshop, CERN, 03-06/12/2013.
- Fabio Cascioli: NLO automation with OpenLoops and irreducible bkg to $H \to WW$
  LHCPhenoNet Workshop, Buenos Aires, 24.04.2013
- Fabio Cascioli: NLO automation with OpenLoops and irreducible bkg to $H \to WW$
  LoopFest XII, Tallahassee (Florida), 14.05.2013

- Fabio Cascioli: NLO automation with OpenLoops and new results for $H \to WW$ irreducible bkg
  PhD Seminars - ETH, Zurich, 29.08.2013
- Fabio Cascioli: Merging NLO and squared-loop corrections to four-lepton+0,1 jet with Sherpa+OpenLoops
  QCD@LHC 2013, DESY-Hamburg, 04.09.2013
- James Currie: antenna subtraction from outer (colour) space
  LHCPhenonet fellows meeting, Buenos Aires, 23/4/2013
- James Currie: integrated antenna dipoles
  seminar, IPPP Durham, 24/5/2013
- James Currie: colourful antenna subtraction for gluon scattering
  RADCOR'13, Lumley Castle, 24/9/2013
- James Currie: NNLO corrections to jet production
  LHCPhenonet annual meeting, CERN, 4/12/2013
- Lorenzo Tancredi: Towards two-loop corrections to vector boson pair production at LHC
  Theory Seminar, University of Mainz, 6.05.2013
- Lorenzo Tancredi: Towards two-loop corrections to vector boson pair production at LHC
  Particle Physics Seminar, MPI Munich, 4.07.2013
- Lorenzo Tancredi: Towards two-loop corrections to vector boson pair production at LHC
  Zurich PhD Seminar, ETH/UZH Zurich, 30.08.2013
- Lorenzo Tancredi: Towards two-loop QCD corrections to ZZ and WW production at LHC
  RADCOR 2013, Durham, 23.09.2013
- Lorenzo Tancredi: Progressi nel calcolo dei grafici di Feynman
  Theory Seminar, University of Bologna, 7.10.2013

- Lorenzo Tancredi: Methods for multi-loop computations
  lecture series, Discussion meeting on radiative corrections, Institute of Physics, Bhubaneswar, India, March 5-10 2014

- Stefano Pozzorini: Automated NLO calculations with OpenLoops
  The first three years of the LHC, Mainz, 20.3.2103

- Stefano Pozzorini: MEPS@NLO predictions for $H \to WW$ background in exclusive jet bins
  LHCP2013, Barcelona, 14.5.2013

- Stefano Pozzorini: ttH(bb) backgrounds with Sherpa+OpenLoops
  ttH Atlas Workshop, CERN, Geneva, 25.6.2013

- Stefano Pozzorini: Precise predictions for ttH(bb) backgrounds with Sherpa+OpenLoops
  RADCOR2013, Lumely Castle, 22-27.9.2013

- Stefano Pozzorini: ttbar+heavy-flavour modelling with Sherpa+OpenLoops
  ATLAS Higgs WG (N)NLO MC and Tools Workshop for LHC Run2, CERN, Geneva, 16.12.2013

- Stefano Pozzorini: Precise predictions for ttH(bb) backgrounds with Sherpa+OpenLoops
  RADCOR2013, Lumely Castle, 22-27.9.2013

- Stefano Pozzorini: ttbar+heavy-flavour modelling with Sherpa+OpenLoops
  ATLAS Higgs WG (N)NLO MC and Tools Workshop for LHC Run2, CERN, Geneva, 16.12.2013

- Stefano Pozzorini: Matching and merging of parton showers and matrix elements
  Autumn School on Particle Physics and Cosmology, Göttingen, 7-11.10.2103

- Hayk Sargsyan: Heavy-quark mass effects in Higgs production
  Higgs Hunting 2013, Paris, 26 July 2013

- Hayk Sargsyan: Heavy-quark mass effects in Higgs production
  LHCPhenoNet annual meeting, CERN, Geneva, 03 Dec. 2013

- Adrian Signer: Testing the Standard Model and waiting for Godot
  2013 CHIPP Annual Plenary Meeting, Sursee, 24 June 2013

- Adrian Signer: Effective-theory approach to off-shell effects at hadron colliders
  KIT Karlsruhe, theory seminar, 11 July 2013

- Stefan Kallweit: Off-shell top-pair production at NLO QCD with massive bottoms
  RADCOR 2013, Lumely Castle, 22-27.9.2013

- Stefan Kallweit: NNLO corrections to gauge-boson pair production: first results on $Z\gamma$
  seminar, University of Freiburg, 12.11.2013

- Jonas Lindert: Combining squark production and decay at NLO QCD
  LHCPhenoNet Annual Meeting, CERN, 2-5.12.2013

- Marius Wiesemann: Transverse momentum resummation for supersymmetric Higgs production
  LHCPhenoNet annual meeting, CERN, December 2-5, 2013

- Alessandro Torre: Soft gluon effects in four parton hard-scattering processes
  LHCPhenoNet Workshop on Particle Physics, Buenos Aires, 23-26 April 2013

- Alessandro Torre: Soft Gluon Effects in Four Parton Hard-Scattering Processes
  RADCOR 2013, Durham, 22-27 September 2013

- Dirk Rathlev: Progress towards vector boson pair production in NNLO QCD
  RADCOR 2013, Lumley Castle, UK, 23.9.2013

- Dirk Rathlev: Vector boson pair production in NNLO QCD
  LHCPhenonet meeting, CERN, 2.12.2013

- Dirk Rathlev: Status of Vgamma production in NNLO QCD
  Terascale Alliance meeting, KIT, Karlsruhe, 3.12.2013

21.1.2 Astrophysics and General Relativity

Articles

- Intensity interferometry with more than two detectors?
  V. Malvimat, O. Wucknitz, and P. Saha, MNRAS437 (2014) 798.

- Mass-galaxy offsets in Abell 3827, 2218 and 1689: intrinsic properties or line-of-sight substructures?
  I. Mohammed, J. Liesenborgs, P. Saha, and L.L.R. Williams, MNRAS439 (2014) 2651.

- Spacecraft clocks and relativity: Prospects for future satellite missions
  R. Angélil, P. Saha, R. Bondarescu, P. Jetzer, A. Schärer, and A. Lundgren, Phys Rev D89(6) (2014) 064067.

- Cosmological parameter determination in free-form strong gravitational lens modelling
  M. Lubini, M. Sereno, J. Coles, P. Jetzer and P. Saha, MNRAS437 (2014) 2461.

- Effective-one-body Hamiltonian with next-to-leading order spin-spin coupling for two nonprecessing black holes with aligned spins
  S. Balmelli and P. Jetzer, Phys Rev D87(12) (2013) 124036.

- The LISA Pathfinder Mission
  P. McNamara, F. Antonucci, M. Armano, H. Audley, G. Auger, M. Benedetti, P. Binetruy, J. Bogenstahl, D. Bortoluzzi, N. Brandt, M. Caleno, A. Cavalleri, G. Congedo, M. Cruise, K. Danzmann, F. De Marchi, M. Diaz-Aguilo, I. Diepholz, G. Dixton, R. Dolesi, N. Dumbar, J. Fauste, L. Ferraioli, V. Ferroni, W. Fichter, E. Fitzsimons, M. Freschi, C. Garcia Marirrodriga, R. Gerndt, L. Gesa, F. Gibert, D. Giardini, C. Grimani, A. Grynagier, F. Guzmán, I. Harrison, G. Heinzel, M. Hewitson, D. Hollington, D. Hoyland, M. Hueller, J. Huesler, O. Jennrich, P. Jetzer, B. Johlander, N. Karnesis, N. Korsakova, N. Killow, X. Llamas, I. Lloro, A. Lobo, R. Maarschalkerweerd, S. Madden, D. Mance, V. Martin, I. Mateos, J. Mendes, E. Mitchell, D. Nicolodi, M. Nofrarias, M. Perreur-Lloyd, E. Plagnol, P. Prat, J. Ramos-Castro, J. Reiche, J. Romera Perez, D. A. Robertson, H. Rozemeijer, G. Russano, A. Schleicher, D. Shaul, C.F. Sopuerta, T. J. Sumner, A. Taylor, D. Texier, C. Trenkel, H.B. Tu, S. Vitale, G. Wanner, H. Ward, S. Waschke, P. Wass, D. Wealthy, S. Wen, W. Weber, T. Ziegler, and P. Zweifel,
  in: *The LISA Pathfinder Mission*, G. Auger, P. Binétruy and E. Plagnol, editors, Astronomical Society of the Pacific Conference Series, 467 (2013) 5.

- State Space Modelling and Data Analysis Exercises in LISA Pathfinder
  M. Nofrarias, F. Antonucci, M. Armano, H. Audley, G. Auger, M. Benedetti, P. Binetruy, J. Bogenstahl, D. Bortoluzzi, N. Brandt, M. Caleno, A. Cavalleri, G. Congedo, M. Cruise, K. Danzmann, F. De Marchi, M. Diaz-Aguilo, I. Diepholz, G. Dixton, R. Dolesi, N. Dumbar, J. Fauste, L. Ferraioli, V. Ferroni, W. Fichter, E. Fitzsimons, M. Freschi, C. Garcia Marirrodriga, R. Gerndt, L. Gesa, F. Gibert, D. Giardini, C. Grimani, A. Grynagier, F. Guzmán, I. Harrison, G. Heinzel, M. Hewitson, D. Hollington, D. Hoyland, M. Hueller, J. Huesler, O. Jennrich, P. Jetzer, B. Johlander, N. Karnesis, N. Korsakova, N. Killow, X. Llamas, I. Lloro, A. Lobo, R. Maarschalkerweerd, S. Madden, D. Mance, V. Martin, I. Mateos, J. Mendes, E. Mitchell, D. Nicolodi, M. Nofrarias, M. Perreur-Lloyd, E. Plagnol, P. Prat, J. Ramos-Castro, J. Reiche, J. Romera Perez, D. A. Robertson, H. Rozemeijer, G. Russano, A. Schleicher, D. Shaul, C.F. Sopuerta, T. J. Sumner, A. Taylor, D. Texier, C. Trenkel, H.B. Tu, S. Vitale, G. Wanner, H. Ward, S. Waschke, P. Wass, D. Wealthy, S. Wen, W. Weber, T. Ziegler, and P. Zweifel,
  9th LISA Symposium, Astronomical Society of the Pacific Conference Series, 467 (2013) 161.

- Power Spectrum of Gravitational Waves from Unbound Compact Binaries
  L. De Vittori, P. Jetzer, and A. Klein,
  9th LISA Symposium, Astronomical Society of the Pacific Conference Series, 467 (2013) 331.

- The M31 Pixel Lensing PLAN Campaign: MACHO Lensing and Self-lensing Signals
  S. Calchi Novati, V. Bozza, I. Bruni, M. Dall'Ora, F. De Paolis, M. Dominik, R. Gualandi, G. Ingrosso, P. Jetzer, L. Mancini, A. Nucita, M. Safonova, G. Scarpetta, M. Sereno, F. Strafella, A. Subramaniam, and A. Gould, (A. PLAN Collaboration), ApJ783 (2014) 86.

- MOND and IMF variations in early-type galaxies from ATLAS^3D
  C. Tortora, A.J. Romanowsky, V. F. Cardone, N. R. Napolitano, and P. Jetzer, MNRAS438 (2014) L46.

- eLISA: Astrophysics and cosmology in the millihertz regime
  P. Amaro-Seoane, S. Aoudia, S. Babak, P. Binétruy, E. Berti, A. Bohé, C. Caprini, M. Colpi, N.J. Cornish, K. Danzmann, J.F. Dufaux, J. Gair, I. Hinder, O. Jennrich, P. Jetzer, A. Klein, R.N. Lang, A. Lobo, T. Littenberg, S.T. McWilliams, G. Nelemans, A. Petiteau, E.K. Porter, B.F. Schutz, A. Sesana, R. Stebbins, T. Sumner, M. Vallisneri, S. Vitale, M. Volonteri, H. Ward, and B. Wardell, GW Notes 6, 4.

- Microlensing towards the SMC: a new analysis of OGLE and EROS results
  S. Calchi Novati, S. Mirzoyan, P. Jetzer, and G. Scarpetta, MNRAS435 (2013) 1582.

Oral Presentations

- Philippe Jetzer: 20 Years of Gravitational Microlensing
  ICRANet Scientific Meeting on Rel. Astrophysics, Pescara (Italy), June 2013.

- Philippe Jetzer: STE-QUEST and the Einstein Equivalence Principle
  GR20-Amaldi Meeting, Warsaw (Poland), July 2013.

- Philippe Jetzer: Gravitational Wave Dection from Space
  Int. Conf. on New Frontiers in Physics, Crete (Greece), August 2013.

- Philippe Jetzer: Gravitationslinsen und Dunkle Materie im Universum
  Kolloquium University of Wuppertal, October 2013.

21.1.3 Miscellaneous

Article

- The brief time-reversibility of the local Lyapunov exponents for a small chaotic Hamiltonian system
  F. Waldner, W.G. Hoover and C.G. Hoover, Chaos, Solitons & Fractals **60** (2014) 68.

21.2 Elementary particles and their interactions

21.2.1 GERDA

Articles

- The Background in the Neutrinoless Double Beta Decay Experiment GERDA
  M. Agostini, M. Allardt, E. Andreotti, A.M. Bakalyarov, M. Balata, I. Barabanov, M. Barnabe Heider, N. Barros, L. Baudis, C. Bauer *et al.* (GERDA Collaboration), Eur. Phys. J. C74, 2764 (2014).

- Pulse Shape Discrimination for GERDA Phase I Data
  M. Agostini, M. Allardt, E. Andreotti, A.M. Bakalyarov, M. Balata, I. Barabanov, M. Barnabe Heider, N. Barros, L. Baudis, C. Bauer *et al.* (GERDA Collaboration), Eur. Phys. J. C73 2583 (2013).

- Monte Carlo Studies for the Calibration System of the GERDA Experiment
  L. Baudis, A.D. Ferella, F. Froborg, M. Tarka, Nucl. Instrum. Meth. A729, 557-564 (2013).

- Results on Neutrinoless Double-Beta Decay of Ge76 from Phase I of the GERDA Experiment
  M. Agostini, M. Allardt, E. Andreotti, A.M. Bakalyarov, M. Balata, I. Barabanov, M. Barnabe Heider, N. Barros, L. Baudis, C. Bauer *et al.* (GERDA Collaboration), Phys. Rev. Lett. 111, 122503 (2013).

- Isotopically Modified Ge Detectors for Gerda: from Production to Operation
  D. Budjas, M. Agostini, L. Baudis, E. Bellotti, *et al.*, JINST 8, P04018 (2013).

Lectures and oral presentations

- L. Baudis: The Unbearable Lightness of Neutrinos
  Colloquium Paco Yndurain, UA Madrid, December 4, 2013.

- M. Walter: The GERDA Experiment for the Search of Neutrinoless Double Beta Decay
  Seminar on Particle and Astrophysics Uni Zurich, 16 October 2013.

- G. Benato: Search of Neutrinoless Double beta decay with the GERDA Experiment
  From Majorana to LHC, Workshop on the Origin of Neutrino Mass, ICTP, 2-5 October 2013.

- G. Benato: Search of Neutrinoless Double Beta Decay with the GERDA Experiment
  Joint Annual Meeting of OPG, SPS, OGAA and SGAA, Linz, 3-6 September 2013.

- M. Walter: The GERDA Experiment for the Search of Neutrinoless Double Beta Decay
  Patras Workshop, Schloss Waldthausen, July 27 2013.

21.2.2 XENON/DARWIN

Articles

- Analysis of the XENON100 Dark Matter Search Data
  E. Aprile, M. Alfonsi, K. Arisaka, F. Arneodo, C. Balan, L. Baudis, B. Bauermeister, *et al.* (XENON Collaboration), Astropart. Phys. 54 11-24 (2014).

- Signatures of Dark Matter Scattering Inelastically Off Nuclei
  L. Baudis, G. Kessler, P. Klos, R. F. Lang, J. Menendez, S. Reichard, and A. Schwenk, Phys. Rev. D88, 115014 (2013).

- Observation and Applications of Single-Electron Charge Signals in the XENON100 Experiment
  E. Aprile, M. Alfonsi, K. Arisaka, F. Arneodo, C. Balan, L. Baudis, B. Bauermeister, *et al.* (XENON Collaboration), J. Phys. G: Nucl. Part. Phys. 41, 035201 (2014).

- Neutrino Physics with Multi-Ton Scale Liquid Xenon Detectors
  L. Baudis, A. Ferella, A. Kish, A. Manalaysay, T. Marrodan Undagoitia, M. Schumann, J. Cosmol. Astropart. Phys. 01, 044 (2014).

- The Neutron Background of the XENON100 Dark Matter Experiment
  E. Aprile, M. Alfonsi, K. Arisaka, F. Arneodo, C. Balan, L. Baudis, B. Bauermeister, *et al.* (XENON Collaboration), J. Phys. G: Nucl. Part. Phys. 40, 115201 (2013).

- Response of the XENON100 Dark Matter Detector to Nuclear Recoils
  E. Aprile, M. Alfonsi, K. Arisaka, F. Arneodo, C. Balan, L. Baudis, B. Bauermeister, *et al.* (XENON Collaboration), Phys. Rev. D 88, 012006 (2013).

- Response of Liquid xenon to Compton Electrons Down to 1.5 keV
  L. Baudis, H. Dujmovic, C. Geis, A. James, A. Kish, A. Manalaysay, T. Marrodan Undagoitia, M. Schumann, Phys. Rev. D 87, 115015 (2013).

- Performance of the Hamamatsu R11410 Photomultiplier Tube in Cryogenic Xenon Environments
  L. Baudis, A. Behrens, A. Ferella, A. Kish, T. Marrodan Undagoitia, D. Mayani, M. Schumann, JINST 8 (2013) P04026.

- Limits on Spin-Dependent WIMP-nucleon Cross Sections from 225 live days of XENON100 Data
  E. Aprile, M. Alfonsi, K. Arisaka, F. Arneodo, C. Balan, L. Baudis, B. Bauermeister, *et al.* (XENON Collaboration), Phys. Rev. Lett. 111, 021301 (2013).

Lectures and oral presentations

- L. Baudis: Dark Matter Design Study
  APPEC general meeting, Paris, February 27, 2014.
- L. Baudis: Underground Physics
  DESY Zeuthen, November 4, 2013.
- L. Baudis: Noble Liquids
  APPEC SAC meeting, Paris, October 15, 2013.
- L. Baudis: WIMP Dark Matter Direct-Detection Searches in Noble Gases
  TAUP 2013, Asilomar, September 10, 2013.
- L. Baudis: Direct WIMP Searches: an Update
  SUSY meeting, ICTP Trieste, August 29, 2013.
- L. Baudis: Dark Matter: Direct Searches for WIMPs
  EPS-HEP meeting, Stockholm, July 23, 2013.
- L. Baudis: First results on the Neutrinoless Double Beta Decay from GERDA
  Invisibles workshop, Durham, July 17, 2013.
- L. Baudis: Searching for Dark Matter with XENON100, XENON1T and DARWIN
  Seminar, Queens University, Kingston, July 2, 2013.
- L. Baudis: XENON100, XENON1T and DARWIN
  CHIPP plenary meeting, Campus Sursee, June 26, 2013.
- L. Baudis: Searching for Dark Matter with XENON
  Seminar, LBNL, Berkeley, April 30, 2013.
- L. Baudis: XENON100 Direct Detection Results and Status of XENON1T
  Seminar, KITP, Santa Barbara, April 24, 2013.
- L. Baudis: Direct Dark Matter Detection in the Milky Way
  Physics Colloquium, Oskar Klein Centre for Cosmoparticle Physics, Stockholm, April 9, 2013.
- M. Auger: XENON and DARWIN R&D in Switzerland
  2nd CHIPP Workshop on Detector R&D, PSI, September 13 2013.
- A. Kish: Dark Matter Search with the XENON100 Experiment
  16th Lomonosov Conference on Elementary Particle Physics, Moscow State University, August 24, 2013.
- A. Behrens: Recent Results from the XENON Experiment
  EPS-HEP 2013, Stockholm, Sweden, July 18th, 2013.
- A. Kish: Dark Matter Search with the XENON100 Experiment
  Latsys Symposium, June 5, 2013.

Outreach

- L. Baudis: Die dunkle Seite des Universums
  SKL Liechtenstein, January 30, 2014.
- L. Baudis: Die dunkle Seite des Universums
  Seniorenforum Werdenberg, Buchs, November 19, 2013.

PhD thesis

- Light Detectors for the XENON100 and XENON1T Dark Matter Search Experiments
  A. Behrens, PhD thesis, Universität Zürich, 2013.

21.2.3 CTA

Articles

- Introducing the CTA concept
  B.S. Acharya *et al* (CTA Consortium), Astroparticle Physics **43** (2013) 3.

Conference contributions

- G. Ambrosi *et. al*: The Cherenkov Telescope Array Large Size Telescope
  33rd International Cosmic Ray Conference (ICRC2013), Rio de Janeiro (Brazil), arXiv:1307.4565v1 [astro-ph.IM].

- G. Pühlhofer *et. al*: FlashCam: A fully digital camera for the Cherenkov Telescope Array
  33rd International Cosmic Ray Conference (ICRC2013), Rio de Janeiro (Brazil), arXiv:1307.3677v1 [astro-ph.IM].

PhD thesis

- Towards the First Imaging Atmospheric Cherenkov Telescope Camera with Continuous Signal Digitization
  A. Gadola, PhD thesis, Universität Zürich, 2013.

21.2.4 H1

Articles

- Measurement of Charged Particle Spectra in Deep-Inelastic ep Scattering at HERA
  H1-Collaboration, C. Alexa *et al.*, Eur. Phys. J. C **73** (2013), 2406.

- Elastic and Proton Dissociative J/Ψ-Meson Photoproduction at HERA
  H1-Collaboration, C. Alexa *et al.*, Eur. Phys. J. C **73** (2013), 2466.

- Measurement of Inclusive ep Cross Sections at High Q^2 at $\sqrt{s} = 225$ and 252 GeV and of the Longitudinal Proton Structure Function F_L at HERA
  H1-Collaboration, V. Andreev *et al.*, Eur. Phys. J. C **74** (2014), 2814.

21.2.5 LHCb

Articles

- Search for Majorana neutrinos in $B^- \to \pi^+\mu^-\mu^-$ decays
  LHCb-Collaboration, R. Aaij *et al.*, Phys. Rev. Lett. **112** (2014) 131802.

- Updated measurements of exclusive J/ψ and ψ(2S) production cross-sections in pp collisions at $\sqrt{s} = 7$ TeV
  LHCb-Collaboration, R. Aaij *et al.*, J. Phys. G **41** (2014) 055002.

- Studies of beauty baryon decays to D^0ph^- and $\Lambda_c^+h^-$ final states
  LHCb-Collaboration, R. Aaij *et al.*, Phys. Rev. D **89** (2014) 032001.

- Measurement of the $\bar{B}_s^0 \to D_s^- D_s^+$ and $\bar{B}_s^0 \to D^- D_s^+$ effective lifetimes
  LHCb-Collaboration, R. Aaij *et al.*, Phys. Rev. Lett. **112** (2014) 111802.

- Study of forward Z plus jet production in pp collisions at $\sqrt{s} = 7$ TeV
  LHCb-Collaboration, R. Aaij *et al.*, JHEP **1401** (2014) 033.

- Search for CP violation in the decay $D^+ \to \pi^-\pi^+\pi^+$s
  LHCb-Collaboration, R. Aaij *et al.*, Phys. Lett. B **728** (2014) 585.

- Measurements of indirect CP asymmetries in $D^0 \to K^-K^+$ and $D^0 \to \pi^-\pi^+$ decays
  LHCb-Collaboration, R. Aaij *et al.*, Phys. Rev. Lett. **112** (2014) 011801.

- Search for the doubly charmed baryon Ξ_{cc}^{+}
LHCb-Collaboration, R. Aaij *et al.*, JHEP **1312** (2013) 090.

- Measurement of CP violation in the phase space of $B^{\pm} \to K^{+}K^{-}\pi^{\pm}$ and $B^{\pm} \to \pi^{+}\pi^{-}\pi^{\pm}$ decays,
LHCb-Collaboration, R. Aaij *et al.*, Phys. Rev. Lett. **112** (2014) 011801.

- Search for the decay $D^{0} \to \pi^{+}\pi^{-}\mu^{+}\mu^{-}$
LHCb-Collaboration, R. Aaij *et al.*, Phys. Lett. B **728** (2014) 234.

- Measurement of D^{0}–$\bar{D}^{0}$ mixing parameters and search for CP violation using $D^{0} \to K^{+}\pi^{-}$ decays
LHCb-Collaboration, R. Aaij *et al.*, Phys. Rev. Lett. **111** (2013) 251801.

- Measurement of the charge asymmetry in $B^{\pm} \to \phi K^{\pm}$ and search for $B^{\pm} \to \phi\pi^{\pm}$ decays
LHCb-Collaboration, R. Aaij *et al.*, Phys. Lett. B **728** (2014) 85.

- First observation of $\bar{B}^{0} \to J/\psi K^{+}K^{-}$ and search for $\bar{B}^{0} \to J/\psi\phi$ decays
LHCb-Collaboration, R. Aaij *et al.*, Phys. Rev. D **88** (2013) 072005.

- Observation of the decay $B_{s}^{0} \to \bar{D}^{0}\phi$
LHCb-Collaboration, R. Aaij *et al.*, Phys. Lett. B **727** (2013) 403.

- Observation of the decay $B_{c}^{+} \to B_{s}^{0}\pi^{+}$
LHCb-Collaboration, R. Aaij *et al.*, Phys. Rev. Lett. **111** (2013) 181801.

- Model-independent search for CP violation in $D^{0} \to K^{-}K^{+}\pi^{-}\pi^{+}$ and $D^{0} \to \pi^{-}\pi^{+}\pi^{+}\pi^{-}$ decays
LHCb-Collaboration, R. Aaij *et al.*, Phys. Lett. B **726** (2013) 623.

- Measurement of form-factor independent observables in the decay $B^{0} \to K^{*0}\mu^{+}\mu^{-}$ 93
LHCb-Collaboration, R. Aaij *et al.*, Phys. Rev. Lett. **111** (2013) 191801.

- First measurement of time-dependent CP violation in $B_{s}^{0}K^{+}K$ decays
LHCb-Collaboration, R. Aaij *et al.*, JHEP **1310** (2013) 183.

- Measurement of the CP asymmetry in $B^{+} \to K^{+}\mu^{+}\mu^{-}$ decays
LHCb-Collaboration, R. Aaij *et al.*, Phys. Rev. Lett. **111** (2013) 151801.

- Observation of B_{s}^{0}-$\bar{B}_{s}^{0}$ mixing and measurement of mixing frequencies using semileptonic B decays
LHCb-Collaboration, R. Aaij *et al.*, Eur. Phys. J. C **73** (2013) 2655.

- Branching fraction and CP asymmetry of the decays $B^{+} \to K_{S}^{0}\pi^{+}$ and $B^{+} \to K_{S}^{0}K^{+}$
LHCb-Collaboration, R. Aaij *et al.*, Phys. Lett. B **726** (2013) 646.

- Measurement of the flavour-specific CP-violating asymmetry a_{sl}^{s} in B_{s}^{0} decays
LHCb-Collaboration, R. Aaij *et al.*, Phys. Lett. B **728** (2014) 607.

- First evidence for the two-body charmless baryonic decay $B^{0} \to p\bar{p}$
LHCb-Collaboration, R. Aaij *et al.*, JHEP **1310** (2013) 005.

- Study of $B_{(s)}^{0} \to K_{S}^{0}h^{+}h'^{-}$ decays with first observation of $B_{s}^{0} \to K_{S}^{0}K^{\pm}\pi^{\mp}$ and $B_{s}^{0} \to K_{S}^{0}\pi^{+}\pi^{-}$
LHCb-Collaboration, R. Aaij *et al.*, JHEP **1310** (2013) 143.

- Observation of a resonance in $B^{+} \to K^{+}\mu^{+}\mu^{-}$ decays at low recoil
LHCb-Collaboration, R. Aaij *et al.*, Phys. Rev. Lett. **111** (2013) 11, 112003.

- Measurement of J/ψ polarization in pp collisions at $\sqrt{s} = 7$ TeV
LHCb-Collaboration, R. Aaij *et al.*, Eur. Phys. J. C **73** (2013) 2631.

- Studies of the decays $B^{+} \to p\bar{p}h^{+}$ and observation of $B^{+} \to \bar{\Lambda}(1520)p$
LHCb-Collaboration, R. Aaij *et al.*, Phys. Rev. D **88** (2013) 052015.

- Measurement of the $B_{s}^{0} \to \mu^{+}\mu^{-}$ branching fraction and search for $B^{0} \to \mu^{+}\mu^{-}$ decays at the LHCb experiment
LHCb-Collaboration, R. Aaij *et al.*, Phys. Rev. Lett. **111** (2013) 101805.

- Search for the lepton-flavor violating decays $B_s^0 \to e^\pm\mu^\mp$ and $B^0 \to e^\pm\mu^\mp$
  LHCb-Collaboration, R. Aaij *et al.*, Phys. Rev. Lett. **111** (2013) 141801.
- Measurement of the relative rate of prompt χ_{c0}, χ_{c1} and χ_{c2} production at $\sqrt{s} = 7$ TeV
  LHCb-Collaboration, R. Aaij *et al.*, JHEP **1310** (2013) 115.
- Measurement of the polarization amplitudes in $B^0 \to J/\psi K^*(892)^0$ decays
  LHCb-Collaboration, R. Aaij *et al.*, Phys. Rev. D **88** (2013) 052002.
- Precision measurement of the Λ_b^0 baryon lifetime
  LHCb-Collaboration, R. Aaij *et al.*, Phys. Rev. Lett. **111** (2013) 102003.
- Measurement of B meson production cross-sections in proton-proton collisions at $\sqrt{s} = 7$ TeV
  LHCb-Collaboration, R. Aaij *et al.*, JHEP **1308** (2013) 117.
- Measurement of the differential branching fraction of the decay $\Lambda_b^0 \to \Lambda\mu^+\mu^-$
  LHCb-Collaboration, R. Aaij *et al.*, Phys. Lett. B **725** (2013) 25.
- First observation of the decay $B_s^0 \to \phi\bar{K}^{*0}$
  LHCb-Collaboration, R. Aaij *et al.*, JHEP **1311** (2013) 092.
- Measurement of CP violation in the phase space of $B^\pm \to K^\pm\pi^+\pi^-$ and $B^\pm \to K^\pm K^+ K^-$ decays
  LHCb-Collaboration, R. Aaij *et al.*, Phys. Rev. Lett. **111** (2013) 101801.
- Observation of $B_s^0 \to \chi_{c1}\phi$ decay and study of $B^0 \to \chi_{c1,2}K^{*0}$ decays
  LHCb-Collaboration, R. Aaij *et al.*, Nucl. Phys. B **874** (2013) 663.
- Search for the rare decay $D^0 \to \mu^+\mu^-$,
  LHCb-Collaboration, R. Aaij *et al.*, Phys. Lett. B **725** (2013) 15.
- Differential branching fraction and angular analysis of the decay $B_s^0 \to \phi\mu^+\mu^-$
  LHCb-Collaboration, R. Aaij *et al.*, JHEP **1307** (2013) 084.
- Measurement of the CKM angle γ from a combination of $B^\pm \to Dh^\pm$ analyses
  LHCb-Collaboration, R. Aaij *et al.*, Phys. Lett. B **726** (2013) 151.
- Production of J/ψ and Υ mesons in pp collisions at $\sqrt{s} = 8$ TeV
  LHCb-Collaboration, R. Aaij *et al.*, JHEP **1306** (2013) 064.
- Precision measurement of D meson mass differences
  LHCb-Collaboration, R. Aaij *et al.*, JHEP **1306** (2013) 065.
- Search for $D_{(s)}^+ \to \pi^+\mu^+\mu^-$ and $D_{(s)}^+ \to \pi^-\mu^+\mu^+$ decays
  LHCb-Collaboration, R. Aaij *et al.*, Phys. Lett. B **724** (2013) 203.
- Differential branching fraction and angular analysis of the decay $B^0 \to K^{*0}\mu^+\mu^-$
  LHCb-Collaboration, R. Aaij *et al.*, JHEP **1308** (2013) 131.
- Measurement of the branching fractions of the decays $B_s^0 \to \overline{D}^0 K^-\pi^+$ and $B^0 \to \overline{D}^0 K^+\pi^-$
  LHCb-Collaboration, R. Aaij *et al.*, Phys. Rev. D **87** (2013) 11, 112009.
- First observation of CP violation in the decays of B_s^0 mesons
  LHCb-Collaboration, R. Aaij *et al.*, Phys. Rev. Lett. **110** (2013) 22, 221601.
- Precision measurement of the B_s^0-$\bar{B}_s^0$ oscillation frequency with the decay $B_s^0 \to D_s^-\pi^+$
  LHCb-Collaboration, R. Aaij *et al.*, New J. Phys. **15** (2013) 053021.
- Observation of $B_c^+ \to J/\psi D_s^+$ and $B_c^+ \to J/\psi D_s^{*+}$ decays
  LHCb-Collaboration, R. Aaij *et al.*, Phys. Rev. D **87** (2013) 11, 112012.
- Searches for violation of lepton flavour and baryon number in tau lepton decays at LHCb
  LHCb-Collaboration, R. Aaij *et al.*, Phys. Lett. B **724** (2013) 36.

- Measurement of the effective $B_s^0 -> J/\psi K_S^0$ lifetime
  LHCb-Collaboration, R. Aaij *et al.*, Nucl. Phys. B **873** (2013) 275.

- Measurement of the $B^0 \to K^{*0} e^+ e^-$ branching fraction at low dilepton mass
  LHCb-Collaboration, R. Aaij *et al.*, JHEP **1305** (2013) 159.

- Measurement of CP violation and the B_s^0 meson decay width difference with $B_s^0 \to J/\psi K^+ K^-$ and $B_s^0 \to J/\psi \pi^+ \pi^-$ decays
  LHCb-Collaboration, R. Aaij *et al.*, Phys. Rev. D **87** (2013) 11, 112010.

- Limits on neutral Higgs boson production in the forward region in pp collisions at $\sqrt{s} = 7$ TeV
  LHCb-Collaboration, R. Aaij *et al.*, JHEP **1305** (2013) 132.

- Measurements of the branching fractions of $B^+ \to p\bar{p}K^+$ decays
  LHCb-Collaboration, R. Aaij *et al.*, Eur. Phys. J. C **73** (2013) 2462.

- First measurement of the CP-violating phase in $B_s^0 \to \phi\phi$ decays
  LHCb-Collaboration, R. Aaij *et al.*, Phys. Rev. Lett. **110** (2013) 24, 241802 [arXiv:1303.7125].

- Study of $B^0 \to D^{*-}\pi^+\pi^-\pi^+$ and $B^0 \to D^{*-}K^+\pi^-\pi^+$ decays
  LHCb-Collaboration, R. Aaij *et al.*, Phys. Rev. D **87** (2013) 092001.

- Search for CP violation in $D^+ \to \phi\pi^+$ and $D_s^+ \to K_S^0\pi^+$ decays
  LHCb-Collaboration, R. Aaij *et al.*, JHEP **1306** (2013) 112.

- Observation of the suppressed ADS modes $B^\pm \to [\pi^\pm K^\mp \pi^+ \pi^-]_D K^\pm$ and $B^\pm \to [\pi^\pm K^\mp \pi^+ \pi^-]_D \pi^\pm$
  LHCb-Collaboration, R. Aaij *et al.*, Phys. Lett. B **723** (2013) 44.

- Search for direct CP violation in $D^0 \to h^- h^+$ modes using semileptonic B decays
  LHCb-Collaboration, R. Aaij *et al.*, Phys. Lett. B **723** (2013) 33.

- Observation of the decay $B_c^+ \to \psi(2S)\pi^+$
  LHCb-Collaboration, R. Aaij *et al.*, Phys. Rev. D **87** (2013) 071103.

- Search for rare $B_{(s)}^0 \to \mu^+\mu^-\mu^+\mu^-$ decays
  LHCb-Collaboration, R. Aaij *et al.*, Phys. Rev. Lett. **110** (2013) 211801.

- Search for the decay $B_s^0 \to D^{*\mp}\pi^\pm$
  LHCb-Collaboration, R. Aaij *et al.*, Phys. Rev. D **87** (2013) 071101.

- First observations of $\bar{B}_s^0 \to D^+D^-$, $D_s^+D^-$ and $D^0\bar{D}^0$ decays
  LHCb-Collaboration, R. Aaij *et al.*, Phys. Rev. D **87** (2013) 9, 092007.

- Measurements of the $\Lambda_b^0 \to J/\psi\Lambda$ decay amplitudes and the Λ_b^0 polarisation in pp collisions at $\sqrt{s} = 7$ TeV
  LHCb-Collaboration, R. Aaij *et al.*, Phys. Lett. B **724** (2013) 27.

- Amplitude analysis and the branching fraction measurement of $\bar{B}_s^0 \to J/\psi K^+K^-$
  LHCb-Collaboration, R. Aaij *et al.*, Phys. Rev. D **87** (2013) 7, 072004.

- Measurement of the Λ_b^0, Ξ_b^- and Ω_b^- baryon masses
  LHCb-Collaboration, R. Aaij *et al.*, Phys. Rev. Lett. **110** (2013) 182001.

- Measurement of the fragmentation fraction ratio f_s/f_d and its dependence on B meson kinematics
  LHCb-Collaboration, R. Aaij *et al.*, JHEP **1304** (2013) 001.

- Electroweak Physics, QCD and Jets in the Forward Region
  N. Chiapolini *et al.*, Acta Physica Polonica B, 44(7):1385.

articles in press

- Angular analysis of charged and neutral $B \to K\mu^+\mu^-$ decays
  LHCb-Collaboration, R. Aaij *et al.*, arXiv:1403.8045.

- Differential branching fractions and isospin asymmetries of $B \to K^{(*)}\mu^+\mu^-$ decays
  LHCb-Collaboration, R. Aaij *et al.*, arXiv:1403.8044.

- Study of beauty hadron decays into pairs of charm hadrons
  LHCb-Collaboration, R. Aaij *et al.*, arXiv:1403.3606.

- Measurement of polarization amplitudes and CP asymmetries in $B^0 \to \phi K^*(892)^0$
  LHCb-Collaboration, R. Aaij *et al.*, arXiv:1403.2888.

- Measurement of $\psi(2S)$ polarisation in pp collisions at $\sqrt{s} = 7$ TeV
  LHCb-Collaboration, R. Aaij *et al.*, arXiv:1403.1339.

- Observation of photon polarization in the $b \to s\gamma$ transition
  LHCb-Collaboration, R. Aaij *et al.*, arXiv:1402.6852.

- Measurement of resonant and CP components in $\overline{B}^0_s \to J/\psi\pi^+\pi^-$ decays
  LHCb-Collaboration, R. Aaij *et al.*, arXiv:1402.6248.

- Precision measurement of the ratio of the Λ^0_b to $\overline{B}^0$ lifetimes
  LHCb-Collaboration, R. Aaij *et al.*, arXiv:1402.6242.

- Measurement of charged particle multiplicities and densities in pp collisions at $\sqrt{s} = 7$ TeV in the forward region
  LHCb-Collaboration, R. Aaij *et al.*, arXiv:1402.4430.

- A study of CP violation in $B^\pm \to DK^\pm$ and $B^\pm \to D\pi^\pm$ decays with $D \to K^0_S K^\pm \pi^\mp$ final states
  LHCb-Collaboration, R. Aaij *et al.*, arXiv:1402.2982.

- Measurements of the B^+, B^0, B^0_s meson and Λ^0_b baryon lifetimes
  LHCb-Collaboration, R. Aaij *et al.*, arXiv:1402.2554.

- Measurement of Υ production in pp collisions at $\sqrt{s} = 2.76$ TeV
  LHCb-Collaboration, R. Aaij *et al.*, arXiv:1402.2539.

- Searches for Λ^0_b and Ξ^0_b decays to $K^0_S p\pi^-$ and $K^0_S pK^-$ final states with first observation of the $\Lambda^0_b \to K^0_S p\pi^-$ decay
  LHCb-Collaboration, R. Aaij *et al.*, arXiv:1402.0770.

- Measurement of the B^+_c meson lifetime using $B^+_c \to J/\psi\mu^+\nu_\mu X$ decays
  LHCb-Collaboration, R. Aaij *et al.*, arXiv:1401.6932.

- Observation of associated production of a Z boson with a D meson in the forward region
  LHCb-Collaboration, R. Aaij *et al.*, arXiv:1401.3245.

- Observation of $B^0_(s) \to J/\psi f_1(1285)$ decays and measurement of the $f_1(1285)$ mixing angle
  LHCb-Collaboration, R. Aaij *et al.*, arXiv:1310.2145.

Conference contributions

- Albert Bursche: New LHCb measurement: Z plus D meson cross section
  The top charm frontier at the LHCb, 14 January 2014, CERN, Switzerland

- Albert Bursche: Measurements with electroweak gauge bosons at LHCb
  MPI@LHC, 2 - 6 December 2013, Antwerp, Belgium

- Christian Elsasser: The LHCb Silicon Tracker
  13th Topical Seminar on Innovative Particle and Radiation Detectors, 7 - 10 October, Siena, Italy

- Jonathan Anderson: Latest results on Z boson production from LHCb
  LHC seminar, 8 October 2013, CERN, Switzerland

- Olaf Steinkamp: LHCb overview talk
  16th Lomonosov Conference on Elementary Particle Physics, 22 - 28 August 2013, Moscow, Russia

- Espen E. Bowen: Studies of the electroweak penguin transitions and radiative B decays at LHCb
  DPF 13, 13 - 17 August 2013, Santa Cruz, USA

- Christian Elsasser: Latest results on $B_s/B_d \to \mu\mu$ from CMS and LHCb
  Collider Cross Talk, 25 July 2013,CERN, Switzerland

- Nicola Serra: Studies of the electroweak penguin transitions $b_s \to \mu\mu$ and $b_d \to \mu\mu$ at LHCb
  EPS, 17 - 24 July 2013, Stockholm, Sweden

- Christian Elsasser: LHCb physics results
  2013 CHIPP Annual Plenary Meeting, 25 June 2013, Sursee, Switzerland

- Katharina Müller: Results and prospects on central exclusive production at LHCb
  Low-x workshop, 30 May - 4 June 2013, Rehovot and Eilat, Israel

- Christian Elsasser: Rare decays
  Large Hadron Collider Physics Conference, 13 - 18 May, 2013, Barcelona, Spain

- Marco Tresch: Rare decays at LHCb
  Phenomenology Symposium, 6 - 8 May 2013, Pittsburgh, USA

Public notes and technical reports

- LHCb Tracker Upgrade Technical Design Report
  LHCb collaboration, CERN-LHCC-2014-001 ; LHCB-TDR-015

- LHCb VELO Upgrade Technical Design Report
  LHCb collaboration, CERN-LHCC-2013-021 ; LHCB-TDR-013

- LHCb PID Upgrade Technical Design Report
  LHCb collaboration, CERN-LHCC-2013-022 ; LHCB-TDR-014

- VeloUT tracking for the LHCb Upgrade
  E. Bowen, B. Storacci, LHCb-PUB-2013-023; CERN-LHCb-PUB-2013-023

PhD thesis

- Track Reconstruction Efficiency and Analysis of $B^0 \to K^{*0}\mu^+\mu^-$ at the LHCb Experiment
  Michel De Cian, PhD Thesis, Universität Zürich, 2013

21.2.6 CMS

Articles (including those in press)

- Measurement of the t-channel single-top-quark production cross section and of the $|V_{tb}|$ CKM matrix element in pp collisions at $\sqrt{s} = 8$ TeV
  V. Khachatryan *et al.* [CMS Collaboration], arXiv:1403.7366 [hep-ex].

- Measurement of WZ and ZZ production in pp collisions at $\sqrt{s} = 8$ TeV in final states with b-tagged jets
  S. Chatrchyan *et al.* [CMS Collaboration], arXiv:1403.3047 [hep-ex].

- Alignment of the CMS tracker with LHC and cosmic ray data
  S. Chatrchyan *et al.* [CMS Collaboration], arXiv:1403.2286 [physics.ins-det].

- Studies of exotic hadrons at Tevatron and LHC
  V. Chiochia *et al.* [CDF and CMS and D0 and LHCb Collaborations], arXiv:1403.0823 [hep-ex].

- Search for new physics in the multijet and missing transverse momentum final state in proton-proton collisions at $\sqrt{s} = 8$ TeV
  S. Chatrchyan *et al.* [CMS Collaboration], arXiv:1402.4770 [hep-ex].

- Measurements of the $t\bar{t}$ charge asymmetry using the dilepton decay channel in pp collisions at $\sqrt{s} = 7$ TeV
  S. Chatrchyan *et al.* [CMS Collaboration], arXiv:1402.3803 [hep-ex].

- Search for W' to tb decays in the lepton + jets final state in pp collisions at $\sqrt{s} = 8$ TeV
  S. Chatrchyan *et al.* [CMS Collaboration], arXiv:1402.2176 [hep-ex].

- Measurement of the production cross sections for a Z boson and one or more b jets in pp collisions at $\sqrt{s} = 7$ TeV
  S. Chatrchyan *et al.* [CMS Collaboration], arXiv:1402.1521 [hep-ex].

- Measurement of inclusive W and Z boson production cross sections in pp collisions at sqrt(s) = 8 TeV
  S. Chatrchyan *et al.* [CMS Collaboration], arXiv:1402.0923 [hep-ex].

- Evidence for the direct decay of the 125 GeV Higgs boson to fermions
  S. Chatrchyan *et al.* [CMS Collaboration], arXiv:1401.6527 [hep-ex].

- Evidence for the 125 GeV Higgs boson decaying to a pair of τ leptons
  S. Chatrchyan *et al.* [CMS Collaboration], arXiv:1401.5041 [hep-ex].

- Studies of dijet pseudorapidity distributions and transverse momentum balance in pPb collisions at $\sqrt{s_{NN}}$=5.02 TeV
  S. Chatrchyan *et al.* [CMS Collaboration], arXiv:1401.4433 [nucl-ex].

- Observation of the associated production of a single top quark and a W boson in pp collisions at $\sqrt{s} = 8$ TeV
  S. Chatrchyan *et al.* [CMS Collaboration], arXiv:1401.2942 [hep-ex].

- Measurement of the $t\bar{t}$ production cross section in the dilepton channel in pp collisions at $\sqrt{s} = 8$ TeV
  S. Chatrchyan *et al.* [CMS Collaboration], arXiv:1312.7582 [hep-ex], JHEP **1402**, 024 (2014).

- Measurement of the production cross section for a W boson and two b jets in pp collisions at $\sqrt{s} = 7$ TeV
  S. Chatrchyan *et al.* [CMS Collaboration], arXiv:1312.6608 [hep-ex].

- Measurement of four-jet production in proton-proton collisions at $\sqrt{s}$=7 TeV
  S. Chatrchyan *et al.* [CMS Collaboration], arXiv:1312.6440 [hep-ex].

- Event activity dependence of Y(nS) production in sqrt(s[NN])=5.02 TeV pPb and sqrt(s)=2.76 TeV pp collisions
  S. Chatrchyan *et al.* [CMS Collaboration], arXiv:1312.6300 [nucl-ex].

- Measurement of the muon charge asymmetry in inclusive pp $\to$ W + X production at $\sqrt{s}$=7 TeV and an improved determination of light parton distribution functions
  S. Chatrchyan *et al.* [CMS Collaboration], arXiv:1312.6283 [hep-ex].

- Study of double parton scattering using W + 2-jet events in proton-proton collisions at $\sqrt{s} = 7$ TeV
  S. Chatrchyan *et al.* [CMS Collaboration], JHEP **1403**, 032 (2014).

- Measurement of the properties of a Higgs boson in the four-lepton final state
  S. Chatrchyan *et al.* [CMS Collaboration], arXiv:1312.5353 [hep-ex].

- Evidence of b-jet quenching in PbPb collisions at $\sqrt{s_{NN}} = 2.76$ TeV
  S. Chatrchyan *et al.* [CMS Collaboration], arXiv:1312.4198 [nucl-ex].

- Search for flavor-changing neutral currents in top-quark decays $t \to Zq$ in pp collisions at $\sqrt{s}$=8 TeV
  S. Chatrchyan *et al.* [CMS Collaboration], arXiv:1312.4194 [hep-ex].

- Search for stop and higgsino production using diphoton Higgs boson decays
  S. Chatrchyan *et al.* [CMS Collaboration], arXiv:1312.3310 [hep-ex].

- Search for top-quark partners with charge 5/3 in the same-sign dilepton final state
  S. Chatrchyan *et al.* [CMS Collaboration], arXiv:1312.2391 [hep-ex].

- Studies of azimuthal dihadron correlations in ultra-central PbPb collisions at $\sqrt{s_{NN}} = 2.76$ TeV
  S. Chatrchyan *et al.* [CMS Collaboration], JHEP **1402**, 088 (2014).

- Measurement of Higgs boson production and properties in the WW decay channel with leptonic final states
  S. Chatrchyan *et al.* [CMS Collaboration], JHEP **1401**, 096 (2014).

- Inclusive search for a vector-like T quark with charge $\frac{2}{3}$ in pp collisions at $\sqrt{s} = 8$ TeV
  S. Chatrchyan *et al.* [CMS Collaboration], Phys. Lett. B **729**, 149 (2014).

- Search for new physics in events with same-sign dileptons and jets in pp collisions at $\sqrt{s} = 8$ TeV
  S. Chatrchyan *et al.* [CMS Collaboration], JHEP **1401**, 163 (2014).

- Measurement of the triple-differential cross section for photon+jets production in proton-proton collisions at $\sqrt{s}$=7 TeV
  S. Chatrchyan *et al.* [CMS Collaboration], arXiv:1311.6141 [hep-ex].

- Probing color coherence effects in pp collisions at $\sqrt{s} = 7$ TeV
  S. Chatrchyan *et al.* [CMS Collaboration], arXiv:1311.5815 [hep-ex].

- Search for pair production of excited top quarks in the lepton+jets final state
  S. Chatrchyan *et al.* [CMS Collaboration], arXiv:1311.5357 [hep-ex].

- Search for supersymmetry in pp collisions at $\sqrt{s} = 8$ TeV in events with a single lepton, large jet multiplicity, and multiple b jets
  S. Chatrchyan *et al.* [CMS Collaboration], arXiv:1311.4937 [hep-ex].

- Measurements of $t\bar{t}$ spin correlations and top-quark polarization using dilepton final states in pp collisions at $\sqrt{s} = 7$ TeV
  S. Chatrchyan *et al.* [CMS Collaboration], arXiv:1311.3924 [hep-ex].

- Searches for light- and heavy-flavour three-jet resonances in pp collisions at $\sqrt{s} = 8$ TeV
  S. Chatrchyan *et al.* [CMS Collaboration], Phys. Lett. B **730**, 193 (2014).

- Measurement of higher-order harmonic azimuthal anisotropy in PbPb collisions at a nucleon-nucleon center-of-mass energy of 2.76 TeV
  S. Chatrchyan *et al.* [CMS Collaboration], arXiv:1310.8651 [nucl-ex].

- Measurement of the differential and double-differential Drell-Yan cross sections in proton-proton collisions at $\sqrt{s} = 7$ TeV
  S. Chatrchyan *et al.* [CMS Collaboration], JHEP **1312**, 030 (2013).

- Jet and underlying event properties as a function of charged-particle multiplicity in protonÃŘproton collisions at $\sqrt{s} = 7$ TeV
  S. Chatrchyan *et al.* [CMS Collaboration], Eur. Phys. J. C **73**, 2674 (2013).

- Search for the standard model Higgs boson produced in association with a W or a Z boson and decaying to bottom quarks
  S. Chatrchyan *et al.* [CMS Collaboration], Phys. Rev. D **89**, 012003 (2014).

- Rapidity distributions in exclusive Z + jet and γ + jet events in pp collisions at $\sqrt{s}$=7 TeV
  S. Chatrchyan *et al.* [CMS Collaboration], Phys. Rev. D **88**, 112009 (2013).

- Search for baryon number violation in top-quark decays
  S. Chatrchyan *et al.* [CMS Collaboration], Phys. Lett. B **731**, 173 (2014).

- Measurement of the cross section and angular correlations for associated production of a Z boson with b hadrons in pp collisions at $\sqrt{s} = 7$ TeV
  S. Chatrchyan *et al.* [CMS Collaboration], JHEP **1312**, 039 (2013).

- Measurement of associated W + charm production in pp collisions at $\sqrt{s} = 7$ TeV
  S. Chatrchyan *et al.* [CMS Collaboration], JHEP **1402**, 013 (2014).

- Modification of jet shapes in PbPb collisions at $\sqrt{s_{NN}} = 2.76$ TeV
  S. Chatrchyan *et al.* [CMS Collaboration], Phys. Lett. B **730**, 243 (2014).

- Observation of a peaking structure in the J/$\psi\phi$ mass spectrum from $B^{\pm} \to J/\psi\phi K^{\pm}$ decays
  S. Chatrchyan *et al.* [CMS Collaboration], arXiv:1309.6920 [hep-ex].

- Searches for new physics using the $t\bar{t}$ invariant mass distribution in pp collisions at $\sqrt{s}$=8??TeV
  S. Chatrchyan *et al.* [CMS Collaboration], Phys. Rev. Lett. **111**, 211804 (2013).

- Measurement of the production cross section for $Z\gamma \to \nu\bar{\nu}\gamma$ in pp collisions at $\sqrt{s} = 7$ TeV and limits on $ZZ\gamma$ and $Z\gamma\gamma$ triple gauge boson couplings
  S. Chatrchyan *et al.* [CMS Collaboration], JHEP **1310**, 164 (2013).

- Search for a new bottomonium state decaying to $\Upsilon(1S)\pi^+\pi^-$ in pp collisions at $\sqrt{s} = 8$ TeV
  S. Chatrchyan *et al.* [CMS Collaboration], Phys. Lett. B **727**, 57 (2013).

- Measurement of the $W\gamma$ and $Z\gamma$ inclusive cross sections in pp collisions at $\sqrt{s} = 7$ TeV and limits on anomalous triple gauge boson couplings
  S. Chatrchyan *et al.* [CMS Collaboration], arXiv:1308.6832 [hep-ex].

- Measurement of the W-boson helicity in top-quark decays from $t\bar{t}$ production in lepton+jets events in pp collisions at $\sqrt{s} = 7$ TeV
  S. Chatrchyan *et al.* [CMS Collaboration], JHEP **1310**, 167 (2013).

- Angular analysis and branching fraction measurement of the decay $B^0 \to K^{*0}\mu^+\mu^-$
  S. Chatrchyan *et al.* [CMS Collaboration], Phys. Lett. B **727**, 77 (2013).

- Search for top-squark pair production in the single-lepton final state in pp collisions at $\sqrt{s} = 8$ TeV
  S. Chatrchyan *et al.* [CMS Collaboration], Eur. Phys. J. C **73**, 2677 (2013).

- Measurement of the prompt J/ψ and $\psi(2S)$ polarizations in pp collisions at $\sqrt{s} = 7$ TeV
  S. Chatrchyan *et al.* [CMS Collaboration], Phys. Lett. B **727**, 381 (2013).

- Search for a Higgs boson decaying into a Z and a photon in pp collisions at $\sqrt{s} = 7$ and 8 TeV
  S. Chatrchyan *et al.* [CMS Collaboration], Phys. Lett. B **726**, 587 (2013).

- Measurement of the B(s) to mu+ mu- branching fraction and search for B0 to mu+ mu- with the CMS Experiment
  S. Chatrchyan *et al.* [CMS Collaboration], Phys. Rev. Lett. **111**, 101804 (2013).

- Measurement of the top-quark mass in all-jets t t-bar events in pp collisions at sqrt(s) = 7 TeV
  S. Chatrchyan *et al.* [CMS Collaboration], Eur. Phys. J. C **74**, 2758 (2014).

- Study of the production of charged pions, kaons, and protons in pPb collisions at $\sqrt{s_{NN}} = 5.02$ TeV
  S. Chatrchyan *et al.* [CMS Collaboration], arXiv:1307.3442 [hep-ex].

- Determination of the top-quark pole mass and strong coupling constant from the $t\bar{t}$ production cross section in pp collisions at $\sqrt{s} = 7$ TeV
  S. Chatrchyan *et al.* [CMS Collaboration], Phys. Lett. B **728**, 496 (2014).

- The performance of the CMS muon detector in proton-proton collisions at sqrt(s) = 7 TeV at the LHC
  S. Chatrchyan *et al.* [CMS Collaboration], JINST **8**, P11002 (2013).

- Search for top squarks in R-parity-violating supersymmetry using three or more leptons and b-tagged jets
  S. Chatrchyan *et al.* [CMS Collaboration], Phys. Rev. Lett. **111**, 221801 (2013).

- Energy calibration and resolution of the CMS electromagnetic calorimeter in pp collisions at ÃČs = 7 TeV
  S. Chatrchyan *et al.* [CMS Collaboration], JINST **8**, P09009 (2013).

- Measurement of the W^+W^- Cross section in pp Collisions at $\sqrt{s} = 7$ TeV and Limits on Anomalous $WW\gamma$ and WWZ couplings
  S. Chatrchyan *et al.* [CMS Collaboration], Eur. Phys. J. C **73**, 2610 (2013).

- Measurement of the hadronic activity in events with a Z and two jets and extraction of the cross section for the electroweak production of a Z with two jets in pp collisions at $\sqrt{s} = 7$ TeV
  S. Chatrchyan *et al.* [CMS Collaboration], JHEP **1310**, 101 (2013).

- Measurement of neutral strange particle production in the underlying event in proton-proton collisions at sqrt(s) = 7 TeV
  S. Chatrchyan *et al.* [CMS Collaboration], Phys. Rev. D **88**, 052001 (2013).

- Study of exclusive two-photon production of W^+W^- in pp collisions at $\sqrt{s} = 7$ TeV and constraints on anomalous quartic gauge couplings
  S. Chatrchyan *et al.* [CMS Collaboration], JHEP **1307**, 116 (2013).

- Search for gluino mediated bottom- and top-squark production in multijet final states in pp collisions at 8 TeV
  S. Chatrchyan *et al.* [CMS Collaboration], Phys. Lett. B **725**, 243 (2013).

- Multiplicity and transverse momentum dependence of two- and four-particle correlations in pPb and PbPb collisions
  S. Chatrchyan *et al.* [CMS Collaboration], Phys. Lett. B **724**, 213 (2013).

- Searches for long-lived charged particles in pp collisions at $\sqrt{s}$=7 and 8 TeV
  S. Chatrchyan *et al.* [CMS Collaboration], JHEP **1307**, 122 (2013).

- Measurement of the ratio of the inclusive 3-jet cross section to the inclusive 2-jet cross section in pp collisions at $\sqrt{s} =$ 7 TeV and first determination of the strong coupling constant in the TeV range
  S. Chatrchyan *et al.* [CMS Collaboration],Eur. Phys. J. C **73**, 2604 (2013).

- Measurement of the Λ_b^0 lifetime in pp collisions at $\sqrt{s} = 7$ TeV
  S. Chatrchyan *et al.* [CMS Collaboration], JHEP **07**, 163 (2013).

- Measurement of masses in the $t\bar{t}$ system by kinematic endpoints in pp collisions at $\sqrt{s} = 7$ TeV
  S. Chatrchyan *et al.* [CMS Collaboration], Eur. Phys. J. C **73**, 2494 (2013).

Conference proceedings

- Operation of the CMS silicon tracker
  S. Taroni [for the CMS Collaboration], Proceedings of Science (RD13) 002.

- Searches for heavy resonances decaying to pairs of massive vector bosons in CMS
  A. Hinzmann [for the CMS Collaboration], Proceedings of EPSHEP 2013, PoS(EPS-HEP 2013)283 (2014).

- Performance of the current CMS pixel detector
  S. Taroni [for the CMS Collaboration], Proceedings of the 2013 IEEE-NSS symposium, CMS CR-2013/096.

- Studies of exotic hadrons at Tevatron and LHC
  V. Chiochia [for the CDF, CMS, D0 and LHCb Collaborations], arXiv:1403.0823, Proceedings of Science (Hadron 2013) 009.

Oral presentations

- F. Canelli: Results from the LHC
  2013 APS meeting, plenary invited talk, April 15, 2013, Denver, Colorado, USA.

- C. Lange: Measurement of W/Z boson + heavy quark production at ATLAS
  XXI International Workshop on Deep-Inelastic Scattering and Related Subjects (DIS 2013), 22-26 April 2013, Marseilles, France.

- F. Canelli: The wisdom of the matrix element method
  2013 Matrix Element Technique Workshop, invited talk, May 27, 2013, Bruxelles, Belgium.

- F. Canelli: The future of the multivariate analyses
  KITP Workshop on LHC physics, invited talk, July 31, 2013, Santa Barbara, California, USA.

- B. Kilminster: New resonant particle searches at CMS
  Frontiers of Science seminar, Kavli Institute, July 2013, Santa Barbara, California, USA.

- S. Taroni: CMS Physics Results
  2013 CHIPP Plenary Meeting, June 25, 2013, Campus Sursee, Switzerland.

- S. Taroni: CMS Silicon Tracker operations
  11th Int. Conference on Large Scale Applications and Radiation Hardness of Semiconductor Detectors, July 3-5, 2013, Florence, Italy.

- A. Hinzmann: Searches for heavy resonances decaying to pairs of massive vector bosons in CMS
  EPSHEP 2013, July 2013, Stockholm, Sweden, 2014.

- M. Verzetti: Search for Higgs bosons at CMS in final states containing a tau
  21st International Conference on Supersymmetry and Unification of Fundamental Interactions, August 26-31, 2013, ICTP Trieste, Italy.

- V. Chiochia: Heavy flavor physics with the CMS experiment
  Seminar, Frankfurt University, September 25-26, 2013, Darmstadt/Frankfurt, Germany.

- B. Kilminster: CCD detectors for dark matter searches
  2nd CHIPP Workshop on Detector R&D, PSI Villigen, September 2013, Switzerland.

- B. Kilminster: Upgrade of the CMS detector
  2nd CHIPP Workshop on Detector R&D, PSI Villigen, September 2013, Switzerland.

- V. Chiochia: The Large Hadron Collider and the Higgs boson: latest news from the energy frontier
  Public lecture given at the Uni-Turm, Zurich University, October 8, 2013, Zurich, Switzerland.

- S. Taroni: Performance of the CMS pixel detector
  IEEE Nuclear Science Symposium, October 28, 2013, Seul, Korea.

- V. Chiochia: Production and spectroscopy of exotic hadrons at hadron colliders
  XV International conference on hadron spectroscopy, November 4-8, 2013, Nara, Japan.

- V. Chiochia: Heavy flavor physics with the CMS experiment
  Seminar, DESY Hamburg and DESY Zeuthen, November 19-20, 2013, Hamburg/Berlin, Germany.

- B. Kilminster: Secrets of the universe beyond the Higgs boson
  Antrittsvorlesung, University of Zurich, December 2013, Zurich, Switzerland.

- V. Chiochia: Heavy flavor physics with the CMS experiment
  Seminar, Purdue University, January 24, 2014, West-Lafayette, Indiana, USA.

- V. Chiochia: The CMS pixel detector: from design to discoveries
  Seminar, LMU University Munich, January 31, 2014, Munich, Germany.

- C. Galloni: Measurement of $R = B\ (t \rightarrow Wb)\ /B\ (t \rightarrow Wq)$ in Top-quark-pair Decays using Dilepton Events
  XLIXth Rencontres de Moriond Electroweak, March 15, 22, 2014, La Thuile, Italy.

- V. Chiochia: Heavy flavor physics with the CMS experiment
  Seminar, Imperial College London, March 25, 2014, London, UK.

PhD theses

- Measurement of the production cross section of prompt J/psi mesons in association with a W boson in pp collisions at sqrts=7 TeV with the ATLAS detector
  C. Melachrinos, University of Chicago, CERN-THESIS-2013-204

- Study of the Associated Production of a Z Boson with b Hadrons in Proton-Proton Collisions with the CMS Experiment
  C. Favaro, University of Zürich, CMS TS-2013/057.

21.3 Condensed matter

21.3.1 Superconductivity and Magnetism

Articles

- Tuning the static spin-stripe phase and superconductivity in $La_{2-x}Ba_xCuO_4$ ($x = 1/8$) by hydrostatic pressure
  Z. Guguchia, A. Maisuradze, G. Ghambashidze, R. Khasanov, A. Shengelaya, and H. Keller,
  New J. Phys. **15**, 093005 (2013).

- Magnetic phase diagram of low-doped $La_{2-x}Sr_xCuO_4$ thin films studied by low-energy muon-spin rotation
  E. Stilp, A. Suter, T. Prokscha, E. Morenzoni, H. Keller, B. M. Wojek, H. Luetkens, A. Gozar, G. Logvenov, and I. Božović, Phys. Rev. B **88**, 064419 (2013).

- Nonlinear pressure dependence of T_N in almost multiferroic $EuTiO_3$
  Z. Guguchia, K. Caslin, R.K. Kremer, H. Keller, A. Shengelaya, A. Maisuradze, J.L. Bettis Jr, J. Köhler, A. Bussmann-Holder, and M.-H. Whangbo, J. Phys.: Condens. Matter **255**, 376002 (2013).

- The low temperature magnetic phase diagram of $Eu_xSr_{1-x}TiO_3$
  Z. Guguchia, H. Keller, A. Bussmann-Holder, J. Köhler, and R.K. Kremer, Eur. Phys. J. B **86**, 409 (2013).

- Magnetic structure of superconducting $Eu(Fe_{0.82}Co_{0.18})_2As_2$ as revealed by single-crystal neutron diffraction
  W.T. Jin, S. Nandi, Y. Xiao, Y. Su, O. Zaharko, Z. Guguchia, Z. Bukowski, S. Price, W.H. Jiao, G.H. Cao, and T. Bruckel, Phys. Rev. B **88**, 4516 (2013).

- Evidence for Cooper pair diffraction on the vortex lattice of superconducting niobium
  A. Maisuradze, A. Yaouanc, R. Khasanov, A. Amato, C. Baines, D. Herlach, R. Henes, P. Keppler, and H. Keller, Phys. Rev. B **88**, 140509(R) (2013).

- Photo-induced persistent inversion of germanium in a 200-nm-deep surface region
  T. Prokscha, K. H. Chow, E. Stilp, A. Suter, H. Luetkens, E. Morenzoni, G. J. Nieuwenhuys, Z. Salman, and R. Scheuermann, Scientific Reports **3**, 2569 (2013).

- Pressure Effects in the Iron Chalcogenides
  M. Bendele, E. Pomjakushina, K. Conder, R. Khasanov, and H. Keller,
  J. Supercond. Nov. Magn., published online 14 November 2013.

- Effect of pressure on the Cu and Pr magnetism in $Nd_{1-x}Pr_xBa_2Cu_3O_{7-\delta}$ investigated by muon spin rotation
  A. Maisuradze, B. Graneli, Z. Guguchia, A. Shengelaya, E. Pomjakushina, K. Conder, and H. Keller,
  Phys. Rev. B **87**, 054401 (2013).

- Oxygen stoichiometry of low-temperature synthesized metastable T'-La_2CuO_4
  R. Hord, F. Pascua, K. Hofmann, G. Cordier, J. Kurian, H. Luetkens, V. Pomjakushin, M. Reehuis, B. Albert, and L. Alff, Supercond. Sci. Technol. **26**, 105026 (2013).

- Low temperature ballistic spin transport in the S=1/2 antiferromagnetic Heisenberg chain compound $SrCuO_2$
  H. Maeter, A.A. Zvyagin, H. Luetkens, G. Pascua, Z. Shermadini, R. Saint-Martin, A. Revcolevschi, C. Hess, B. Buechner, and H.H. Klauss, J. Phys.: Condens. Matter **25**, 365601 (2013).

- Short-range magnetic order and effective suppression of superconductivity by manganese doping in $LaFe_{1-x}Mn_xAsO_{1-y}F_y$
  R. Frankovsky, H. Luetkens, F. Tambornino, A. Marchuk, G. Pascua, A. Amato, H.H. Klauss, and D. Johrendt,
  Phys. Rev. B **87**, 174515 (2013).

- Evidence for superconductivity with broken time-reversal symmetry in locally noncentrosymmetric SrPtAs
  P.K. Biswas, H. Luetkens, T. Neupert, T. Stuerzer, C. Baines, G. Pascua, A.P. Schnyder, M.H. Fischer, J. Goryo, M.R. Lees, H. Maeter, F. Brueckner, H.H. Klauss, M. Nicklas, P.J. Baker, A.D. Hillier, M. Sigrist, A. Amato, and D. Johrendt, Phys. Rev. B **87**, 180503 (2013).

- Lattice and polarizability mediated spin activity in $EuTiO_3$
  K. Caslin, R.K. Kremer, Z. Guguchia, H. Keller, J. Köhler, and A. Bussmann-Holder,
  J. Phys.: Condens. Matter **26**, 022202 (2014).

- Existence of anisotropic spin fluctuations at low temperature in the normal phase of the superconducting ferromagnet UCoGe
M. Taupin, L. Howald, D. Aoki, J. Flouquet and J. P. Brison, Phys. Rev. B **89**, 041108 (2014).

- Modifications of the Meissner screening profile in $YBa_2Cu_3O_{7-\delta}$ thin films by gold nanoparticles
E. Stilp, A. Suter, T. Prokscha, Z. Salman, E. Morenzoni, H. Keller, C. Katzer, F. Schmidl and M. Döbeli, Phys. Rev. B **89**, 020510(R) (2014).

- Magnetic field distribution and characteristic fields of the vortex lattice for a clean superconducting niobium sample in an external field applied along a three-fold axis
A. Yaouanc, A. Maisuradze, N. Nakai, K. Machida, R. Khasanov, A. Amato, P.K. Biswas, C. Baines, D. Herlach, R. Henes, P. Keppler, and H. Keller, Phys. Rev. B **89** 184503 (2014).

PhD theses

- Investigations of Superconductivity and Magnetism in Iron-Based and Cuprate High-Temperature Superconductors
Zurab Guguchia, PhD Thesis, Physik-Institut, Universität Zürich, 2013.

- Torque Magnetometry Studies of High-Temperature Superconductors and Magnetic Materials
Saskia Bosma, PhD Thesis, Physik-Institut, Universität Zürich, 2013.

- Structural and Magnetic Properties of the Insulating T'-RE_2CuO_4 Parent Compounds of Electron-Doped Superconductors
Gwendolyne Banasan Pascua, PhD Thesis, Physik-Institut, Universität Zürich, 2014.

Articles in press

- Superconductivity in a new layered bismuth oxyselenide: $LaO_{0.5}F_{0.5}BiSe_2$
A. Krzton-Maziopa, Z. Guguchia, E. Pomjakushina, V. Pomjakushin, R. Khasanov, H. Luetkens, P.K. Biswas, A. Amato, H. Keller, and K. Conder, J. Phys.: Condens. Matter.

Conference reports

- Influence of photo illumination on the Meissner screening profile of underdoped $YBa_2Cu_3O_{7-\delta}$
E. Stilp, A. Suter, E. Morenzoni, T. Prokscha, Z. Salman, H. Keller, P. Pahlke, R. Huehne, J. C. Baglo, R. Liang, R. F. Kiefl,
Swiss Workshop on Materials with Novel Electronic Properties, Les Diablerets, Switzerland, June 24-28, 2013.

- Microscopic Coexistence and Competition of Magnetism and Superconductivity in $Ba_{1-x}K_xFe_2As_2$: A Structural, Magnetic, and Superconducting Phase Diagram
G. Pascua, H. Luetkens, E. Wiesenmayer, Z. Shermadini, R. Khasanov, A. Amato, H. Maeter, H.-H. Klauss, H. Keller, E. Morenzoni, and D. Johrendt,
Swiss Workshop on Materials with Novel Electronic Properties, Les Diablerets, Switzerland, June 24-28, 2013.

- Strong Pressure Dependence of the Magnetic Penetration Depth in Single Crystals of the Heavy-Fermion Superconductor $CeCoIn_5$ Studied by Muon Spin Rotation
L. Howald, A. Maisuradze, P. Dalmas de Reótier, A. Yaouanc, C. Baines, G. Lapertot, K. Mony, J.-P. Brison and H. Keller,
Joint Annual Meeting of the Austrian Physical Society and Swiss Physical Society, Linz, September 3-6, 2013.

- Magnetic phase diagram of thin film $La_{2-x}Sr_xCuO_4$ studied by low energy muon spin rotation
E. Stilp, B. M. Wojek, H. Keller, A. Suter, T. Prokscha, H. Luetkens, E. Morenzoni, A. Gozar, G. Logvenov, and I. Bozovic, APS March Meeting, Denver, USA, March 3-7, 2014.

- Probing Spin Fluctuations in the Paramagnetic Phase of $EuTiO_3$ by Muon Spin Rotation techniques
Z. Guguchia, H. Keller, A. Shengelaya, J. Köhler, and A. Bussmann-Holder,
APS March Meeting, Denver, USA, March 3-7, 2014.

- Muon-spin rotation and magnetization studies of chemical and hydrostatic pressure effects in $EuFe_2(As_{1-x}P_x)_2$
Z. Guguchia, A. Shengelaya, A. Maisuradze, L. Howald, Z. Bukowski, M. Chikovani, H. Luetkens, S. Katrych, J. Karpinski, and H. Keller, APS March Meeting, Denver, USA, March 3-7, 2014.

- Lattice and polarizability mediated spin activity in $EuTiO_3$: muon spin rotation and magnetization studies
  Z. Guguchia, K. Caslin, R. Kremer, P. Reuvenkamp, H. Keller, A. Shengelaya, J. Köhler, and A. Bussmann-Holder, German Physical Society (DPG) Spring Meeting, Dresden, Germany, March 31 - April 4, 2014.

Invited lectures

- E. Stilp: Direct investigation of the Meissner screening in $YBa_2Cu_3O_{6+x}$ by low-energy muon-spin rotation
  Colloquia at the Institute of Solid State Physics, Friedrich-Schiller-University Jena, Germany, July 6, 2013.
- Z. Guguchia: Tuning the Structural and Magnetic Phase Transitions of $EuTiO_3$ by Sr Doping: the Phase Diagram of $Eu_xSr_{1-x}TiO_3$
  13^{th} International Meeting on Ferroelectricity, Krakow, Poland September 2-6, 2013.
- Z. Guguchia: Probing Spin Fluctuations in the Paramagnetic Phase of $EuTiO_3$ by Muon Spin Rotation
  13^{th} International Meeting on Ferroelectricity, Krakow, Poland September 2-6, 2013.
- H. Keller: The interplay of magnetism and lattice dynamics in the perovskite oxide system $Sr_{1-x}Eu_xTiO_3$ $(0 \leq x \leq 1)$
  European Congress and Exhibition on Advanced Materials and Processes, EUROMAT 2013, Sevilla (Spain), September 8 - 13, 2013.
- L. Howald: Superconductivity, Quantum Critical Points and Magnetism in the Heavy Fermion System $CeCoIn_5$
  Seminar of the Laboratory for Synchrotron Radiationï£¡-Condensed Matter (LSC), Paul Scherrer Institut, Villigen, Switzerland, November 27, 2013.

21.3.2 Phase transitions and superconducting photon detectors

Articles

- Separating the bulk and surface n- to p-type transition in the topological insulator $GeBi_{4-x}Sb_xTe_7$
  S. Muff, F. von Rohr, G. Landolt, B. Slomski, A. Schilling, R. J. Cava, J. Osterwalder and J. H. Dil, Phys. Rev. B **88** (2013) 035407.
- AC-magnetic susceptibility in the peak-effect region of Nb_3Sn
  O. Bossen, A. Schilling, and N. Toyota, Physica C **492** (2013) 133-137.
- Structure and magnetic interaction in the solid solution $Ba_{3-x}Sr_xCr_2O_8$
  H. Grundmann, A. Schilling, C. A. Marjerrison, H. A. Dabkowska and B. D. Gaulin, Mat. Res. Bull. **48** (2013) 3108-3111.
- Conventional superconductivity and CDW ordering in $Ba_{1-x}Na_xTi_2Sb_2O$
  F. von Rohr, A. Schilling, R. Nesper, C. Baines and M. Bendele, Phys. Rev. B **88** (2013) 140501(R).
- Numerical analysis of detection-mechanism models of superconducting nanowire single-photon detector
  A. Engel and A. Schilling, J. Appl. Phys. **114**, (2013) 214501.
- Superconductivity in rubidium substituted $Ba_{1-x}Rb_xTi_2Sb_2O$
  F. von Rohr, R. Nesper and A. Schilling, Phys. Rev. B **89** (2014) 094505.
- Low-temperature magnetic fluctuations in the Kondo insulator SmB_6
  P.K. Biswas, Z. Salman, T. Neupert, E. Morenzoni, E. Pomjakushina, F. von Rohr, K. Conder, G. Balakrishnan, M. Ciomaga Hatnean, M.R. Lees, D. McK. Paul, A. Schilling, C. Baines, H. Luetkens, R. Khasanov, and A. Amato, Phys. Rev. B **89**, (2014) 161107(R).

PhD-Theses

- Superconducting Nanowires for Soft X-Ray Single-Photon Detectors
  Kevin Inderbitzin, PhD thesis, Physik-Institut, Universität Zürich, 2013.
- Calorimetric and Magnetic Studies on the Vortex Lattice of Low-T_c Superconductors
  Olaf Bossen, PhD thesis, Physik-Institut, Universität Zürich, 2013.

Contributed Conference Presentations

- A. Engel: Superconducting Nanowires for Soft X-Ray Single-Photon Detection
  Swiss Workshop on Materials with Novel Electronic Properties 2013, Les Diablerets, 27.6.2013.

- F. von Rohr: Characterization of the Bulk Properties and Surface States of the Topological Insulator $GeBi_4Te_7$
  14th European Conference on Solid State Chemistry (ECSSC14), Bordeaux (France), 10.7.2013.

- A. Engel: Vortices in SNSPD: Magnetic field dependence of dark and photon count rates
  11th European Conference on Applied Superconductivity (EUCAS 2013), Genova (Italy), 16.9.2013.

- A. Engel: Detection mechanism in SNSPD: comparison of numerical models with experimental data (Poster)
  11th European Conference on Applied Superconductivity (EUCAS 2013), Genova (Italy), 18.9.2013.

- F. von Rohr: Chemistry of Topological Insulators
  Christmas Symposium at the Laboratory of Inorganic Chemistry, ETH Zürich, 11.12.2013.

Invited Lectures

- A. Engel: Detection-mechanism models of superconducting single-photon detectors
  Quantum Optics Seminar, University of Leiden, The Netherlands, 8.11.2013.

- A. Schilling: Experimental tests for macroscopic phase coherence of magnetic-quasiparticle condensates in insulating spin systems
  Solid-State Physics Seminar, ETH Zürich, 12.12.2013.

21.3.3 Surface Physics

Articles

- Immobilizing individual atoms beneath a corrugated single layer of boron nitride
  H. Y. Cun, M. Iannuzzi, A. Hemmi, S. Roth, J. Osterwalder, and T. Greber, Nano Letters 13, 2098 (2013).

- Chemical vapor deposition and characterization of aligned and incommensurate graphene/hexagonal boron nitride heterostack on Cu(111)
  S. Roth, F. Matsui, T. Greber, J. Osterwalder, Nano Letters 13, 2668 (2013).

- Separating the bulk and surface n- to p- transition in the topological insulator $GeBi_{4-x}Sb_xTe_7$
  S. Muff, F. von Rohr, G. Landolt, B. Slomski, A. Schilling, R. J. Cava, J. Osterwalder, J. H. Dil,
  Phys. Rev. B 88, 035407 (2013).

- Bulk and surface Rashba splitting in single termination BiTeCl
  G. Landolt, S. V. Eremeev, O. E. Tereshchenko, S. Muff, B. Slomski, A. Kokh, M. Kobayashi, T. Schmitt, V. N. Strocov, J. Osterwalder, E. V. Chulkov, J. H. Dil, New J. Phys. 15, 085022 (2013).

- Tuning of the Rashba effect in Pb quantum well states via a variable Schottky barrier
  B. Slomski, G. Landolt, G. Bihlmayer, J. Osterwalder, J. H. Dil, Sci. Rep. 3, 1963 (2013).

- Trends in adsorption characteristics of benzene on transition metal surfaces: role of surface chemistry and van der Waals interactions
  H. Yildirim, T. Greber, A. Kara, J. Phys. Chem. C 117, 20572 (2013).

- Moiré beatings in graphene on Ru(0001)
  M. Iannuzzi, I. Kalichava, H. F. Ma, S. J. Leake, H. T. Zhou, G. Li, Y. Zhang, O. Bunk, H. J. Gao, J. Hutter,
  P. R. Willmott, T. Greber, Phys. Rev. B 88, 125433 (2013).

- Note: an ion source for alkali metal implantation beneath graphene and hexagonal boron nitride monolayers on transition metals
  L. H. de Lima, H. Y. Cun, A. Hemmi, T. Kälin, T. Greber, Rev. Sci. Instrum. 84, 126104 (2013).

- Interband spin-orbit coupling between anti-parallel spin states in Pb quantum well states
  B. Slomski, G. Landolt, S. Muff, F. Meier, J. Osterwalder, J. H. Dil, New J. Phys. 15, 125031 (2013).

- Implantation length and thermal stability of interstitial Ar atoms in boron nitride nanotents
  H. Y. Cun, M Iannuzzi, A. Hemmi, J. Osterwalder, T. Greber, ACS Nano 8, 1014 (2014).

- Spin texture of Bi_2Se_3 thin films in the quantum tunneling limit
  G. Landolt, S. Schreyeck, S. V. Eremeev, B. Slomski, S. Muff, J. Osterwalder, E. V. Chulkov, C. Gould, G. Karczewski, K. Brunner, H. Buhmann, L. W. Molenkamp, J. H. Dil, Phys. Rev. Lett. 112, 057601 (2014).

- Versatile attosecond beamline in a two-foci configuration for simultaneous time-resolved measurements
  R. Locher, M. Lucchini, J. Herrmann, M. Sabbar, M. Weger, A. Ludwig, L. Castiglioni, M. Greif, M. Hengsberger, L. Gallmann, U. Keller, Rev. Sci. Instrum. 85, 013113 (2014).

- Low-cost photoelectron yield setup for surface process monitoring
  A. Hemmi, H. Y. Cun, S. Roth, J. Osterwalder, T. Greber, J. Vac. Sci. Technol. A 32, 02302 (2014).

- Tunneling, remanence, and frustration in dysprosium-based endohedral single-molecule magnets
  R. Westerström, J. Dreiser, C. Piamonteze, M. Muntwiler, S. Weyeneth, K. Krämer, S. X. Liu, S. Decurtins, A. Popov, S. F. Yang, L. Dunsch, T. Greber, Phys. Rev. B 89, 060406(R) (2014).

- High-quality single-atomic-layer deposition of hexagonal boron nitride on single-crystalline Rh(111) four-inch wafers
  A. Hemmi, C. Bernard, H. Y. Cun, S. Roth, M. Klöckner, T. Kälin, M. Weinl, S. Gsell, M. Schreck, J. Osterwalder, T. Greber, Rev. Sci. Instrum. 85, 035101 (2014).

PhD thesis

- Graphene on metal surfaces and hexagonal boron nitride
  Silvan Roth, PhD Thesis, Physik-Institut, Universität Zürich, 2013.

Contributed conference presentations

- Growth and characterization of graphene/hexagonal boron nitride heterostrack on Cu(111)
  J. Osterwalder, Graphene 2013, Bilbao, Spain, 26.04.13

- Reaction of tetrahuydrofuran on Si(001) studied by STM and XPS
  G. Mette, Gordon Research Conference - Chemical Reactions at Surfaces, Les Diablerets, 29.04.13

- Nanotents - immobilizing single atoms beneath a monolayer of boron nitride
  H. Y. Cun, Graphene Week 2013, Chemnitz, Germany, 07.06.13

- Adsorption of tetrahyudrofuran on a Si(001) surface studied by STM, XPS and UPS
  G. Mette, 8th MolCHsurf Discussion Meeting, Bern, 10.06.13

- A novel route towards absolute photoemission delays from surfaces by sub-cycle-resolved laser-assisted photoemission
  L. Castiglioni, ATTO 2013, Paris, France, 10.07.2013

- Tunneling, remanence, and frustration in endohedral single-molecule magnets on surfaces
  R. Westerström, International Symposium on Atomic-Level Characterization (ALC'13), Kona, Hawaii, USA, 14.12.2013

- Nanoscale lateral segregation on h-BN/PtRh(111)
  T. Greber, Symposium on Surface Science (3S Conference), St. Christoph, Austria, 12.03.14

Invited lectures

- T. Greber: Single atom magnets on surfaces: from spin shuttles to nanotents
  Workshop on Surface Supported Molecular Nanostructures: Foundations and Functionality, Institute of Advanced Studies Garching, 11.04.13

- T. Greber: UZH on the Graphene Flagship
  Kick-off Meeting, Work Package Materials, Flagship Graphene, Madrid, Spain, 20.06.13

- T. Greber: sp^2-hybridized single layers: from templates to nanotents
  International Workshop on Nanomaterials and Nanodevices, Beijing, China, 02.07.13
- T. Greber: Endohedral single-molecule magnets 1-2-3
  International Workshop on Nanomaterials and Nanodevices, Guilin, China, 05.07.13
- J. Osterwalder: Surface science approach to graphene and boronitrene (keynote talk)
  1st Hayashi Conference, Hayama, Japan, 19.07.13.
- J. Osterwalder: A surface scientist's view on topological insulators
  12th PSI Summer School on Condensed Matter Research, Zuoz, 21.08.13
- J. Osterwalder: Functionalities from corrugated sp^2-bonded monolayers
  International Vacuum Congress (IVC-19), Paris, France, 13.09.13
- T. Greber: Nanotents and controlled 2 nm hole formation in single layers of graphene and hexagonal boron nitride
  International Symposium on Atomic Level Characterization (ALC'13), Kona, Hawaii, USA, 15.12.13
- T. Greber: Ion implantation beneath a boron nitride super-honeycomb: nanotent formation and 'can-opener' effect
  Seminar, Abt. Kern, Max-Planck-Institut für Festkörperphysik, Stuttgart, Germany, 18.12.13
- T. Greber: Nanotents
  Symposium on Surface and Nano Science (SSNS14), Furano, Japan, 17.01.14
- T. Greber: Spin shuttles: single-molecule magnets on surfaces
  Seminar, Nara Institute of Science and Technology (NAIST), Nara, Japan, 20.01.14

- M. Hengsberger: Attosecond dynamics of photoexcitations in solids
  4th Assembly Meeting of the NCCR MUST, Engelberg, 08.01.14
- T. Greber: Physics with a monolayer of hexagonal boron nitride: from nanomesh to nanotents
  Solid State Physics Seminar, ETHZ, 20.03.14
- T. Greber: Building blocks for molecular spintronics: from C_{60} to spin shuttles on surfaces
  Hauptvortrag, Frühjahrstagung der Deutschen Physikalischen Gesellschaft, Dresden, Germany, 31.03.14

21.3.4 Biological systems

Articles

- Coherent microscopy at resolution beyond diffraction limit using post-experimental data extrapolation
  T. Latychevskaia and H.-W. Fink, Appl. Phys. Lett. 103(20), 204105 (2013).
- Graphene Unit Cell Imaging by Holographic Coherent Diffraction
  J.-N. Longchamp, T. Latychevskaia, C. Escher, and H.-W. Fink, Phys. Rev. Lett. 110(25), 255501 (2013).
- Pulsed electron holography
  M. Germann, T. Latychevskaia, C. Escher, and H.-W. Fink, Appl. Phys. Lett. 102(20), 203115 (2013).
- Coherent diffraction and holographic imaging of individual biomolecules using low-energy electrons
  T. Latychevskaia, J.-N. Longchamp, C. Escher, and H.-W. Fink,
  in *Present and Future Methods for Biomolecular Crystallography* (Springer, 2013).
- Resolution enhancement in digital holography by self-extrapolation of holograms
  T. Latychevskaia and H.-W. Fink, Optics Express 21(6), 7726-7733 (2013).
- Electron beam collimation with a 40 000 tip metallic double-gate field emitter array and in-situ control of nanotip sharpness distribution
  P. Helfenstein, V. A. Guzenko, H.-W. Fink, S. Tsujino, J. Appl. Phys. 113(4) 043306 (2013).

Articles in press

- Low-energy electron holographic imaging of gold nanorods supported by ultraclean graphene
  J.-N. Longchamp, C. Escher, T. Latychevskaia, and H.-W. Fink, Ultramicroscopy, (2014).

- On artefact-free reconstruction of low-energy (30âĂŞ250 eV) electron holograms
  T. Latychevskaia, J.-N. Longchamp, C. Escher, and H.-W. Fink, Ultramicroscopy, (2014).

Oral presentations

- T. Latychevskaia, J.-N. Longchamp, and H.-W. Fink:
  On the reconstruction of ultra low-energy electron holograms and diffraction pattern
  Microscopy Conference, Regensburg (Germany), 25-30 August 2013.

- J.-N. Longchamp, C. Escher and H.-W. Fin: Ultra-clean freestanding graphene by Pt-metal catalysis
  Graphene 2013 Bilbao, Spain, April 23 - 26, 2013.

- T. Latychevskaia, Jessica Britschgi and H.-W. Fink: Holographic time-resolved particle tracking using 3D-deconvolution
  Digital Holography and 3-D Imaging 2013, OSA Meeting, Hawaii, 21-25 April 2013.

- T. Latychevskaia and H.-W. Fink: Imaging outside the box: Resolution enhancement by hologram self-extrapolation
  Digital Holography and 3-D Imaging 2013, OSA Meeting, Hawaii, 21-25 April 2013.

- J.-N. Longchamp, T. Latychevskaia, C.Escher and H.-W. Fink: Probing the surface of graphene by means of low-energy electron coherent diffraction and holographic imaging
  Symposium on Surface Science, Åre (Sweden), March 3-9, 2013.

21.3.5 Disordered and Biological Soft Matter

Articles

- Mechanical Control of Organ Size in the Development of the Drosophila Wing Disc
  T. Schluck, U. Nienhaus, T. Aegerter-Wilmsen, and C.M. Aegerter, PLoSOne **8**, e76171 (2013).

- Coarsening dynamics of three dimensional levitated foams: from wet to dry
  N. Isert, G. Maret, and C.M. Aegerter, Europ. Phys. J. E, **36**, 116 (2013).

- Reply to comment on Direct determination of the transition to localization of light in three dimensions
  G. Maret, T. Sperling, W. Bührer, A. Lubatsch, R. Frank, and C.M. Aegerter, Nature Photonics **7**, 934 (2013).

- Direct imaging of fluorescent structures behind turbid layers
  G. Ghielmetti, and C.M. Aegerter, Optics Express **22**, 1981 (2014).

Theses

- On growth and From and Patterning of Drosophila Wing Imaginal Discs
  U. Nienhaus, PhD Thesis, Universität Zürich, 2013.

- Mechanical Perturbation and Stimulation of Drosophila Wing Imaginal Discs
  T. Schluck, PhD Thesis, Universität Zürich, 2013.

- Experimental Study on bending properties of zebrafish fins
  S. Puri, Master Thesis, Universität Zürich, 2014.

Conference reports

- Direct determination of the transition to Anderson localization of light (poster)
  T. Sperling, W. Bührer, C.M. Aegerter, and G. Maret,
  Workshop "ondes et images", Cargese, France (May27 - June 1, 2013)

- Determination of the transmission matrix through thick turbid samples (poster)
  M. Ackermann, T. Sperling, G. Maret, and C.M. Aegerter,
  Workshop "ondes et images", Cargese, France (May27 - June 1, 2013)

- Mechanical stresses and boundaries. (poster)
  U. Nienhaus, and C.M. Aegerter, Swiss Drosophila Day; ETH, Zurich, Switzerland (June 7, 2013).

- Mechanical growth regulation of Drosophila wing discs. (poster)
  U. Nienhaus, T. Aegerter-Wilmsen, T. Schluck, M.B. Heimlicher, K. Basler and C.M. Aegerter,
  Gordon Research Conference on soft condensed matter; Colby College, New London, USA (August 19-23, 2013).

- Transition in the coarsening dynamics of foams with different liquid content. (poster)
  N. Isert, G. Maret and C.M. Aegerter,
  Gordon Research Conference on soft condensed matter; Colby College, New London, USA (August 19-23, 2013).

- Transition in the coarsening dynamics of foams with different liquid content. (poster)
  N. Isert, G. Maret and C.M. Aegerter, Soft Matter Conference; Rome, Italy (September 16-19, 2013).

- The role of mechanical forces in the regulation of organ growth (poster)
  D. Eder, C.M. Aegerter, and K. Basler, Physics of living matter, Cambridge, UK (September 19-20, 2013)

- Mechanical growth regulation of Drosophila wing discs. (poster)
  T. Aegerter-Wilmsen, T. Schluck, U. Nienhaus, M.B. Heimlicher, K. Basler and C.M. Aegerter,
  Physics of Biology meeting; Geneva, Switzerland (November 26-28, 2013).

Invited lectures

- C.M. Aegerter: Light transport in turbid media: from Anderson localization to imaging
  Physics Colloquium, University of Bayreuth, Germany (07.05.2013).

- C.M. Aegerter: Transition in the coarsening dynamics of foams with different liquid content
  ESA workshop "emulsions in space", Noordwijk, The Netherlands (13.05.2013).

- C.M. Aegerter: Mechanical growth control in the wing imaginal disc of Drosophila
  The Physics of emergent behaviour, Brighton, U.K. (24.06.2013).

- C.M. Aegerter: Microscopy with scattered light
  Biophysics Seminar at the Ecole Normale Superieur, Paris, France. (13.09.2013).

- C.M. Aegerter: Growth control via mechanical feedback in the wing disc of Drosophila
  International Soft Matter conference, Rome, Italy (16.09.2013).

- C.M. Aegerter: Die Physik der Farben
  Weiterbildung für Gymnasiallehrpersonen, University of Zurich (24.10.2013).

- C.M. Aegerter: Growth control via mechanical feedback in the wing disc of Drosophila
  Workshop on "Mechanics and growth of tissues: From Development to Cancer", Institut Curie, Paris, France (14.01.2014).

- C.M. Aegerter: Spannung mit Strom und Magneten
  Project day in Physics, Primarschule Elsau, Switzerland, (24.01.2014).

- C.M. Aegerter: Growth control via mechanical feedback in the wing disc of Drosophila
  MRC Laboratory for molecular cell biology, University College London, London, UK (29.01.2014).

21.4 Bachelor and Master Theses

21.4.1 Bachelor theses

- Rating and Ranking Method for Financial Market Assets Based on Stability Criteria
  Michael F. Dimmler

- 4d particle tracking by holography
  Jessica Britschgi

- Study of charge sharing in the LHCb Tracker Turicensis using proton-proton collisions at the LHCb
  Philipp Gloor

- Generation of ultrashort pulses via hollow fiber compression
  Michael Locher

- Mass model of Abell 2029
  Christina Wentz

- Hydrodynamic simulations of collisions between planets and protoplanets
  Christian Reinhardt

- Jitter-Messungen an TaN-basierten supraleitenden Einzelphotonenzählern
  Daniel Destraz

- Strukturelle und magnetische Eigenschaften des Spin-Dimer-Systems $Ba_{3-x}Sr_xCr_20_8$
  Leonie Ulrich

- Nanostruktur der Zebrafischhaut
  Rubina Arulanantham

- Höhenstrahlungsexperiment
  Nathalie E. Chételat Soto

- Comparison of Measured and Simulated Light Yield in Plastic Scintillators
  Markus Baumgartner

- Avalanche Photodiode Testing in Liquid Xenon
  Michael Miloradovic

- Monte Carlo simulation of the liquid xenon detector response to low-energy neutrons
  Dario Biasini

- Photomultiplier Tube Test in Liquid Xenon for Direct Dark Matter Detection Experiments
  Andrea Gmür

- Aufbau eines Teststandes für die Produktion einer AMC Kleinserie
  Michael Hochstrasser

- Calculation of two Master Integrals for $qq \to VV$
  Yanick Volpez

- Der Stern-Gerlach Versuch - Stolpersteine eines historischen Experiments
  Ruth Bründler Denzer

- Towards Freestanding Hexagonal Boron Nitride: Delamination by Etching and Bubbling
  Ronny Rüttimann

21.4.2 Master theses

- Inbetriebnahme einer spinpolarisierten Elektronenquelle und Nachweis der Spinpolarisation
  Eveline U. Eisenring

- Study of the molecular switch of TBA/Au(111) by photoelectron diffraction and absorption spectroscopy
  Adrian Schuler

- Angle-Resolved Photoemission Spectroscopy of the Topological Insulator $GeBi_{4-x}Sb_xTe_7$
  Stefan Muff

- Determination of the Binding Energy of Water to GFP with TDS
  Simon Obrecht

- Constraints on Scalar Field Models from Tests of General Relativity
  Andreas Schärer

- The Role of Mergers in the Formation of Boxy Galaxies
  Rebekka Bieri

- Optical Characterisation of Quantum Dots
  Michael Locher

- A study on 3-pt Hanbury-Brown and Twiss Interferometry
  Christina Wentz

- Study of molecular switch of TBA/Au(111) by photoelectron diffraction and absorption spectroscopy
  Adrian Schuler